Energy-Efficient Bipedal Locomotion Using Hybrid Zero Dynamics and Elastic Couplings: Modeling, Control, and Optimization

---

Zur Erlangung des akademischen Grades eines

DOKTORS DER INGENIEURWISSENSCHAFTEN (Dr.-Ing.)

von der KIT-Fakultät für Maschinenbau des
Karlsruher Instituts für Technologie (KIT)
genehmigte

DISSERTATION

von

M.Sc. Yinnan Luo

Tag der mündlichen Prüfung: 6. Juni 2025
Hauptreferent: Prof. Dr.-Ing. habil. Alexander Fidlin
Korreferent: Prof. Dr.-Ing. Ulrich J. Römer

Vorwort

Die vorliegende Dissertation entstand während meiner Tätigkeit als wissenschaftlicher Mitarbeiter am Institut für Technische Mechanik (ITM), Bereich Dynamik/Mechatronik, des Karlsruher Instituts für Technologie (KIT).
Mein besonderer Dank gilt **Herrn Prof. Dr.-Ing. habil. Alexander Fidlin** für die Übernahme des Hauptreferats. Sein Vertrauen und seine stets konstruktiven Anregungen haben diese Arbeit maßgeblich geprägt und meine persönliche Entwicklung nachhaltig gefördert.
Ebenso danke ich **Herrn Prof. Dr.-Ing. Ulrich J. Römer** für die fachliche Betreuung, die zahlreichen Impulse und die engagierten Diskussionen, aus denen immer wieder neue Ideen hervorgingen.
Mein Dank gilt ferner **Frau Prof. Dr.-Ing. Luise Kärger**, die als Prüfungsvorsitzende für einen reibungslosen und angenehmen Ablauf der Verteidigung sorgte.
Für die hervorragende Zusammenarbeit am Institut danke ich **Herrn Prof. Dr.-Ing. Carsten Proppe** sowie **Herrn Prof. Dr.-Ing. Wolfgang Seemann** für ihre wertvollen Hinweise zu Beginn meiner Doktorandenzeit. Besonderer Dank gilt auch den emeritierten Professoren **Herrn Prof. Dr.-Ing. Dr. h. c. Jörg Wauer**, **Herrn Prof. Dr.-Ing. Walter Wedig** und **Herrn Prof. Dr.-Ing. Dr. h. c. Jens Wittenburg**, die trotz Ruhestands weiterhin aktiv am Institutsleben – insbesondere an den Abteilungsseminaren – teilnahmen und mit ihren Kommentaren maßgeblich zum Gelingen dieser Arbeit beitrugen.
Für die intensive Zusammenarbeit im Rahmen des DFG-Projekts (Grant FI 1761/4-1 | ZE 714/16-1) danke ich **Frau Prof. Dr.-Ing. habil. Lena Zentner**, **Herrn Dr.-Ing. Erik Gerlach** und **Herrn Marten Zirkel** vom Fachgebiet Mechanik Nachgiebiger Systeme der Technischen Universität Ilmenau.
Den Kolleginnen und Kollegen des ITM danke ich für die stets hilfsbereite Zusammenarbeit in Lehre, Forschung und allen weiteren Institutsaufgaben. Ihr seid für mich weit mehr als Arbeitskollegen – ihr seid zu engen Freunden geworden. Besonderer Dank gilt meinem langjährigen Bürokollegen **Alexander Bitner** für den intensiven fachlichen Austausch und die vielen persönlichen Gespräche.

Mein Dank gilt ebenso allen Bachelor-, Master- und hilfswissenschaftlichen Studierenden, deren Arbeiten ich betreuen durfte. Unsere Zusammenarbeit hat kontinuierlich neue Ideen hervorgebracht und diese Dissertation bereichert.
Zu guter Letzt danke ich meiner Familie, die ich während meiner Doktorandenzeit leider nicht oft persönlich besuchen konnte, für ihre bedingungslose Unterstützung, Geduld und Ermutigung. Ohne euch wäre diese Arbeit nicht möglich gewesen.

Karlsruhe, Juni 2025
Yinnan Luo

Kurzfassung

Zweibeinige Roboter bieten das Potenzial, unterschiedliche Geländearten zu überwinden und Aufgaben mit hoher Mobilität und Agilität auszuführen. Dennoch bestehen weiterhin erhebliche Herausforderungen hinsichtlich der Energieeffizienz und der komplexen hybriden Dynamik. In dieser Dissertation werden Methoden vorgestellt, die darauf abzielen, die Energieeffizienz periodischer Geh- und Rennbewegungen eines ebenen zweibeinigen Roboters durch den Einsatz paralleler elastischer Kopplungen zu steigern, ohne dabei die Stabilität der Lokomotion bei unterschiedlichen Geschwindigkeiten und Bodenverhältnissen zu beeinträchtigen.
Es wird ein Fünf-Segmente-Modell betrachtet, das aus vier angetriebenen Drehgelenken und punktförmigen Füßen besteht. Die Gangplanung erfolgt mithilfe des Hybriden-Nulldynamik-Regelungskonzeptes, um periodische Bewegungen mit konstanter Durchschnittsgeschwindigkeit zu gewährleisten. Insbesondere werden verschiedene Gangarten untersucht, darunter Gehen mit sowohl instantaner als auch nicht-instantaner Doppelstützphase auf hartem Untergrund sowie Rennen auf hartem und nachgiebigem Boden. Die periodischen Lösungen des daraus resultierenden hybriden Dynamiksystems werden über ein Mehrfachschießverfahren ermittelt, das als numerisches Optimierungsproblem zur Minimierung des Energieverbrauchs (bewertet über die Transportkosten) formuliert ist. Zu den Nebenbedingungen zählen Stabilitätskriterien der periodischen Bewegung nach der Floquet-Theorie sowie physikalische Bedingungen in Simulation, beispielsweise das Vermeiden von Rutschen im Fußkontakt. Ein sequentielles quadratisches Programmierungsverfahren löst das Optimierungsproblem mit Nebenbedingungen für ein breites Spektrum an Lokomotionsgeschwindigkeiten.
Studien zur Energieeffizienz des starren Robotermodells ohne elastische Kopplungen zeigen, dass beim Gehen mit einer instantanen Doppelstützphase ein nahezu linearer Zusammenhang zwischen den Transportkosten und der Ganggeschwindigkeit besteht. Dabei werden insbesondere in der mittleren Phase des Einzelfußkontakts freie Schwingungen der Glieder ausgenutzt, um den Energieverbrauch im Aktuator zu verringern. Das Einführen einer nicht-instantanen Doppelstützphase verbessert zwar das Konvergenzverhältnis kleiner Störungen an den Referenz-Grenzzyklus, mindert

jedoch die Energieeffizienz, da die natürlichen, freien Systemschwingungen - bedingt durch das Punktfuß-Modell - unterdrückt werden. Auch beim Rennen auf hartem Boden ist eine lineare Abhängigkeit der normierten Energiekosten von der Geschwindigkeit zu beobachten. Ab einer kritischen Übergangsgeschwindigkeit wird Rennen energieeffizienter als Gehen. Auf nachgiebigem Untergrund steigen die Dämpfungsverluste, doch die Bodennachgiebigkeit unterstützt die Energierückgewinnung, was den Energieverbrauch im Aktuator insgesamt reduziert. Zudem werden Stoßkräfte reduziert, was die mechanische Belastung verringert.
Die gleichzeitige Optimierung der elastischen Kopplungen und der Gangtrajektorien bei einer festen Geschwindigkeit zeigt, dass die Einbindung von Nachgiebigkeit in das Starrkörper-Modell den Energieverbrauch weiter senkt. Die elastischen Komponenten werden an die natürlichen Schwingungen der Roboterglieder angepasst und reduzieren den Aktuatoraufwand. So kann kinetische Energie kurzzeitig als elastische potenzielle Energie gespeichert werden, was den Energieverlust beim Bremsen durch negative Aktuatorarbeit verringert. Im weiteren Verlauf der Bewegung wird diese gespeicherte Energie freigesetzt, um die Segmente zu beschleunigen. Bemerkenswerterweise wirkt sich die zusätzliche elastische Kopplung nicht wesentlich negativ auf die Gangstabilität aus.
Insgesamt zeigt diese Dissertation, dass sich durch den Einsatz optimal gestalteter und adaptierbarer elastischer Kopplungen die Energieeffizienz zweibeiniger Lokomotion in verschiedenen Gangarten und Umgebungen deutlich verbessern lässt. Zukünftige Forschungsarbeiten umfassen die Weiterentwicklung des optimierungsbasierten Gangplanungsverfahrens hinsichtlich höherer numerischer Genauigkeit und Recheneffizienz sowie die experimentelle Validierung der Ergebnisse an einem realen zweibeinigen Roboterprototypen.

Abstract

Bipedal robots offer the potential to traverse diverse terrains and perform tasks with high mobility and agility. However, they still face significant challenges related to efficiency and the complexities of hybrid dynamics. This dissertation presents methods for improving the energy efficiency of periodic walking and running gaits in a planar biped robot through the use of parallel elastic couplings, while preserving stable locomotion across varying speeds and ground conditions.

A five-link rigid-body model, comprising four actuated revolute joints and point feet, is employed. Gait generation is conducted using a Hybrid Zero Dynamics control framework to ensure stable periodic motions at a constant average speed. In particular, diverse gaits are systematically studied, including walking with both instantaneous and non-instantaneous double support phases on rigid ground, as well as running on both rigid and compliant ground surfaces. Periodic solutions of the resultant hybrid dynamical system are identified by a multiple shooting method, formulated as a numerical optimization problem that minimizes energy consumption evaluated by the cost of transport. Optimization constraints include stability criteria according to Floquet theory and physical gait feasibility, such as ensuring nonslip foot contact. A Sequential Quadratic Programming algorithm solves the constrained optimization problem across a range of locomotion speeds.

Efficiency studies on the rigid-body model without elastic couplings show a nearly linear dependence of the cost of transport on walking speed when using an instantaneous double support phase. Exploiting free oscillations of the robot segments, particularly in the middle of single support, helps reduce actuator effort. Introducing a non-instantaneous double support phase enhances the convergence of small perturbations back to the reference limit cycle, though it diminishes energy efficiency by suppressing the natural dynamics—a result largely attributed to the point foot model. Running on rigid ground likewise exhibits a linear relationship between cost of transport and speed, and a critical transfer speed emerges above which running becomes more efficient than walking. On compliant ground, damping losses increase due to ground deformation,

but the elasticity aids energy recovery, lowering overall actuator demands. Additionally, impact forces are smoothed, reducing mechanical stress.
Simultaneous optimization of the parallel elastic couplings and gait trajectories at a specific speed demonstrates that incorporating compliance into the rigid-body model reduces energy consumption. The elastic couplings are tuned to align with the natural oscillations of the robot segments, thereby decreasing actuation requirements. Kinetic energy is temporarily stored as elastic potential energy, aiding in deceleration and minimizing losses when the actuator performs negative mechanical work. This stored energy is subsequently released to accelerate the robot segments later in the cycle. Notably, adding elastic couplings does not substantially compromise gait stability.
Overall, this dissertation shows that integrating optimally designed and adjustable elastic couplings can markedly improve energy efficiency in bipedal locomotion across a wide range of gaits and environments. Future directions include enhancing the optimization-based gait generation framework for greater numerical accuracy and computational efficiency, as well as experimentally validating these findings on a physical biped robot prototype.

Contents

Appendix

1 Introduction

1.1 Motivation

Humans are capable of traversing intricate terrains at various speeds and inclinations with notable efficiency and adaptability [95, 162]. This capability is sustained by a harmonious interaction among muscles, tendons, bones, and neuromuscular control, wherein energy is stored in elastic tissues and subsequently released to energize the subsequent stride [101]. Replicating such versatile performance in bipedal robots has been a long-standing objective in robotics research, as enhancements in energy efficiency, resilience to disturbances, and wide-ranging applicability result from imitating the inherent dynamics that characterize human or animal locomotion [145].

The pursuit of achieving efficient, robust, and agile locomotion in engineered bipedal systems represents a fundamental challenge. This challenge is exacerbated by the underactuated characteristic of bipedal motion, characterized by only partial or point-foot contacts, and the intrinsic hybrid structure of walking and running, involving ongoing support phases interspersed with discrete impact and liftoff events [20]. This hybrid, underactuated environment complicates both the modeling of the robot's dynamics and the development of controllers to maintain dynamic stability, particularly under varying velocities or when confronted with uncertain terrain conditions [159].

Practical applications highlight the essential requirement for adaptable locomotion. In the domains of disaster response, remote exploration, or daily service operations, bipeds are required to acclimate to diverse terrains and tasks [38]. Nevertheless, numerous robots are tailored for narrowly defined environments or demonstrate optimal efficiency only at a specific speed, with their performance markedly declining outside this range [182]. This specialization constrains their practical applicability and underscores the need for systematic strategies to enhance efficiency across a broad spectrum of operational conditions.

Elastic components, such as springs, have the potential to address these challenges by facilitating the storage and release of mechanical energy and diminishing peak torque demands. Research in passive dynamic walking has, in fact, shown that high

energy efficiency can be realized solely through the utilization of gravity and the inherent geometry of the system [36, 114]. By expanding upon these concepts, the integration of elastic couplings, either in series or parallel with the actuator, can enable robots to synchronize with their inherent gait frequency [193], thereby reducing power consumption and enhancing efficiency [76].
Building upon these insights, this dissertation concentrates on the incorporation of elastic couplings into the mechanical structure of a biped and the development of suitable controllers that leverage compliance to minimize energy consumption. In particular, the investigation focuses on enhanced energy efficiency across a diverse array of gait scenarios and varying ground compliances using numerical optimization methods. Ultimately, a more profound comprehension of how to effectively exploit compliance for energy-efficient locomotion not only propels advancements in bipedal robotics but also extends its implications to broader applications, such as wearable exoskeletons [166], prosthetics [63], and service robots [58].

1.2 State of the Art

This section provides an analysis of the state-of-the-art methodologies employed in the development of bipedal robotic systems, with a specific focus on control architecture. Initially, pivotal research topics and challenges encountered in the current advancement of bipedal robots are scrutinized in 1.2.1. Thereafter, sophisticated control strategies for bipedal robots are detailed in 1.2.2. Finally, techniques for the integration of elastic couplings within the rigid body framework of the robot are explored in 1.2.3.

1.2.1 Challenges in Developing Biped Robot

Hybrid Dynamics of Bipedal Gaits

Bipedal robots face unique complexities compared to wheeled [105] or quadrupedal [99] systems. Specifically, biped walking and running motion exhibit a hybrid system structure wherein continuous-time dynamics (single support, double support, or flight phases) are interspersed with discrete foot-strike events [164].
The continuous dynamical phase can be categorized as fully actuated [98], underactuated [112], or passive [36], depending on the availability of actuators and the degrees of freedom present. Remarkably, the flight phase within the running gaits induces additional underactuation due to the brief absence of ground contact by the feet [35]. Discrete transition events occur between the continuous dynamical phases. For example, the event of contact with the ground is considered either as a discontinuous inelastic impact or is modeled through ground deformation [52]. A diverse array of foot-ground interaction models is examined in [43, 103]. These variations collectively constitute

a sophisticated hybrid dynamical system, which is crucial for the characterization of cyclic gait motions. To effectively address these challenges, it is imperative to employ advanced numerical methods that offer both high accuracy and computational efficiency in determining the numerical solutions of such multibody dynamical systems [47].
Furthermore, the inherent transitions between distinct phases and the delineation of the transition mapping pose significant complexities in the areas of stability analysis and control design, as compared to systems characterized by purely continuous dynamics [20]. The control architecture is structured to ensure stable transitions during impacts, for instance in the form of a finite-state machine [129], and to provide real-time adaptability, thereby effectively addressing disturbances and inaccuracies in modeling within both planar [72, 176] and three-dimensional gait scenarios [61].

Energy Efficiency of Locomotion

One of the primary objectives in the development of bipedal robotic systems is to achieve autonomous functionality or facilitate teleoperated control by humans, particularly in remote environments, thereby substituting human presence in contexts such as disaster response situations or space applications [38]. In these autonomous scenarios, the robot is required to carry its own energy source, for instance, a battery, which implies that the energy efficiency essentially determines the operational duration before recharging the battery.
Nonetheless, the humanoid robot DURUS [143], despite its advanced capabilities, exhibits inferior efficiency when compared to that of human beings [132]. Specifically, human locomotion attains notable efficiency in steady cyclic gaits by leveraging the body's passive dynamics to minimize actuation. During this process, kinetic energy is converted into potential energy, attributable to gravitation or tendon elasticity, which is subsequently utilized to propel the body in a cyclical manner [101]. Furthermore, as the velocity of locomotion undergoes substantial variation, humans can transition between walking and running gaits at approximately 2.0 m/s, thereby maintaining high efficiency for a range of different speeds [46].
In contrast, when bipedal gaits are derived from empirical human motion data, the robot frequently expends an inordinate amount of energy to uphold balance and gait stability, necessitating a compromise between efficiency and stability [189]. To elucidate the disparities between human and robotic gaits, preliminary insights into highly efficient bipedal walking mechanisms are gleaned from the notion of passive walkers [114]. The research demonstrates that stable, highly efficient walking on gentle slopes can be achieved without motors, provided the robot's geometry and mass distribution harness gravity effectively. Building on this, [36] studies highly efficient robots with minimum

actuation in hip and ankle joints, emphasizing that the system's natural dynamics are essential for improving locomotion efficiency.
Contemporary humanoid robots integrate passive principles within their mechanical framework by attaching and adjusting serial and parallel compliances. Also, advanced control strategies are investigated to harness natural dynamics, as reviewed in [87]. However, this approach predominantly depends on meticulous parameter tuning, which is typically determined only for a specific gait or speed. Consequently, the integration of energetic efficiency with robust disturbance rejection across a wide array of application scenarios, wherein the robot's gait varies significantly, remains an unresolved challenge in the design of bipedal systems.
In the preliminary stages of development, it is crucial to apply methodologies that systematically address both the mechanical design and the associated controller tuning in order to minimize the overall costs of development. To address this unresolved issue, this thesis introduces an optimization-based approach aimed at exploring the viability of employing parallel elastic couplings between the robot's segments to improve bipedal locomotion, encompassing both walking and running, across various scenarios.

1.2.2 Control Strategies of Actuated Biped Robot

The control architecture for bipedal robots encompasses a series of stages and methodologies dedicated to the generation, regulation, and stabilization of gait patterns. [145] concludes two fundamental steps in advanced biped robot control, including

- Motion Planning (or Motion Generation): The process of computing optimal or feasible gait trajectories, typically formulated as an offline optimization procedure that accounts for robot dynamics and environmental constraints [89].
- Trajectory Tracking (or Trajectory Regulation): The real-time control layer, which enforces convergence of the robot's measured joint or limb trajectories to the desired reference profiles derived from motion planning [130].

In actual practice, the aforementioned two steps are not distinctly delineated. For example, sophisticated robotic controllers perform motion generation through a trajectory governor in real time to improve robustness with respect to disturbances [27]. Notably, control designs based on learning are particularly adept at adapting to variations in environmental conditions [73, Section 4], or online system identification to achieve robust simulation-to-reality transfer while high-speed locomotion [111].
Within the framework of model-based controller design, the control strategy is significantly influenced by the abstraction level of the model, particularly concerning its degrees of freedom and the number of independent actuators. The inverted pendulum model, serving as a foundational element, initially facilitates the approximation of

center-of-mass dynamics in bipedal locomotion [184]. The model provides essential insights into balance and momentum transfer, thus establishing the groundwork for the development of more sophisticated methodologies. Subsequently, both model-based controller design and data-driven concepts are explored.

Zero Moment Point

As introduced in [172], the Zero Moment Point (ZMP) control approach stands as one of the most prevalently employed strategies, specifically tailored for fully or over-actuated robotic systems equipped with multiple actuators to facilitate both walking [165, 167] and running gaits [115]. The goal of ZMP control is to keep the Zero Moment Point within a support polygon, thereby preventing foot rotation or slipping [5].
A succession of humanoid robots has been engineered in Japan, incorporating ZMP-based controllers. Notably, humanoid robots such as WL and WABIAN, which encompass over 40 degrees of freedom, are equipped with vision systems and voice recognition capabilities to replicate human sensory and ambulatory functions [102]. The HRP-Series robots focus on achieving a human-like design with more than 30 degrees of freedom, and are particularly designed for roles in disaster response [84]. HRP-5P represents a more recent, large-scale humanoid model designed for demanding applications, including construction and disaster response. This model integrates high-power joints utilizing harmonic drive gears alongside advanced sensors, such as LiDAR and RGB-D cameras, complemented by robust motion planners for the facilitation of autonomous operations within complex environments [85]. Due to their significant flexibility, ZMP control criteria are often favored in industrial or service-oriented humanoids that necessitate accurate balance. However, this preference results in the primary disadvantage of the control strategy, which is its low energy efficiency.

Contact Wrench Sum

Recent advancements have led to the consideration of the Contact Wrench Sum (CWS) control criteria, serving as an alternate method to evaluate the combined wrench arising from contact and gravitational forces compared to the ZMP criteria. This ensemble is regarded as equivalent to changes in the robot's translational and rotational momentum with respect to the center of mass [37]. CWS control notably allows for the analysis of a broader spectrum of contact scenarios [71].
Consequently, CWS control expands upon the capabilities of traditional ZMP-based methods, enabling humanoid and bipedal robots to traverse uneven terrains or perform sophisticated maneuvers where multiple limbs work in unison to manage load distribution and balance, as exemplified by the ATLAS humanoid robot [39], a full-scale humanoid using hydraulic actuators and electric motors developed by Boston Dynamics

[94]. An instance of scenarios involving multiple contacts is the ATLAS robot's ability to open a door and advance through it [14].

Virtual Model Control

Virtual Model Control (VMC) conceptualizes actuators and the interaction between the robot and its environment as analogous to mechanical components such as virtual springs, dampers, or virtual linkages [139]. This viewpoint, notably, facilitates the natural and uncomplicated integration of Series Elastic Actuator (SEA), which consists of physical compliance and actuators, into the control framework [140]. A high-level finite state machine orchestrates locomotion gaits by modifying the virtual components in accordance with specific walking sequences, such as single support phase, double support phase, or discrete transition events. The simulation and experimental investigations reported in [141] demonstrate that the force-based controller is proficient in generating robust transient recovery maneuvers in response to considerable disturbances or in enabling locomotion across uneven terrain in three-dimensional spaces.
Nevertheless, a significant limitation of this approach is the necessity for a profound understanding and extensive experience with the specific robotic system to accurately select appropriate virtual components.

Hybrid Zero Dynamics

Underactuated robotic systems have attracted considerable scholarly attention due to their enhanced energy efficiency [87]. Within this class of systems, the Hybrid Zero Dynamics (HZD) controller is recognized as one of the most promising control methodologies for generating periodic locomotion gaits. This has been successfully applied to both planar walking [175] and running [188], as well as in three-dimensional underactuated robots, as documented in [61].
The control strategy is fundamentally predicated on the incorporation of either holonomic or nonholonomic virtual constraints [4, 59], which are enforced via position-based feedback control on the actuated joints. Consequently, the overall system dynamics of the biped model are confined to the zero dynamics submanifold of a reduced order, wherein the underactuated system manifests limit cycles corresponding to the periodic gait. The stability of the periodic locomotion gait can be assessed by analyzing the limit cycle of the hybrid zero dynamics using the Poincaré map method as referenced in [175, 176].
Robots, including RABBIT [34], MABEL [60, 161], ATRIAS [74], DURUS [91], and Cassie [31], have effectively demonstrated robust walking facilitated by HZD controllers. Moreover, advancements extending HZD to three-dimensional and multi-contact scenarios further expand its range of applicability [57, 61].

Model Predictive Control

Model Predictive Control (MPC) forecasts the future states of the system model and employs online optimization to implicitly ascertain the optimal control strategy [153]. Within the domain of bipedal robotic systems, MPC can function as a motion regulator, with the goal of tracking a reference trajectory formulated through offline optimization or derived from the observation of human movements. This facilitates agile locomotion even in the presence of considerable disturbances and environmental variability.
Given the stringent real-time requirements, [62] proposes a real-time iteration framework utilizing the Sequential Quadratic Programming (SQP) method in conjunction with a warm-start approach to efficiently address nonlinear-MPC challenges. [123, 124] deploy this nonlinear-MPC for the control of robots with distinct actuator mechanisms to accomplish gaits, such as trotting and jumping. [29] employs the Koopman Operator Theory [23] for data-driven system identification, thereby enhancing the MPC design to attain superior tracking performance in a soft robot.

Data-Driven Artificial Intelligence Concepts

In recent decades, dynamical systems have been characterized using traditional model-based methodologies. Despite their mathematical sophistication, these approaches frequently demand significant human expertise in the areas of modeling, tuning, and parameter identification. Conversely, contemporary Artificial Intelligence (AI) and machine learning techniques possess the capability to acquire knowledge from data, adapt to unforeseen dynamics, and enhance performance progressively [149].
In the field of robotics, encompassing design, control, and perception, AI-related methodologies are undergoing significant advancements. For example, contemporary Reinforcement Learning (RL) algorithms acquire control policies through trial and error, either in simulated environments [78] or on actual hardware [104], and are utilized to enhance traditional feedback controllers for performance optimization [82]. In the context of bipedal locomotion, the reward function frequently encodes parameters such as stability and energy efficiency. Techniques such as domain randomization facilitate the bridging of the reality gap, enabling the safe transfer of policies from simulation to physical robots [100]. Gait generators can be trained utilizing motion capture data from humans [158] to accommodate varying speeds and inclined ground surfaces [159]. The utilization of learning-based control for online gait adaptation in response to environmental condition changes is demonstrated through experiments in [77]. AI algorithms are capable of simultaneously optimizing both a robot's mechanical structure and its controller, thus enhancing energy efficiency [33].
The incorporation of classical control techniques, in conjunction with learning-based and data-driven methodologies, continues to enhance the agility and autonomy of

bipedal robots. However, learning-based approaches generally necessitate extensive data collection [119], which can be both costly and hazardous when applied to high-value humanoid prototypes. Consequently, such learning-based strategies are not addressed within this thesis, though their consideration is left open for future investigations.

1.2.3 Application of Elastic Mechanisms in Robot Design

Adding elastic elements can substantially boost the energy efficiency of bipedal robots by storing and releasing kinetic energy and smoothing impacts. Specifically, [87, Section 2] provides an overview of the concepts of attaching elastic compliance to the rigid body system of the robot.
Among various approaches, the attachment of compliance mechanisms in either a serial or parallel configuration to the actuator at a robot's joint represents two of the most extensively researched techniques due to their straightforward modeling and manufacturing processes. Both simulation and experimental studies based on a single pendulum, as reported in [171], affirm that serial and parallel elastic compliances contribute to improved energy efficiency of actuators. In particular, the parallel compliance is adjusted to align with the pendulum's natural oscillation frequency, thereby facilitating a reduction in the drivetrain's torque. Conversely, the serial compliance is calibrated proximate to the antiresonance frequency to decrease the actuator speed, consequently leading to a substantial reduction in viscous friction losses. Furthermore, [19] underscores the critical importance of calibrating the operating equilibrium point of the parallel compliance to augment actuator efficiency. Therefore, it is imperative to employ techniques for identifying and modifying the equilibrium point appropriate to specific operational conditions. For example, [44] introduces the concept of variable stiffness in actuator design, which involves two distinct actuators: one generates the driving torque for motion, while the other alters the compliance characteristics to optimize energy savings.

Series Elastic Actuators

Series Elastic Actuators (SEA) are engineered by incorporating compliant elastic components, such as a spring, between the actuator, typically equipped with a gearbox, and the load. The drivetrain provides notable advantages, including enhanced shock tolerance attributed to the low-pass filter characteristics and the ability for temporary energy storage [138]. These actuators are commonly utilized within the Virtual Model Control framework to achieve precise force control [127], since the output torque is calculated based on the deflection angle of the spring, which is quantified by an encoder [86].
Building upon the conventional SEA architecture, [128] enhances the mechanical configuration of both the actuator and the drivetrain, yielding a compact, lightweight

actuator that exhibits high output power and mechanical efficiency. As introduced in [97], various SEA configurations have been developed, differing primarily in the specific placement of integrated compliance within the drivetrain, including a motor and a gearbox. These adaptations enable the exploration of optimal SEA designs for application in biped robots. For example, robots such as MABEL [60], ATRIAS [74], and Cassie [31] demonstrate the effectiveness of SEAs in achieving efficient bipedal locomotion.
Nevertheless, the compromise lies in the fact that stiffness has a direct effect on the control bandwidth. Consequently, a balance between impact absorption, necessitating softer springs, and control bandwidth, demanding stiffer springs, must invariably be evaluated. Especially during static motion characterized by zero angular velocity, the motor produces a static torque attributable to the compliance inherent in the serial connection, leading to the dissipation of electrical energy.

Parallel Elastic Couplings

Parallel elastic couplings represent an alternative technique to introduce elasticity into rigid body systems [148], thereby altering system resonances to align with step frequencies [193]. As a result, the actuation efforts required for locomotion are minimized. For example, springs are incorporated parallel to the knee joint of the ERNIE robot, which is a planar biped robot comprising five rigid body segments, to enhance energy efficiency [186]. In the 3D fully actuated STEPPR robot, parallel springs are also employed, where they play a significant role in supporting quasi-static loads, resulting in reduced actuator torque demands and increased efficiency [113]. Specifically, the implementation of springs in the hip and ankle joints yields substantial improvements, whereas the benefits derived from elastic couplings in other joints are comparatively less pronounced.
In contrast to SEA, the incorporation and modification of elastic couplings parallel to actuators within joints or between robotic segments are more practicable to implement, as the drivetrain and mechanical system design remain unaltered. This facilitates opportunities for advancements in the design of parallel elastic couplings, such as the implementation of real-time adjustable stiffness in the framework of variable stiffness actuators [44]. Furthermore, the rigid interface between the load and the actuator facilitates precise position control, which is beneficial within frameworks such as Hybrid Zero Dynamics control.

1.3 Research Goal

This dissertation builds upon the previously established principles by concentrating on the application of optimized parallel elastic couplings to enhance energy efficiency in bipedal locomotion, while maintaining gait stability. Due to its superior energy efficiency, the Hybrid Zero Dynamics control strategy is employed for the generation of bipedal walking and running gaits. The process of simultaneously creating highly efficient gaits and determining the optimal nonlinear characteristics of the elastic coupling is formulated as an offline optimization problem. This problem is resolved using gradient-based optimization algorithms, thus enabling an efficient numerical evaluation across a wide range of gait scenarios within the context of the energy efficiency study. Two key aspects of the research goal include:

- Formulate an optimization strategy designed to generate efficient and stable locomotion gaits—comprising phases with varying levels of underactuation and overactuation—within the framework of Hybrid Zero Dynamics control. This should include an analysis of the resultant gait's efficiency and stability, as discussed in Section 1.3.1.
- Simultaneously optimize nonlinear characteristics of the elastic couplings and gait trajectories to improve energy efficiency across various gait patterns, as detailed in Section 1.3.2.

1.3.1 Variation of Biped Gait Scenarios

This dissertation examines walking and running gaits, which are considered periodic at a specific constant average speed. The exploration of variation across different gait scenarios is conducted through the following aspects:

- Variations across a spectrum of target speeds for the periodic walking (at 0.5, 0.6, . . . , 1.5 m/s) and running (at 1.8, 1.9, . . . , 2.8 m/s) gaits;
- Variations in the duration of the double support phase while walking on rigid ground, leading to
  - Walking with instantaneous double support phase, where the robot model in single support phase has one degree of underactuation;
  - Walking with non-instantaneous double support phase, where the model in the double support phase is overactuated;
- Variations of rigid and compliant ground models for running, resulting in

- Running on rigid ground, where the contact is modeled as inelastic impact, and the model in single support phase has one degree of underactuation;
- Running on compliant ground, where the model in single support phase has three degrees of underactuation;

Non-Instantaneous Double Support Phase

Within the predominant scholarly discourse pertaining to the Hybrid Zero Dynamics control framework, the double support phase of walking is typically characterized as an instantaneous, inelastic impact mapping [175]. During the single support phase, the absolute orientation of the robot's body remains unaffected by the joint actuators, leading to its dynamics being characterized as the zero dynamics of the closed-loop system. The stability of the periodic gait is assessed through the convergence behavior of the stable limit cycle inherent to the hybrid zero dynamics. A manifest limitation of this approach is that the resultant gait stability is not directly mediated by the actuators, thereby rendering the gait susceptible to significant perturbations.
Given the concerns regarding gait stability when running on compliant surfaces, this thesis aims to develop methodologies to augment the Hybrid Zero Dynamics control framework by incorporating overactuated phases to enhance the convergence towards a stable limit cycle. Specifically, the proposed method is applied within the context of the non-instantaneous double support phase of periodic walking gaits. Future research could extend this approach to overactuated phases occurring during running, such as those generated by a flat foot equipped with an actuated ankle, thereby utilizing the proposed method.
In particular, when the double support phase is modeled as non-instantaneous, the biped is able to leverage overactuation for enhancing the gait stability [66]. During this phase, the robot model is characterized by a closed kinematic chain involving both stance legs, providing three degrees of freedom and four independent actuators. Although this introduces additional complexity into the control design, the overactuation is employed effectively to manage significant disturbances [178, 179]. Since all degrees of freedom are directly affected by the actuator, the overactuation ultimately facilitates an improved convergence behavior of the stable limit cycle of the gait, as opposed to the conventional gait where the double support phase is merely described as inelastic impact [194]. Moreover, overactuation is employed to initiate bipedal motion in scenarios where there are substantial deviations in initial conditions, such as when the velocity is zero [40]. Consequently, this enhancement in stability behavior considerably simplifies the experimental implementation of a bipedal robot.
Furthermore, transient gait sequences involving overactuated phases may be devised to address significant disturbances in intricate environmental conditions or to initiate

motion from a stationary state in future work. This enhancement broadens the applicability of the current study, as it primarily focuses on periodic motions. A notable disadvantage of overactuated systems is their low energy efficiency. Consequently, the research explores the potential of employing elastic couplings to enhance efficiency.

Rigid and Compliant Ground Surfaces

This thesis endeavors to elucidate the influence of ground compliance on the efficiency and stability of gait. Specifically, it examines running gaits, which are characterized by alternating single support and flight phases, across both rigid and compliant surface conditions. Due to the increased velocities intrinsic to running, the interaction process between the foot and the ground surface is distinctly defined; consequently, the presence of concurrent multiple contact points is considered insignificant in the context of running, thus enabling the derivation of approximate solutions through numerical, event-driven methodologies.
Contrastingly, the incorporation of the compliant contact model within the formulation of walking gaits is indeed practicable, albeit with certain constraints. As elucidated in study [195], the influence of optimal elastic coupling on the energy efficiency of bipedal walking on compliant surfaces is studied. The compliant contact model is specifically employed during the single support phase, with the double support phase being presumed instantaneous. This presumption presents a notable limitation, considering empirical evidence which indicates that the double support phase is a continuous process. Efforts to incorporate a non-instantaneous double support phase, while concurrently considering the compliant contact model at both stance feet, engender significant numerical challenges for the proposed optimization framework. Consequently, an analysis of walking on compliant substrates surpasses the purview of this thesis. However, the investigation of bipedal walking involving a non-instantaneous double support phase on rigid terrain yields essential insights and control strategies, which may be extended in subsequent studies to walking on compliant surfaces.

1.3.2 Optimal Parallel Elastic Couplings

The subsequent major contribution pertains to the enhancement of energy efficiency in newly introduced walking and running gaits through the implementation of parallel elastic couplings affixed between the robot's rigid body segments. For practical application, investigations focus on couplings between adjacent segments. Assuming the robot model exhibits symmetry, three configurations emerge as a result:

- Coupling between upper-body and thighs in hip joints through two identical mechanisms;

- Coupling between thighs through a single symmetric mechanism;
- Coupling between thighs and shanks in knee joints through two identical mechanisms.

Prior research [17, 18] indicates that the incorporation of elastic couplings in the knee joints results in only marginal improvements in energy efficiency; therefore, this aspect is not considered within the scope of the thesis.
A numerical optimization process is employed to simultaneously refine the nonlinear elastic properties and the parameters governing gait trajectory, as both elements are critical to determining the gait efficiency [147]. To harness the full potential, the elastic property is tailored for each specific walking or running speed, where the locomotion gait is assumed to be periodic. This approach necessitates an auxiliary actuator, which modifies the elastic property in alignment with the gait condition, akin to variable stiffness actuators [44]. The practical implementation of the targeted nonlinear, adjustable stiffness behavior is being explored by the research project collaborator of the author through the use of compliant systems [187]. The central hypothesis posits that optimized nonlinear spring elements are capable of aligning a biped's intrinsic mechanical resonances with its gait frequency [193] and the characteristics of the ground, thus diminishing energy consumption across diverse walking and running scenarios.

1.4 Outline

The remainder of this dissertation is organized as follows:

- Chapter 2 delineates the fundamental theories and methodologies pertinent to the modeling, control, and analysis of bipedal walking and running as explored in this thesis.
- Chapter 3 elucidates the biped model for walking gaits, characterized by alternating single support and double support phases; discontinuous transition events, such as inelastic impacts, are defined to complete the hybrid dynamical model for formulating cyclic walking sequences.
- Chapter 4 expounds upon the control design within the Hybrid Zero Dynamics control framework to produce periodic walking gaits, with a discussion on methods for stability analysis.
- Chapter 5 details the biped model for running gaits, which encompass single support and flight phases, notably introducing contact with rigid and compliant ground surfaces during the single support phase.

- Chapter 6 explores the control design for generating periodic running gaits on both rigid and compliant ground within the Hybrid Zero Dynamics control framework.
- Chapter 7 outlines the optimization framework designed to produce energy-efficient and stable walking and running gaits, while also addressing the simultaneous optimization of elastic coupling and gait trajectories to enhance energy efficiency.
- Chapter 8 presents simulation outcomes of periodic walking and running across various scenarios, specifically highlighting walking with instantaneous and non-instantaneous double support phases, alongside running on rigid and compliant ground surfaces.
- Chapter 9 discusses optimization results demonstrating the improved energy efficiency of the introduced biped locomotion employing optimal parallel elastic couplings, with particular attention to different configurations of elastic couplings and the desired properties for specific gaits.
- Chapter 10 concludes the research by summarizing findings and identifying potential avenues for future work.

2 Fundamental Theory and Methods

This chapter elucidates the fundamental methodologies pertinent to the thesis. In the interest of comprehensiveness, and to furnish a broad perspective within the relevant literature, analogous methodologies are delineated. Basic academic models are utilized to critically examine the advantages and disadvantages of the selected methodologies ultimately employed in the thesis.
The structure of the chapter is delineated as follows: Section 2.1 explicates the notations pertinent to the mathematical expressions utilized throughout the thesis; Section 2.2 provides a comprehensive overview of state-of-the-art techniques for simulating dynamical systems consisting of multiple rigid bodies; Section 2.3 explores the contact mechanics of multibody dynamical systems through the employment of nonsmooth or compliant regulation formulations; Section 2.4 articulates methodologies for assessing the stability of equilibrium points and periodic orbits in dynamical systems; Section 2.5 elaborates on nonlinear control theory with a particular focus on linearization methods; Section 2.6 investigates advanced numerical methodologies for the identification of periodic solutions in dynamical systems, particularly in relation to gait generation; Section 2.7 expounds upon the principles of nonlinear numerical optimization, which are critical to the thesis for formulating energy-efficient gaits.

2.1 Notation of Mathematical Expressions

This section defines the mathematical notations used consistently throughout the thesis. The symbol ":=" declares a definition, while "=" denotes equality. Scalars are represented by lowercase italic letters, e.g., a, b, c.

Vectors are illustrated as column vectors and are symbolized by bold lowercase letters, as exemplified in

$$\mathbf{x} := \begin{bmatrix} x_1 \\ x_2 \\ \vdots \\ x_n \end{bmatrix} \in \mathbb{R}^{n\times 1}\,, \text{ or } \qquad \mathbf{x} := [x_1, x_2, \ldots, x_n]^\top \in \mathbb{R}^{n\times 1}\,,$$

with the transformation of a row vector into a column vector achieved through the application of the transposition operator "$\top$". Matrices are depicted using bold uppercase letters, exemplified in

$$\mathbf{M} := \begin{bmatrix} \mathbf{m}_1 & \mathbf{m}_2 & \ldots & \mathbf{m}_k \end{bmatrix}\,,$$

wherein each $\mathbf{m}_i \in \mathbb{R}^n$, $i \in [1, k]$ constitutes a column vector. Consequently, $\mathbf{M} \in \mathbb{R}^{n\times k}$ characterizes a matrix comprising n rows and k columns. A comprehensive summary of the principal symbols utilized throughout this thesis can be found in Table 2.1.

Table 2.1: Summary of mathematical notations

Symbol	Definition
∞	Infinity
$O(\varepsilon^k)$	Asymptotic order of ε^k
$\mathbb{R}$	Set of real numbers
$\mathbb{R}^n$	n-dimensional real space
$\mathbf{x}$	Column vector in $\mathbb{R}^{n\times 1}$
$\mathbf{A}$	Matrix in $\mathbb{R}^{m\times n}$
$\mathbf{A}^\top$	Transpose of matrix $\mathbf{A}$
$\mathbf{I}_n$	Identity matrix of size $n \times n$
$\mathbf{0}$	Zero vector or matrix of appropriate dimensionality
$\mathrm{d}f/\mathrm{d}t$	Derivative of f with respect to time t, equavelent to $\dot{f}$
$\partial f/\partial x$	Partial derivative of f with respect to x
$\mathrm{d}^n f/\mathrm{d}t^n$	n-th order derivative of f with respect to time t
$\partial^n f/\partial x^n$	n-th order partial derivative of f with respect to x
$\mathcal{L}_f h$	Lie derivative of h with respect to vector field f
$\mathcal{L}_f^n h$	n-th Lie derivative of h with respect to vector field f

2.2 Simulation of Multibody Dynamical Systems

Multibody dynamics deal with modeling and simulating mechanical systems composed of interconnected rigid [180, Chapter 3] or flexible bodies [156, Chapter 4] subjected

to constraints and external forces. Typical applications include robotic manipulators [81, Chapter 3] and biomechanical analysis of human motion [7]. As the number of bodies or the complexity of their interactions grows, the computational demands for simulating such systems can increase significantly. Consequently, a variety of advanced techniques have been developed to improve efficiency in constraint enforcement and handle large-scale models [47, Chapter 10].
In order to attain robust simulations of multibody systems, numerous commercial software packages, including *MSC Adams* [117], *RecurDyn* [185], and *Simpack* [152], integrate methodologies such as advanced DAE solvers in Section 2.2.1, index reduction with constraint stabilization techniques in Section 2.2.2, and ODE solvers employing generalized coordinates in Section 2.2.3.

2.2.1 Advanced DAE Solvers

Due to holonomic constraints, mechanical multibody systems usually result in differential-algebraic equations (DAE) characterized by an index-3 formulation, necessitating three differentiations for their transformation into ordinary differential equations (ODE). For example, such a DAE is stated as

$$\mathbf{M}(\mathbf{q})\,\ddot{\mathbf{q}} = \mathbf{f}(\mathbf{q}, \dot{\mathbf{q}}, t) + \mathbf{J}_\Psi(\mathbf{q})^\top \boldsymbol{\lambda}\,, \tag{2.1a}$$

$$\boldsymbol{\Psi}(\mathbf{q}) = \mathbf{0}\,, \tag{2.1b}$$

where $\mathbf{q} \in \mathbb{R}^n$ signifies the n generalized coordinates, $\mathbf{M}(\mathbf{q})$ stands for the inertia matrix, $\mathbf{f}(\mathbf{q}, \dot{\mathbf{q}}, t)$ comprises the generalized forces, and $\boldsymbol{\lambda} \in \mathbb{R}^m$ pertains to the Lagrange multipliers that enforce the holonomic scleronomic constraints $\boldsymbol{\Psi}(\mathbf{q})$ with $\boldsymbol{\Psi} : \mathbb{R}^n \to \mathbb{R}^m$. Notably, $\mathbf{J}_\Psi(\mathbf{q}) := \partial\boldsymbol{\Psi}(\mathbf{q})/\partial\mathbf{q}$ represents the Jacobian of the constraints with respect to $\mathbf{q}$. The DAE problem (2.1) can be directly addressed using advanced DAE solvers, such as *RADAU IIA* [65], which exhibit competence in handling stiff problems through adaptive time-stepping, event detection, and sparse linear algebra methodologies. These solvers are adept at directly integrating constraints (2.1b) within the system equations, making them especially suitable for high-fidelity models characterized by multiple interacting components. It is noteworthy that the implementation of implicit integration techniques requires the solution of a predominantly nonlinear system of equations at every integration step, which results in significant computational demands.

2.2.2 Index Reduction and Constraint Stabilization

Formulations of DAEs with high indices inherently encounter numerical challenges. Consequently, the index-3 formulation presented in (2.1) is often transformed into an

index-1 form through the process of differentiating the constraints (2.1b) twice, thereby yielding

$$\begin{bmatrix} \mathbf{M}(\mathbf{q}) & -\mathbf{J}_\Psi^\top \\ -\mathbf{J}_\Psi & \mathbf{0} \end{bmatrix} \begin{bmatrix} \ddot{\mathbf{q}} \\ \boldsymbol{\lambda} \end{bmatrix} = \begin{bmatrix} \mathbf{f}(\mathbf{q}, \dot{\mathbf{q}}, t) \\ \dot{\mathbf{J}}_\Psi \dot{\mathbf{q}} \end{bmatrix} . \tag{2.2}$$

As the constraints are expressed at the level of acceleration, the approximations and numerical inaccuracies inherent in integration algorithms can lead to constraint drift, resulting in behavior that may not accurately represent the physical reality. The constraint stabilization methods delineated in this section are utilized as strategies designed to mitigate or eradicate this drift, thereby ensuring the consistency of constraints at both the position and velocity levels [16].

Baumgarte Stabilization

Fundamentally, virtual spring-damping elements are incorporated into the constraint equation as presented in (2.2), resulting in the augmented constraints delineated in

$$\frac{\mathrm{d}^2 \boldsymbol{\Psi}}{\mathrm{d}t^2} = \mathbf{J}_\Psi \ddot{\mathbf{q}} + \dot{\mathbf{J}}_\Psi \dot{\mathbf{q}} = -2\alpha \frac{\mathrm{d}\boldsymbol{\Psi}}{\mathrm{d}t} - \beta^2 \boldsymbol{\Psi} . \tag{2.3}$$

Within this framework, $\alpha > 0$ and $\beta^2 > 0$ are positive-valued constants signifying virtual damping and spring elements, which serve to guarantee the asymptotic stability of the constraints $\boldsymbol{\Psi}$. Alternatively, these constants can be understood as a representation of a proportional-derivative (PD) feedback control law, as described in [181, Section 5.9.2]. Owing to its simplicity, the Baumgarte stabilization method incurs moderate computational overhead and is straightforward to incorporate into existing solvers. Nonetheless, the approximated dynamics may deviate from the true physical system due to the presence of virtual damping forces. Typically, the virtual forces result in trajectories that oscillate around the constraint surface. Moreover, the performance of this method is highly contingent upon the selection of the parameters α and β.

Coordinate Projection

The coordinate projection method facilitates the projection of position $\mathbf{q}$ and velocity $\dot{\mathbf{q}}$ onto the constraint manifold, incorporating $\boldsymbol{\Psi}(\mathbf{q}) = \mathbf{0}$ and $\dot{\boldsymbol{\Psi}}(\mathbf{q}) = \mathbf{0}$ at each step of integration, thereby ensuring precise adherence to constraints even for long simulations. Specifically, the projection can be structured as an optimization problem necessitating iterative procedures, consequently requiring substantial computational resources, as noted in [181, Section 5.9.2]. Furthermore, the high nonlinearity inherent in the constraints presents a possible obstacle to the convergence process.

Penalty Formulations

Penalty methods circumvent the direct algebraic resolution of constraint equations by introducing substantial artificial forces or potentials that impose penalties for deviations from the constraints, as illustrated in [90]. As the penalty parameter increases, the solutions are compelled to adhere closely to the constraint manifold. Although the implementation is straightforward and any constraint can be transformed into a penalty form, the resultant differential equations generally exhibit significant stiffness contingent upon the chosen penalty parameter, resulting in heightened numerical evaluation demands. Furthermore, the constraint surface is never perfectly satisfied.

2.2.3 ODE Solvers using Generalized Coordinates

Rather than imposing constraints through the utilization of Lagrange multipliers or stabilization techniques, holonomic constraints may be directly incorporated within the constrained system of differential equations, thereby yielding an ODE problem, as stated in

$$\frac{\mathrm{d}^2\mathbf{r}}{\mathrm{d}t^2} = \mathbf{g}(\mathbf{r}, \dot{\mathbf{r}}, t) \,, \tag{2.4}$$

where $\mathbf{r} \in \mathbb{R}^{n-m}$ represents a minimal set of independent generalized coordinates that are intrinsically consistent with the constraints. A notable advantage lies in the reduction of the problem's dimensionality; however, while constraints are presumed to be satisfied by design, the actual enforcement is contingent upon the accuracy of the coordinate transformations and may deviate due to the accumulation of numerical errors. In dynamical systems characterized by varying structures, particularly hybrid dynamical systems, the process of deriving the equations of motion necessitates considerable effort, as the constraints must be meticulously addressed in each distinct phase.

2.2.4 Academic Example

In order to illustrate various methodologies for imposing constraints within simulations, the three stabilization methods and the ODE formulation detailed in this study are analyzed through the simulation of a single pendulum. This pendulum is defined by the coordinates x and y, which exhibit interdependence due to the holonomic constraint $\varphi(x, y) = x^2 + y^2 - L^2 = 0$. The initial conditions for the simulation involving stabilization methods are chosen with minor deviations from the constraint surface. The violation of the constraint ϕ, as illustrated in Figure 2.1, indicates that the Baumgarte stabilization method results in an oscillatory path around the constraint surface, which is attributed

to virtual stiffness-damping forces. As the simulation duration approaches infinity ($t \longrightarrow \infty$), the oscillations asymptotically converge to zero.

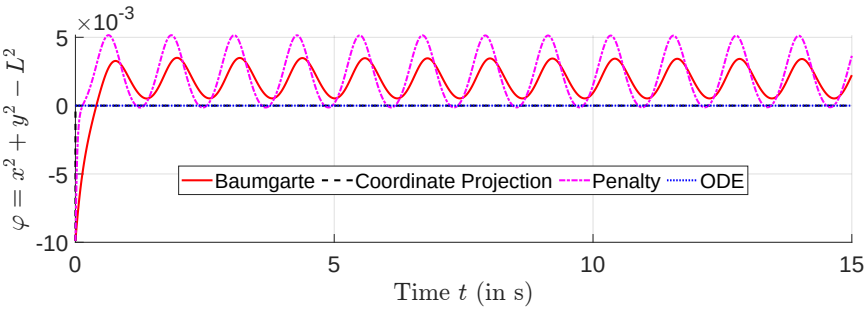

Figure 2.1: Constraint violation in the simulation of a single pendulum using different formulations.

Analogous to Baumgarte stabilization, the penalty method displays oscillations in constraint violations. Parameters in both methods are chosen to keep the plotted outcomes of similar magnitude. However, the penalty method perpetually fails to fully meet the constraints, as the constraint equation is continually approximated via penalty potential forces. In contrast, the coordinate projection method and the ODE formulation employing the generalized minimal coordinate (angular displacement of the pendulum) strictly comply with the constraints. Notably, the ODE formulation is advantageous due to its significantly reduced computational requirements.
This thesis predominantly focuses on enhancing the energy efficiency of a biped robot across various gaits and environments. The efficiency of numerical evaluation is pivotal for optimization. Additionally, extended simulation durations are unnecessary since the gaits are characterized as periodic, and thus simulating a single, short step period suffices. The equations of motion are analytically generated using the software *Maple*, facilitating an efficient substitution of holonomic constraints, which encompass both the constraints arising from contact and the virtual constraints imposed by the controller. Consequently, the dynamics examined in this thesis are formulated using generalized minimal coordinates, where feasible.

2.3 Contact Mechanics in Multibody Systems

Contact mechanics within multibody dynamical systems concerns the analysis and prediction of the interactions between contacting bodies, focusing on force transmission and deformation at their interfaces [83]. It involves understanding surface interactions at both microscopic and macroscopic scales, addressing phenomena such as friction, wear, adhesion, and impact [28]. Consideration of these effects within contact mechanics

is crucial for the design of reliable mechanical components, optimization of system behavior, and assurance of safety in diverse applications.
The study in [52] examines two advanced methodologies for characterizing contact-impact events in multibody dynamics: the nonsmooth formulation as introduced in Section 2.3.1, and the regulation formulation utilizing compliant contact models as outlined in Section 2.3.2. These two methodologies act as foundations for the development of locomotion gaits on both rigid and compliant surfaces within the scope of this thesis.

2.3.1 Nonsmooth Dynamics with Unilareral Constraints

Nonsmooth dynamical systems under unilateral contact constraints commonly manifest in diverse physical contexts distinguished by discontinuities or rapid changes in velocity or acceleration [134, 135]. Examples that elucidate these concepts include impact phenomena that lead to instantaneous modifications in velocity, as described in [133, Section 12.1], and frictional constraints often modeled through Coulomb friction, which result in stick-slip transitions, as discussed in [133, Section 13.1]. To address the fundamental theory, a prototypical dynamical system is constructed as

$$\mathbf{M}(\mathbf{q})\,\ddot{\mathbf{q}} = \mathbf{f}(\mathbf{q}, \dot{\mathbf{q}}, t) + \mathbf{J}_{\Phi}^{\top}\boldsymbol{\lambda}\,, \tag{2.5a}$$

$$\boldsymbol{\Phi}(\mathbf{q}) \geq \mathbf{0}\,, \quad \boldsymbol{\lambda} \geq \mathbf{0}\,, \quad \boldsymbol{\lambda}^{\top}\boldsymbol{\Phi}(\mathbf{q}) = 0\,, \tag{2.5b}$$

wherein $\mathbf{f}(\mathbf{q}, \dot{\mathbf{q}}, t)$ signifies the smooth, applied force, while $\mathbf{J}_{\Phi}^{\top}\boldsymbol{\lambda}$ delineates the nonsmooth impulsive force, stemming from m unilateral constraints $\boldsymbol{\Phi} : \mathbb{R}^n \to \mathbb{R}^m$. For example, $\boldsymbol{\Phi}(\mathbf{q})$ is characterized by the separation distance between colliding entities, thereby functioning as a gap measurement for identifying a collision occurrence. The term $\mathbf{J}_{\Phi} := \partial\boldsymbol{\Phi}(\mathbf{q})/\partial\mathbf{q}$ refers to the Jacobian associated with the constraint.
Due to the limitations of smooth ODE and DAE solvers in handling sudden velocity transitions $\dot{\mathbf{q}}$, two numerical methods are introduced: event-driven and time-stepping complementarity methods, following the notation in [1] and [28, Section 5.7].

Event-Driven Method

Event-driven methodologies facilitate the integration of continuous dynamics while simultaneously managing the identification of discrete collision events assessed by the gap function $\boldsymbol{\Phi}(\mathbf{q})$. Upon the detection of a constraint violation $\boldsymbol{\Phi}(\mathbf{q}) \geq \mathbf{0}$, the solver pauses temporarily, executes instantaneous modifications to the state, such as revising velocities in accordance with the impact law, and then proceeds with its operation. The precise timing of event occurrences can be determined through the application of root-finding algorithms, thereby guaranteeing high accuracy.

The primary advantages of this approach include enhanced accuracy during events, and efficiency when handling sparse contacts. In contrast, this methodology demands the implementation of rigorous mechanisms for the detection and management of events, may face performance difficulties in scenarios characterized by frequent or simultaneous contacts, and demonstrates a considerable reliance on the capabilities of the solver's event detection functions alongside the associated numerical tolerances.

Time-Stepping Complementarity Method

Time-stepping methodologies for nonsmooth dynamics manage discrete occurrences, such as collisions and friction, within each discrete time interval without explicitly identifying collision instances. Rather, they construct a complementarity problem, as outlined in (2.5b), within each interval to impose contact constraints and frictional laws in an integrated manner, in accordance with the procedure in [1].
The advantages encompass efficient management of frequent or concurrent events, seamless integration with optimization frameworks [32, 137], and improved scalability for intricate systems [10]. Conversely, the disadvantages involve the potential introduction of numerical damping and minor temporal inaccuracies due to fixed-step discretization, as well as the necessity for specialized solvers in handling large complementarity systems.

Academic Example

To elucidate the characteristics of the discussed methodologies, Figure 2.2 presents the comparative simulation outcomes of a bouncing ball employing event-driven and time-stepping complementarity methods.
Specifically, the event-driven method efficiently assesses the system's behavior during the initial four seconds. Nevertheless, once the simulation exceeds the four-second mark, where contact events become frequent, the event-driven method encounters a significant escalation in the number of iteration steps, each represented by circles as elaborated in Figure 2.2. Conversely, the time-stepping complementarity method exhibits enhanced scalability by circumventing the computational challenges associated with dynamic event detection during frequent interactions. This example utilizes a forward Euler integration scheme with a fixed step size of $\mathrm{d}t = 1$ ms in the formulation of the time-stepping approach.
Within the framework of simulating bipedal locomotion, the frequent occurrence of contact events is typically not a primary concern. Specifically, this thesis examines gaits of a periodic nature wherein the contact events are distinctly separated. Nonetheless, precise identification of these contact events is essential for the adjustment of reference

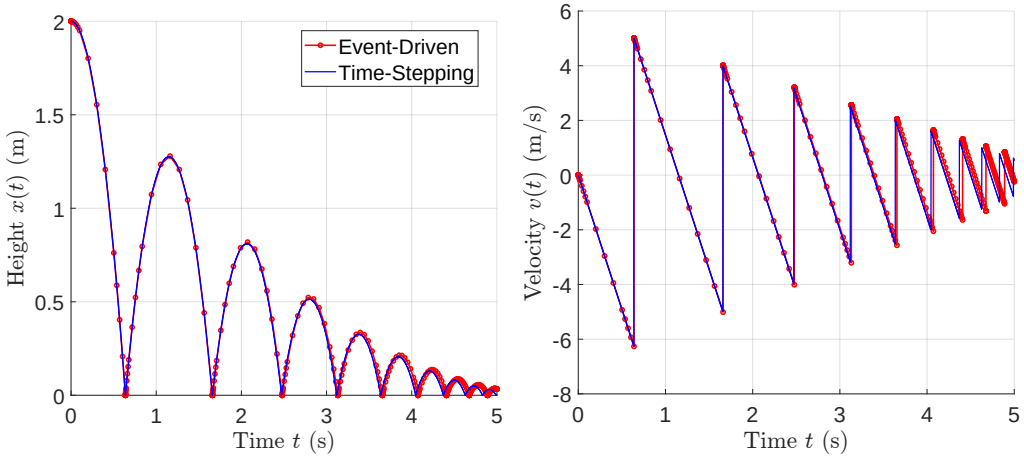

(a) Position of the bouncing ball.

(b) Velocity of the bouncing ball.

Figure 2.2: Simulation of a bouncing ball using event-driven and time-stepping complementarity methods.

trajectories within the control system. Therefore, the event-driven method is considered the foundational principle of the simulation framework.

2.3.2 Compliant Contact Model

The formulation of nonsmooth dynamics as delineated in Section 2.3.1 addresses the interaction between non-deformable bodies. Alternatively, rigid impacts are approximated through compliant contact between deformable materials, resulting in elastic or viscoelastic deformation dynamics at the interface [49]. These models commonly represent the behaviors of real-world materials (e.g., steel, rubber, soft tissues) and assist in predicting phenomena such as collisions and friction.
The normal contact force can be characterized using two fundamental modeling approaches: the static Hertz contact model, which involves purely elastic deformation without explicit damping dissipation; and viscoelastic models, which incorporate both elastic and damping components, thereby facilitating a more precise depiction of rebound and energy dissipation.

Static Hertz Contact Model

Hertz contact theory establishes a fundamental framework for the modeling of elastic, quasi-static contacts, initially described in [70]. For two spherical bodies, the normal force F induced by an indentation δ is characterized as

$$F(\delta) = k_{\mathrm{HZ}}\delta^{\frac{3}{2}} ,$$

where k_{HZ} represents a material-dependent constant. A significant limitation of the Hertz model lies in its omission of critical factors such as damping dissipation, friction, and plasticity.

Viscoelastic Contact Models

Due to the inherent energy dissipation observed in real-world impacts, the limitations of the Hertz model necessitated the advancement of viscoelastic extensions. As depicted in Figure 2.3a, viscoelastic models improve the depiction of contact dynamics through the integration of a velocity-dependent damping term, as delineated by a general form written as

$$F(\delta, \dot{\delta}) = F_{\mathrm{elastic}}(\delta) + F_{\mathrm{damp}}(\delta, \dot{\delta}) \,, \qquad \delta \geq 0 \,,$$

wherein F_{elastic} may conform to a $\delta^{\frac{3}{2}}$ law in alignment with the Hertzian paradigm or employ a linear spring model $k\delta$, while the damping force F_{damp} incorporates velocity dependencies, which are predominantly nonlinear, to account for energy dissipation. This section provides a succinct overview of significant contact models, including the Kelvin-Voigt model and the Hunt-Crossley model [75].

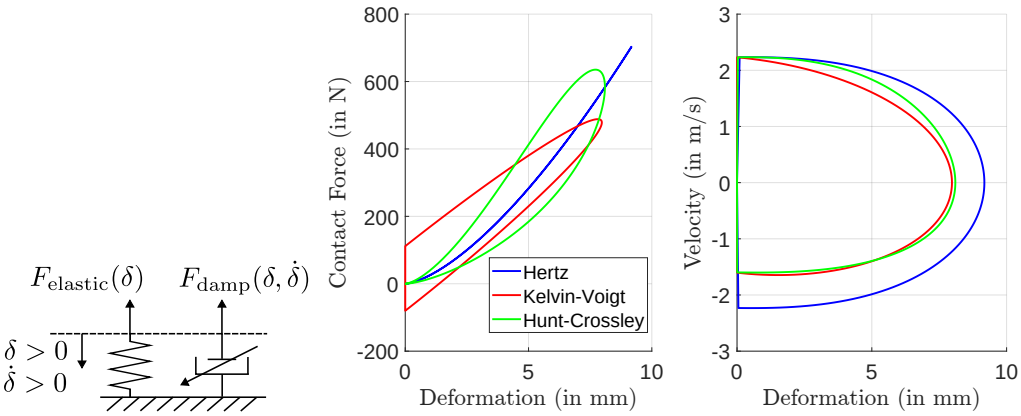

(a) General form of a viscoelastic contact model.

(b) Normal contact force over penetration δ.

(c) Contact velocity $\dot{\delta}$ over penetration δ.

Figure 2.3: Illustration of viscoelastic contact model and corresponding responce behaviors.

Kelvin-Voigt Model illustrates the interaction via a basic parallel arrangement of a linear spring and damper, expressed as

$$F(\delta, \dot{\delta}) = k_{\mathrm{KV}}\delta + c_{\mathrm{KV}}\dot{\delta} \,, \qquad \delta \geq 0 \,.$$

While the simplicity of the model presents certain advantages, a notable limitation arises from the linear viscoelastic behavior $c_{\mathrm{KV}}\dot{\delta}$, which leads to an unrealistic discontinuity in the response force at the initial instance of contact and separation, as illustrated in Figure 2.3b. Additionally, another non-physical issue observed is the generation of a negative reaction force towards the conclusion of the contact period.

Hunt-Crossley Model , as originally proposed in [75], integrates the Hertzian framework with a damping component that increases proportionally to $\delta^{\frac{3}{2}}$, as delineated in

$$F(\delta, \dot{\delta}) = k_{\mathrm{HC}}\delta^{\frac{3}{2}}\left(1 + \frac{3(1-c_{\mathrm{r}})}{2}\frac{\dot{\delta}}{\dot{\delta}^{(-)}}\right), \qquad \delta \geq 0\,,$$

where c_{r} serves as the damping coefficient, and $\dot{\delta}^{(-)}$ represents the velocity of approach at the moment of impact. This formulation eradicates damping in the event of $\delta = 0$, thereby averting the manifestation of non-physical negative forces when the entities are not in contact, as well as eliminating the abrupt change in the response force at the moment of impact.
In addition, the trajectories depicted in Figure 2.3c for both the Hertz model and the Hunt-Crossley model are developed employing the same nominal stiffness parameter, namely $k_{\mathrm{HC}} = k_{\mathrm{HZ}}$. It is apparent that the neglect of energy dissipation in the Hertz model leads to an overestimation of the maximum penetration into the ground. Furthermore, the hysteresis of the response force observed in the Kelvin-Voigt model and the Hunt-Crossley model in Figure 2.3b is attributed to the presence of damping dissipations.
In conjunction with the previously outlined compliant models, a multitude of alternative approaches have been proposed, as documented in studies [6, 30, 51, 110], to address the resolution of the normal contact force on compliant surfaces. The research presented in [55] examines the interaction of coupled normal and tangential compliant contacts. Investigations, such as [67], propose simulation techniques to account for friction at the contact point. Sophisticated finite element simulations further facilitate the approximation of intricate contact behaviors within data-driven approaches for complex surfaces [108], whereas alternative data-driven methodologies depend on empirical measurements [103].
From a practical perspective, the determination of suitable ground parameters is essential for the implementation of compliant contact models, as these parameters often hinge on the geometric and material characteristics of the colliding entities [53]. The damping terms, in particular, necessitate meticulous experimentation, such as drop tests and impact assessments [154]. Furthermore, large stiffness and damping parameters frequently result in stiff differential equations, necessitating implicit integration schemes for both efficiency and numerical stability [50]. Additionally, the presence of multiple

contacts increases complexity, particularly in contact detection during simulation. This thesis employs the models and associated parameters proposed in [155] and [30] to simulate running gaits on compliant terrain, as expounded in Section 5.2.1.

2.4 Stability Theory

The stability of a dynamical system delineates the trajectory behavior near an operating point when influenced by minor perturbations in initial conditions or parameters. In particular, this section considers an autonomous system of nonlinear ordinary differential equations expressed as

$$\frac{\mathrm{d}\mathbf{x}}{\mathrm{d}t} = \mathbf{f}(\mathbf{x}) \,, \tag{2.6}$$

wherein the vector field $\mathbf{f} : \mathbb{R}^n \to \mathbb{R}^n$ maintains continuous differentiability C^∞ within the neighborhood of an equilibrium point $\mathbf{x}_{\mathrm{eq}} \in \mathbb{R}^n$, namely $\mathbf{f}(\mathbf{x}_{\mathrm{eq}}) = \mathbf{0}$.
This section offers an overview of fundamental stability principles pertinent to nonlinear autonomous dynamical systems, as exemplified by (2.6). It includes the analysis of Lyapunov stability of equilibrium points as discussed in Section 2.4.1, an evaluation of local stability via linearization around equilibrium points, as outlined in Section 2.4.2, an assessment of orbital stability of limit cycles as described in Section 2.4.3, and the investigation of Lyapunov Exponents pertinent to chaotic dynamics, as indicated in Section 2.4.4.

2.4.1 Lyapunov Stability

As per [122, Section 1.4], the equilibrium point $\mathbf{x}_{\mathrm{eq}}$ of the autonomous system (2.6) is categorized as

- Lyapunov stable if a solution initiated close to the point $\mathbf{x}_{\mathrm{eq}}$ also remains close enough for all time $t > t_0$;
- Asymptotically stable if a solution initiated close to the point $\mathbf{x}_{\mathrm{eq}}$ is stable and in addition converges to $\mathbf{x}_{\mathrm{eq}}$ for $t \to \infty$.

Direct Lyapunov Method

According to [116, Section 2.1], the direct Lyapunov method bypasses the need to solve the system explicitly. Instead, a continuous, Lyapunov candidate function $V : \mathbb{R}^n \to \mathbb{R}$ is constructed, which is characterized as positive definite around $\mathbf{x}_{\mathrm{eq}}$, evaluated as

$$V(\mathbf{x}) > 0 \quad \text{for} \quad \mathbf{x} \neq \mathbf{x}_{\mathrm{eq}} \,, \quad \text{and} \quad V(\mathbf{x}_{\mathrm{eq}}) = 0 \,.$$

Subsequently, the time derivative of V along the trajectories, delineated by $\dot{V}(\mathbf{x}) := (\partial V(\mathbf{x})/\partial \mathbf{x})\mathbf{f}(\mathbf{x})$, serves as an indicator of the stability of $\mathbf{x}_{\text{eq}}$:

- Lyapunov stable if $\dot{V}(\mathbf{x}) \leq 0$, in accordance to [116, Section 2.2];
- Asymptotically stable if $\dot{V}(\mathbf{x}) < 0$, in accordance to [116, Section 2.3].

The direct Lyapunov method serves as a potent instrument for analyzing the stability of nonlinear dynamical systems. However, the selection of an appropriate Lyapunov candidate function necessitates expertise and a deep understanding of the system design [122, Section 1.4.5]. In addition to its application in stability analysis, the Lyapunov function is employed within the control design framework to enhance stability in the context of bipedal locomotion, as discussed in the works [8, 54, 144].

2.4.2 Local Analysis of Stationary Solutions

Owing to its inherent simplicity, the local stability of the system (2.6) is typically examined in practice through its first-order approximation, or linearization, around the equilibrium point $\mathbf{x}_{\text{eq}}$. In this regard, the Hartman-Grobman theorem provides essential verification of the equivalence between the local dynamics of the nonlinear system and its linearized counterpart.

Hartman-Grobman Theorem

The nonlinear system (2.6) is represented through its first-order approximation [116, Section 1.2], expressed as

$$\frac{\mathrm{d}\Delta\mathbf{x}}{\mathrm{d}t} = \left.\frac{\partial \mathbf{f}(\mathbf{x})}{\partial \mathbf{x}}\right|_{\mathbf{x}=\mathbf{x}_{\text{eq}}} \Delta\mathbf{x} = \mathbf{J}(\mathbf{x}_{\text{eq}})\Delta\mathbf{x}\,, \tag{2.7}$$

where $\Delta\mathbf{x} = \mathbf{x} - \mathbf{x}_{\text{eq}}$ denotes a small perturbation (or variation) from the equilibrium point $\mathbf{x}_{\text{eq}}$. According to the definition provided in [131, Section 2.6], the equilibrium point $\mathbf{x}_{\text{eq}}$ is deemed hyperbolic if the Jacobian $\mathbf{J}(\mathbf{x}_{\text{eq}})$ assessed at the point $\mathbf{x}_{\text{eq}}$ exhibits no eigenvalues with real parts equal to zero.
As articulated by [131, Section 2.8], the Hartman-Grobman Theorem posits the existence of a neighborhood $\mathcal{U}$ around $\mathbf{x}_{\text{eq}}$ and a homeomorphism $\mathbf{h} : \mathcal{U} \to \mathbb{R}^n$, whereby $\mathbf{h}(\mathbf{x}_{\text{eq}}) = \mathbf{0}$. The homeomorphism $\mathbf{h}$ maps the trajectories of the nonlinear system onto those of its linear counterpart. Consequently, the nonlinear system (2.6) is topologically conjugate to its linearization (2.7) within the neighborhood $\mathcal{U}$ of the fixed point $\mathbf{x}_{\text{eq}}$, and their phase portraits display qualitative similarity.

Stability in First Approximation

The Hartman-Grobman Theorem aids in the analysis of local dynamics within a nonlinear system by studying its linear approximation, thereby considerably simplifying the stability analysis. Notably, if all eigenvalues of $\mathbf{J}(\mathbf{x}_{\text{eq}})$ possess strictly negative real parts, the hyperbolic equilibrium point $\mathbf{x}_{\text{eq}}$ is locally asymptotically stable. Conversely, the presence of at least one eigenvalue with a positive real part renders $\mathbf{x}_{\text{eq}}$ unstable [131, Section 2.9].
In the case of non-hyperbolic equilibrium points, characterized by eigenvalues of the Jacobian with zero real components, the dynamics can manifest substantial complexity. The stability of the nonlinear system cannot be reasonably approximated by examining the linearized version. Therefore, methodologies such as Center Manifold Theorems, as elucidated in [150, Section 7.6], are employed to facilitate further examination.

2.4.3 Orbital Stability of Periodic Solutions

At a constant average velocity, the periodic locomotion gaits of bipedal robots are conceptualized as periodic orbits within the hybrid dynamical system, exhibiting nonsmooth characteristics due to discontinuous transitions. As noted in [163, Section 7], these isolated closed orbits, denoting the absence of other periodic solutions in their vicinity, constitute limit cycles of the closed-loop system. Owing to the phase-dependent design principle, the closed-loop system formulated on the basis of the Hybrid Zero Dynamics controller is deemed autonomous. Within this framework, a periodic solution curve $\mathbf{\Phi}(\mathbf{x}_0, t)$ for the example system (2.6) is established as

$$\mathbf{\Phi}(\mathbf{x}_0, t + T) = \mathbf{\Phi}(\mathbf{x}_0, t)\,, \quad \forall t \in \mathbb{R}\,, \tag{2.8}$$

demonstrating periodicity T and adhering to the initial condition $\mathbf{\Phi}(\mathbf{x}_0, t = 0) = \mathbf{x}_0$. Unlike the stability analysis of a stationary solution as previously described, a limit cycle is deemed orbitally stable (or Poincaré stable) if trajectories originating in its vicinity maintain a close proximity concerning distance to the orbit, albeit potentially with a phase shift [122, Section 1.4.3]. The assessment of orbital stability is conducted using the Poincaré return map and Floquet theory.

Poincaré Return Map

As reported by [122, Section 3.3], a prevalent methodological approach in the analysis of limit cycles involves the establishment of a Poincaré section, a hypersurface that is transverse to the flow, and the examination of the successive intersections of trajectories with this section. This methodological approach results in the formulation of a Poincaré

return map, which effectively transforms a continuous-time system into a discrete map of reduced dimensionality, as evidenced

$$\mathbf{x}[k+1] = \mathcal{P}\left(\mathbf{x}[k]\right) \ ,$$

where $\mathbf{x}[k]$ denotes the point of intersection at the k-th crossing. The limit cycle is represented by a fixed point of $\mathbf{x}^* = \mathcal{P}(\mathbf{x}^*)$, with its stability being determined by the eigenvalues of the Jacobian $\mathbf{J}_{\mathcal{P}}(\mathbf{x}^*) := \partial\mathcal{P}(\mathbf{x})/\partial\mathbf{x}\,\big|_{\mathbf{x}=\mathbf{x}^*}$ at that fixed point.
[177, Section 4.2] examines the utilization of the Poincaré return map approach for hybrid dynamical systems that incorporate impulsive effects. Furthermore, an extended Poincaré return map is suggested in [168] for considering uncertainties in the guard function, which locates the transition events, to improve the robustness of the resultant gait with respect to uncertain terrain. Nevertheless, the assessment of the Poincaré map is carried out numerically, resulting in demanding computations throughout the optimization process, as discussed in [118]. Consequently, the Poincaré return map method is considered a validation procedure for the stability analysis established in this thesis within the framework of Floquet Theory.

Floquet Theory

As elucidated in [122, Section 3.2], Floquet theory is primarily concerned with the dynamics of a perturbation $\delta\mathbf{x}(t)$ imposed on the periodic solution $\mathbf{\Phi}(\mathbf{x}_0, t)$, these dynamics being dictated by the differential equations

$$\frac{\mathrm{d}\,\delta\mathbf{x}}{\mathrm{d}t} = \frac{\partial\mathbf{f}(\mathbf{x})}{\partial\mathbf{x}}\,\delta\mathbf{x} + O(\|\delta\mathbf{x}\|^2) \ , \text{ or } \quad \frac{\mathrm{d}\,\delta\mathbf{x}}{\mathrm{d}t} \approx \frac{\partial\mathbf{f}(\mathbf{x})}{\partial\mathbf{x}}\,\delta\mathbf{x} \ . \tag{2.9}$$

The n-independent solutions of the linearized differential equations (2.9) constitute the fundamental matrix solution $\delta\mathbf{X}(t) \in \mathbb{R}^{n\times n}$, which is assessed at the period $t = T$, thereby yielding the monodromy matrix $\mathbf{D} = \delta\mathbf{X}(T)$. The monodromy matrix $\mathbf{D}$ specifically elucidates the evolution of perturbations over the given period T, thereby defining the stability characteristics of the periodic solution. Within this framework, the eigenvalues of $\mathbf{D}$, known as Floquet multipliers, are evaluated to quantify orbital stability. As evidenced in [122, Section 3.2], autonomous systems inherently possess a trivial multiplier equal to unity, indicative of a phase shift in the flow direction. Consequently, a limit cycle is deemed asymptotically stable when all nontrivial multipliers are less than unity.
In order to accommodate nonsmooth dynamics, the study presented in [3] augments the monodromy matrix through the employment of the saltation matrix, which precisely addresses the first-order approximation of the variation update as it traverses discrete transition events [92]. Nonetheless, the eigenvalue analysis for hybrid dynamical systems

remains unaltered. Owing to its high numerical efficiency in handling limit cycles of high dimensionality, Floquet Theory is employed in this thesis to conduct stability analysis.

2.4.4 Lyapunov Exponents and Chaotic Systems

In addition to fixed points and limit cycles, numerous dynamical systems demonstrate chaotic behavior, characterized by trajectories that exhibit extreme sensitivity to initial conditions. Lyapunov Exponents serve to quantify the average exponential rates at which proximate trajectories diverge (or converge), thus playing a crucial role in stability analysis [122, Section 7.8]. Specifically, the identical linearized perturbation dynamics, as defined in (2.9), are considered for deriving the Lyapunov Exponents, which are expressed as

$$\overline{\lambda}_i = \lim_{t\to\infty} \frac{1}{t} \ln\left(\frac{\|\delta\mathbf{x}(t)\|}{\|\delta\mathbf{x}_i(t=0)\|}\right), \quad i \in [1, n]\,. \tag{2.10}$$

A limit cycle is deemed stable when one of its Lyapunov Exponents equals zero, whereas the other exponents assume negative values. In contrast, chaotic dynamics is indicated by the existence of a Lyapunov Exponent that possesses a positive value. Additionally, the derivation of Lyapunov Exponents for dynamical systems with discontinuous transitions follows the methodology proposed in [120]. However, owing to the asymptotic nature of the method that necessitates numerical evaluations as outlined in $t \to \infty$, it is deemed unsuitable for application in numerical optimization.

2.5 Nonlinear Control Theory

Nonlinear control theory is concerned with the investigation and development of control strategies for systems governed by nonlinear differential equations. Unlike linear systems, for which the principles of superposition and established methodologies are applicable, nonlinear dynamical systems, according to [150, Section 1.1], demonstrate considerable differences from linear systems in various critical aspects:

1. **Superposition Principle:** In contrast to linear systems, nonlinear systems are not governed by the principle of superposition, as elaborated in [107, Section 4.2]. Consequently, the output of a nonlinear system is not a linear aggregate of its inputs, thereby complicating both analysis and prediction.

2. **Equilibria and Stability:** Nonlinear systems are capable of having multiple equilibrium points, each of which may exhibit different stability characteristics, as

indicated in [163, Section 2.2]. These equilibria can include stable nodes, saddle points, spiral points, as well as unstable or semi-stable configurations.

3. **Complex Dynamics:** Nonlinear systems are capable of exhibiting intricate behaviors, including limit cycles, bifurcations, and chaotic dynamics, whereby slight deviations in initial conditions can result in markedly different outcomes, as noted in [163, Section 9.3].

4. **Analysis Techniques:** The analysis of nonlinear systems requires the utilization of specialized tools, such as Lyapunov stability theory as noted in [150, Section 5.3] and the Poincaré map as described in [122, Section 7.6]. In contrast, linear systems can be effectively analyzed using more straightforward methodologies, including eigenvalue analysis as outlined in [11, Section 5.3] and frequency-domain techniques documented in [107, Section 6.3].

A multitude of methodologies has surfaced to comprehend and manipulate these nonlinear systems. In particular, the employment of various linearization methods affords a profound understanding of nonlinear system behaviors by employing control strategies originally devised for linear systems.
This section expounds upon the fundamental concepts underlying these methodologies, offering a comprehensive overview of the simplification, analysis, and control of nonlinear systems. The discussion starts with local Taylor linearization in Section 2.5.1 as a tool to approximate nonlinear dynamics near an operating point. Feedback linearization in Section 2.5.2 follows, demonstrating how canceling nonlinearities extends the use of linear control strategies across a wider domain.

2.5.1 Local Taylor Linearization

Local Taylor linearization employs the Hartman-Grobman Theorem, as introduced in Section 2.4.2, for the development of controllers within a nonlinear system. Specifically, the nonlinear behavior in the vicinity of an equilibrium point is approximated through its linearization, allowing the application of linear control laws.
Consider a nonlinear system:

$$\frac{\mathrm{d}\mathbf{x}}{\mathrm{d}t} = \mathbf{f}(\mathbf{x}, \mathbf{u}) \,, \tag{2.11}$$

with state $\mathbf{x} \in \mathbb{R}^n$ and control input $\mathbf{u} \in \mathbb{R}^m$.

Let $(\mathbf{x}_{\text{eq}}, \mathbf{u}_{\text{eq}})$ be an equilibrium point, meaning $\mathbf{f}(\mathbf{x}_{\text{eq}}, \mathbf{u}_{\text{eq}}) = \mathbf{0}$. A first-order Taylor expansion around $(\mathbf{x}_{\text{eq}}, \mathbf{u}_{\text{eq}})$ is presented as

$$\mathbf{f}(\mathbf{x}, \mathbf{u}) \approx \mathbf{f}(\mathbf{x}_{\text{eq}}, \mathbf{u}_{\text{eq}}) + \underbrace{\left.\frac{\partial \mathbf{f}(\mathbf{x}, \mathbf{u})}{\partial \mathbf{x}}\right|_{(\mathbf{x}_{\text{eq}}, \mathbf{u}_{\text{eq}})}}_{\mathbf{A}(\mathbf{x}_{\text{eq}}, \mathbf{u}_{\text{eq}})} \underbrace{(\mathbf{x} - \mathbf{x}_{\text{eq}})}_{\Delta \mathbf{x}} + \underbrace{\left.\frac{\partial \mathbf{f}(\mathbf{x}, \mathbf{u})}{\partial \mathbf{u}}\right|_{(\mathbf{x}_{\text{eq}}, \mathbf{u}_{\text{eq}})}}_{\mathbf{B}(\mathbf{x}_{\text{eq}}, \mathbf{u}_{\text{eq}})} \underbrace{(\mathbf{u} - \mathbf{u}_{\text{eq}})}_{\Delta \mathbf{u}} , \tag{2.12}$$

Given $\mathbf{f}(\mathbf{x}_{\text{eq}}, \mathbf{u}_{\text{eq}}) = \mathbf{0}$, the linearized system of (2.11) becomes

$$\frac{\mathrm{d}\Delta \mathbf{x}}{\mathrm{d}t} = \mathbf{A}(\mathbf{x}_{\text{eq}}, \mathbf{u}_{\text{eq}})\Delta \mathbf{x} + \mathbf{B}(\mathbf{x}_{\text{eq}}, \mathbf{u}_{\text{eq}})\Delta \mathbf{u} . \tag{2.13}$$

Following the linearization process, the system becomes suitable for the application of linear control techniques, including the Pole Placement approach outlined in [11, Section 7.2] and the Linear Quadratic Regulators (LQR) methodologies detailed in [11, Section 7.5], to achieve stabilization or adjust performance in the vicinity of the equilibrium point. The linearization approach is supported by the Hartman-Grobman Theorem, which posits that the local dynamics of the nonlinear system are equivalent to those of the linearized model, assuming the equilibrium point is hyperbolic.
Although the procedure appears straightforward, its limitations are markedly evident. The localized approach to managing the nonlinear system results in diminished precision of feedback control as the system deviates from its equilibrium state. Furthermore, as the control law is predicated on a first-order approximation, it becomes difficult to address complex systems with high-order nonlinear terms. Additionally, in scenarios involving multiple operating points, it is necessary to conduct separate linearizations for each equilibrium or operational region, thus increasing the implementation effort required for the control law.

2.5.2 Feedback Linearization

As initially proposed in [79], feedback linearization constitutes a crucial methodology within the realm of nonlinear control theory. It enables the conversion of a nonlinear system into an equivalent linear system through the application of state feedback, drawing upon concepts from differential geometry, especially differentiable manifolds [174]. In contrast to Taylor linearization, as discussed in Section 2.5.1, the feedback linearization approach is not restricted to the analysis of local behavior around a hyperbolic equilibrium point. Extensions, particularly the feedforward linearization approach cited in [64], employ flatness-based control methods as described in [48] to improve trajectory tracking efficacy. Subsequent extensions are exemplified in [121, 142], wherein feedback linearization is applied to facilitate real-time model predictive control.

The core concept is investigated through a single-input, single-output nonlinear control-affine system, as described in

$$\frac{\mathrm{d}\mathbf{x}}{\mathrm{d}t} = \mathbf{f}(\mathbf{x}) + \mathbf{g}(\mathbf{x})\, u \,, \tag{2.14a}$$

$$y = h(\mathbf{x}) = 0 \,, \tag{2.14b}$$

where $\mathbf{x} := [x_1, x_2, \ldots, x_n]^\top \in \mathbb{R}^n$ denotes the state variable, $u \in \mathbb{R}$ represents the input, $y \in \mathbb{R}$ signifies the output, and $\mathbf{f} : \mathbb{R}^n \to \mathbb{R}^n$ along with $\mathbf{g} : \mathbb{R}^n \to \mathbb{R}^n$ are nonlinear, sufficiently smooth [1] vector fields.
In order to construct the state transformation as outlined in $\mathbf{z} = \mathbf{\Phi}(\mathbf{x})$, which is identified as a diffeomorphism in accordance with [174, Definition 1.27], the Lie derivatives of the output $h(\mathbf{x})$ are performed by following the procedure described in [79, Section 4.1]. This approach yields the sequence

$$\mathcal{L}_\mathbf{g} h,\ \mathcal{L}_\mathbf{g}\mathcal{L}_\mathbf{f} h,\ \ldots,\ \mathcal{L}_\mathbf{g}\mathcal{L}_\mathbf{f}^k h \,, \tag{2.15}$$

where $\mathcal{L}_\mathbf{g} h := (\partial h/\partial \mathbf{x})\mathbf{g}(\mathbf{x})$ and $\mathcal{L}_\mathbf{g}\mathcal{L}_\mathbf{f} h := (\partial \mathcal{L}_\mathbf{f} h/\partial \mathbf{x})\mathbf{g}(\mathbf{x})$ specifically represent the Lie derivatives of h and $\mathcal{L}_\mathbf{f} h$ with respect to the vector field $\mathbf{g}(\mathbf{x})$, respectively. The sequence (2.15) identifies the relative degree of the output function $h(\mathbf{x})$ in relation to the system input u. Formally, the relative degree r is defined as the smallest integer such that

$$\mathcal{L}_\mathbf{g}\mathcal{L}_\mathbf{f}^{r-1} h \neq 0 \,.$$

When the relative degree r is equal to the system order $n = r$, full-state feedback linearization can be attained through the utilization of an input transformation, as elucidated in

$$u = \alpha(\mathbf{x}) + \beta(\mathbf{x}) v = -\left(\mathcal{L}_\mathbf{g}\mathcal{L}_\mathbf{f}^{r-1} h\right)^{-1} \mathcal{L}_\mathbf{f}^r h + \left(\mathcal{L}_\mathbf{g}\mathcal{L}_\mathbf{f}^{r-1} h\right)^{-1} \frac{\mathrm{d}^r y}{\mathrm{d}t^r} \,. \tag{2.16}$$

Specifically, $\mathcal{L}_\mathbf{g}\mathcal{L}_\mathbf{f}^{r-1} h$ is designated as the decoupling matrix, and its invertibility is imperative for the formulation of the linearization. The new input $v := \mathrm{d}^r y/\mathrm{d}t^r$ demonstrates a linear dependency on the output y through the employment of r integrators. As a result, feedback techniques devised for linear systems are employed to design the input (2.16) to facilitate the (asymptotic) convergence of the output $y = 0$.

[1] "Sufficiently smooth" indicates that the function possesses enough differentiability to ensure that mathematical expressions such as Jacobians, Lie derivatives, and transformations are well-defined and continuous.

Zero Dynamics

In contrast, the condition $r < n$ signifies the presence of unobservable (internal) dynamics with a dimension of $n - r$. These internal or zero dynamics delineate the behavior of the system state when the output is restricted to remain at zero or be maintained at a constant reference value. In other words, zero dynamics are the state variables that are not controllable or observable [106]. In numerous design frameworks, it is imperative to ensure the stability of the internal dynamics, as instability in these unforced dynamics could compromise a control strategy, even if the output accurately tracks its intended reference.
Zero dynamics have both linear and nonlinear interpretations:

- In a linear system, zero dynamics pertain to the internal modes of the system when the output is consistently zero. Specifically, these zero dynamics are characterized by the zeros of the transfer function that relates the output to the input, as demonstrated in [107, Section 5.5.4]. Should the zero dynamics be unstable (i.e., possessing an eigenvalue with a positive real part), the internal states may diverge even if the output can be perfectly regulated to zero via a feedback law. Such a system is termed non-minimum phase.

- In nonlinear systems, zero dynamics are determined by imposing $y(t) = 0$ and then analyzing the remaining dynamics on the zero dynamics manifold, which serves as a submanifold embedded within the complete system. Similar to the linear scenario, if these induced zero dynamics exhibit instability, it is not possible to correct this instability solely through output-based feedback while preserving $y(t) = 0$. Therefore, ensuring the stability of the resulting zero dynamics is crucial for controller design using the feedback linearization approach.

Virtual Constraints

The notion of zero dynamics is pivotal in the formulation of virtual constraints [157], particularly in the context of bipedal or hybrid dynamics control. The Hybrid Zero Dynamics control strategy employs feedback control mechanisms to enforce reference trajectories within the actuated joints [177, Section 6.1]. Synchronization of the joint angles with the reference is identified as holonomic virtual constraints. This synchronization facilitates the simplification of complex locomotion system dynamics to the reduced-dimensional zero dynamics. These reduced dimensions specifically represent the degrees of freedom that remain uninfluenced by the actuators within the joints. Consequently, the examination of gait stability is expressed through the stability of the zero dynamics.

2.5.3 Academic Example

A first-order nonlinear system is characterized by the differential equation $\dot{x} = 2x^2 + u$, where x denotes the state of the system and u signifies the control input. The primary objective is to regulate x to reach the equilibrium point $(x_{\text{eq}}, u_{\text{eq}}) = (0, 0)$. An evaluation of two distinct linearization methods is conducted, with results illustrated in Figure 2.4. Simulations are conducted across a range of diverse initial conditions $x(t = 0) \in [-2, 3]$ to assess the effectiveness of both linearization methods. The results suggest that although local Taylor linearization (Figure 2.4a) shows satisfactory performance for minor initial perturbations due to its local linearization, feedback linearization (Figure 2.4b) consistently demonstrates robust performance across a more extensive range of initial conditions.

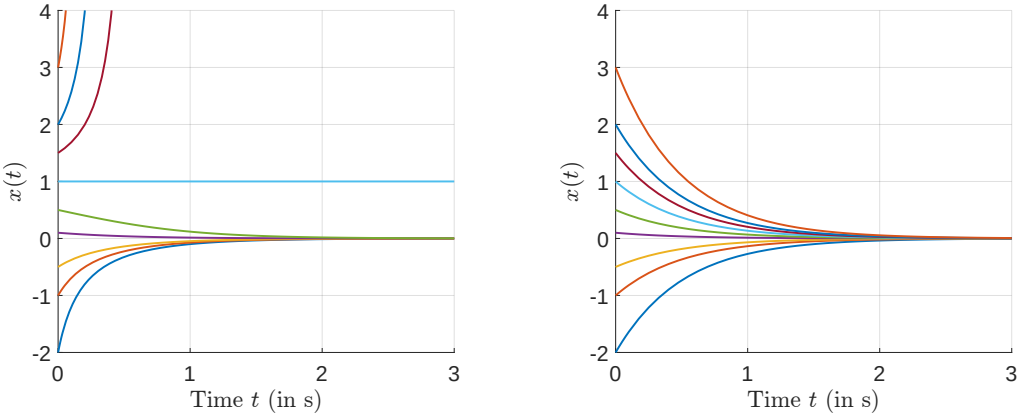

(a) Local Linear Taylor Controller.

(b) Feedback Linearization Controller.

Figure 2.4: Output response to varying initial deviations by employing diverse linearization techniques.

2.6 Numerical Methods to Locate Periodic Solutions

A multitude of physical and engineering systems exhibit periodic behavior. In the area of bipedal robotics, the periodic nature of locomotion gaits is frequently recognized [87]. The numerical determination of a periodic solution of the form (2.8) is essential for understanding limit cycles, oscillators, and other recurrent phenomena. As articulated in [122, Section 6.5], methods formulated in the time domain include the brute-force simulation approach, finite-difference method, shooting method, and Poincaré map method. In frequency domain formulation, harmonic balance method approximates periodic [93, Chapter 2] and quasi-periodic [13] solutions in nonlinear systems with considerable numerical efficiency.

Within the framework of generating periodic solutions pertinent to biped locomotion, which necessitates elevated numerical efficiency and precision [21], this section conducts an evaluation of three well-established numerical methodologies. These include the collocation method as articulated in Section 2.6.1, the single shooting method as deliberated in Section 2.6.2, and the multiple shooting method as explicated in Section 2.6.3.

2.6.1 Collocation Method

Generating locomotion trajectories with the collocation method can be formulated as a nonlinear optimization problem in which both the system states $\mathbf{x}$ and control inputs $\mathbf{u}$ over a full gait cycle are simultaneously treated as decision variables [69]. The trajectory is typically represented by discretized, piecewise polynomial segments [88]. The resultant endpoints (i.e., collocation points) must satisfy dynamic feasibility and other gait-related constraints, such as joint limits or specified contact events, imposed by the optimization [12], and augmented stabilization techniques addressing constraint violations [26]. As the state variables over the entire period are simultaneously considered in the objective function, the method yields a favorable gradient structure and can improve numerical conditioning [136].
However, collocation's performance is highly dependent on the quality of the initial guess for both the state trajectory $\mathbf{x}(t)$ and the gait period T. This sensitivity can be particularly pronounced in problems featuring multiple distinct solutions. Compared to shooting-based approaches, which forward-simulate the dynamics from an initial condition (thereby naturally preserving physical feasibility if they converge), collocation methods solve a boundary-value formulation and may converge to an unphysical solution if the initial guess or constraints are not well chosen.
[182] undertakes a comparative analysis of the direct collocation method, configured with complementary conditions, and the multiple shooting method, and deduces that a significant limitation of the direct collocation technique is its poor numerical accuracy. The significance of numerical accuracy is paramount within this thesis, as the behavior on compliant ground necessitates efficient and precise numerical approximations due to the intrinsic stiffness characteristic of the underlying differential equations. Consequently, the collocation method is not employed in this research work.

2.6.2 Single Shooting Method

The single shooting method recasts the computation of a periodic orbit as a root-finding problem:

$$\mathbf{\Phi}(\mathbf{x}_0, T) - \mathbf{x}_0 = \mathbf{0}\,,$$

where $\mathbf{\Phi}(\mathbf{x}_0, T)$ represents the state of the system after integrating the ODE from $t = 0$ to $t = T$, starting with the initial condition $\mathbf{x}_0$. If $\mathbf{x}_0$ lies on a true periodic orbit of period T, integrating one full period must bring the system back to $\mathbf{x}_0$. Solvers such as Newton's method iteratively adjust $\mathbf{x}_0$ and T to satisfy this periodicity condition.
One notable advantage of the single shooting method is its conceptual simplicity, as it requires the resolution of only one initial value problem per iteration. Nonetheless, this approach is often highly sensitive to initial estimates and susceptible to numerical instabilities. Specifically, owing to the extended integration horizon and the hybrid characteristics of the system dynamics, slight variations in the initial conditions can lead to significant modifications in the optimization objectives or constraints. This, in turn, negatively impacts the gradient's condition, thereby complicating the convergence of the optimization process [22, Section 3.3].

2.6.3 Multiple Shooting Method

In order to mitigate certain limitations inherent in the single shooting technique, the multiple shooting method segments the time interval $[0, T]$ into M shorter equidistant intervals:

$$0 = t_0 < t_1 < \cdots < t_{M-1} < t_M = T \, .$$

This approach effectively diminishes the trajectory solution's sensitivity to the initial conditions over the entire interval [22, Section 3.4]. Furthermore, it incorporates intermediate states $\mathbf{x}_i = \mathbf{x}(t_i)$ as variables within the optimization process. Two essential steps are:

1. The initial value problem must be resolved within each sub-interval $t \in [t_i, t_{i+1}]$, ensuring that the solution in every segment is consistent with the system's dynamics.

2. Continuity at the boundaries of sub-intervals must be maintained, as noted in $\mathbf{x}_i(t_{i+1}) = \mathbf{x}_{i+1}$, and a periodic boundary condition is imposed as specified in $\mathbf{x}_M = \mathbf{x}_0$.

The full set of unknowns $[\mathbf{x}_0^\top, \mathbf{x}_1^\top, \ldots, \mathbf{x}_{M-1}^\top, T]^\top$ is then solved simultaneously using a nonlinear system solver, such as Newton's method [41, Section 1.2]. In addition, multiple shooting is often advantageous because each sub-interval can be tailored to different phases of the gait (e.g., single support, double support), and advanced ODE/DAE solvers can be chosen accordingly.
Finally, when combined with solution continuation techniques or model-predictive control schemes that use warm-starting (i.e., initial guesses derived from neighboring

solutions), multiple shooting primarily refines an already close approximation as a corrective mechanism. This can substantially improve convergence speed and robustness, making it a popular method for online [183] and offline [68] trajectory generation and real-time control [42].

2.7 Nonlinear Numerical Optimization

Optimization is the process of finding the "best" solution to a problem under specified constraints. The notion of "best" is captured in a scalar-valued objective function, which typically quantifies cost, profit, performance, or other relevant metrics. A general nonlinear optimization problem can be formulated as follows:

$$\begin{aligned} &\min_{\mathbf{x}\in\mathbb{R}^n} \quad f(\mathbf{x})\,, \\ &\text{subject to} \quad \mathbf{g}(\mathbf{x}) \leq \mathbf{0}\,, \quad \mathbf{h}(\mathbf{x}) = \mathbf{0}\,, \end{aligned} \tag{2.17}$$

where $\mathbf{x}$ represents the decision variables or optimization parameters, $f : \mathbb{R}^n \to \mathbb{R}$ is the objective function. $\mathbf{g} : \mathbb{R}^n \to \mathbb{R}^m$ and $\mathbf{h} : \mathbb{R}^n \to \mathbb{R}^p$ denote the inequality and equality constraints, respectively.
Generating bipedal gaits naturally lends itself to this nonlinear formulation, due to the complex dynamics and various constraints involved. Consequently, this section highlights three major methodologies for solving such problems: the Karush–Kuhn–Tucker conditions (Section 2.7.1), Interior-Point methods (Section 2.7.2), and Sequential Quadratic Programming (Section 2.7.3).

2.7.1 Karush-Kuhn-Tucker Conditions

The Karush-Kuhn-Tucker (KKT) conditions constitute a first-order necessary criterion for determining an optimal solution within the framework of a nonlinear programming problem, incorporating both equality and inequality constraints as delineated in (2.17). In particular, the KKT conditions extend the traditional Lagrange multiplier approach, which solely addresses equality constraints [125, Section 12.3]. Thus, the Lagrangian function of the constrained optimization problem (2.17) is represented as

$$L(\mathbf{x}, \boldsymbol{\mu}, \boldsymbol{\lambda}) = f(\mathbf{x}) + \boldsymbol{\mu}^\top \mathbf{g}(\mathbf{x}) + \boldsymbol{\lambda}^\top \mathbf{h}(\mathbf{x})\,, \tag{2.18}$$

wherein $\boldsymbol{\mu} \in \mathbb{R}^m$ and $\boldsymbol{\lambda} \in \mathbb{R}^p$ denote the KKT multipliers associated with inequality and equality constraints, respectively.

As elucidated in [125, Theorem 12.1], the KKT conditions for a prospective local optimal solution $\mathbf{x}^*$ are delineated as follows:

$$\underbrace{\left.\frac{\partial L(\mathbf{x},\boldsymbol{\mu},\boldsymbol{\lambda})}{\partial \mathbf{x}}\right|_{\mathbf{x}=\mathbf{x}^*}}_{\nabla_{\mathbf{x}} L(\mathbf{x}^*,\boldsymbol{\mu},\boldsymbol{\lambda})} = \underbrace{\left.\frac{\partial f(\mathbf{x})}{\partial \mathbf{x}}\right|_{\mathbf{x}=\mathbf{x}^*}}_{\nabla f(\mathbf{x}^*)} + \boldsymbol{\mu}^\top \underbrace{\left.\frac{\partial \mathbf{g}(\mathbf{x})}{\partial \mathbf{x}}\right|_{\mathbf{x}=\mathbf{x}^*}}_{\nabla \mathbf{g}(\mathbf{x}^*)} + \boldsymbol{\lambda}^\top \underbrace{\left.\frac{\partial \mathbf{h}(\mathbf{x})}{\partial \mathbf{x}}\right|_{\mathbf{x}=\mathbf{x}^*}}_{\nabla \mathbf{h}(\mathbf{x}^*)} = \mathbf{0}\,, \tag{2.19a}$$

$$\mathbf{g}(\mathbf{x}^*) \leq \mathbf{0}\,, \quad \mathbf{h}(\mathbf{x}^*) = \mathbf{0}\,, \tag{2.19b}$$

$$\boldsymbol{\mu} \geq \mathbf{0}\,, \tag{2.19c}$$

$$\boldsymbol{\mu}^\top \mathbf{g}(\mathbf{x}^*) = \mathbf{0}\,. \tag{2.19d}$$

Specifically, condition (2.19a) is termed as stationarity, condition (2.19b) signifies primal feasibility, condition (2.19c) denotes dual feasibility, and finally, condition (2.19d) is referred to as the complementary condition (or complementary slackness).
The KKT conditions form the cornerstone of algorithms in constrained nonlinear optimization. The traditional method of Lagrange multipliers, which considers only equality constraints, posits that at an optimal solution, the gradient of the objective function aligns as a linear combination with the gradients of the equality constraints. The KKT conditions extend this principle by incorporating dual variables and the concept of complementary slackness to encompass inequality constraints. Consequently, active inequality constraints exert a direct influence on the optimality criteria of a solution.

2.7.2 Interior-Point Methods

Originally developed for linear optimization problems, Interior-Point methods have been extended to handle general nonlinear programs by introducing barrier functions, often of a logarithmic form, that penalize any approach to a constraint boundary. According to [125, Section 19.1], the nonlinear optimization problem (2.17) is rewritten into

$$\begin{aligned} \min_{\mathbf{x},\mathbf{s}} \quad & f(\mathbf{x}) - \mu_{\mathrm{IP}} \sum_{i=1}^{m} \log s_i\,, \\ \text{subject to} \quad & \mathbf{g}(\mathbf{x}) + \mathbf{s} = \mathbf{0}\,, \quad \mathbf{h}(\mathbf{x}) = \mathbf{0}\,, \end{aligned} \tag{2.20}$$

wherein $\mathbf{s} \in \mathbb{R}^m$ represent the slack variables employed to convert the inequality constraints $\mathbf{g}(\mathbf{x})$ into equalities. The barrier parameter $\mu_{\mathrm{IP}} > 0$ denotes a penalty term that takes positive values. Consequently, the penalty operator $\log(\cdot)$ ensures that the condition $\mathbf{s} > \mathbf{0}$ is upheld throughout the optimization process.
The barrier subproblem (2.20) is generally addressed through the application of a Newton or quasi-Newton method. Each iteration necessitates the resolution of a linear system formulated on the basis of the KKT conditions of the barrier-augmented objective.

Upon approximation of a local minimizer for the barrier subproblem, adjustment of μ_{IP} and subsequent resolution are performed. This process produces a sequence of solutions that asymptotically converge to a point fulfilling the original constraints at the limit $\mu_{\mathrm{IP}} \to 0$, as presented in [125, Algorithm 19.1].

2.7.3 Sequential Quadratic Programming

Sequential Quadratic Programming (SQP) represents one of the most efficacious approaches for addressing smooth nonlinear optimization tasks that involve equality and inequality constraints. SQP is distinguished by its superlinear convergence properties within the proximity of a solution. Fundamentally, iterative quasi-Newton steps are employed to fulfill the KKT conditions (2.19) associated with the nonlinear optimization problem (2.17), wherein these iterative steps are structured as a succession of Quadratic Program (QP) subproblems.
Specifically, at the k-th iteration $(\mathbf{x}_k, \boldsymbol{\mu}_k, \boldsymbol{\lambda}_k)$, the QP subproblem with linearized constraints is formulated as

$$\begin{aligned} \min_{\mathbf{p}} \quad & \nabla f(\mathbf{x}_k)^\top \mathbf{p} + \frac{1}{2}\mathbf{p}^\top \underbrace{\left.\frac{\partial^2 L(\mathbf{x}, \boldsymbol{\mu}, \boldsymbol{\lambda})}{\partial \mathbf{x}^2}\right|_{\mathbf{x}_k, \boldsymbol{\mu}_k, \boldsymbol{\lambda}_k}}_{\nabla^2_{\mathbf{xx}} L(\mathbf{x}_k, \boldsymbol{\mu}_k, \boldsymbol{\lambda}_k)} \mathbf{p} \\ \text{subject to} \quad & \nabla \mathbf{h}(\mathbf{x}_k)^\top \mathbf{p} + \mathbf{h}(\mathbf{x}_k) = \mathbf{0}\,, \\ & \nabla \mathbf{g}(\mathbf{x}_k)^\top \mathbf{p} + \mathbf{g}(\mathbf{x}_k) \leq \mathbf{0}\,, \end{aligned} \tag{2.21}$$

in which $\nabla^2_{\mathbf{xx}} L(\mathbf{x}_k, \boldsymbol{\mu}_k, \boldsymbol{\lambda}_k)$ represents the Hessian of the Lagrangian function (2.18). This Hessian is typically approximated by employing a Broyden–Fletcher–Goldfarb–Shanno (BFGS) algorithm [125, Section 6.1] to enhance computational efficiency while preserving positive definiteness. The resolution $\mathbf{p}$ of the subproblem (2.21) informs the subsequent iteration $\mathbf{x}_{k+1} = \mathbf{x}_k + \alpha_k \mathbf{p}$, which utilizes either a line search [125, Section 18.4] or a trust-region approach [125, Section 18.5]. The Lagrange multipliers $(\boldsymbol{\mu}_{k+1}, \boldsymbol{\lambda}_{k+1})$ are revised based on the violation of the optimization constraints.
Since each iteration of the SQP method may necessitate solving a substantial QP, it can be computationally intensive for problems characterized by high dimensionality or significant nonlinearity. Notwithstanding these challenges, SQP is recognized as one of the most robust and precise methodologies for constrained nonlinear optimization, especially when solutions of high quality and rapid local convergence are imperative. In the realm of Model Predictive Control, real-time iteration strategies that leverage warm starts have been developed to facilitate the application of the SQP algorithm in online control scenarios [62].

2.7.4 Academic Example

The nonlinear optimization problem, as delineated in

$$\begin{aligned} \min_{x_1,x_2} \quad & f(x_1,x_2) = x_1^2 + x_2^2 \\ \text{Subject to} \quad & 1-(x_1+x_2) \leq 0\,, \quad -x_1 \leq 0\,, \quad -x_2 \leq 0\,, \end{aligned}$$

demonstrates MATLAB's `fmincon` proficiency in solving a simple convex problem by deploying two nonlinear programming techniques with identical initialization. The Interior-Point method in Figure 2.5a effectively manages constraints via barrier functions, resulting in an initial iteration that outperforms the SQP method. However, as the iterations progress towards the optimal solution, the Interior-Point method does not exhibit a marked advantage in convergence efficiency, requiring 10 iteration steps.

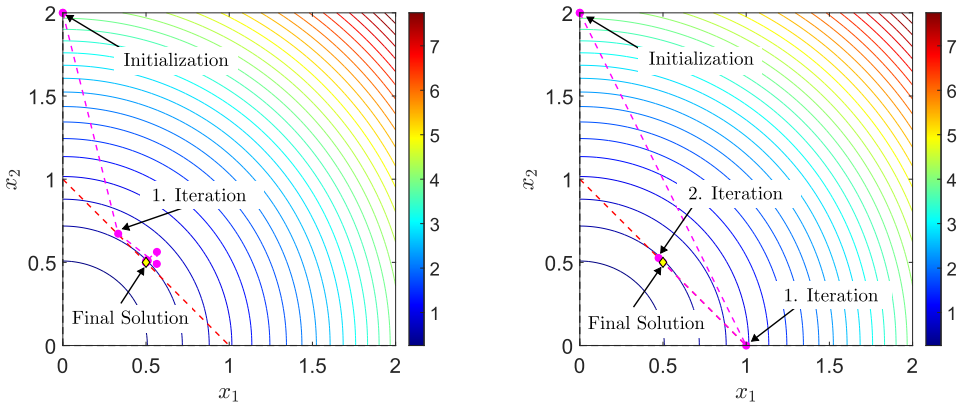

(a) Interior-Point method.

(b) Sequential Quadratic Programming.

Figure 2.5: Illustration of nonlinear optimization resolved through two distinct nonlinear programming methodologies.

In contrast, the SQP method outlined in Figure 2.5b demonstrates accelerated convergence proximate to the optimum, necessitating merely 3 iteration steps. This prompt convergence is predominantly attributed to the linear constraint, which is effectively represented within the QP subproblem.
Furthermore, the SQP method exhibits substantial performance in contexts involving solution continuations. This is relevant to the optimization strategy elucidated in this thesis, as the gait parameters at varying walking and running velocities are utilized for initializing the neighboring speeds.

2.7.5 Calculation of Derivatives

The precise computation of derivative information is essential for the efficacy of optimization algorithms, especially those based on gradients and Newton-type methods. In instances where analytical computation of derivatives is impractical, practitioners resort to techniques such as Finite Difference, Complex Step Differentiation, and Automatic Differentiation.

Finite Difference

Finite Difference methodologies provide an estimation of derivatives through the perturbation of input values, as articulated in a scalar function $f(x)$:

$$\frac{\mathrm{d}f(x)}{\mathrm{d}x} \approx \frac{f(x+h) - f(x)}{h},$$

where h denotes a minor incremental value. In the multivariate case $f : \mathbb{R}^n \to \mathbb{R}$, each component of x is perturbed in turn. This approach is easy to implement but can be sensitive to round-off errors (if h is too small) or truncation errors (if h is too large).

Complex Step Differentiation

Using complex perturbations can reduce the numerical cancellation issues of the Finite Difference method. For a real-valued function f, the derivative at x_0 can be approximated by:

$$\left.\frac{\mathrm{d}f(x)}{\mathrm{d}x}\right|_{x=x_0} \approx \frac{\mathrm{Im}\big(f(x_0 + i\,h)\big)}{h}.$$

This technique provides highly accurate results if the function can be evaluated for complex inputs.

Automatic Differentiation

Automatic Differentiation (AD) leverages the chain rule at the level of elementary operations within a computer program, producing exact derivatives up to machine precision [125, Section 8.2]. Its two primary modes are:

- Forward Mode, propagating derivatives from inputs to outputs (effective when the number of independent variables is small).
- Reverse Mode, propagating derivatives from outputs to inputs (efficient when there are many inputs but few outputs, as in neural networks).

To exploit the advantages of AD in optimizing bipedal walking and running gaits within this thesis, numerical evaluations of the dynamics are carried out using the programming language *Julia*. Notably, *Julia*'s core design is centered around multiple dispatch, enabling functions to exhibit behavior contingent upon the types of all their arguments [24]. This paradigm naturally facilitates the writing of generic code that seamlessly integrates both numerical operations and their derivative counterparts. AD tools harness this capability by defining specialized methods for types representing dual numbers or other AD data structures, thereby allowing derivative calculations to be seamlessly integrated with standard computation without significant overhead.
Julia's metaprogramming features, including macros and generated functions, permit developers to write code that can inspect, transform, and generate other code. AD frameworks in *Julia* frequently utilize these capabilities to automatically transform source code, embedding derivative computations into the code's abstract syntax tree. This process, known as source-to-source transformation, is more straightforward in *Julia* than in numerous other programming languages.

3 Model for Bipedal Walking

This chapter elaborates on the dynamical model of the planar bipedal walking robot, which consists of five rigid body segments. The robot model is well-established and thoroughly examined within the research community focusing on bipedal robots, especially those controlled by a hybrid-zero-dynamics controller [175, 177]. Previous studies typically characterize walking gaits as periodic sequences comprising alternating continuous single support phases and discontinuous double support phases. This thesis advances the existing gait sequence by treating the double support phase as continuous. Section 3.1 presents the comprehensive full-order free-body model that characterizes the two distinct walking gaits. Furthermore, this chapter describes the distinct walking gait characterized by an instantaneous double support phase as delineated in Section 3.2, along with a non-instantaneous double support phase as analyzed in Section 3.3.

3.1 Free-Body Model

The robot model under examination is regarded as planar and consists of five rigid body segments: one upper body, two thighs, and two shanks, as depicted in Figure 3.1a. These segments are interconnected through four actuated revolute joints, with two located in the hip region and the other two positioned in the knee region. Electric drivetrains are incorporated within the robot's joints to provide the requisite driving torque. A point foot is represented at the distal extremity of the shank segment. Consequently, no torque is conveyed between the ground and the robot body, with the point foot in contact being modeled as an ideal pivot joint that is free from any resistive forces.
To address the dynamical model of the biped robot, this section is structured in the following manner: The symbols and terminologies utilized to depict the robot model and its gait within this thesis are clarified in Section 3.1.1; the derivation of the equations of motion for the entire biped model is elucidated in Section 3.1.2.

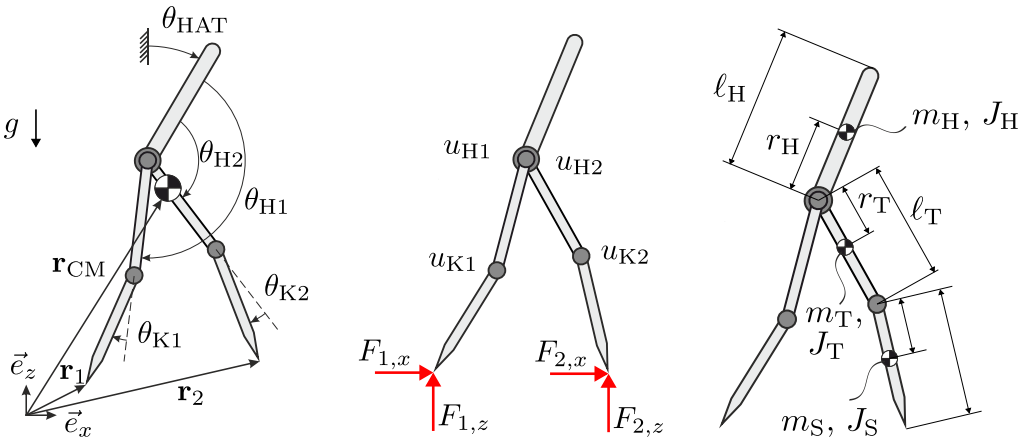

(a) Coordinates of the free-body model.

(b) Actuators in joint and forces at point foot.

(c) Mechanical parameters of model.

Figure 3.1: Specification of coordinates, external forces, torques on the free-body diagram, and mechanical parameters.

3.1.1 Notation

In the main text, the single support phase is abbreviated as "SSP", the double support phase as "DSP", and the flight phase as "FLP". During the SSP, when only one leg is in contact with the ground, the stance leg is designated as "1" and the swing leg as "2". The roles of the front and trailing legs remain unchanged during the transition from SSP to FLP, meaning the leg designations from the SSP carry over into the FLP. In the DSP, the front leg is designated as "1" and the trailing leg as "2". According to this convention, the position $\mathbf{r}_1 := [r_{1,x}, r_{1,z}]^\top \in \mathbb{R}^2$ of the front (or stance) foot and, $\mathbf{r}_2 := [r_{2,x}, r_{2,z}]^\top \in \mathbb{R}^2$ of the trailing (or swing) foot are defined in the coordinate system $\left\{\vec{\mathbf{e}}_x, \vec{\mathbf{e}}_z\right\}$, as depicted in Figure 3.1a.

The comprehensive planar robot model, situated in the coordinate system $\left\{\vec{\mathbf{e}}_x, \vec{\mathbf{e}}_z\right\}$, exhibits seven degrees of freedom. Its dynamical behavior is characterized by the coordinates $\mathbf{q}_{\mathrm{f}} := [\mathbf{r}_{\mathrm{CM}}^\top, \theta_{\mathrm{HAT}}, \mathbf{q}_{\mathrm{b}}^\top]^\top \in \mathcal{Q}_{\mathrm{f}} \subset \mathbb{R}^2 \times \mathbb{T}^5$, where a five-dimensional torus $\mathbb{T}^5 = (S^1)^5$ is formulated as the Cartesian product of five circles S^1. The coordinates of the system $\mathbf{q}_{\mathrm{f}}$ comprehensively include the position $\mathbf{r}_{\mathrm{CM}} := [x_{\mathrm{CM}}, z_{\mathrm{CM}}]^\top$ of the robot's center of mass, the absolute orientation θ_{HAT} of the upper body, and the angular coordinates $\mathbf{q}_{\mathrm{b}} := [\theta_{\mathrm{H1}}, \theta_{\mathrm{H2}}, \theta_{\mathrm{K1}}, \theta_{\mathrm{K2}}]^\top$ relevant to the hip and knee joints, which are powered by the integrated electric motors $\mathbf{u} := [u_{\mathrm{H1}}, u_{\mathrm{H2}}, u_{\mathrm{K1}}, u_{\mathrm{K2}}]^\top$, as demonstrated in Figure 3.1b. Forces $\mathbf{F}_1 := [F_{1,x}, F_{1,z}]^\top$ and $\mathbf{F}_2 := [F_{2,x}, F_{2,z}]^\top$ can dissipate or be activated as either applied or constraint forces within the equations of motion of the

full-order system, depending on the interaction between the robot and its surrounding environment.
Both walking and running gaits are presumed to exhibit periodicity characterized by a consistent average velocity v_{avg}, which is delineated as

$$v_{\text{avg}} := \frac{\ell_{\text{step}}}{t_{\text{step}}} \, . \tag{3.1}$$

The step length ℓ_{step} and step duration t_{step} are computed based on the specific arrangement of the gait trajectory. Specifically, the minimal step duration t_{step} is typically constrained to exceed a negligible magnitude in order to preclude the Zeno effect [1] (also referred to as the chattering sequence) from the scope of this thesis.

3.1.2 Full-Order System Dynamics

Provided the coordinates $\mathbf{q}_{\text{f}}$ and the associated velocities $\dot{\mathbf{q}}_{\text{f}}$ of the comprehensive full-order robot model as referenced in Figure 3.1a, the kinetic energy K_{f} is determined as

$$K_{\text{f}}(\mathbf{q}_{\text{f}}, \dot{\mathbf{q}}_{\text{f}}) = \frac{1}{2}\dot{\mathbf{q}}_{\text{f}}^{\top}\mathbf{M}_{\text{f}}(\mathbf{q}_{\text{f}})\dot{\mathbf{q}}_{\text{f}} = \frac{1}{2}\begin{bmatrix}\dot{\mathbf{r}}_{\text{CM}}^{\top} & \dot{\theta}_{\text{HAT}} & \dot{\mathbf{q}}_{\text{b}}^{\top}\end{bmatrix}\begin{bmatrix}\mathbf{M}_{\text{f},00} & \mathbf{0} & \mathbf{0} \\ \mathbf{0} & M_{\text{f},11} & \mathbf{M}_{\text{f},12} \\ \mathbf{0} & \mathbf{M}_{\text{f},21} & \mathbf{M}_{\text{f},22}\end{bmatrix}\begin{bmatrix}\dot{\mathbf{r}}_{\text{CM}} \\ \dot{\theta}_{\text{HAT}} \\ \dot{\mathbf{q}}_{\text{b}}\end{bmatrix} \, , \tag{3.2}$$

where $\mathbf{M}_{\text{f}}$ denotes the mass-inertia matrix of the multibody model. It is important to highlight that the (2×2)-dimensional submatrix [2] $\mathbf{M}_{\text{f},00} = m_{\text{total}}\mathbf{I}_2$ represents the robot's overall mass m_{total}, which is ascertained by

$$m_{\text{total}} := m_{\text{HAT}} + 2m_{\text{t}} + 2m_{\text{s}} \, . \tag{3.3}$$

The expression for the gravitational potential energy V_{f} is presented in

$$V_{\text{f}}(\mathbf{q}_{\text{f}}) = m_{\text{total}} g z_{\text{CM}} = m_{\text{total}} g \begin{bmatrix}0 & 1 & \mathbf{0}\end{bmatrix}\mathbf{q}_{\text{f}} \, , \tag{3.4}$$

which is then utilized in the derivation of the Lagrangian as demonstrated in $L_{\text{f}} = K_{\text{f}} - V_{\text{f}}$.

[1] As delineated in [20, Section 2.2], the Zeno effect in hybrid dynamical systems is characterized by the manifestation of an infinite number of discrete events or transitions occurring within a finite time interval, which presents difficulties for simulation and necessitates meticulous modeling to address.

[2] This submatrix is identified as the leading principal minor of order two, which is constructed by retaining the initial two rows and columns of the complete matrix.

The dynamics of the comprehensive full-order robot model are governed by the equations of motion, which are derived through Lagrange's equations of the second kind as

$$\frac{\mathrm{d}}{\mathrm{d}t}\frac{\partial L_\mathrm{f}}{\partial \dot{\mathbf{q}}_\mathrm{f}} - \frac{\partial L_\mathrm{f}}{\partial \mathbf{q}_\mathrm{f}} = \mathbf{M}_\mathrm{f}(\mathbf{q}_\mathrm{f}) \underbrace{\begin{bmatrix} \ddot{\mathbf{r}}_\mathrm{CM} \\ \ddot{\theta}_\mathrm{HAT} \\ \ddot{\mathbf{q}}_\mathrm{b} \end{bmatrix}}_{\ddot{\mathbf{q}}_\mathrm{f}} + \underbrace{\begin{bmatrix} \boldsymbol{\Gamma}_{\mathrm{f},0} \\ \boldsymbol{\Gamma}_{\mathrm{f},1} \\ \boldsymbol{\Gamma}_{\mathrm{f},2} \end{bmatrix}}_{\boldsymbol{\Gamma}_\mathrm{f}(\mathbf{q}_\mathrm{f},\dot{\mathbf{q}}_\mathrm{f})} = \underbrace{\begin{bmatrix} \mathbf{0} \\ \mathbf{0} \\ \mathbf{I}_4 \end{bmatrix}}_{\mathbf{B}_\mathrm{f}} \mathbf{u} + \mathbf{G}_1^\top \mathbf{F}_1 + \mathbf{G}_2^\top \mathbf{F}_2 \,, \tag{3.5}$$

wherein $\boldsymbol{\Gamma}_\mathrm{f}$ represents the generalized forces, encompassing both Coriolis and gravitational forces, and $\mathbf{B}_\mathrm{f}$ denotes the actuation projection matrix, composed of the zero matrix $\mathbf{0}$ alongside a (4×4)-dimensional identity matrix $\mathbf{I}_4$. The forces $\mathbf{F}_1$ and $\mathbf{F}_2$ acting at the stance foot are incorporated into the equations via Jacobian $\mathbf{G}_1 := (\partial \mathbf{r}_1 / \partial \mathbf{q}_\mathrm{f})$ and $\mathbf{G}_2 := (\partial \mathbf{r}_2 / \partial \mathbf{q}_\mathrm{f})$, adhering to the principle of virtual work.

3.2 Walking with Instantaneous DSP

As illustrated in Figure 3.2, the periodic walking gait is conceptualized as a series of alternating sequences comprising a single support phase (SSP) and a double support phase (DSP). In particular, the dynamical model of the robot during the continuous SSP is elucidated in Section 3.2.1. Conversely, the instantaneous DSP is characterized as a discontinuous mapping, as examined in Section 3.2.2. These models are articulated in state space, culminating in a hybrid dynamical system as delineated in Section 3.2.3.

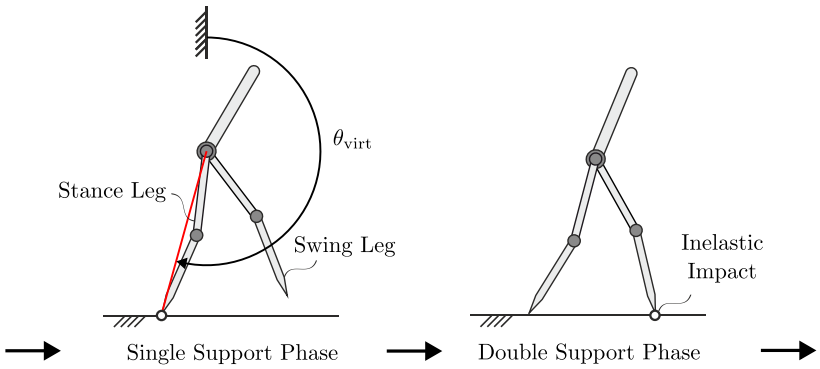

Figure 3.2: Periodic walking gait with an instantaneous double support phase. The red line indicates the virtual leg defined in the single support phase.

3.2.1 Single Support Phase

The equations of motion for the SSP on rigid ground are derived by enforcing the condition that the stance foot remains fixed without slipping, a condition guaranteed through the application of holonomic scleronomic constraints [9], as cited in $\hat{\mathbf{h}}_s : \mathcal{Q}_f \to \mathbb{R}^2;\ \mathbf{q}_f \mapsto \hat{\mathbf{h}}_s(\mathbf{q}_f)$, which are defined with respect to the position $\mathbf{r}_1$ of the stance foot. These constraints, alongside their time derivatives, are articulated as

$$\hat{\mathbf{h}}_s(\mathbf{q}_f) := \mathbf{r}_1(\mathbf{q}_f) = \mathbf{0}\,, \tag{3.6a}$$

$$\dot{\hat{\mathbf{h}}}_s(\mathbf{q}_f, \dot{\mathbf{q}}_f) := \frac{\partial \mathbf{r}_1}{\partial \mathbf{q}_f}\dot{\mathbf{q}}_f = \mathbf{G}_1\dot{\mathbf{q}}_f = \mathbf{0}\,, \tag{3.6b}$$

$$\ddot{\hat{\mathbf{h}}}_s(\mathbf{q}_f, \dot{\mathbf{q}}_f, \ddot{\mathbf{q}}_f) := \mathbf{G}_1\ddot{\mathbf{q}}_f + \frac{\mathrm{d}\mathbf{G}_1}{\mathrm{d}t}\dot{\mathbf{q}}_f = \mathbf{G}_1\ddot{\mathbf{q}}_f + \dot{\mathbf{G}}_1\dot{\mathbf{q}}_f = \mathbf{0}\,. \tag{3.6c}$$

The mutual linear independence of the two constraints referenced in $\hat{\mathbf{h}}_s$, as elaborated in $\vec{\mathbf{e}}_x$ and $\vec{\mathbf{e}}_z$ respectively, indicates the presence of a full-rank Jacobian $\mathbf{G}_1$, which consists of normal vectors pertinent to the constraint surface. Specifically, for non-slipping contact to be maintained, both the positional $\hat{\mathbf{h}}_s = \mathbf{0}$ and velocity constraints $\dot{\hat{\mathbf{h}}}_s = \mathbf{0}$ must be rigorously enforced. In the event of $\ddot{\hat{\mathbf{h}}}_s \neq \mathbf{0}$, an imminent detachment of the stance foot from the ground is foreseen, manifesting either as a slip along the tangent of the ground surface or as a lift-off from the ground.

In contrast, the sustained contact within the SSP is delineated in $\ddot{\hat{\mathbf{h}}}_s = \mathbf{0}$, as elaborated in [133, Section 6]. Accordingly, by integrating the acceleration constraints $\ddot{\hat{\mathbf{h}}}_s = \mathbf{0}$ derived from equation (3.6c) into the equations of motion (3.5) of the full-order system, one attains a Differential-Algebraic Equation (DAE) system characterized by a differentiation index of one [3], which is stated as

$$\begin{bmatrix} \mathbf{M}_f & -\mathbf{G}_1^\top \\ -\mathbf{G}_1 & \mathbf{0} \end{bmatrix} \begin{bmatrix} \ddot{\mathbf{q}}_f \\ \mathbf{F}_1 \end{bmatrix} = \begin{bmatrix} -\boldsymbol{\Gamma}_f + \mathbf{B}_f\mathbf{u} \\ \dot{\mathbf{G}}_1\dot{\mathbf{q}}_f \end{bmatrix}, \tag{3.7}$$

with initial conditions specified in $[\dot{\mathbf{q}}_f(t_0)^\top, \mathbf{q}_f(t_0)^\top, \mathbf{F}_1(t_0)^\top]^\top$. Herein, $\mathbf{q}_f$ and $\dot{\mathbf{q}}_f$ represent the state variables of the system, while the magnitude of the constraint

[3] The differentiation index is defined as the minimum number of differentiations needed to transform the algebraic equations into an ordinary differential equation (ODE) system. When the acceleration constraints $\ddot{\hat{\mathbf{h}}}_s = \mathbf{0}$ are integrated into the formulation (3.7), only a single time differentiation is necessary to derive the time derivative $\dot{\mathbf{F}}_1$, thus yielding an ODE. In contrast, when the position constraint $\hat{\mathbf{h}}_s = \mathbf{0}$ is incorporated with the complete equations of motion, it necessitates three time differentiations to convert the DAE into an ODE, thereby resulting in an index-three DAE problem. This poses considerable challenges in terms of obtaining a solution.

force $\mathbf{F}_1$ functions as the Lagrange multipliers. Specifically, $\mathbf{F}_1$ is formulated by omitting $\ddot{\mathbf{q}}_\mathrm{f}$ from the equation system (3.7), resulting in the expression

$$\mathbf{F}_1 = \begin{bmatrix} F_{1,x} \\ F_{1,z} \end{bmatrix} = \left(\mathbf{G}_1 \mathbf{M}_\mathrm{f}^{-1} \mathbf{G}_1^\top \right)^{-1} \left(\mathbf{G}_1 \mathbf{M}_\mathrm{f}^{-1} \boldsymbol{\Gamma}_\mathrm{f} - \mathbf{G}_1 \mathbf{M}_\mathrm{f}^{-1} \mathbf{B}_\mathrm{f} \mathbf{u} - \dot{\mathbf{G}}_1 \dot{\mathbf{q}}_\mathrm{f} \right) . \tag{3.8}$$

An alternative approach for ascertaining the constraint force $\mathbf{F}_1$ becomes essential due to the particular structure of the Jacobian $\mathbf{G}_1$. The first two columns of $\mathbf{G}_1$ are represented by a unit matrix, denoted as $\begin{bmatrix} \mathbf{I}_2 & \mathbf{0} \end{bmatrix} \mathbf{G}_1 = (\partial \mathbf{r}_1 / \partial \mathbf{r}_\mathrm{CM}) = \mathbf{I}_2$. By specifically extracting the first two rows from the complete system of equations (3.7), the resulting expression is obtained as

$$\mathbf{F}_1 = m_\mathrm{total} \mathbf{I}_2 \ddot{\mathbf{r}}_\mathrm{CM} + \begin{bmatrix} \mathbf{I}_2 & \mathbf{0} \end{bmatrix} \boldsymbol{\Gamma}_\mathrm{f} . \tag{3.9}$$

The prerequisite for non-slipping contact $\hat{\mathbf{h}}_\mathrm{s}$ is governed by the presence of static friction. In accordance with Coulomb's frictional law [133, Section 6.2], both the tangential $F_{1,x}$ and orthogonal forces $F_{1,z}$ are required to remain within the friction cone at all times within the SSP, thus leading to the constraints:

$$\mu F_{1,z} > F_{1,x} > -\mu F_{1,z} , \tag{3.10}$$

characterized by the static friction coefficient $\mu = 0.6$. Simultaneously, unilateral contact demands a positive orthogonal force $F_{1,z}$, which signifies

$$F_{1,z} > 0 . \tag{3.11}$$

Specifically, the inequalities (3.10) and (3.11) are regarded as prerequisites for the feasibility of a SSP on rigid surfaces. These prerequisites are articulated as inequality constraints within the numerical optimization framework elucidated in Chapter 7.

Formulation with Minimal Coordinates

The direct solution of the DAE problem, as detailed in (3.7), demands considerable computational resources, as noted in Section 2.2. Consequently, assuming the strict satisfaction of conditions (3.10) and (3.11) for unilateral contact, the equations of motion in the SSP can be reformulated as ordinary differential equations. This entails the use of five independent and minimal generalized coordinates, which correspond to the five degrees of freedom inherent to the SSP system.

By considering the contact on rigid ground as an ideal pivot, the dynamics of the system are succinctly articulated via a reduced set of generalized coordinates $\hat{\mathbf{q}}_\mathrm{s} \in \hat{\mathcal{Q}}_\mathrm{s}$, defined as

$$\hat{\mathbf{q}}_\mathrm{s} := \begin{bmatrix} \theta_\mathrm{HAT} \\ \mathbf{q}_\mathrm{b} \end{bmatrix} \in \hat{\mathcal{Q}}_\mathrm{s} := \{\mathbf{q}_\mathrm{f} \in \mathcal{Q}_\mathrm{f} | \, \hat{\mathbf{h}}_\mathrm{s}(\mathbf{q}_\mathrm{f}) = \mathbf{0}\} \, . \tag{3.12}$$

The configuration space $\hat{\mathcal{Q}}_\mathrm{s}$ and its corresponding tangent space $T_{\hat{\mathbf{q}}_\mathrm{s}}\hat{\mathcal{Q}}_\mathrm{s}$, wherein the velocities $\dot{\hat{\mathbf{q}}}_\mathrm{s} \in T_{\hat{\mathbf{q}}_\mathrm{s}}\hat{\mathcal{Q}}_\mathrm{s} \subset \mathbb{R}^5$ are articulated, collectively constitute the tangent bundle $T\hat{\mathcal{Q}}_\mathrm{s}$ of the model in the SSP. In this context, the position $\mathbf{r}_\mathrm{CM}\big|_{\hat{\mathcal{Q}}_\mathrm{s}} := \mathbf{r}_\mathrm{CM}(\hat{\mathbf{q}}_\mathrm{s})$ and velocity $\dot{\mathbf{r}}_\mathrm{CM}\big|_{T\hat{\mathcal{Q}}_\mathrm{s}} := \dot{\mathbf{r}}_\mathrm{CM}(\hat{\mathbf{q}}_\mathrm{s}, \dot{\hat{\mathbf{q}}}_\mathrm{s})$ of the center of mass are represented as functions of $\hat{\mathbf{q}}_\mathrm{s}$ and $\dot{\hat{\mathbf{q}}}_\mathrm{s}$. In a similar manner, acceleration $\ddot{\mathbf{r}}_\mathrm{CM}\big|_{TT\hat{\mathcal{Q}}_\mathrm{s}} := \ddot{\mathbf{r}}_\mathrm{CM}(\hat{\mathbf{q}}_\mathrm{s}, \dot{\hat{\mathbf{q}}}_\mathrm{s}, \ddot{\hat{\mathbf{q}}}_\mathrm{s})$ is evaluated within the second tangent bundle $TT\hat{\mathcal{Q}}_\mathrm{s}$, complying with the holonomic constraints (3.6a) and their linearized conditions of the first and second order. This acceleration $\ddot{\mathbf{r}}_\mathrm{CM}\big|_{TT\hat{\mathcal{Q}}_\mathrm{s}}$ is utilized in deriving the constraint force $\mathbf{F}_1$, as elucidated in equation (3.9).
Accordingly, the kinematic relations enable the reconstruction of the full-order model coordinates $\mathbf{q}_\mathrm{f}$ and $\dot{\mathbf{q}}_\mathrm{f}$, as delineated in

$$\mathbf{q}_\mathrm{f}\Big|_{\hat{\mathcal{Q}}_\mathrm{s}} = \begin{bmatrix} \mathbf{r}_\mathrm{CM}(\hat{\mathbf{q}}_\mathrm{s}) \\ \hat{\mathbf{q}}_\mathrm{s} \end{bmatrix} , \qquad \dot{\mathbf{q}}_\mathrm{f}\Big|_{T\hat{\mathcal{Q}}_\mathrm{s}} = \begin{bmatrix} \dot{\mathbf{r}}_\mathrm{CM}(\hat{\mathbf{q}}_\mathrm{s}, \dot{\hat{\mathbf{q}}}_\mathrm{s}) \\ \dot{\hat{\mathbf{q}}}_\mathrm{s} \end{bmatrix} = \underbrace{\begin{bmatrix} \frac{\partial}{\partial \hat{\mathbf{q}}_\mathrm{s}} \mathbf{r}_\mathrm{CM}(\hat{\mathbf{q}}_\mathrm{s}) \\ \mathbf{I}_5 \end{bmatrix}}_{\mathbf{J}_{\hat{\mathbf{q}}_\mathrm{s}}(\hat{\mathbf{q}}_\mathrm{s})} \dot{\hat{\mathbf{q}}}_\mathrm{s} \, . \tag{3.13}$$

The evaluation of the robot's kinetic energy $\hat{K}_\mathrm{s}$ during the single support phase is performed, as delineated in

$$\begin{aligned} \hat{K}_\mathrm{s}(\hat{\mathbf{q}}_\mathrm{s}, \dot{\hat{\mathbf{q}}}_\mathrm{s}) &= \frac{1}{2} \dot{\hat{\mathbf{q}}}_\mathrm{s}^\top \underbrace{\left(\mathbf{J}_{\hat{\mathbf{q}}_\mathrm{s}}^\top \mathbf{M}_\mathrm{f}(\mathbf{q}_\mathrm{f}) \mathbf{J}_{\hat{\mathbf{q}}_\mathrm{s}} \right)\Big|_{\hat{\mathcal{Q}}_\mathrm{s}}}_{\hat{\mathbf{M}}_\mathrm{s}(\hat{\mathbf{q}}_\mathrm{s})} \dot{\hat{\mathbf{q}}}_\mathrm{s} \\ &= \frac{1}{2} \dot{\hat{\mathbf{q}}}_\mathrm{s}^\top \left(\begin{bmatrix} M_{\mathrm{f},11} & \mathbf{M}_{\mathrm{f},12} \\ \mathbf{M}_{\mathrm{f},21} & \mathbf{M}_{\mathrm{f},22} \end{bmatrix} + m_\mathrm{total} \left(\frac{\partial \mathbf{r}_\mathrm{CM}}{\partial \hat{\mathbf{q}}_\mathrm{s}} \right)^\top \frac{\partial \mathbf{r}_\mathrm{CM}}{\partial \hat{\mathbf{q}}_\mathrm{s}} \right)\Big|_{\hat{\mathcal{Q}}_\mathrm{s}} \dot{\hat{\mathbf{q}}}_\mathrm{s} \, , \end{aligned} \tag{3.14}$$

in conformity with [177, Equation (3.88)]. Subsequently, the potential energy $\hat{V}_\mathrm{s}$, which arises from gravitational influences, is calculated as exemplified in

$$\hat{V}_\mathrm{s}(\hat{\mathbf{q}}_\mathrm{s}) = m_\mathrm{total} g \, z_\mathrm{CM}\Big|_{\hat{\mathcal{Q}}_\mathrm{s}} = m_\mathrm{total} g \begin{bmatrix} 0 & 1 \end{bmatrix} \mathbf{r}_\mathrm{CM}(\hat{\mathbf{q}}_\mathrm{s}) \, , \tag{3.15}$$

thereby culminating in the formulation of the Lagrangian $\hat{L}_\mathrm{s} = \hat{K}_\mathrm{s} - \hat{V}_\mathrm{s}$.

Within the manifold $T\hat{\mathcal{Q}}_\mathrm{s}$, the derivation of the equations of motion is accomplished through the application of Lagrange's equations of the second kind, resulting in the following system of second-order, ordinary differential equations:

$$\frac{\mathrm{d}}{\mathrm{d}t}\frac{\partial \hat{L}_\mathrm{s}}{\partial \dot{\hat{\mathbf{q}}}_\mathrm{s}} - \frac{\partial \hat{L}_\mathrm{s}}{\partial \hat{\mathbf{q}}_\mathrm{s}} = \underbrace{\begin{bmatrix} \hat{M}_{\mathrm{s},11} & \hat{\mathbf{M}}_{\mathrm{s},12} \\ \hat{\mathbf{M}}_{\mathrm{s},21} & \hat{\mathbf{M}}_{\mathrm{s},22} \end{bmatrix}}_{\hat{\mathbf{M}}_\mathrm{s}(\hat{\mathbf{q}}_\mathrm{s})} \underbrace{\begin{bmatrix} \ddot{\theta}_\mathrm{HAT} \\ \ddot{\mathbf{q}}_\mathrm{b} \end{bmatrix}}_{\ddot{\hat{\mathbf{q}}}_\mathrm{s}} + \underbrace{\begin{bmatrix} \hat{\Gamma}_{\mathrm{s},1} \\ \hat{\mathbf{\Gamma}}_{\mathrm{s},2} \end{bmatrix}}_{\hat{\mathbf{\Gamma}}_\mathrm{s}(\hat{\mathbf{q}}_\mathrm{s},\dot{\hat{\mathbf{q}}}_\mathrm{s})} = \underbrace{\begin{bmatrix} \mathbf{0} \\ \mathbf{I}_4 \end{bmatrix}}_{\hat{\mathbf{B}}_\mathrm{s}} \mathbf{u}\,, \tag{3.16}$$

wherein $\hat{\mathbf{\Gamma}}_\mathrm{s}$ encompasses Coriolis and gravitational forces. The coordinate θ_HAT delineates the dynamics of underactuation in relation to the actuators $\mathbf{u}$ within the SSP model.

3.2.2 Double Support Phase

The Double Support Phase (DSP) is comprehended as a momentary transition event marked by an inelastic impact of the swing leg with the rigid ground, coupled with the interchange of the leading and trailing legs. This modeling technique is utilized to simulate the single-step period requisite for the depiction of periodic walking gaits. During this impact, the prior stance leg detaches from the ground, ceasing further interaction.

The inelastic impact [4] is approximated through the integration of the full-order system dynamics from (3.7) for an infinitesimally brief period from t^- to t^+, resulting in the formulation of the momentum equation

$$\mathbf{M}_\mathrm{f}(\mathbf{q}_\mathrm{f}^+)\dot{\mathbf{q}}_\mathrm{f}^+ - \mathbf{M}_\mathrm{f}(\mathbf{q}_\mathrm{f}^-)\dot{\mathbf{q}}_\mathrm{f}^- = \lim_{t^-\to t^+} \int_{t^-}^{t^+} \mathbf{G}_2^\top \mathbf{F}_2 \,\mathrm{d}t = \mathbf{G}_2^\top(\mathbf{q}_\mathrm{f}^-)\hat{\mathbf{F}}_2\,. \tag{3.17}$$

This equation delineates that the velocities $\dot{\mathbf{q}}_\mathrm{f}$ undergo an impulsive modification during the impact. In contrast, the positional configuration $\mathbf{q}_\mathrm{f}$ is preserved, i.e., $\mathbf{q}_\mathrm{f}^+ = \mathbf{q}_\mathrm{f}^-\big|_{\hat{\mathcal{Q}}_\mathrm{s}}$. Specifically, the system configuration $\mathbf{q}_\mathrm{f}^-$ immediately antecedent to the impact is assessed within the SSP configuration space $\hat{\mathcal{Q}}_\mathrm{s}$. Correspondingly, the position $\mathbf{r}_\mathrm{CM}^-\big|_{\hat{\mathcal{Q}}_\mathrm{s}} := \mathbf{r}_\mathrm{CM}(\hat{\mathbf{q}}_\mathrm{s}^-)$ and velocity $\dot{\mathbf{r}}_\mathrm{CM}^-\big|_{T\hat{\mathcal{Q}}_\mathrm{s}} := \dot{\mathbf{r}}_\mathrm{CM}(\hat{\mathbf{q}}_\mathrm{s}^-, \dot{\hat{\mathbf{q}}}_\mathrm{s}^-)$ of the center of mass just prior to the impact are articulated as functions of $\hat{\mathbf{q}}_\mathrm{s}^-$ and $\dot{\hat{\mathbf{q}}}_\mathrm{s}^-$ within the SSP manifold $T\hat{\mathcal{Q}}_\mathrm{s}$.

Immediately following the inelastic impact, the stance foot comes to rest without slipping, implying

$$\dot{\mathbf{r}}_2^+ := \left.\frac{\partial \mathbf{r}_2(\mathbf{q}_\mathrm{f})}{\partial \mathbf{q}_\mathrm{f}}\right|_{\mathbf{q}_\mathrm{f}=\mathbf{q}_\mathrm{f}^+} \dot{\mathbf{q}}_\mathrm{f}^+ = \mathbf{G}_2(\mathbf{q}_\mathrm{f}^+)\dot{\mathbf{q}}_\mathrm{f}^+ = \mathbf{0}\,. \tag{3.18}$$

[4] System state variables and time before impact are indicated with a "-", and after impact with a "+".

Therefore, equations (3.13), (3.17), and (3.18), in conjunction with the maintenance of the body configuration $\mathbf{q}_\mathrm{f}^+ = \mathbf{q}_\mathrm{f}^-$, are integrated into a system of linear equations that pertain to the unknown variables $\dot{\mathbf{q}}_\mathrm{f}^+$ and $\hat{\mathbf{F}}_2$ post-impact, as denoted by

$$\underbrace{\begin{bmatrix} \mathbf{M}_\mathrm{f}(\mathbf{q}_\mathrm{f}^-) & -\mathbf{G}_2^\top \\ \mathbf{G}_2 & \mathbf{0} \end{bmatrix}}_{\mathbf{\Pi}_{\mathrm{w,lhs}}(\hat{\mathbf{q}}_\mathrm{s}^-)} \begin{bmatrix} \dot{\mathbf{q}}_\mathrm{f}^+ \\ \hat{\mathbf{F}}_2 \end{bmatrix} = \underbrace{\begin{bmatrix} \mathbf{M}_\mathrm{f}(\mathbf{q}_\mathrm{f}^-) \\ \mathbf{0} \end{bmatrix} \begin{bmatrix} \frac{\partial \mathbf{r}_\mathrm{CM}}{\partial \hat{\mathbf{q}}_\mathrm{s}} \Big|_{\hat{\mathbf{q}}_\mathrm{s}=\hat{\mathbf{q}}_\mathrm{s}^-} \\ \mathbf{I}_4 \end{bmatrix}}_{\mathbf{\Pi}_{\mathrm{w,rhs}}(\hat{\mathbf{q}}_\mathrm{s}^-)} \dot{\hat{\mathbf{q}}}_\mathrm{s}^- \,. \tag{3.19}$$

Inverting [5] the matrix $\mathbf{\Pi}_{\mathrm{w,lhs}}$ results in the system states immediately after the impact. Considering also the swap of the front and trailing legs, the complete mapping in the instantaneous DSP is evaluated by

$$\hat{\mathbf{q}}_\mathrm{s}^+ = \mathbf{R}_-^+(5)\hat{\mathbf{q}}_\mathrm{s}^- \,, \qquad \dot{\hat{\mathbf{q}}}_\mathrm{s}^+ = \begin{bmatrix} \mathbf{0} & \mathbf{R}_-^+(5) & \mathbf{0} \end{bmatrix} \mathbf{\Pi}_{\mathrm{w,lhs}}^{-1} \mathbf{\Pi}_{\mathrm{w,rhs}} \dot{\hat{\mathbf{q}}}_\mathrm{s}^- \,, \tag{3.20}$$

utilizing the (5×5)-dimensional relabeling matrix $\mathbf{R}_-^+(5)$, which is characterized as

$$\mathbf{R}_-^+(5) := \begin{bmatrix} 1 & 0 & 0 & 0 & 0 \\ 0 & 0 & 1 & 0 & 0 \\ 0 & 1 & 0 & 0 & 0 \\ 0 & 0 & 0 & 0 & 1 \\ 0 & 0 & 0 & 1 & 0 \end{bmatrix} . \tag{3.21}$$

Specifically, $\mathbf{R}_-^+(5)$ is an involutory matrix, implying that $\mathbf{R}_-^+(5)\mathbf{R}_-^+(5) = \mathbf{I}_5$. Additionally, the impact forces $\hat{\mathbf{F}}_2$ are determined based on

$$\hat{\mathbf{F}}_2 := \begin{bmatrix} \hat{F}_{2,x} \\ \hat{F}_{2,z} \end{bmatrix} = \begin{bmatrix} \mathbf{0} & \mathbf{I}_2 \end{bmatrix} \mathbf{\Pi}_{\mathrm{w,lhs}}^{-1} \mathbf{\Pi}_{\mathrm{w,rhs}} \dot{\hat{\mathbf{q}}}_\mathrm{s}^- \,, \tag{3.22}$$

which are analyzed under the friction cone condition to avert slipping, as delineated in

$$\mu \hat{F}_{2,z} > \hat{F}_{2,x} > -\mu \hat{F}_{2,z} \,, \tag{3.23}$$

employing the static friction coefficient $\mu = 0.6$. Furthermore, unilateral contact is secured through a positive normal impact force, leading to

$$\hat{F}_{2,z} > 0 \,. \tag{3.24}$$

[5] According to [177, p. 56], the matrix $\mathbf{\Pi}_{\mathrm{w,lhs}}$ is invertible. LU factorization is applied in this thesis for numerically solving the system of linear equations with a dimension of nine.

3.2.3 State Space Expression

In order to facilitate the design of controllers, a coordinate transformation is executed during the continuous SSP. Thereafter, the SSP and DSP are articulated through state-space expressions, which coalesce into a hybrid dynamical system that represents the walking gait.

Coordinate Transformation

A coordinate transformation is applied to the model (3.16) to aid in the establishment of a state-dependent control framework. Unlike a time-dependent control law, a state-dependent controller is considered more robust owing to its ability to adjust to unexpected occurrences, such as perturbations, utilizing real-time measurements [126]. A prevalent method for engineering controlled gaits in a state-dependent context involves identifying an appropriate state variable of the robot and utilizing it as the independent coordinate for control design. It is imperative for the state variable to monotonically increase or decrease throughout the entire phase to ensure that the control feedback can be distinctly determined.
Empirical analyses of human locomotion suggest that the conceptual virtual leg, which can be visualized as a linear segment extending between the hip and the stance foot as depicted in Figure 3.2, demonstrates a behavior that is approximately monotonic, as documented in [175]. Specifically concerning the mechanical structure depicted in Figure 3.1c, it is posited that the lengths of the robot's thigh and shank are equal. This assumption consequently yields a linear expression for the orientation θ_{virt} of the virtual leg in relation to the configuration $\hat{\mathbf{q}}_{\text{s}}$, as represented by

$$\theta_{\text{virt}} = \theta_{\text{HAT}} + \theta_{\text{H1}} + \frac{\theta_{\text{K1}}}{2} = \begin{bmatrix} 1 & 1 & 0 & \frac{1}{2} & 0 \end{bmatrix} \hat{\mathbf{q}}_{\text{s}} \,. \tag{3.25}$$

Consequently, to enhance the formulation of the subsequent control strategy, the orientation of the virtual leg θ_{virt} is utilized as a substitute for θ_{HAT} in (3.16) to define the robot's body orientation. This approach establishes the generalized coordinates $\mathbf{q}_{\text{s}} \in \mathcal{Q}_{\text{s}}$, symbolized as

$$\mathbf{q}_{\text{s}} := \begin{bmatrix} \theta_{\text{virt}} \\ \mathbf{q}_{\text{b}} \end{bmatrix} \in \mathcal{Q}_{\text{s}} := \{ \mathbf{H}_{\text{s}} \hat{\mathbf{q}}_{\text{s}} | \, \hat{\mathbf{q}}_{\text{s}} \in \hat{\mathcal{Q}}_{\text{s}} \} \,, \tag{3.26}$$

which are ascertained through a linear and invertible transformation of the configuration space $\hat{\mathcal{Q}}_{\mathrm{s}}$ by virtue of the kinematic relation elucidated in (3.25). Herein, the transformation matrix $\mathbf{H}_{\mathrm{s}}$ and its inverse $\mathbf{H}_{\mathrm{s}}^{-1}$ are presented as

$$\mathbf{H}_{\mathrm{s}} = \begin{bmatrix} 1 & 1 & 0 & \frac{1}{2} & 0 \\ 0 & 1 & 0 & 0 & 0 \\ 0 & 0 & 1 & 0 & 0 \\ 0 & 0 & 0 & 1 & 0 \\ 0 & 0 & 0 & 0 & 1 \end{bmatrix}, \qquad \mathbf{H}_{\mathrm{s}}^{-1} = \begin{bmatrix} 1 & -1 & 0 & -\frac{1}{2} & 0 \\ 0 & 1 & 0 & 0 & 0 \\ 0 & 0 & 1 & 0 & 0 \\ 0 & 0 & 0 & 1 & 0 \\ 0 & 0 & 0 & 0 & 1 \end{bmatrix}. \tag{3.27}$$

As delineated in [177, Section B.4.10], the coordinate transformation $\mathbf{q}_{\mathrm{s}} = \mathbf{H}_{\mathrm{s}}\hat{\mathbf{q}}_{\mathrm{s}}$ is established as a local diffeomorphism, attributable to the invertible matrix $\mathbf{H}_{\mathrm{s}} = \partial \mathbf{q}_{\mathrm{s}} / \partial \hat{\mathbf{q}}_{\mathrm{s}}$. Consequently, the kinetic energy K_{s} manifests in the form elucidated in

$$K_{\mathrm{s}}(\mathbf{q}_{\mathrm{s}}, \dot{\mathbf{q}}_{\mathrm{s}}) = \frac{1}{2}\dot{\mathbf{q}}_{\mathrm{s}}^{\top}\mathbf{M}_{\mathrm{s}}(\mathbf{q}_{\mathrm{s}})\dot{\mathbf{q}}_{\mathrm{s}} = \frac{1}{2}\dot{\mathbf{q}}_{\mathrm{s}}^{\top}\left(\mathbf{H}_{\mathrm{s}}^{-\top}\hat{\mathbf{M}}_{\mathrm{s}}(\hat{\mathbf{q}}_{\mathrm{s}})\mathbf{H}_{\mathrm{s}}^{-1}\right)\Big|_{\mathcal{Q}_{\mathrm{s}}}\dot{\mathbf{q}}_{\mathrm{s}}, \tag{3.28}$$

contingent upon the transformed coordinates $\mathbf{q}_{\mathrm{s}} \in \mathcal{Q}_{\mathrm{s}}$ and velocities $\dot{\mathbf{q}}_{\mathrm{s}} = \mathbf{H}_{\mathrm{s}}\dot{\hat{\mathbf{q}}}_{\mathrm{s}}$. In subsequent analysis, the gravitational potential energy V_{s} is determined as

$$V_{\mathrm{s}}(\mathbf{q}_{\mathrm{s}}) = m_{\mathrm{total}} g \, z_{\mathrm{CM}}\Big|_{\mathcal{Q}_{\mathrm{s}}}, \tag{3.29}$$

thereby leading to the Lagrangian $L_{\mathrm{s}} = K_{\mathrm{s}} - V_{\mathrm{s}}$. Within the context of the manifold $T\hat{\mathcal{Q}}_{\mathrm{s}}$, the derivation of the equations of motion is achieved through the utilization of Lagrange's equations of the second kind, which result in a system of ordinary, second-order differential equations

$$\frac{\mathrm{d}}{\mathrm{d}t}\frac{\partial L_{\mathrm{s}}}{\partial \dot{\mathbf{q}}_{\mathrm{s}}} - \frac{\partial L_{\mathrm{s}}}{\partial \mathbf{q}_{\mathrm{s}}} = \underbrace{\begin{bmatrix} M_{\mathrm{s},11} & \mathbf{M}_{\mathrm{s},12} \\ \mathbf{M}_{\mathrm{s},21} & \mathbf{M}_{\mathrm{s},22} \end{bmatrix}}_{\mathbf{M}_{\mathrm{s}}(\mathbf{q}_{\mathrm{s}})} \underbrace{\begin{bmatrix} \ddot{\theta}_{\mathrm{virt}} \\ \ddot{\mathbf{q}}_{\mathrm{b}} \end{bmatrix}}_{\ddot{\mathbf{q}}_{\mathrm{s}}} + \underbrace{\begin{bmatrix} \Gamma_{\mathrm{s},1} \\ \mathbf{\Gamma}_{\mathrm{s},2} \end{bmatrix}}_{\mathbf{\Gamma}_{\mathrm{s}}(\mathbf{q}_{\mathrm{s}}, \dot{\mathbf{q}}_{\mathrm{s}})} = \underbrace{\begin{bmatrix} \mathbf{0} \\ \mathbf{I}_4 \end{bmatrix}}_{\mathbf{B}_{\mathrm{s}}} \mathbf{u}. \tag{3.30}$$

In this framework, $\ddot{\mathbf{q}}_{\mathrm{s}} = \mathbf{H}_{\mathrm{s}}\ddot{\hat{\mathbf{q}}}_{\mathrm{s}}$, $\mathbf{\Gamma}_{\mathrm{s}} = \mathbf{H}_{\mathrm{s}}^{-\top}\hat{\mathbf{\Gamma}}_{\mathrm{s}}$, and $\mathbf{B}_{\mathrm{s}} = \mathbf{H}_{\mathrm{s}}^{-\top}\hat{\mathbf{B}}_{\mathrm{s}} = \hat{\mathbf{B}}_{\mathrm{s}}$ establish the connections to the equations of motion as exemplified in (3.16). Furthermore, the dissection of equation (3.30) results in the formulation of the expression articulated in

$$M_{\mathrm{s},11}\ddot{\theta}_{\mathrm{virt}} + \mathbf{M}_{\mathrm{s},12}\ddot{\mathbf{q}}_{\mathrm{b}} = -\Gamma_{\mathrm{s},1}, \tag{3.31a}$$

$$\mathbf{M}_{\mathrm{s},21}\ddot{\theta}_{\mathrm{virt}} + \mathbf{M}_{\mathrm{s},22}\ddot{\mathbf{q}}_{\mathrm{b}} = -\mathbf{\Gamma}_{\mathrm{s},2} + \mathbf{u}. \tag{3.31b}$$

The absence of the actuators $\mathbf{u}$ within the expression (3.31a) renders the dynamics associated with coordinate θ_{virt} uncontrollable through actuation $\mathbf{u}$, with the notion of controllability being outlined in [160, Section 3.3]. By isolating $\ddot{\theta}_{\text{virt}}$ from equation (3.31a) and incorporating it into equation (3.31b), the inverse dynamics formulation is subsequently derived, as documented in

$$\mathbf{u} = \underbrace{\left(\mathbf{M}_{\text{s},22} - \mathbf{M}_{\text{s},21} M_{\text{s},11}^{-1} \mathbf{M}_{\text{s},12}\right)}_{\overline{\mathbf{M}}_{\text{s,rg}}} \underbrace{\ddot{\mathbf{q}}_{\text{b}}}_{\mathbf{w}} + \underbrace{\left(\mathbf{\Gamma}_{\text{s},2} - \mathbf{M}_{\text{s},21} M_{\text{s},11}^{-1} \Gamma_{\text{s},1}\right)}_{\overline{\mathbf{\Gamma}}_{\text{s,rg}}} . \tag{3.32}$$

SSP in State Space

The state space

$$\mathcal{X}_{\text{s}} = T\mathcal{Q}_{\text{s}} := \left\{ [\mathbf{q}_{\text{s}}^{\top}, \dot{\mathbf{q}}_{\text{s}}^{\top}]^{\top} \mid \mathbf{q}_{\text{s}} \in \mathcal{Q}_{\text{s}}, \dot{\mathbf{q}}_{\text{s}} \in T_{\mathbf{q}_{\text{s}}} \mathcal{Q}_{\text{s}} \subset \mathbb{R}^5 \right\} \tag{3.33}$$

of the second-order system within the SSP is constituted by the tangent bundle $T\mathcal{Q}_{\text{s}}$ of the configuration space $\mathcal{Q}_{\text{s}}$. The velocity vector $\dot{\mathbf{q}}_{\text{s}} \in T_{\mathbf{q}_{\text{s}}} \mathcal{Q}_{\text{s}}$ associated with a specific configuration $\mathbf{q}_{\text{s}}$ is determined within the tangent space $T_{\mathbf{q}_{\text{s}}} \mathcal{Q}_{\text{s}}$ at the point $\mathbf{q}_{\text{s}}$. Expressed in terms of the state variables $\mathbf{x}_{\text{s}} \in T\mathcal{Q}_{\text{s}}$, the vector field $\tilde{X}_{\text{s,r}}(\mathbf{x}_{\text{s}}, \mathbf{u}) := \tilde{\mathbf{f}}_{\text{s}}(\mathbf{x}_{\text{s}}) + \tilde{\mathbf{g}}_{\text{s}}(\mathbf{x}_{\text{s}})\mathbf{u}$, denoted as

$$\underbrace{\begin{bmatrix} \dot{\mathbf{q}}_{\text{s}} \\ \ddot{\mathbf{q}}_{\text{s}} \end{bmatrix}}_{\dot{\mathbf{x}}_{\text{s}}} = \begin{bmatrix} \dot{\mathbf{q}}_{\text{s}} \\ \mathbf{M}_{\text{s}}^{-1} \left(-\mathbf{\Gamma}_{\text{s}} + \mathbf{B}_{\text{s}} \mathbf{u}\right) \end{bmatrix} = \underbrace{\begin{bmatrix} \dot{\mathbf{q}}_{\text{s}} \\ -\mathbf{M}_{\text{s}}^{-1} \mathbf{\Gamma}_{\text{s}} \end{bmatrix}}_{\tilde{\mathbf{f}}_{\text{s}}(\mathbf{x}_{\text{s}})} + \underbrace{\begin{bmatrix} \mathbf{0} \\ \mathbf{M}_{\text{s}}^{-1} \mathbf{B}_{\text{s}} \end{bmatrix}}_{\tilde{\mathbf{g}}_{\text{s}}(\mathbf{x}_{\text{s}})} \mathbf{u} , \tag{3.34}$$

governs the dynamics of position $\mathbf{q}_{\text{s}}$ and velocity $\dot{\mathbf{q}}_{\text{s}}$ with respect to time. This formulation is precisely derived by inverting the positive definite [6] mass-inertia matrix $\mathbf{M}_{\text{s}}$ and transferring it to the right-hand side of the equations of motion (3.30).

[6] In this chapter, each rigid-body segment of the robot model possesses a positive mass and non-zero moments of inertia about their respective centers of mass. Furthermore, the SSP model as referenced in (3.30) is characterized by a minimal set of generalized coordinates, strategically excluding those that are redundant or constrained. This configuration guarantees the positive definiteness of the mass-inertia matrix.

As an alternative, considering the acceleration $\mathbf{w} := \ddot{\mathbf{q}}_\mathrm{b}$ of the actuated joints as the system input results in the vector field $X_{\mathrm{s,r}}(\mathbf{x}_\mathrm{s}, \mathbf{w}) := \mathbf{f}_\mathrm{s}(\mathbf{x}_\mathrm{s}) + \mathbf{g}_\mathrm{s}(\mathbf{x}_\mathrm{s})\mathbf{w}$, which is delineated as

$$\underbrace{\begin{bmatrix} \dot{\mathbf{q}}_\mathrm{s} \\ \ddot{\theta}_\mathrm{virt} \\ \mathbf{w} \end{bmatrix}}_{\dot{\mathbf{x}}_\mathrm{s}} = \underbrace{\begin{bmatrix} \dot{\mathbf{q}}_\mathrm{s} \\ -M_{\mathrm{s},11}^{-1}\Gamma_{\mathrm{s},1} \\ \mathbf{0} \end{bmatrix}}_{\mathbf{f}_\mathrm{s}(\mathbf{x}_\mathrm{s})} + \underbrace{\begin{bmatrix} \mathbf{0} \\ -M_{\mathrm{s},11}^{-1}\mathbf{M}_{\mathrm{s},12} \\ \mathbf{I}_4 \end{bmatrix}}_{\mathbf{g}_\mathrm{s}(\mathbf{x}_\mathrm{s})} \mathbf{w} \,, \tag{3.35}$$

with $\ddot{\theta}_\mathrm{virt}$ derived from equation (3.31a). A comparative analysis of the vector field $\tilde{X}_{\mathrm{s,r}}$, as detailed in (3.34), demonstrates that the formulation presented in (3.35) eliminates the necessity of inverting the (5×5)-dimensional mass-inertia matrix $\mathbf{M}_\mathrm{s}$. In particular, the controller initially determines the system input $\mathbf{w}$ (acceleration) in accordance with the feedback law. Subsequently, $\mathbf{w}$ is integrated into the inverse dynamics procedure outlined in (3.32) to identify the actuators $\mathbf{u}$.
Therefore, due to its high computational efficiency, the two-stage approach is implemented in the closed-loop simulations to impose virtual constraints on the actuated joints within this thesis, aimed at validating the controller design. The formulation of vector fields related to the physical actuators $\mathbf{u}$ is employed for controller development, adhering to the conventions established in the literature [177].

DSP in State Space

The transition mapping delineated in manifold $T\hat{\mathcal{Q}}_\mathrm{s}$ of Section 3.2.2 is reformulated as functions of the state variables $\mathbf{x}_\mathrm{s} \in T\mathcal{Q}_\mathrm{s}$ through the application of the coordinate transformation (3.26). To accomplish this, integrating $\hat{\mathbf{q}}_\mathrm{s} = \mathbf{H}_\mathrm{s}^{-1}\mathbf{q}_\mathrm{s}$ and $\dot{\hat{\mathbf{q}}}_\mathrm{s} = \mathbf{H}_\mathrm{s}^{-1}\dot{\mathbf{q}}_\mathrm{s}$ into the mapping (3.20) results in

$$\mathbf{q}_\mathrm{s}^+ = \boldsymbol{\Delta}_{\mathrm{w},\mathbf{q}_\mathrm{s}}\mathbf{q}_\mathrm{s}^- := \mathbf{H}_\mathrm{s}\mathbf{R}_-^+(5)\mathbf{H}_\mathrm{s}^{-1}\mathbf{q}_\mathrm{s}^- \,, \tag{3.36a}$$

$$\dot{\mathbf{q}}_\mathrm{s}^+ = \boldsymbol{\Delta}_{\mathrm{w},\dot{\mathbf{q}}_\mathrm{s}}(\mathbf{q}_\mathrm{s}^-)\,\dot{\mathbf{q}}_\mathrm{s}^- := \mathbf{H}_\mathrm{s}\begin{bmatrix}\mathbf{0} & \mathbf{R}_-^+(5) & \mathbf{0}\end{bmatrix}\left(\boldsymbol{\Pi}_{\mathrm{w,lhs}}^{-1}\boldsymbol{\Pi}_{\mathrm{w,rhs}}\right)\Big|_{\hat{\mathbf{q}}_\mathrm{s}^- = \mathbf{H}_\mathrm{s}^{-1}\mathbf{q}_\mathrm{s}^-} \mathbf{H}_\mathrm{s}^{-1}\dot{\mathbf{q}}_\mathrm{s}^- \,. \tag{3.36b}$$

With the system states $\mathbf{x}_\mathrm{s}^- := [(\mathbf{q}_\mathrm{s}^-)^\top, (\dot{\mathbf{q}}_\mathrm{s}^-)^\top]^\top$ before and $\mathbf{x}_\mathrm{s}^+ := [(\mathbf{q}_\mathrm{s}^+)^\top, (\dot{\mathbf{q}}_\mathrm{s}^+)^\top]^\top$ after impact, the mappings (3.36) are presented in state space as

$$\mathbf{x}_\mathrm{s}^+ = \boldsymbol{\Delta}_{\mathrm{w,i}}(\mathbf{x}_\mathrm{s}^-) := \begin{bmatrix}\boldsymbol{\Delta}_{\mathrm{w},\mathbf{q}_\mathrm{s}} & \boldsymbol{\Delta}_{\mathrm{w},\dot{\mathbf{q}}_\mathrm{s}}(\mathbf{q}_\mathrm{s}^-)\end{bmatrix}\begin{bmatrix}\mathbf{q}_\mathrm{s}^- \\ \dot{\mathbf{q}}_\mathrm{s}^-\end{bmatrix} \,, \tag{3.37}$$

with the subscript "w, i" referring **w**alking with **i**nstantaneous DSP on rigid ground.

Hybrid Dynamics in State Space

The hybrid dynamical system for walking on rigid ground is formulated by combining the continuous dynamics in (3.34) and the discrete mapping in (3.37), yielding

$$\Sigma_{\mathrm{w,i}} : \begin{cases} \dot{\mathbf{x}}_{\mathrm{s}} = \tilde{\mathbf{f}}_{\mathrm{s}}(\mathbf{x}_{\mathrm{s}}) + \tilde{\mathbf{g}}_{\mathrm{s}}(\mathbf{x}_{\mathrm{s}})\mathbf{u} \,, & \mathbf{x}_{\mathrm{s}} \notin \mathcal{S}_{\mathrm{s}} \,, \\ \mathbf{x}_{\mathrm{s}}^{+} = \boldsymbol{\Delta}_{\mathrm{w,i}}(\mathbf{x}_{\mathrm{s}}^{-}) \,, & \mathbf{x}_{\mathrm{s}}^{-} \in \mathcal{S}_{\mathrm{s}} \,, \\ \mathcal{S}_{\mathrm{s}} := \{\mathbf{x}_{\mathrm{s}} \in TQ_{\mathrm{s}} |\, g_{-}^{+}(\mathbf{x}_{\mathrm{s}}) = 0, r_{2,x}(\mathbf{x}_{\mathrm{s}}) > 0\} \,. \end{cases} \tag{3.38}$$

Within this framework, the switching surface $\mathcal{S}_{\mathrm{s}}$ is identified precisely at the moment when the swing foot makes contact with the ground, as determined by the guard function $g_{-}^{+}(\mathbf{x}_{\mathrm{s}}) := r_{2,z}(\mathbf{x}_{\mathrm{s}})$ with $g_{-}^{+} : TQ_{\mathrm{s}} \to \mathbb{R}$. This contact specifically occurs ahead of the stance foot $\mathbf{r}_1 = \mathbf{0}$ due to the constraint (3.6a). Consequently, the condition is articulated as $r_{2,x}(\mathbf{x}_{\mathrm{s}}) > 0$.
At this juncture, the conclusion of a complete step cycle is established, and the subsequent step ensues with the rearrangement of the anterior and posterior leg configurations, taking into account the gait's periodic nature. Accordingly, the configuration $\mathbf{x}_{\mathrm{s}}^{-}$ is utilized to compute the step length ℓ_{step}, which is expressed as

$$\ell_{\mathrm{step}} = \|\mathbf{r}_2(\mathbf{x}_{\mathrm{s}}^{-}) - \mathbf{r}_1(\mathbf{x}_{\mathrm{s}}^{-})\|_2 = \|\mathbf{r}_2(\mathbf{x}_{\mathrm{s}}^{-}) - \mathbf{0}\|_2 \,. \tag{3.39}$$

3.3 Walking with Non-Instantaneous DSP

As depicted in Figure 3.3, the walking pattern characterized by a non-instantaneous DSP is delineated by alternating sequences of the continuous single support phase, as elucidated in Section 3.2.2, and the continuous DSP, as illustrated in Section 3.3.1. These sequences are interspersed with distinct transitions, specifically termed touch-down in Section 3.3.2 and lift-off in Section 3.3.3. These continuous dynamics and the discontinuities are represented within the state space, culminating in a hybrid dynamical model, as expounded in Section 3.3.4.

3.3.1 Double Support Phase

The Double Support Phase (DSP) is characterized by the condition in which both stance feet remain in contact with the ground without any slippage, thus ensuring a constant and nonzero step length $\ell_{\mathrm{step}} > 0$. Assuming the point foot is modeled as an ideal pivot joint, this arrangement causes the two stance legs to establish a closed kinematic chain. Consequently, the robotic model during the DSP exhibits three degrees of freedom. In association with the full-order robot model, which comprises seven degrees of freedom, there are four holonomic scleronomic constraints $\hat{\mathbf{h}}_{\mathrm{d}} : Q_{\mathrm{f}} \to \mathbb{R}^4;\ \mathbf{q}_{\mathrm{f}} \mapsto \hat{\mathbf{h}}_{\mathrm{d}}(\mathbf{q}_{\mathrm{f}})$ that are

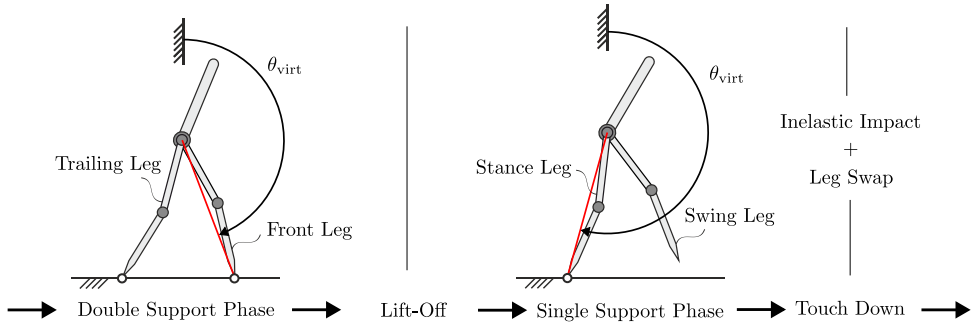

Figure 3.3: Periodic walking gait with a non-instantaneous double support phase. The red line indicates the virtual leg defined in the single and double support phases.

defined in relation to the stance foot positions $\mathbf{r}_1$ and $\mathbf{r}_2$, as illustrated in Figure 3.1a. These constraints, along with their respective time derivatives, are articulated as

$$\hat{\mathbf{h}}_{\text{d}}(\mathbf{q}_{\text{f}}) := \begin{bmatrix} \mathbf{r}_1(\mathbf{q}_{\text{f}}) \\ \mathbf{r}_2(\mathbf{q}_{\text{f}}) \end{bmatrix} = \mathbf{0}\,, \tag{3.40a}$$

$$\dot{\hat{\mathbf{h}}}_{\text{d}}(\mathbf{q}_{\text{f}}, \dot{\mathbf{q}}_{\text{f}}) := \begin{bmatrix} \partial \mathbf{r}_1(\mathbf{q}_{\text{f}})/\partial \mathbf{q}_{\text{f}} \\ \partial \mathbf{r}_2(\mathbf{q}_{\text{f}})/\partial \mathbf{q}_{\text{f}} \end{bmatrix} \dot{\mathbf{q}}_{\text{f}} = \begin{bmatrix} \mathbf{G}_1 \\ \mathbf{G}_2 \end{bmatrix} \dot{\mathbf{q}}_{\text{f}} = \mathbf{0}\,, \tag{3.40b}$$

$$\ddot{\hat{\mathbf{h}}}_{\text{d}}(\mathbf{q}_{\text{f}}, \dot{\mathbf{q}}_{\text{f}}, \ddot{\mathbf{q}}_{\text{f}}) := \underbrace{\begin{bmatrix} \mathbf{G}_1 \\ \mathbf{G}_2 \end{bmatrix}}_{\mathbf{G}_{\text{d}}} \ddot{\mathbf{q}}_{\text{f}} + \underbrace{\begin{bmatrix} \dot{\mathbf{G}}_1 \\ \dot{\mathbf{G}}_2 \end{bmatrix}}_{\dot{\mathbf{G}}_{\text{d}}} \dot{\mathbf{q}}_{\text{f}} = \mathbf{0}\,. \tag{3.40c}$$

The full-rank Jacobian matrix $\mathbf{G}_{\text{d}}$ is derived from the four normal vectors associated with the linearly independent constraint surfaces defined in $\hat{\mathbf{h}}_{\text{d}}(\mathbf{q}_{\text{f}}) = \mathbf{0}$. It is particularly crucial that the step length $\ell_{\text{step}} = \|\mathbf{r}_2(\mathbf{q}_{\text{f}}) - \mathbf{r}_1(\mathbf{q}_{\text{f}})\|_2 > 0$ remains nonzero; otherwise, the constraint surfaces $\mathbf{r}_1(\mathbf{q}_{\text{f}})$ and $\mathbf{r}_2(\mathbf{q}_{\text{f}})$ would become identical, leading to the Jacobian $\mathbf{G}_{\text{d}}$ losing its full rank.

Incorporating the acceleration constraints $\ddot{\hat{\mathbf{h}}}_{\text{d}}$ from (3.40c), which are presupposed to be strictly satisfied, into the equations of motion (3.5) for the full-order system yields a DAE system characterized by a differentiation index of one, as expressed in

$$\begin{bmatrix} \mathbf{M}_{\text{f}} & -\mathbf{G}_1^{\top} & -\mathbf{G}_2^{\top} \\ -\mathbf{G}_1 & \mathbf{0} & \mathbf{0} \\ -\mathbf{G}_2 & \mathbf{0} & \mathbf{0} \end{bmatrix} \begin{bmatrix} \ddot{\mathbf{q}}_{\text{f}} \\ \mathbf{F}_1 \\ \mathbf{F}_2 \end{bmatrix} = \begin{bmatrix} -\boldsymbol{\Gamma}_{\text{f}} + \mathbf{B}_{\text{f}}\mathbf{u} \\ \dot{\mathbf{G}}_1 \dot{\mathbf{q}}_{\text{f}} \\ \dot{\mathbf{G}}_2 \dot{\mathbf{q}}_{\text{f}} \end{bmatrix}\,, \tag{3.41}$$

with initial conditions articulated in $[\dot{\mathbf{q}}_\mathrm{f}(t_0)^\top, \mathbf{q}_\mathrm{f}(t_0)^\top, \mathbf{F}_1(t_0)^\top, \mathbf{F}_2(t_0)^\top]^\top$. The magnitudes of the constraint forces $\mathbf{F}_1$ and $\mathbf{F}_2$ (Lagrange multipliers) are determined by eliminating $\ddot{\mathbf{q}}_\mathrm{f}$ from the equation system (3.41), which is stated as

$$\begin{bmatrix}\mathbf{F}_1\\ \mathbf{F}_2\end{bmatrix} = \begin{bmatrix}F_{1,x}\\ F_{1,z}\\ F_{2,x}\\ F_{2,z}\end{bmatrix} = \left(\mathbf{G}_\mathrm{d}\mathbf{M}_\mathrm{f}^{-1}\mathbf{G}_\mathrm{d}^\top\right)^{-1}\left(\mathbf{G}_\mathrm{d}\mathbf{M}_\mathrm{f}^{-1}\boldsymbol{\Gamma}_\mathrm{f} - \mathbf{G}_\mathrm{d}\mathbf{M}_\mathrm{f}^{-1}\mathbf{B}_\mathrm{f}\mathbf{u} - \dot{\mathbf{G}}_\mathrm{d}\dot{\mathbf{q}}_\mathrm{f}\right) . \tag{3.42}$$

The non-slipping contact condition as established in the holonomic constraints (3.40) is fulfilled by static friction. Consequently, Coulomb's frictional law is employed to derive the inequality constraints

$$\mu F_{1,z} > F_{1,x} > -\mu F_{1,z} , \qquad \mu F_{2,z} > F_{2,x} > -\mu F_{2,z} , \tag{3.43}$$

involving the static friction coefficient $\mu = 0.6$. Concurrently, unilateral contact necessitates positive normal forces $F_{1,z}$ and $F_{2,z}$, which are written as

$$F_{1,z} > 0 , \qquad F_{2,z} > 0 . \tag{3.44}$$

Formulation with Minimal Coordinates

To circumvent the direct resolution of the DAE system delineated in (3.41), the dynamics of three degrees of freedom are articulated through a minimal set of generalized coordinates $\hat{\mathbf{q}}_\mathrm{d} \in \hat{\mathcal{Q}}_\mathrm{d}$, as defined in

$$\hat{\mathbf{q}}_\mathrm{d} := \begin{bmatrix}\theta_\mathrm{HAT}\\ \mathbf{q}_\mathrm{di}\end{bmatrix} = \begin{bmatrix}\theta_\mathrm{HAT}\\ \theta_\mathrm{H1}\\ \theta_\mathrm{K1}\end{bmatrix} \in \hat{\mathcal{Q}}_\mathrm{d} := \{\mathbf{q}_\mathrm{f} \in \mathcal{Q}_\mathrm{f} \,|\, \hat{\mathbf{h}}_\mathrm{d}(\mathbf{q}_\mathrm{f}) = \mathbf{0}, \|\mathbf{r}_2(\mathbf{q}_\mathrm{f}) - \mathbf{r}_1(\mathbf{q}_\mathrm{f})\|_2 > 0\} , \tag{3.45}$$

and illustrated in Figure 3.4.
Herein, $\hat{\mathcal{Q}}_\mathrm{d}$ represents a three-dimensional configuration space embedded within $\mathcal{Q}_\mathrm{f}$. Notably, the independent coordinates $\mathbf{q}_\mathrm{di} := [\theta_\mathrm{H1}, \theta_\mathrm{K1}]^\top$ signify the joint angles of the hip θ_H1 and knee θ_K1 in the leading leg, adhering to the notation as delineated in Section 3.1.1. The corresponding velocity vector $\dot{\hat{\mathbf{q}}}_\mathrm{d} \in T_{\hat{\mathbf{q}}_\mathrm{d}}\hat{\mathcal{Q}}_\mathrm{d} \subset \mathbb{R}^3$ is articulated within the tangent space $T_{\hat{\mathbf{q}}_\mathrm{d}}\hat{\mathcal{Q}}_\mathrm{d}$ of $\hat{\mathcal{Q}}_\mathrm{d}$. These elements collectively constitute the tangent bundle $T\hat{\mathcal{Q}}_\mathrm{d}$ associated with the DSP, which is characterized as a smooth manifold possessing a dimensionality of six.

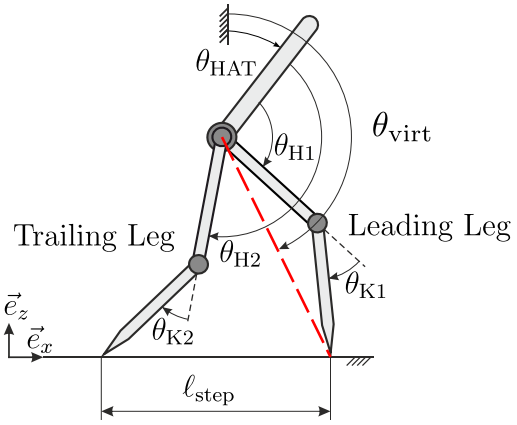

Figure 3.4: Specification of coordinates during the non-instantaneous double support phase. The red line signifies the virtual leg with orientation θ_{virt}.

According to the holonomic kinematic relationship, the angular position and velocity

$$\mathbf{q}_{\text{dd}} := \begin{bmatrix} \theta_{\text{H2}} \\ \theta_{\text{K2}} \end{bmatrix} = \hat{\mathbf{\Omega}}(\hat{\mathbf{q}}_{\text{d}}) \,, \qquad \dot{\mathbf{q}}_{\text{dd}} = \frac{\partial \hat{\mathbf{\Omega}}(\hat{\mathbf{q}}_{\text{d}})}{\partial \hat{\mathbf{q}}_{\text{d}}} \dot{\hat{\mathbf{q}}}_{\text{d}} = \mathbf{J}_{\hat{\Omega}}(\hat{\mathbf{q}}_{\text{d}}) \dot{\hat{\mathbf{q}}}_{\text{d}} \,, \tag{3.46}$$

of the joints in the trailing leg are expressed as functions dependent on $\hat{\mathbf{q}}_{\text{d}}$, enabled by an explicit mapping $\hat{\mathbf{\Omega}} : \hat{\mathcal{Q}}_{\text{d}} \to \mathbb{T}^2$, as derived in Appendix A. The robot's kinetic energy K_{d} is assessed during the DSP, as outlined in

$$K_{\text{d}}(\hat{\mathbf{q}}_{\text{d}}, \dot{\hat{\mathbf{q}}}_{\text{d}}) = \frac{1}{2} \dot{\hat{\mathbf{q}}}_{\text{d}}^{\top} \hat{\mathbf{M}}_{\text{d}}(\hat{\mathbf{q}}_{\text{d}}) \dot{\hat{\mathbf{q}}}_{\text{d}} = \frac{1}{2} \dot{\hat{\mathbf{q}}}_{\text{d}}^{\top} \left(\left(\frac{\partial \mathbf{q}_{\text{f}}}{\partial \hat{\mathbf{q}}_{\text{d}}} \right)^{\top} \mathbf{M}_{\text{f}}(\mathbf{q}_{\text{f}}) \frac{\partial \mathbf{q}_{\text{f}}}{\partial \hat{\mathbf{q}}_{\text{d}}} \right) \Bigg|_{\hat{\mathcal{Q}}_{\text{d}}} \dot{\hat{\mathbf{q}}}_{\text{d}} \,. \tag{3.47}$$

The potential energy V_{d}, derived from gravitational effects, is computed as illustrated in

$$V_{\text{d}}(\hat{\mathbf{q}}_{\text{d}}) = m_{\text{total}} g \, z_{\text{CM}} \Big|_{\hat{\mathcal{Q}}_{\text{d}}} \,, \tag{3.48}$$

ultimately leading to the derivation of the Lagrangian $L_{\text{d}} = K_{\text{d}} - V_{\text{d}}$. Utilizing Lagrange's equations of the second kind facilitates the derivation of the equations of motion, which are expressed as the following system of ordinary, second-order differential equations

$$\frac{\mathrm{d}}{\mathrm{d}t} \frac{\partial L_{\text{d}}}{\partial \dot{\hat{\mathbf{q}}}_{\text{d}}} - \frac{\partial L_{\text{d}}}{\partial \hat{\mathbf{q}}_{\text{d}}} = \underbrace{\begin{bmatrix} \hat{M}_{\text{d},11} & \hat{\mathbf{M}}_{\text{d},12} \\ \hat{\mathbf{M}}_{\text{d},21} & \hat{\mathbf{M}}_{\text{d},22} \end{bmatrix}}_{\hat{\mathbf{M}}_{\text{d}}(\hat{\mathbf{q}}_{\text{d}})} \underbrace{\begin{bmatrix} \ddot{\theta}_{\text{HAT}} \\ \ddot{\mathbf{q}}_{\text{di}} \end{bmatrix}}_{\ddot{\hat{\mathbf{q}}}_{\text{d}}} + \underbrace{\begin{bmatrix} \hat{\Gamma}_{\text{d},1} \\ \hat{\mathbf{\Gamma}}_{\text{d},2} \end{bmatrix}}_{\hat{\mathbf{\Gamma}}_{\text{d}}(\hat{\mathbf{q}}_{\text{d}}, \dot{\hat{\mathbf{q}}}_{\text{d}})} = \underbrace{\begin{bmatrix} \mathbf{0} \\ \mathbf{I}_2 \end{bmatrix}}_{} \underbrace{\begin{bmatrix} u_{\text{H1}} \\ u_{\text{K1}} \end{bmatrix}}_{\mathbf{u}_{\text{i}}} + \mathbf{J}_{\hat{\Omega}}^{\top} \underbrace{\begin{bmatrix} u_{\text{H2}} \\ u_{\text{K2}} \end{bmatrix}}_{\mathbf{u}_{\text{d}}} \,, \tag{3.49}$$

with $\hat{\mathbf{\Gamma}}_\mathrm{d}$ including Coriolis and gravitational forces. Given that the number of independent actuations, which is four, exceeds the system's degrees of freedom, which is three, the DSP system is characterized as overactuated.

3.3.2 Touch-Down

The touch-down event is modeled as an inelastic collision at both stance feet with the rigid ground. Notably, variables prior to the impact are denoted by the symbol "-", while those following the impact are represented by "+". The integration of the complete system dynamics as outlined in (3.41), conducted over a negligibly brief time interval extending from t^- to t^+, results in the momentum equation

$$\mathbf{M}_\mathrm{f}(\mathbf{q}_\mathrm{f}^+)\dot{\mathbf{q}}_\mathrm{f}^+ - \mathbf{M}_\mathrm{f}(\mathbf{q}_\mathrm{f}^-)\dot{\mathbf{q}}_\mathrm{f}^- = \lim_{t^- \to t^+} \int_{t^-}^{t^+} \left(\mathbf{G}_1^\top \mathbf{F}_1 + \mathbf{G}_2^\top \mathbf{F}_2\right) \mathrm{d}t = \mathbf{G}_1^\top(\mathbf{q}_\mathrm{f}^-)\hat{\mathbf{F}}_1 + \mathbf{G}_2^\top(\mathbf{q}_\mathrm{f}^-)\hat{\mathbf{F}}_2 \,, \tag{3.50}$$

wherein the configuration $\mathbf{q}_\mathrm{f}^+\big|_{\hat{\mathcal{Q}}_\mathrm{d}} = \mathbf{q}_\mathrm{f}^-\big|_{\hat{\mathcal{Q}}_\mathrm{s}}$ remains unchanged due to the impact. Following the inelastic collision, the stance feet instantaneously halt their motion without any slippage, strictly complying with the holonomic constraints (3.40), as articulated in

$$\dot{\mathbf{r}}_1^+ := \left.\frac{\partial \mathbf{r}_1(\mathbf{q}_\mathrm{f})}{\partial \mathbf{q}_\mathrm{f}}\right|_{\mathbf{q}_\mathrm{f}=\mathbf{q}_\mathrm{f}^+} \dot{\mathbf{q}}_\mathrm{f}^+ = \mathbf{G}_1(\mathbf{q}_\mathrm{f}^+)\dot{\mathbf{q}}_\mathrm{f}^+ = \mathbf{0} \,, \tag{3.51a}$$

$$\dot{\mathbf{r}}_2^+ := \left.\frac{\partial \mathbf{r}_2(\mathbf{q}_\mathrm{f})}{\partial \mathbf{q}_\mathrm{f}}\right|_{\mathbf{q}_\mathrm{f}=\mathbf{q}_\mathrm{f}^+} \dot{\mathbf{q}}_\mathrm{f}^+ = \mathbf{G}_2(\mathbf{q}_\mathrm{f}^+)\dot{\mathbf{q}}_\mathrm{f}^+ = \mathbf{0} \,. \tag{3.51b}$$

As a result, equations (3.50) and (3.51) are formulated into a system of linear equations involving the unknown variables $\dot{\mathbf{q}}_\mathrm{f}^+$, $\hat{\mathbf{F}}_1$, and $\hat{\mathbf{F}}_2$ following the impact, which is denoted as

$$\underbrace{\begin{bmatrix} \mathbf{M}_\mathrm{f}(\mathbf{q}_\mathrm{f}^-) & -\mathbf{G}_1^\top & -\mathbf{G}_2^\top \\ \mathbf{G}_1 & \mathbf{0} & \mathbf{0} \\ \mathbf{G}_2 & \mathbf{0} & \mathbf{0} \end{bmatrix}}_{\mathbf{\Pi}_{\mathrm{w,n,lhs}}(\hat{\mathbf{q}}_\mathrm{s}^-)} \begin{bmatrix} \dot{\mathbf{q}}_\mathrm{f}^+ \\ \hat{\mathbf{F}}_1 \\ \hat{\mathbf{F}}_2 \end{bmatrix} = \underbrace{\begin{bmatrix} \mathbf{M}_\mathrm{f}(\mathbf{q}_\mathrm{f}^-) \\ \mathbf{0} \\ \mathbf{0} \end{bmatrix} \begin{bmatrix} \left.\frac{\partial \mathbf{r}_\mathrm{CM}}{\partial \hat{\mathbf{q}}_\mathrm{s}}\right|_{\hat{\mathbf{q}}_\mathrm{s}=\hat{\mathbf{q}}_\mathrm{s}^-} \\ \mathbf{I}_4 \end{bmatrix}}_{\mathbf{\Pi}_{\mathrm{w,n,rhs}}(\hat{\mathbf{q}}_\mathrm{s}^-)} \dot{\hat{\mathbf{q}}}_\mathrm{s}^- \,. \tag{3.52}$$

The numerical solution of the system of equations (3.52) is accomplished via the LU factorization of the (11×11)-dimensional matrix $\mathbf{\Pi}_{\mathrm{w,n,lhs}}(\hat{\mathbf{q}}_\mathrm{s}^-)$, wherein the position $\hat{\mathbf{q}}_\mathrm{s}^- \in \hat{\mathcal{Q}}_\mathrm{s}$ is delineated in the SSP immediately preceding the impact.
The simulation of the periodic walking gait, incorporating a non-instantaneous DSP, recognizes the single-step period, wherein the leading and trailing legs are exchanged

at the touch-down event. This exchange is facilitated through the multiplication of the system state variables by the (3×5)-dimensional relabeling matrix $\mathbf{R}_{\mathrm{s}}^{\mathrm{d}}$ as defined in

$$\mathbf{R}_{\mathrm{s}}^{\mathrm{d}} := \begin{bmatrix} 1 & 0 & 0 & 0 & 0 \\ 0 & 0 & 1 & 0 & 0 \\ 0 & 0 & 0 & 0 & 1 \end{bmatrix} . \tag{3.53}$$

As a result, the dimensionality of the independent coordinates decreases from five during the SSP to three in the DSP. Importantly, both the post-impact position $\hat{\mathbf{q}}_{\mathrm{d}}^{+}$ and velocity $\dot{\hat{\mathbf{q}}}_{\mathrm{d}}^{+}$ are expressed within the manifold $T\hat{Q}_{\mathrm{d}}$, as elaborated in

$$\hat{\mathbf{q}}_{\mathrm{d}}^{+} = \mathbf{R}_{\mathrm{s}}^{\mathrm{d}} \hat{\mathbf{q}}_{\mathrm{s}}^{-} , \qquad \dot{\hat{\mathbf{q}}}_{\mathrm{d}}^{+} = \begin{bmatrix} \mathbf{0} & \mathbf{R}_{\mathrm{s}}^{\mathrm{d}} & \mathbf{0} \end{bmatrix} \mathbf{\Pi}_{\mathrm{w,n,lhs}}^{-1} \mathbf{\Pi}_{\mathrm{w,n,rhs}} \dot{\hat{\mathbf{q}}}_{\mathrm{s}}^{-} . \tag{3.54}$$

Additionally, the computations related to the impact forces are detailed in

$$\begin{bmatrix} \hat{\mathbf{F}}_1 \\ \hat{\mathbf{F}}_2 \end{bmatrix} := \begin{bmatrix} \hat{F}_{1,x} \\ \hat{F}_{1,z} \\ \hat{F}_{2,x} \\ \hat{F}_{2,z} \end{bmatrix} = \begin{bmatrix} \mathbf{0} & \mathbf{I}_4 \end{bmatrix} \mathbf{\Pi}_{\mathrm{w,n,lhs}}^{-1} \mathbf{\Pi}_{\mathrm{w,n,rhs}} \dot{\hat{\mathbf{q}}}_{\mathrm{s}}^{-} , \tag{3.55}$$

being examined under the friction cone condition to prevent slipping, as described in

$$\mu \hat{F}_{1,z} > \hat{F}_{1,x} > -\mu \hat{F}_{1,z} , \qquad \mu \hat{F}_{2,z} > \hat{F}_{2,x} > -\mu \hat{F}_{2,z} , \tag{3.56}$$

utilizing the static friction coefficient $\mu = 0.6$. Moreover, unilateral contact is maintained through a positive normal force, resulting in

$$\hat{F}_{1,z} > 0 , \qquad \hat{F}_{2,z} > 0 . \tag{3.57}$$

3.3.3 Lift-Off

The transition of the system state variables from the DSP to the SSP is formulated in the discrete lift-off event. In particular, according to [133, Section 6], lifting off one of the stance feet is measured by the violation of the acceleration constraint $\ddot{\hat{\mathbf{h}}}_{\mathrm{d}}(\mathbf{q}_{\mathrm{f}}, \dot{\mathbf{q}}_{\mathrm{f}}, \ddot{\mathbf{q}}_{\mathrm{f}}) \neq \mathbf{0}$, which is, according to the definition in (3.40c), a function of the acceleration $\ddot{\mathbf{q}}_{\mathrm{f}}$ and thus also a function of the torque provided by the drivetrain. In other words, it is physically feasible to assume that the position and velocity undergo a continuous transition throughout the lift-off mapping.
In accordance with the notation convention outlined in Section 3.3.2, variables preceding the transition are represented by the symbol "-", whereas those succeeding the transition

are denoted by "+". The position $\hat{\mathbf{q}}_{\mathrm{s}}^{+}$ and velocity $\dot{\hat{\mathbf{q}}}_{\mathrm{s}}^{+}$ within the manifold $T\hat{\mathcal{Q}}_{\mathrm{s}}$ of the SSP are ascertained by the mapping

$$\hat{\mathbf{q}}_{\mathrm{s}}^{+} = \mathbf{R}_{\mathrm{d}}^{\mathrm{s}} \begin{bmatrix} \hat{\mathbf{q}}_{\mathrm{d}}^{-} \\ \mathbf{q}_{\mathrm{dd}} \end{bmatrix} \Bigg|_{\hat{\mathcal{Q}}_{\mathrm{d}}} = \mathbf{R}_{\mathrm{d}}^{\mathrm{s}} \begin{bmatrix} \hat{\mathbf{q}}_{\mathrm{d}}^{-} \\ \hat{\mathbf{\Omega}}(\hat{\mathbf{q}}_{\mathrm{d}}^{-}) \end{bmatrix}, \quad \dot{\hat{\mathbf{q}}}_{\mathrm{s}}^{+} = \mathbf{R}_{\mathrm{d}}^{\mathrm{s}} \begin{bmatrix} \dot{\hat{\mathbf{q}}}_{\mathrm{d}}^{-} \\ \dot{\mathbf{q}}_{\mathrm{dd}} \end{bmatrix} \Bigg|_{T\hat{\mathcal{Q}}_{\mathrm{d}}} = \mathbf{R}_{\mathrm{d}}^{\mathrm{s}} \begin{bmatrix} \mathbf{I}_3 \\ \mathbf{J}_{\hat{\Omega}}(\hat{\mathbf{q}}_{\mathrm{d}}^{-}) \end{bmatrix} \dot{\hat{\mathbf{q}}}_{\mathrm{d}}^{-}, \tag{3.58}$$

and the relabeling matrix

$$\mathbf{R}_{\mathrm{d}}^{\mathrm{s}} := \begin{bmatrix} 1 & 0 & 0 & 0 & 0 \\ 0 & 1 & 0 & 0 & 0 \\ 0 & 0 & 0 & 1 & 0 \\ 0 & 0 & 1 & 0 & 0 \\ 0 & 0 & 0 & 0 & 1 \end{bmatrix}. \tag{3.59}$$

3.3.4 State Space Expression

In alignment with the state space representation (3.33) of the SSP, a coordinate transformation is established in the non-instantaneous DSP. Essentially, the orientation θ_{virt} of the virtual leg is incorporated as an independent coordinate within the DSP domain, as illustrated in Figure 3.3. Subsequently, the continuous dynamics are integrated with the discrete transition events to constitute a hybrid dynamical model formulated in state space.

Coordinate Transformation

Assuming the virtual leg is located in the anterior leg during the continuous DSP, as illustrated in Figure 3.4, the orientation θ_{virt} of the virtual leg is determined utilizing the equation (3.25). Specifically, the orientation θ_{virt} functions as an independent coordinate that defines the robot's absolute orientation, attributable to its monotonic increase in the DSP. The coordinate transformation is articulated as a linear mapping, as exemplified in

$$\mathbf{q}_{\mathrm{d}} := \begin{bmatrix} \theta_{\mathrm{virt}} \\ \mathbf{q}_{\mathrm{di}} \end{bmatrix} \in \mathcal{Q}_{\mathrm{d}} := \{ \mathbf{H}_{\mathrm{d}} \hat{\mathbf{q}}_{\mathrm{d}} \,|\, \hat{\mathbf{q}}_{\mathrm{d}} \in \hat{\mathcal{Q}}_{\mathrm{d}} \}, \tag{3.60}$$

with

$$\mathbf{H}_{\mathrm{d}} = \begin{bmatrix} 1 & 1 & \frac{1}{2} \\ 0 & 1 & 0 \\ 0 & 0 & 1 \end{bmatrix}, \qquad \mathbf{H}_{\mathrm{d}}^{-1} = \begin{bmatrix} 1 & -1 & -\frac{1}{2} \\ 0 & 1 & 0 \\ 0 & 0 & 1 \end{bmatrix}. \tag{3.61}$$

The coordinate transformation $\mathbf{q}_\mathrm{d} = \mathbf{H}_\mathrm{d}\hat{\mathbf{q}}_\mathrm{d}$ essentially constitutes a local diffeomorphism, attributed to the invertibility of the transformation matrix $\mathbf{H}_\mathrm{d} = \partial\mathbf{q}_\mathrm{d}/\partial\hat{\mathbf{q}}_\mathrm{d}$. Consequently, the integration of the coordinate transformation (3.60) into the equations of motion (3.49) culminates in the formulation depicted in

$$\mathbf{M}_\mathrm{d}(\mathbf{q}_\mathrm{d})\ddot{\mathbf{q}}_\mathrm{d} + \boldsymbol{\Gamma}_\mathrm{d}(\mathbf{q}_\mathrm{d}, \dot{\mathbf{q}}_\mathrm{d}) = \begin{bmatrix}\mathbf{0}\\ \mathbf{I}_2\end{bmatrix}\begin{bmatrix}u_{\mathrm{H1}}\\ u_{\mathrm{K1}}\end{bmatrix} + \mathbf{J}_{\boldsymbol{\Omega}}^\top\begin{bmatrix}u_{\mathrm{H2}}\\ u_{\mathrm{K2}}\end{bmatrix} = \mathbf{B}_\mathrm{d}\mathbf{u}\,, \tag{3.62}$$

synthesizing components $\mathbf{M}_\mathrm{d} = \mathbf{H}_\mathrm{d}^{-\top}\hat{\mathbf{M}}_\mathrm{d}\mathbf{H}_\mathrm{d}^{-1}$ and $\boldsymbol{\Gamma}_\mathrm{d} = \mathbf{H}_\mathrm{d}^{-\top}\hat{\boldsymbol{\Gamma}}_\mathrm{d}$. Additionally, the mapping $\mathbf{q}_{\mathrm{dd}} = \boldsymbol{\Omega}(\mathbf{q}_\mathrm{d}) = \hat{\boldsymbol{\Omega}}\left(\mathbf{H}_\mathrm{d}^{-1}\mathbf{q}_\mathrm{d}\right)$ with $\boldsymbol{\Omega} : \mathcal{Q}_\mathrm{d} \to \mathbb{T}^2$, considering $\mathbf{q}_\mathrm{d}$ as independent coordinates, is derived from the equation (3.46). Consequently, the Jacobian is articulated as $\mathbf{J}_{\boldsymbol{\Omega}}(\mathbf{q}_\mathrm{d}) := \partial\boldsymbol{\Omega}(\mathbf{q}_\mathrm{d})/\partial\mathbf{q}_\mathrm{d} = \mathbf{J}_{\hat{\boldsymbol{\Omega}}}\mathbf{H}_\mathrm{d}^{-1}$. Moreover, $\mathbf{B}_\mathrm{d} \in \mathbb{R}^{3\times4}$ is derived by reorganizing the actuators on the right-hand side of equation (3.62), thereby ensuring the presence of the ordered actuator $\mathbf{u} := [u_{\mathrm{H1}}, u_{\mathrm{H2}}, u_{\mathrm{K1}}, u_{\mathrm{K2}}]^\top$, as specified using the notations in Section 3.1.1.

Virtual Actuators in DSP

The system characterized by the equations of motion in (3.62) demonstrates three degrees of freedom while accommodating four physical actuators, thus signifying an overactuated system. In addressing such redundant overactuation, techniques such as least-squares projection are explored in [151]. In a more general formulation, the preceding study in [194] establishes an actuator projection technique to virtually couple the physical actuators by two independent virtual actuators post-projection. This notably leads to one degree of underactuation in the DSP, similar to the underactuated SSP, which corresponds with the Hybrid Zero Dynamics control framework.
In light of the thesis' objective to employ the continuous DSP for the enhancement of gait stability, it is advantageous to construct a fully actuated model within the DSP framework, where the degrees of freedom are equivalent to the number of independent virtual actuators. This approach circumvents the intricacies associated with resolving a redundant overactuated problem, while concurrently allowing for direct control over all degrees of freedom to achieve enhanced stability. Consequently, an actuator projection matrix $\mathbf{P}_{\mathbf{u},(3)} \in \mathbb{R}^{4\times3}$ is delineated to facilitate the generation of three independent virtual actuators $\tilde{\mathbf{u}}_{(3)} \in \mathbb{R}^3$, which are represented in

$$\mathbf{u} = \mathbf{P}_{\mathbf{u},(3)}\tilde{\mathbf{u}}_{(3)} := \mathbf{P}_{\mathbf{u},(3)}\begin{bmatrix}\tilde{u}_{(3),1}\\ \tilde{u}_{(3),2}\\ \tilde{u}_{(3),3}\end{bmatrix}. \tag{3.63}$$

To prevent arbitrary scaling of virtual actuators during the projection process, the norm of each row of the projection matrix $\mathbf{P}_{\mathbf{u},(3)}$ is constrained to unity. Furthermore, linear independence in the projection is guaranteed by imposing the condition that the inner product of any two distinct rows is zero. These stipulations are fulfilled through equality constraints within the numerical optimization framework. The incorporation of the projections delineated in (3.63) into the equations of motion specified in (3.62) results in a fully actuated model governed by the equations

$$\mathbf{M}_{\mathrm{d}}\ddot{\mathbf{q}}_{\mathrm{d}} + \mathbf{\Gamma}_{\mathrm{d}} = \mathbf{B}_{(3)}\tilde{\mathbf{u}}_{(3)} \text{ , with } \quad \mathbf{B}_{(3)} := \mathbf{B}_{\mathrm{d}}\mathbf{P}_{\mathbf{u},(3)} \text{ .} \tag{3.64}$$

In this context, $\mathbf{B}_{(3)} \in \mathbb{R}^{3\times 3}$ possesses full rank, namely $\operatorname{rank}(\mathbf{B}_{(3)}) = 3$. To further refine the controller's formulation predicated upon the models delineated in (3.64), the projection matrix $\mathbf{B}_{(3)}$ in equation (3.64) is transformed into a lower triangular configuration. This is accomplished through the implementation of three Givens rotations $\tilde{\mathbf{G}}_i$, $i \in \{1,2,3\}$, as detailed in [56, Section 5], with the aim of eliminating the components associated with the index number $(2,1)$, $(1,1)$, and subsequently $(1,2)$ within the matrix $\mathbf{B}_{(3)}$, represented as

$$\underbrace{\tilde{\mathbf{G}}_3\tilde{\mathbf{G}}_2\tilde{\mathbf{G}}_1}_{\mathbf{P}_{\tilde{\mathbf{G}}}(\mathbf{B}_{(3)})}\mathbf{B}_{(3)} = \underbrace{\begin{bmatrix} 0 & 0 & \tilde{B}_{(3),13} \\ 0 & \tilde{B}_{(3),22} & \tilde{B}_{(3),23} \\ \tilde{B}_{(3),31} & \tilde{B}_{(3),32} & \tilde{B}_{(3),33} \end{bmatrix}}_{\tilde{\mathbf{B}}_{(3)}} . \tag{3.65}$$

The application of these Givens rotations ultimately leads to the derivation of an orthogonal projection matrix $\mathbf{P}_{\tilde{\mathbf{G}}} \in \mathbb{R}^{3\times 3}$, characterized by $\mathbf{P}_{\tilde{\mathbf{G}}}^{\top}\mathbf{P}_{\tilde{\mathbf{G}}} = \mathbf{P}_{\tilde{\mathbf{G}}}\mathbf{P}_{\tilde{\mathbf{G}}}^{\top} = \mathbf{I}_3$. Subsequently, applying projection matrix $\mathbf{P}_{\tilde{\mathbf{G}}}$ to equations of motion in (3.64) results in the transformed form as depicted in

$$\underbrace{\mathbf{P}_{\tilde{\mathbf{G}}}\mathbf{M}_{\mathrm{d}}}_{\mathbf{M}_{\mathrm{d},(3)}}\ddot{\mathbf{q}}_{\mathrm{d}} + \underbrace{\mathbf{P}_{\tilde{\mathbf{G}}}\mathbf{\Gamma}_{\mathrm{d}}}_{\mathbf{\Gamma}_{\mathrm{d},(3)}} = \tilde{\mathbf{B}}_{(3)}\tilde{\mathbf{u}}_{(3)} \text{ .} \tag{3.66}$$

Equation (3.66) expressing the fully actuated model is structured as

$$M_{\mathrm{d},(3),11}\ddot{\theta}_{\mathrm{virt}} + \mathbf{M}_{\mathrm{d},(3),12}\ddot{\mathbf{q}}_{\mathrm{di}} + \Gamma_{\mathrm{d},(3),1} = \tilde{B}_{(3),13}\tilde{u}_{(3),3} \text{ ,} \tag{3.67a}$$

$$\mathbf{M}_{\mathrm{d},(3),21}\ddot{\theta}_{\mathrm{virt}} + \mathbf{M}_{\mathrm{d},(3),22}\ddot{\mathbf{q}}_{\mathrm{di}} + \mathbf{\Gamma}_{\mathrm{d},(3),2} = \underbrace{\begin{bmatrix} 0 & \tilde{B}_{(3),22} \\ \tilde{B}_{(3),31} & \tilde{B}_{(3),32} \end{bmatrix}}_{\tilde{\mathbf{B}}_{(3),21}}\underbrace{\begin{bmatrix} \tilde{u}_{(3),1} \\ \tilde{u}_{(3),2} \end{bmatrix}}_{\tilde{\mathbf{u}}_{(3),12}} + \underbrace{\begin{bmatrix} \tilde{B}_{(3),23} \\ \tilde{B}_{(3),33} \end{bmatrix}}_{\tilde{\mathbf{B}}_{(3),22}}\tilde{u}_{(3),3} \text{ .} \tag{3.67b}$$

Given the system's (virtually) fully actuated nature, the dynamics linked to the coordinate θ_{virt}, which signifies the absolute orientation of the robot's body, can be precisely controlled via the virtual actuators, particularly $\tilde{u}_{(3),3}$, as depicted in equation (3.67a). Then the acceleration $\ddot{\theta}_{\text{virt}}$ is eliminated from both equations (3.67), resulting in the inverse dynamics expression

$$\tilde{\mathbf{u}}_{(3),12} := \begin{bmatrix} \tilde{u}_{(3),1} \\ \tilde{u}_{(3),2} \end{bmatrix} = \underbrace{\begin{bmatrix} -\frac{\tilde{B}_{(3),32}}{\tilde{B}_{(3),31}\tilde{B}_{(3),22}} & \frac{1}{\tilde{B}_{(3),31}} \\ \frac{1}{\tilde{B}_{(3),22}} & 0 \end{bmatrix}}_{\left(\tilde{\mathbf{B}}_{(3),21}\right)^{-1}} \left(\overline{\mathbf{M}}_{\mathrm{d},(3)} \underbrace{\ddot{\mathbf{q}}_{\mathrm{di}}}_{\mathbf{w}_{\mathrm{d}}} + \overline{\mathbf{\Gamma}}_{\mathrm{d},(3)} + \overline{\mathbf{B}}_{\mathrm{d},(3)} \tilde{u}_{(3),3} \right), \tag{3.68}$$

with

$$\overline{\mathbf{M}}_{\mathrm{d},(3)} := \mathbf{M}_{\mathrm{d},(3),22} - \mathbf{M}_{\mathrm{d},(3),21} M^{-1}_{\mathrm{d},(3),11} \mathbf{M}_{\mathrm{d},(3),12} \,, \tag{3.69a}$$

$$\overline{\mathbf{\Gamma}}_{\mathrm{d},(3)} := \mathbf{\Gamma}_{\mathrm{d},(3),2} - \mathbf{M}_{\mathrm{d},(3),21} M^{-1}_{\mathrm{d},(3),11} \Gamma_{\mathrm{d},(3),1} \,. \tag{3.69b}$$

$$\overline{\mathbf{B}}_{\mathrm{d},(3)} := \mathbf{M}_{\mathrm{d},(3),21} M^{-1}_{\mathrm{d},(3),11} \tilde{B}_{(3),13} - \tilde{\mathbf{B}}_{(3),22} \,. \tag{3.69c}$$

The inverse dynamics formulation delineated in (3.68) reveals that the initial two virtual actuators $\tilde{\mathbf{u}}_{(3),12} \in \tilde{\mathbf{u}}_{(3)}$ are contingent upon the acceleration $\mathbf{w}_{\mathrm{d}} := \ddot{\mathbf{q}}_{\mathrm{di}}$, as is the third redundant [7] virtual actuator $\tilde{u}_{(3),3} \in \tilde{\mathbf{u}}_{(3)}$. This property is harnessed in formulating control objectives aimed at directly influencing the convergence behavior of the periodic solution pertaining to the walking gait, as elaborated in Section 4.2.1.

DSP in State Space

The state space

$$\mathcal{X}_{\mathrm{d}} = T\mathcal{Q}_{\mathrm{d}} := \left\{ [\mathbf{q}_{\mathrm{d}}^{\top}, \dot{\mathbf{q}}_{\mathrm{d}}^{\top}]^{\top} \mid \mathbf{q}_{\mathrm{d}} \in \mathcal{Q}_{\mathrm{d}}, \dot{\mathbf{q}}_{\mathrm{d}} \in T_{\mathbf{q}_{\mathrm{d}}}\mathcal{Q}_{\mathrm{d}} \subset \mathbb{R}^3 \right\} \tag{3.70}$$

of the second-order system within the DSP consists of the tangent bundle $T\mathcal{Q}_{\mathrm{d}}$ linked to the configuration space $\mathcal{Q}_{\mathrm{d}}$. The velocity vector $\dot{\mathbf{q}}_{\mathrm{d}} \in T_{\mathbf{q}_{\mathrm{d}}}\mathcal{Q}_{\mathrm{d}}$ is specified within the tangent space $T_{\mathbf{q}_{\mathrm{d}}}\mathcal{Q}_{\mathrm{d}}$ at the point $\mathbf{q}_{\mathrm{d}}$.
In accordance with the equations of motion governing the virtually fully actuated DSP dynamics as described in (3.66), the vector field $\tilde{X}_{\mathrm{d,f}}(\mathbf{x}_{\mathrm{d}}, \tilde{\mathbf{u}}_{(3)}) := \tilde{\mathbf{f}}_{\mathrm{d,f}}(\mathbf{x}_{\mathrm{d}}) + \tilde{\mathbf{g}}_{\mathrm{d,f}}(\mathbf{x}_{\mathrm{d}})\tilde{\mathbf{u}}_{(3),12} +$

[7] The term "redundant" is employed because setting the actuator $\tilde{u}_{(3),3} = 0$ to zero results in the configuration of an underactuated DSP.

$\tilde{\mathbf{h}}_{\mathrm{d,f}}(\mathbf{x}_\mathrm{d})\tilde{u}_{(3),3}$ is constructed in relation to the state variables $\mathbf{x}_\mathrm{d} \in TQ_\mathrm{d}$ and the three virtual actuators $\tilde{\mathbf{u}}_{(3)}$, as referenced in

$$\begin{aligned}\underbrace{\begin{bmatrix}\dot{\mathbf{q}}_\mathrm{d}\\ \ddot{\mathbf{q}}_\mathrm{d}\end{bmatrix}}_{\dot{\mathbf{x}}_\mathrm{d}} &= \begin{bmatrix}\dot{\mathbf{q}}_\mathrm{d}\\ \mathbf{M}^{-1}_{\mathrm{d},(3)}\left(-\mathbf{\Gamma}_{\mathrm{d},(3)} + \tilde{\mathbf{B}}_{(3)}\tilde{\mathbf{u}}_{(3)}\right)\end{bmatrix}\\ &= \underbrace{\begin{bmatrix}\dot{\mathbf{q}}_\mathrm{d}\\ -\mathbf{M}^{-1}_{\mathrm{d},(3)}\mathbf{\Gamma}_{\mathrm{d},(3)}\end{bmatrix}}_{\tilde{\mathbf{f}}_{\mathrm{d,f}}(\mathbf{x}_\mathrm{d})} + \underbrace{\begin{bmatrix}\mathbf{0}\\ \mathbf{M}^{-1}_{\mathrm{d},(3)}\tilde{\mathbf{B}}_{(3)}\begin{bmatrix}\mathbf{I}_2\\ \mathbf{0}\end{bmatrix}\end{bmatrix}}_{\tilde{\mathbf{g}}_{\mathrm{d,f}}(\mathbf{x}_\mathrm{d})}\tilde{\mathbf{u}}_{(3),12} + \underbrace{\begin{bmatrix}\mathbf{0}\\ \mathbf{M}^{-1}_{\mathrm{d},(3)}\tilde{\mathbf{B}}_{(3)}\begin{bmatrix}\mathbf{0}\\ 1\end{bmatrix}\end{bmatrix}}_{\tilde{\mathbf{h}}_{\mathrm{d,f}}(\mathbf{x}_\mathrm{d})}\tilde{u}_{(3),3}\,.\end{aligned} \tag{3.71}$$

Notably, the redundant virtual actuator $\tilde{u}_{(3),3}$ is differentiated from the other two actuators $\tilde{\mathbf{u}}_{(3),12}$ due to their distinct roles in the control design. Specifically, the two actuators $\tilde{\mathbf{u}}_{(3),12}$ are primarily responsible for imposing virtual constraints on the actuated joints, while the redundant actuator $\tilde{u}_{(3),3}$ is employed to enhance the stability characteristics of the periodic solution.
To facilitate the controller design for the virtual constraints, the actuators $\tilde{\mathbf{u}}_{(3),12}$ have been substituted with the acceleration $\mathbf{w}_\mathrm{d}$ in accordance with the inverse dynamics relation delineated in (3.68). Consequently, the vector field $X_{\mathrm{d,f}}(\mathbf{x}_\mathrm{d}, \mathbf{w}_\mathrm{d}, \tilde{u}_{(3),3}) := \mathbf{f}_{\mathrm{d,f}}(\mathbf{x}_\mathrm{d}) + \mathbf{g}_{\mathrm{d,f}}(\mathbf{x}_\mathrm{d})\mathbf{w}_\mathrm{d} + \mathbf{h}_{\mathrm{d,f}}(\mathbf{x}_\mathrm{d})\tilde{u}_{(3),3}$ is expressed as a function of the state variable $\mathbf{x}_\mathrm{d} \in TQ_\mathrm{d}$, the acceleration $\mathbf{w}_\mathrm{d}$, and the redundant virtual actuator $\tilde{u}_{(3),3} \in \tilde{\mathbf{u}}_{(3)}$. This is encapsulated by

$$\underbrace{\begin{bmatrix}\dot{\mathbf{q}}_\mathrm{d}\\ \ddot{\theta}_\mathrm{virt}\\ \mathbf{w}_\mathrm{d}\end{bmatrix}}_{\dot{\mathbf{x}}_\mathrm{d}} = \underbrace{\begin{bmatrix}\dot{\mathbf{q}}_\mathrm{d}\\ -M^{-1}_{\mathrm{d},(3),11}\Gamma_{\mathrm{d},(3),1}\\ \mathbf{0}\end{bmatrix}}_{\mathbf{f}_{\mathrm{d,f}}(\mathbf{x}_\mathrm{d})} + \underbrace{\begin{bmatrix}\mathbf{0}\\ -M^{-1}_{\mathrm{d},(3),11}\mathbf{M}_{\mathrm{d},(3),12}\\ \mathbf{I}_2\end{bmatrix}}_{\mathbf{g}_{\mathrm{d,f}}(\mathbf{x}_\mathrm{d})}\mathbf{w}_\mathrm{d} + \underbrace{\begin{bmatrix}\mathbf{0}\\ M^{-1}_{\mathrm{d},(3),11}\tilde{B}_{(3),13}\\ \mathbf{0}\end{bmatrix}}_{\mathbf{h}_{\mathrm{d,f}}(\mathbf{x}_\mathrm{d})}\tilde{u}_{(3),3}\,, \tag{3.72}$$

where $\ddot{\theta}_\mathrm{virt}$ is derived from equation (3.67a).

Discrete Mappings

The discrete mappings, which include touch-down as referenced in Section 3.3.2 and lift-off as cited in Section 3.3.3, are articulated within the state space expression. The touch-down mapping (3.54) delineates the transition of the system state $\mathbf{x}_\mathrm{s}^- :=$

$[(\mathbf{q}_\mathrm{s}^-)^\top, (\dot{\mathbf{q}}_\mathrm{s}^-)^\top]^\top \in TQ_\mathrm{s}$ at the termination of the SSP domain to the initial state variables $\mathbf{x}_\mathrm{d}^+ := [(\mathbf{q}_\mathrm{d}^+)^\top, (\dot{\mathbf{q}}_\mathrm{d}^+)^\top]^\top \in TQ_\mathrm{d}$ of the DSP domain, as represented by

$$\mathbf{x}_\mathrm{d}^+ = \boldsymbol{\Delta}_\mathrm{TD}(\mathbf{x}_\mathrm{s}^-) := \begin{bmatrix} \mathbf{H}_\mathrm{d}\mathbf{R}_\mathrm{s}^\mathrm{d}\mathbf{H}_\mathrm{s}^{-1}\mathbf{q}_\mathrm{s}^- \\ \mathbf{H}_\mathrm{d}\begin{bmatrix}\mathbf{0} & \mathbf{R}_\mathrm{s}^\mathrm{d} & \mathbf{0}\end{bmatrix}\boldsymbol{\Pi}_{\mathrm{w,n,lhs}}^{-1}\boldsymbol{\Pi}_{\mathrm{w,n,rhs}}\mathbf{H}_\mathrm{s}^{-1}\dot{\mathbf{q}}_\mathrm{s}^- \end{bmatrix} . \tag{3.73}$$

Notably, the coordinate transformations $\hat{\mathbf{q}}_\mathrm{s}^- = \mathbf{H}_\mathrm{s}^{-1}\mathbf{q}_\mathrm{s}^-$ and $\dot{\hat{\mathbf{q}}}_\mathrm{s}^- = \mathbf{H}_\mathrm{s}^{-1}\dot{\mathbf{q}}_\mathrm{s}^-$, with matrix $\mathbf{H}_\mathrm{s}^{-1}$ described in (3.27), are executed for coordinates $\hat{\mathbf{q}}_\mathrm{s}^- \in \hat{Q}_\mathrm{s}$ within the SSP. In a parallel manner, the transformations $\mathbf{q}_\mathrm{d}^+ = \mathbf{H}_\mathrm{d}\hat{\mathbf{q}}_\mathrm{d}^+$ and $\dot{\mathbf{q}}_\mathrm{d}^+ = \mathbf{H}_\mathrm{d}\dot{\hat{\mathbf{q}}}_\mathrm{d}^+$, as detailed in (3.60), are applied to coordinates $\hat{\mathbf{q}}_\mathrm{d}^+ \in \hat{Q}_\mathrm{d}$ within the DSP.
The lift-off mapping (3.58) is reformulated by utilizing the state variables $\mathbf{x}_\mathrm{d}^- := [(\mathbf{q}_\mathrm{d}^-)^\top, (\dot{\mathbf{q}}_\mathrm{d}^-)^\top]^\top \in TQ_\mathrm{d}$ at the termination of the DSP, and $\mathbf{x}_\mathrm{s}^+ := [(\mathbf{q}_\mathrm{s}^+)^\top, (\dot{\mathbf{q}}_\mathrm{s}^+)^\top]^\top \in TQ_\mathrm{s}$ at the initiation of the SSP, resulting in

$$\mathbf{x}_\mathrm{s}^+ = \boldsymbol{\Delta}_\mathrm{LO}(\mathbf{x}_\mathrm{d}^-) := \begin{bmatrix} \mathbf{H}_\mathrm{s}\mathbf{R}_\mathrm{d}^\mathrm{s}\begin{bmatrix}\mathbf{H}_\mathrm{d}^{-1}\mathbf{q}_\mathrm{d}^- \\ \boldsymbol{\Omega}(\mathbf{q}_\mathrm{d}^-)\end{bmatrix} \\ \mathbf{H}_\mathrm{s}\mathbf{R}_\mathrm{d}^\mathrm{s}\begin{bmatrix}\mathbf{I}_3 \\ \mathbf{J}_{\boldsymbol{\Omega}}(\mathbf{q}_\mathrm{d}^-)\end{bmatrix}\dot{\mathbf{q}}_\mathrm{d}^- \end{bmatrix} . \tag{3.74}$$

Hybrid Dynamical System in State Space

The hybrid dynamical system pertaining to walking with a non-instantaneous double support phase is synthesized using the state space expressions (3.34) and (3.72) during the single support phase and the double support phase, respectively, in conjunction with the transition events encompassing touch-down (3.73) and lift-off (3.74).
Consequently, the SSP domain is initially defined as

$$\Sigma_\mathrm{w,SSP} : \begin{cases} \dot{\mathbf{x}}_\mathrm{s} = \tilde{\mathbf{f}}_\mathrm{s}(\mathbf{x}_\mathrm{s}) + \tilde{\mathbf{g}}_\mathrm{s}(\mathbf{x}_\mathrm{s})\mathbf{u} , & \mathbf{x}_\mathrm{s} \notin \mathcal{S}_\mathrm{s}^\mathrm{d} , \\ \mathbf{x}_\mathrm{d}^+ = \boldsymbol{\Delta}_\mathrm{TD}(\mathbf{x}_\mathrm{s}^-) , & \mathbf{x}_\mathrm{s}^- \in \mathcal{S}_\mathrm{s}^\mathrm{d} , \\ \mathcal{S}_\mathrm{s}^\mathrm{d} := \{\mathbf{x}_\mathrm{s} \in TQ_\mathrm{s} |\, g_\mathrm{s}^\mathrm{d}(\mathbf{x}_\mathrm{s}) = 0, r_{2,x}(\mathbf{x}_\mathrm{s}) > 0\} , & \end{cases} \tag{3.75}$$

wherein the switching surface $\mathcal{S}_\mathrm{s}^\mathrm{d}$ is determined by the guard function $g_\mathrm{s}^\mathrm{d}(\mathbf{x}_\mathrm{s}) := r_{2,z}(\mathbf{x}_\mathrm{s})$ with the parameter $g_\mathrm{s}^\mathrm{d} : TQ_\mathrm{s} \to \mathbb{R}$. Furthermore, it is imperative for the touchdown position to be situated anterior to the stance foot $\mathbf{r}_1 = \mathbf{0}$ (as a result of the constraint (3.6a)), as imposed by the inequality condition $r_{2,x}(\mathbf{x}_\mathrm{s}) > 0$.

The DSP model (3.71) is used to specify the DSP domain, as illustrated in

$$\Sigma_{\mathrm{w,fd}}: \begin{cases} \dot{\mathbf{x}}_{\mathrm{d}} = \tilde{\mathbf{f}}_{\mathrm{d,f}}(\mathbf{x}_{\mathrm{d}}) + \tilde{\mathbf{g}}_{\mathrm{d,f}}(\mathbf{x}_{\mathrm{d}})\tilde{\mathbf{u}}_{(3),12} + \tilde{\mathbf{h}}_{\mathrm{d,f}}(\mathbf{x}_{\mathrm{d}})\tilde{u}_{(3),3}\,, & \mathbf{x}_{\mathrm{d}} \notin \mathcal{S}_{\mathrm{d}}^{\mathrm{s}}\,, \\ \mathbf{x}_{\mathrm{s}}^{+} = \boldsymbol{\Delta}_{\mathrm{LO}}\left(\mathbf{x}_{\mathrm{d}}^{-}\right)\,, & \mathbf{x}_{\mathrm{d}}^{-} \in \mathcal{S}_{\mathrm{d}}^{\mathrm{s}}\,, \\ \mathcal{S}_{\mathrm{d}}^{\mathrm{s}} := \{\mathbf{x}_{\mathrm{d}} \in T\boldsymbol{Q}_{\mathrm{d}} |\, g_{\mathrm{d}}^{\mathrm{s}}(\mathbf{x}_{\mathrm{d}}) = 0\}\,, \end{cases} \tag{3.76}$$

wherein the switching surface $\mathcal{S}_{\mathrm{d}}^{\mathrm{s}}$ is delineated by the guard function $g_{\mathrm{d}}^{\mathrm{s}}(\mathbf{x}_{\mathrm{d}}) := (\begin{bmatrix}1 & \mathbf{0}\end{bmatrix}\mathbf{x}_{\mathrm{d}} - \theta_{\mathrm{LO}}) = (\theta_{\mathrm{virt}} - \theta_{\mathrm{LO}})$ with $g_{\mathrm{d}}^{\mathrm{s}} : T\boldsymbol{Q}_{\mathrm{d}} \to \mathbb{R}$.
Specifically, θ_{LO} details the phase-specific event that initiates the controller's action to disengage the trailing leg from contact with the ground, thereby concluding the double support phase. Importantly, θ_{LO} is identified as a critical gait parameter that affects the energy efficiency and stability of the periodic walking gait. Consequently, θ_{LO} is optimized while finding optimal gaits through the optimization framework as detailed in Chapter 7.

4 Control Design for Walking

The principal objective of Hybrid Zero Dynamics (HZD) control is to develop a time-invariant controller that facilitates the generation of periodic walking and running gaits for a bipedal robot. In particular, feedback controllers impose holonomic virtual constraints on the actuated joints, thereby aligning the rotation angles of these joints with a reference trajectory defined by a phase-dependent, high-order polynomial. Upon the mitigation of synchronization errors, the dynamics of the full-order system during the continuous phase are reduced to the invariant zero dynamics submanifold of a lower dimension. By considering discrete transition events, periodic solutions to the resultant hybrid zero dynamics are ascertained through numerical methods conceptualized as an optimization problem. As a result, a stable limit cycle within the hybrid zero dynamics manifold is indicative of a stable periodic walking gait of the full-order robot system.
The HZD controller has already been well established for generating stable and energy-efficient walking and running gaits, as demonstrated in [177]. This thesis employs the established framework and further extends it to account for variations in gait and environmental conditions. Indeed, Section 4.1 articulates the control design methodology for the generation of periodic walking gaits that incorporate an instantaneous double support phase, a subject extensively examined in the pertinent literature. Consequently, it provides a foundational framework with a high degree of adaptability for various gaits or differing environmental conditions, which this thesis extends. In particular, Section 4.2 adapts the controller to accommodate walking gaits that feature a non-instantaneous double support phase on rigid ground.

4.1 Walking with Instantaneous DSP

The periodic walking gaits of the robot are characterized through a hybrid dynamical system as delineated in (3.38). To mitigate the dimensional complexity of this system, a feedback controller, as presented in Section 4.1.1, is utilized to impose virtual constraints on the four actuated joints, thereby synchronizing the rotation angle with the reference trajectory. Upon the elimination of the synchronization error, the comprehensive system

dynamics are articulated on the invariant zero dynamics submanifolds, as elucidated in Section 4.1.2. The stability assessment of the resultant periodic orbit of the hybrid system is conducted using Floquet theory, as expounded in Section 4.1.3.

4.1.1 Feedback Control in SSP

The primary function of the feedback controller is to ensure the synchronization of the actuated joints $\mathbf{q}_\mathrm{b}$ with the designated reference trajectory $\mathbf{q}_{\mathrm{r,s}}(\theta_\mathrm{virt})$. To achieve this, a vector-valued function $\mathbf{q}_{\mathrm{r,s}} : S^1 \to \mathbb{T}^4; \theta_\mathrm{virt} \mapsto \mathbf{q}_{\mathrm{r,s}}(\theta_\mathrm{virt})$ is established using high-order polynomial expressions. The vector $\mathbf{h}_\mathrm{s}(\mathbf{q}_\mathrm{s})$, which describes the synchronization error as elaborated by $\mathbf{h}_\mathrm{s} : \mathcal{Q}_\mathrm{s} \to \mathbb{R}^4; \mathbf{q}_\mathrm{s} \mapsto \mathbf{h}_\mathrm{s}(\mathbf{q}_\mathrm{s})$, constitutes the control output $\mathbf{y}_\mathrm{s}$, formulated as

$$\mathbf{y}_\mathrm{s} := \mathbf{h}_\mathrm{s}(\mathbf{q}_\mathrm{s}) = \mathbf{q}_\mathrm{b} - \mathbf{q}_{\mathrm{r,s}}(\theta_\mathrm{virt}) \,. \tag{4.1}$$

Synchronization in $\mathbf{h}_\mathrm{s}(\mathbf{q}_\mathrm{s})$, as elucidated in [177, Section 5.1], is termed virtual holonomic constraints, as they emerge from feedback control laws rather than traditional passive mechanical kinematic linkages. According to the definition presented in [181, Section 5.1], the virtual constraints articulated in (4.1) are identified as holonomic and scleronomous, attributable to the absence of explicit time dependency within the constraint. Notably, the time dependency is implicitly contained within the independent phase variable $\theta_\mathrm{virt}(t)$, which is regarded as a monotonic function of time during locomotion.
A significant distinction between the virtual constraints and the classical constraints, which manifest as passive mechanical linkages, involves the analysis of the work of the constraint forces. Specifically, the virtual work of the reaction forces associated with ideal holonomic constraints is nullified in accordance with the classical d'Alembert principle [96, Section 4.1]. For ideal constraints that are scleronomous, the actual work of the constraint forces also becomes null, as specified in [181, Section 5.5].
However, it is crucial to recognize that this nullification does not apply to virtual constraints that are classified as non-ideal [169, 170]. Consequently, although the actuator derived from feedback is regarded as reaction forces of the virtual holonomic scleronomous constraints, the actual work associated with them does not diminish. Rather, the minimization of this actual work, with an emphasis on reducing the positive mechanical work, is considered the foremost optimization objective in order to attain highly efficient locomotion gaits.
In accordance with the feedback linearization method elucidated in Section 2.5.2, the nonlinear characteristics associated with the output $\mathbf{y}_\mathrm{s}$ are mitigated through nonlinear state feedback. The formulation of this feedback involves the computation of the Lie

derivative of the output function $\mathbf{h}_\mathrm{s}(\mathbf{q}_\mathrm{s})$ along the vector field $\tilde{X}_{\mathrm{s,r}}(\mathbf{x}_\mathrm{s}, \mathbf{u}) := \tilde{\mathbf{f}}_\mathrm{s}(\mathbf{x}_\mathrm{s}) + \tilde{\mathbf{g}}_\mathrm{s}(\mathbf{x}_\mathrm{s})\mathbf{u}$ on TQ_s, as delineated in (3.34), leading to

$$\begin{aligned}\dot{\mathbf{y}}_\mathrm{s} &= \left[\left[-\frac{\partial \mathbf{q}_{\mathrm{r,s}}}{\partial \theta_\mathrm{virt}} \quad \mathbf{I}_4\right] \quad \mathbf{0}\right]\left(\begin{bmatrix}\dot{\mathbf{q}}_\mathrm{s}\\ -\mathbf{M}_\mathrm{s}^{-1}\mathbf{\Gamma}_\mathrm{s}\end{bmatrix} + \begin{bmatrix}\mathbf{0}\\ \mathbf{M}_\mathrm{s}^{-1}\mathbf{B}_\mathrm{s}\end{bmatrix}\mathbf{u}\right)\\ &= \underbrace{\left[-\frac{\partial \mathbf{q}_{\mathrm{r,s}}}{\partial \theta_\mathrm{virt}} \quad \mathbf{I}_4\right]\dot{\mathbf{q}}_\mathrm{s}}_{\mathcal{L}_{\tilde{f}}\mathbf{h}_\mathrm{s}(\mathbf{q}_\mathrm{s},\dot{\mathbf{q}}_\mathrm{s})} + \underbrace{\left(\left[-\frac{\partial \mathbf{q}_{\mathrm{r,s}}}{\partial \theta_\mathrm{virt}} \quad \mathbf{I}_4\right]\mathbf{0} + \mathbf{0}\left(\mathbf{M}_\mathrm{s}^{-1}\mathbf{B}_\mathrm{s}\right)\right)\mathbf{u}}_{\mathcal{L}_{\tilde{g}}\mathbf{h}_\mathrm{s}(\mathbf{q}_\mathrm{s})=\mathbf{0}}.\end{aligned} \tag{4.2}$$

Subsequently, the second Lie derivative is expressed as

$$\begin{aligned}\ddot{\mathbf{y}}_\mathrm{s} &= \left[\left[-\frac{\partial^2 \mathbf{q}_{\mathrm{r,s}}}{\partial \theta_\mathrm{virt}^2}\dot{\theta}_\mathrm{virt} \quad \mathbf{0}\right] \quad \left[-\frac{\partial \mathbf{q}_{\mathrm{r,s}}}{\partial \theta_\mathrm{virt}} \quad \mathbf{I}_4\right]\right]\left(\begin{bmatrix}\dot{\mathbf{q}}_\mathrm{s}\\ -\mathbf{M}_\mathrm{s}^{-1}\mathbf{\Gamma}_\mathrm{s}\end{bmatrix} + \begin{bmatrix}\mathbf{0}\\ \mathbf{M}_\mathrm{s}^{-1}\mathbf{B}_\mathrm{s}\end{bmatrix}\mathbf{u}\right)\\ &= \underbrace{\left(-\frac{\partial^2 \mathbf{q}_{\mathrm{r,s}}}{\partial \theta_\mathrm{virt}^2}\dot{\theta}_\mathrm{virt}^2 - \left[-\frac{\partial \mathbf{q}_{\mathrm{r,s}}}{\partial \theta_\mathrm{virt}} \quad \mathbf{I}_4\right]\mathbf{M}_\mathrm{s}^{-1}\mathbf{\Gamma}_\mathrm{s}\right)}_{\mathcal{L}_{\tilde{f}}^2\mathbf{h}_\mathrm{s}(\mathbf{q}_\mathrm{s},\dot{\mathbf{q}}_\mathrm{s})} + \underbrace{\left(\left[-\frac{\partial \mathbf{q}_{\mathrm{r,s}}}{\partial \theta_\mathrm{virt}} \quad \mathbf{I}_4\right]\mathbf{M}_\mathrm{s}^{-1}\mathbf{B}_\mathrm{s}\right)}_{\mathcal{L}_{\tilde{g}}\mathcal{L}_{\tilde{f}}\mathbf{h}_\mathrm{s}(\mathbf{q}_\mathrm{s})}\mathbf{u}.\end{aligned} \tag{4.3}$$

Considering $\mathcal{L}_{\tilde{g}}\mathbf{h}_\mathrm{s} = \mathbf{0}$ in equation (4.2) and $\mathcal{L}_{\tilde{g}}\mathcal{L}_{\tilde{f}}\mathbf{h}_\mathrm{s} \neq \mathbf{0}$ in equation (4.3), the current control system exhibits a vector-valued relative degree $\{r_{\mathrm{s},1}, r_{\mathrm{s},2}, r_{\mathrm{s},3}, r_{\mathrm{s},4}\} = \{2, 2, 2, 2\}$ for defining the control output $\mathbf{y}_\mathrm{s}$ in relation to the input $\mathbf{u}$, as delineated in [2, Definition 33]. Consequently, for the design of a flat control output according to [2, Section 3.2], the polynomials $\mathbf{q}_{\mathrm{r,s}}(\theta_\mathrm{virt})$ in output (4.1) are required to be at least twice continuously differentiable with respect to the independent variable θ_virt, i.e., $\mathbf{q}_{\mathrm{r,s}} \in C^2(S^1)$. Within this study, sixth-order Bézier polynomials are utilized as reference trajectories that meet the flatness criterion, attributable to their smooth properties as C^∞-functions and $C^\infty \subset C^2$. As a result, the control input is formulated as an algebraic function of the flat output and a finite number of its derivatives.
Moreover, the total relative degree ($\sum_{i=1}^{4} r_{\mathrm{s},i} = 8$) is less than the dimension of the system's state space ($\dim(\mathbf{x}_\mathrm{s}) = 10$); this discrepancy indicates the presence of a two-dimensional internal dynamics, which is not directly controllable through the input $\mathbf{u}$. Consequently, the system is delineated into two distinct subsystems: a two-dimensional nonlinear internal dynamics subsystem and an eight-dimensional subsystem that can be linearized through nonlinear state feedback, as will be further elaborated upon below.

State Feedback for Linearization

The construction of the nonlinear state feedback is predicated on the Lie derivatives as identified in (4.2) and (4.3). The principal aim of this feedback is to convert the nonlinear control problem, wherein virtual constraints as specified in (4.1) are imposed,

into a linear and controllable configuration. Specifically, by establishing $\mathbf{v}_s := \ddot{\mathbf{y}}_s$ as a new system input, the system manifests a linear double integrator behavior between the input $\mathbf{v}_s$ and the output $\mathbf{y}_s$.
In essence, the imposition of virtual constraints is examined through the study of convergence behavior in proximity to the equilibrium point $\mathbf{y}_s^0 = \mathbf{0}$ of the double integrator. This linearization process is effected by the nonlinear state feedback:

$$\mathbf{u} = \mathbf{u}_s(\mathbf{q}_s, \dot{\mathbf{q}}_s) := \left(\mathcal{L}_{\tilde{g}}\mathcal{L}_{\tilde{f}}\mathbf{h}_s(\mathbf{q}_s)\right)^{-1}\left(\mathbf{v}_s - \mathcal{L}_{\tilde{f}}^2\mathbf{h}_s(\mathbf{q}_s, \dot{\mathbf{q}}_s)\right), \tag{4.4}$$

which is defined in an open subset $\mathcal{Q}_{s,0} \subset \mathcal{Q}_s$, where the decoupling matrix $\mathcal{L}_{\tilde{g}}\mathcal{L}_{\tilde{f}}\mathbf{h}_s(\mathbf{q}_s)$ is invertible, i.e. $\det\left(\mathcal{L}_{\tilde{g}}\mathcal{L}_{\tilde{f}}\mathbf{h}_s(\mathbf{q}_s)\right) \neq 0, \forall \mathbf{q}_s \in \mathcal{Q}_{s,0}$.

Coordinate Transformation for Linearization

To enhance comprehension, the partition of the system into two subsystems is demonstrated through a coordinate transformation derived from the Lie derivatives in (4.2) and (4.3). As elucidated by the method in [79, Section 5.1], the coordinate transformations $\boldsymbol{\eta}_{s,1} := \mathbf{y}_s = \mathbf{h}_s(\mathbf{x}_s)$ and $\boldsymbol{\eta}_{s,2} := \mathcal{L}_{\tilde{f}}\mathbf{h}_s(\mathbf{x}_s)$, characterized by their linear independence and smoothness, exemplify the linearizable partition, which is actualized through the state feedback in (4.4). Particularly, the research focus is directed towards examining the stability characteristics at the equilibrium point $\mathbf{y}_s^0 = \mathbf{h}_s(\mathbf{x}_s^0) = \mathbf{0}$ of the linearized subsystem.
To articulate the dynamics of the residual subsystem (specifically, the internal dynamics), two independent coordinates, $\boldsymbol{\xi}_s := [\xi_{s,1}, \xi_{s,2}]^\top$, are arbitrarily selected, provided that the Jacobian corresponding to the coordinate transformation is non-singular, as delineated in [79, Proposition 4.1.3]. Consequently, the coordinates $\boldsymbol{\xi}_s$ are chosen such that the internal dynamics remain unaffected by the input actuators $\mathbf{u}$. This necessitates that the Lie derivatives $\mathcal{L}_{\tilde{g}}\xi_{s,1} = 0$, $\mathcal{L}_{\tilde{g}}\xi_{s,2} = 0$ with respect to the vector field $\tilde{\mathbf{g}}_s(\mathbf{x}_s)\mathbf{u}$, as elaborated in (3.34), must vanish. Therefore, the decoupling of the internal dynamics from the actuators $\mathbf{u}$ enables the formulation and examination of the solution within these coordinates through a simplified autonomous system characterized by a diminished system order.
Notably, $\xi_{s,1} = \theta_{\text{virt}}$ serves as an independent coordinate, determined through a linear scalar function $c_\theta : \mathcal{Q}_s \to \mathbb{R}$, articulated as

$$\theta_{\text{virt}} = c_\theta(\mathbf{q}_s) := \begin{bmatrix} 1 & \mathbf{0} \end{bmatrix} \mathbf{q}_s \,. \tag{4.5}$$

As established in Section 3.2.3, θ_{virt} is linearly independent from the actuated joint angles $\mathbf{q}_b$, and consequently, from the output function $\mathbf{h}_s(\mathbf{q}_s)$. In accordance with the

recommendation in [175], the second coordinate $\xi_{s,2} = \sigma_s$ arises as a result of the scalar function $c_\sigma : \mathcal{Q}_s \times T_{\mathbf{q}_s}\mathcal{Q}_s \to \mathbb{R}$, represented as

$$\sigma_s = c_\sigma(\mathbf{q}_s, \dot{\mathbf{q}}_s) := \begin{bmatrix} 1 & \mathbf{0} \end{bmatrix} \mathbf{M}_s(\mathbf{q}_s)\dot{\mathbf{q}}_s \,, \tag{4.6}$$

wherein σ_s denotes the generalized momentum conjugate to the coordinate θ_{virt}. These coordinate transformations establish the mapping $\Psi_s : T\mathcal{Q}_s \to \mathbb{R}^{10}$; $\mathbf{x}_s \mapsto \Psi_s(\mathbf{x}_s)$ as delineated in

$$\mathbf{z}_s = \begin{bmatrix} \boldsymbol{\eta}_{s,1} \\ \boldsymbol{\eta}_{s,2} \\ \xi_{s,1} \\ \xi_{s,2} \end{bmatrix} = \Psi_s(\mathbf{x}_s) := \begin{bmatrix} \mathbf{h}_s(\mathbf{q}_s) \\ \mathcal{L}_{\tilde{f}}\mathbf{h}_s(\mathbf{q}_s, \dot{\mathbf{q}}_s) \\ c_\theta(\mathbf{q}_s) \\ c_\sigma(\mathbf{q}_s, \dot{\mathbf{q}}_s) \end{bmatrix} . \tag{4.7}$$

The Jacobian $\mathbf{J}_{\Psi,s} := \partial\Psi_s/\partial\mathbf{x}_s = \begin{bmatrix} \partial\Psi_s/\partial\mathbf{q}_s \,, \partial\Psi_s/\partial\dot{\mathbf{q}}_s \end{bmatrix}$ is anticipated to be non-singular owing to the linear independence of the transformed coordinates, thus evaluated in $\mathcal{Q}_{s,0}$. Owing to the presence of a smooth inverse $\mathbf{x}_s = \Psi_s^{-1}(\mathbf{z}_s)$, the mapping Ψ_s is recognized as a diffeomorphism in accordance with [2, p. 262]. Subsequently, the system dynamics are articulated in the Byrnes-Isidori form utilizing the coordinates $\mathbf{z}_s$:

$$\begin{bmatrix} \dot{\boldsymbol{\eta}}_{s,1} \\ \dot{\boldsymbol{\eta}}_{s,2} \\ \dot{\xi}_{s,1} \\ \dot{\xi}_{s,2} \end{bmatrix} = \begin{bmatrix} \boldsymbol{\eta}_{s,2} \\ \mathcal{L}_{\tilde{f}}^2\mathbf{h}_s(\mathbf{x}_s) \\ \mathcal{L}_{\tilde{f}}\xi_{s,1}(\mathbf{x}_s) \\ \mathcal{L}_{\tilde{f}}\xi_{s,2}(\mathbf{x}_s) \end{bmatrix}\Bigg|_{\mathbf{x}_s=\Psi_s^{-1}(\mathbf{z}_s)} + \begin{bmatrix} \mathbf{0} \\ \mathcal{L}_{\tilde{g}}\mathcal{L}_{\tilde{f}}\mathbf{h}_s(\mathbf{x}_s) \\ 0 \\ 0 \end{bmatrix}\Bigg|_{\mathbf{x}_s=\Psi_s^{-1}(\mathbf{z}_s)} \mathbf{u} \,. \tag{4.8}$$

Representing the feedback $\mathbf{u} = \mathbf{u}_s\left(\Psi_s^{-1}(\mathbf{z}_s)\right)$ from (4.4) as a function of the coordinates $\mathbf{z}_s$ and reintegrating it into the Byrnes-Isidori form as in (4.8) reveals the identical characteristics of the double integrator behavior between the input $\mathbf{v}_s$ and the output $\boldsymbol{\eta}_{s,1}$. This linearizable subsystem is delineated by the coordinates $\boldsymbol{\eta}_{s,1}$ and $\boldsymbol{\eta}_{s,2}$. Concurrently, the two-dimensional nonlinear internal dynamics, defined by $\xi_{s,1}$ and $\xi_{s,2}$, remain unaffected by the feedback $\mathbf{u} = \mathbf{u}_s\left(\Psi_s^{-1}(\mathbf{z}_s)\right)$ due to the necessity for arbitrary selection as required by $\mathcal{L}_{\tilde{g}}\xi_{s,1} = 0$, $\mathcal{L}_{\tilde{g}}\xi_{s,2} = 0$.

Linear Feedback Controller

In addressing the linearizable subsystem, methodologies originating from linear control theory are employed to secure asymptotic stability proximate to the equilibrium point $\boldsymbol{\eta}_{s,1}^0 = \mathbf{y}_s^0 = \mathbf{0}$. This approach ensures the enforcement of the nonlinear virtual constraints

as stipulated in (4.1). Owing to its inherent simplicity and efficiency, the design of a linear, high-gain PD-feedback controller

$$\mathbf{v}_\mathrm{s} = -\mathbf{K}_{\mathrm{p,s}}\mathbf{y}_\mathrm{s} - \mathbf{K}_{\mathrm{d,s}}\dot{\mathbf{y}}_\mathrm{s}\,, \tag{4.9}$$

has been implemented, wherein positive definite matrices $\mathbf{K}_{\mathrm{p,s}} \in \mathbb{R}^{4\times4}$ and $\mathbf{K}_{\mathrm{d,s}} \in \mathbb{R}^{4\times4}$ function as feedback gains. Thus, the entire closed-loop structure is illustrated in Figure 4.1.

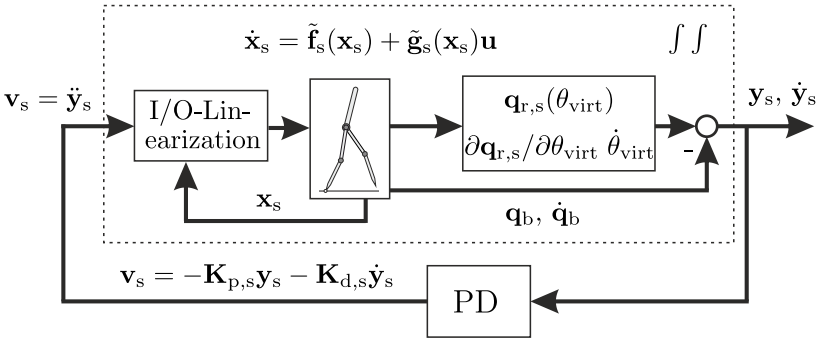

Figure 4.1: Configuration of the closed-loop control architecture for the imposition of virtual constraints on the actuated joints during the single support phase.

To achieve improved convergence, it may be beneficial to consider control strategies with increased design complexity. Nevertheless, the central aim of the thesis is to produce highly efficient reference gaits, under the presumption that the conditions related to virtual constraints are reliably fulfilled, as denoted in $\mathbf{y}_\mathrm{s} = \mathbf{0}$. Consequently, convergence around the equilibrium point $\boldsymbol{\eta}^0_{\mathrm{s},1} = \mathbf{y}^0_\mathrm{s} = \mathbf{0}$ assumes a secondary importance in the gait optimization process. Therefore, alternative feedback methodologies are not explored.

Two-Stage Control Law

The Lie derivatives described in equations (4.2) and (4.3) are employed to construct state feedback mechanisms for linearization. To enhance numerical efficiency, a two-stage formulation is implemented to impose the virtual constraints as outlined in (4.1). Notably, the Lie derivative of the output function $\mathbf{h}_\mathrm{s}(\mathbf{q}_\mathrm{s})$ is conducted along the vector field $X_{\mathrm{s,r}}(\mathbf{x}_\mathrm{s}, \mathbf{w})$, which is defined in relation to the acceleration $\mathbf{w}$ as specified in (3.35), yielding

$$\dot{\mathbf{y}}_\mathrm{s} = \begin{bmatrix} -\frac{\partial\mathbf{q}_{\mathrm{r,s}}}{\partial\theta_\mathrm{virt}} & \mathbf{I}_4 \end{bmatrix} \dot{\mathbf{q}}_\mathrm{s} + \underbrace{\left(\begin{bmatrix} -\frac{\partial\mathbf{q}_{\mathrm{r,s}}}{\partial\theta_\mathrm{virt}} & \mathbf{I}_4 \end{bmatrix} \mathbf{0} + \mathbf{0} \begin{bmatrix} -M^{-1}_{\mathrm{s},11}\mathbf{M}_{\mathrm{s},12} \\ \mathbf{I}_4 \end{bmatrix} \right)}_{=\mathbf{0}} \mathbf{w}\,. \tag{4.10}$$

Subsequently, the second Lie derivative is expressed as

$$\ddot{\mathbf{y}}_{\mathrm{s}} = \underbrace{\left(-\frac{\partial^2 \mathbf{q}_{\mathrm{r,s}}}{\partial \theta_{\mathrm{virt}}^2}\dot{\theta}_{\mathrm{virt}}^2 + \frac{\partial \mathbf{q}_{\mathrm{r,s}}}{\partial \theta_{\mathrm{virt}}} M_{\mathrm{s},11}^{-1}\Gamma_{\mathrm{s},1}\right)}_{\mathcal{L}_f^2 \mathbf{h}_{\mathrm{s}}(\mathbf{q}_{\mathrm{s}},\dot{\mathbf{q}}_{\mathrm{s}})} + \underbrace{\left(\mathbf{I}_4 + \frac{\partial \mathbf{q}_{\mathrm{r,s}}}{\partial \theta_{\mathrm{virt}}} M_{\mathrm{s},11}^{-1}\mathbf{M}_{\mathrm{s},12}\right)}_{\mathcal{L}_g \mathcal{L}_f \mathbf{h}_{\mathrm{s}}(\mathbf{q}_{\mathrm{s}})} \mathbf{w} \,. \tag{4.11}$$

Employing the feedback law detailed in (4.4), the acceleration $\mathbf{w}$ is derived as

$$\mathbf{w} = \left(\mathcal{L}_g \mathcal{L}_f \mathbf{h}_{\mathrm{s}}(\mathbf{q}_{\mathrm{s}})\right)^{-1} \left(\mathbf{v}_{\mathrm{s}} - \mathcal{L}_f^2 \mathbf{h}_{\mathrm{s}}(\mathbf{q}_{\mathrm{s}}, \dot{\mathbf{q}}_{\mathrm{s}})\right) \,, \tag{4.12}$$

under the assumption of an invertible decoupling matrix $\mathcal{L}_g \mathcal{L}_f \mathbf{h}_{\mathrm{s}}(\mathbf{q}_{\mathrm{s}})$ close to the equilibrium point $\boldsymbol{\eta}_{\mathrm{s},1}^0 = \mathbf{y}_{\mathrm{s}}^0 = \mathbf{0}$. Thereafter, the actuator $\mathbf{u} = \overline{\mathbf{M}}_{\mathrm{s,rg}}\mathbf{w} + \overline{\boldsymbol{\Gamma}}_{\mathrm{s,rg}}$ is delineated in alignment with the inverse dynamics as outlined in (3.32).

4.1.2 Zero Dynamics

In light of the hybrid dynamical attributes inherent in a periodic walking pattern, the corresponding zero dynamics exhibit both a continuous dynamical domain and a discontinuous transition mapping. Within this context, the zero dynamics are defined as hybrid invariant [1] if they are preserved under the continuous dynamics of the closed-loop system as well as the discrete impact mapping. Notably, hybrid invariance is essential in reducing the dimensionality of the full-order system dynamics to a simplified lower-order representation within the zero dynamics.

Continuous Invariance

Dynamics of the closed-loop system at the equilibrium point $\boldsymbol{\eta}_{\mathrm{s},1}^0 = \mathbf{0}$ form the zero dynamics manifold $\mathcal{Z}_{\mathrm{s,r}}$, defined as

$$\mathcal{Z}_{\mathrm{s,r}} := \{\mathbf{x}_{\mathrm{s}} \in T\mathcal{Q}_{\mathrm{s},0} | \, \mathbf{h}_{\mathrm{s}}(\mathbf{x}_{\mathrm{s}}) = \mathbf{0}, \mathcal{L}_{\tilde{f}} \mathbf{h}_{\mathrm{s}}(\mathbf{x}_{\mathrm{s}}) = \mathbf{0}\} \,, \tag{4.13}$$

which is a two-dimensional submanifold embedded in $T\mathcal{Q}_{\mathrm{s},0}$. Thus, the equilibrium point $\mathbf{y}_{\mathrm{s}}^0 = \mathbf{h}_{\mathrm{s}}(\mathbf{x}_{\mathrm{s}}^0) = \mathbf{0}$ of the linearized subsystem aligns with an equivalent equilibrium point $\mathbf{x}_{\mathrm{s}}^0$ of the vector field $\tilde{X}_{\mathrm{s,r}}(\mathbf{x}_{\mathrm{s}}, \mathbf{u})$ with $\mathbf{x}_{\mathrm{s}} \in T\mathcal{Q}_{\mathrm{s},0}$ of the closed-loop system.

[1] [177, Section 4.4] asserts that "hybrid invariance" arises under conditions in which a submanifold remains both forward invariant and impact invariant. Continuous invariance, as termed in this thesis, pertains to forward invariance. This work further extends the notion of impact invariance, herein referred to as discontinuous invariance, to encompass a broader spectrum of discontinuous transitions, including phenomena such as take-off and landing that are characteristic of running gaits.

By employing the local coordinates $\boldsymbol{\xi}_\mathrm{s} := [\xi_{\mathrm{s},1}, \xi_{\mathrm{s},2}]^\top \in \mathcal{Z}_{\mathrm{s,r}}$, the system states $\mathbf{x}_\mathrm{s} \in T\mathcal{Q}_{\mathrm{s},0}$ within the SSP state space are ascertained through the inverse mapping Ψ_s^{-1} of the diffeomorphism, articulated as

$$\mathbf{x}_\mathrm{s}\Big|_{\mathcal{Z}_{\mathrm{s,r}}} = \begin{bmatrix}\mathbf{q}_\mathrm{s}\\ \dot{\mathbf{q}}_\mathrm{s}\end{bmatrix}\Bigg|_{\mathcal{Z}_{\mathrm{s,r}}} = \Psi_\mathrm{s}^{-1}\left(\begin{bmatrix}\boldsymbol{\eta}_{\mathrm{s},1} = \mathbf{0}\\ \boldsymbol{\eta}_{\mathrm{s},2} = \mathbf{0}\\ \boldsymbol{\xi}_\mathrm{s}\end{bmatrix}\right)\Bigg|_{\boldsymbol{\xi}_\mathrm{s}\in\mathcal{Z}_{\mathrm{s,r}}} . \tag{4.14}$$

The process of implementing linearizing state feedback at the equilibrium point $\boldsymbol{\eta}_{\mathrm{s},1}^0 = \mathbf{0}$ is realized through the assumption of a negligible feedback error $\mathbf{v}_\mathrm{s} = -\mathbf{K}_{\mathrm{p,s}}\mathbf{y}_\mathrm{s}^0 - \mathbf{K}_{\mathrm{d,s}}\dot{\mathbf{y}}_\mathrm{s}^0 = \mathbf{0}$ within the context of expression (4.4), consequently leading to

$$\mathbf{u}_\mathrm{s}^0 := \mathbf{u}_\mathrm{s}(\mathbf{q}_\mathrm{s}, \dot{\mathbf{q}}_\mathrm{s})\Big|_{\mathcal{Z}_{\mathrm{s,r}}} = -\left(\mathcal{L}_{\tilde{g}}\mathcal{L}_{\tilde{f}}\mathbf{h}_\mathrm{s}(\mathbf{q}_\mathrm{s})\right)^{-1}\mathcal{L}_{\tilde{f}}^2\mathbf{h}_\mathrm{s}(\mathbf{q}_\mathrm{s}, \dot{\mathbf{q}}_\mathrm{s})\Big|_{\mathcal{Z}_{\mathrm{s,r}}} . \tag{4.15}$$

By adhering to the rationale elucidated in [79, p. 170] and utilizing the expression outlined in [177, Equation (5.36)], the feedback $\mathbf{u}_\mathrm{s}^0$ guarantees that the vector field $\dot{\mathbf{x}}_\mathrm{s}^0 = \tilde{\mathbf{f}}_\mathrm{s}(\mathbf{x}_\mathrm{s}^0) + \tilde{\mathbf{g}}_\mathrm{s}(\mathbf{x}_\mathrm{s}^0)\mathbf{u}_\mathrm{s}^0$ is tangential to the zero dynamics manifold $\mathcal{Z}_{\mathrm{s,r}}$, residing within the nullspace of the gradient $(\partial\mathbf{h}_\mathrm{s}/\partial\mathbf{x}_\mathrm{s})$ of the constraint surface, thereby aligning with the expression $\mathcal{L}_{\tilde{f}}\mathbf{h}_\mathrm{s}(\mathbf{x}_\mathrm{s}^0) = (\partial\mathbf{h}_\mathrm{s}/\partial\mathbf{x}_\mathrm{s})\big|_{\mathbf{x}_\mathrm{s}=\mathbf{x}_\mathrm{s}^0}\dot{\mathbf{x}}_\mathrm{s}^0 = \mathbf{0}$ in (4.13), as illustrated in Figure 4.2.

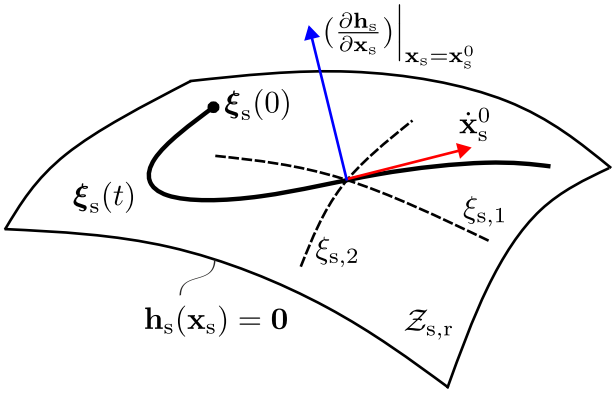

Figure 4.2: Representation of the invariant zero dynamics manifold $\mathcal{Z}_{\mathrm{s,r}}$, in which the red arrow indicates the tangent vector $\dot{\mathbf{x}}_\mathrm{s}^0$ of a solution curve $\boldsymbol{\xi}_\mathrm{s}(t)$, whereas the blue arrow represents the gradient of the virtual constraints surface orthogonal to $\dot{\mathbf{x}}_\mathrm{s}^0$.

Consequently, a trajectory $\boldsymbol{\xi}_\mathrm{s}(t)$ initialized at the condition $\boldsymbol{\xi}_\mathrm{s}(0) \in \mathcal{Z}_{\mathrm{s,r}}$ persists within $\mathcal{Z}_{\mathrm{s,r}}$ as time progresses, unfalteringly contained within the virtual constraints manifold. Hence, the zero dynamics maintain their invariance under the closed-loop dynamics. The continuous invariant zero dynamics describe the internal dynamics subsystem

within the equation system (4.8) and are expressed in the local coordinates $\boldsymbol{\xi}_\mathrm{s} := [\xi_{\mathrm{s},1}, \xi_{\mathrm{s},2}]^\top \in \mathcal{Z}_{\mathrm{s,r}}$ as a set of ordinary differential equations:

$$\begin{bmatrix} \dot{\xi}_{\mathrm{s},1} \\ \dot{\xi}_{\mathrm{s},2} \end{bmatrix} = \mathbf{f}_{\mathrm{s,ZD}}(\boldsymbol{\xi}_\mathrm{s}) := \begin{bmatrix} \mathcal{L}_{\tilde{f}} \xi_{\mathrm{s},1}(\mathbf{x}_\mathrm{s}) \\ \mathcal{L}_{\tilde{f}} \xi_{\mathrm{s},2}(\mathbf{x}_\mathrm{s}) \end{bmatrix} \Bigg|_{\mathcal{Z}_{\mathrm{s,r}}} = \begin{bmatrix} \kappa_{\mathrm{s},1}(\xi_{\mathrm{s},1})\xi_{\mathrm{s},2} \\ \kappa_{\mathrm{s},2}(\xi_{\mathrm{s},1}) \end{bmatrix}, \tag{4.16}$$

in which the formulations $\kappa_{\mathrm{s},1}(\xi_{\mathrm{s},1})$ and $\kappa_{\mathrm{s},2}(\xi_{\mathrm{s},1})$ bear resemblance to those documented in the scholarly literature [175, Equations (28)-(29)].

Discontinuous Invariance

The discrete impact mapping within the state space as delineated in (3.38) constitutes a one-dimensional submanifold $\mathcal{Z}_{\mathrm{s,r}} \cap \mathcal{S}_\mathrm{s}$ embedded in $T\mathcal{Q}_{\mathrm{s},0}$. By employing local coordinates $\boldsymbol{\xi}_\mathrm{s}^- \in \mathcal{Z}_{\mathrm{s,r}} \cap \mathcal{S}_\mathrm{s}$ on the impact surface, the impact mapping is expressed in the form

$$\boldsymbol{\xi}_\mathrm{s}^+ = \begin{bmatrix} c_\theta(\mathbf{x}_\mathrm{s}^+) \\ c_\sigma(\mathbf{x}_\mathrm{s}^+) \end{bmatrix} \Bigg|_{\mathcal{Z}_{\mathrm{s,r}}} = \boldsymbol{\Delta}_{\mathrm{w,i}}^{\mathrm{HZD}}(\boldsymbol{\xi}_\mathrm{s}^-) := \begin{bmatrix} c_\theta(\boldsymbol{\Delta}_{\mathrm{w,i}}(\mathbf{x}_\mathrm{s}^-)) \\ c_\sigma(\boldsymbol{\Delta}_{\mathrm{w,i}}(\mathbf{x}_\mathrm{s}^-)) \end{bmatrix} \Bigg|_{\mathcal{Z}_{\mathrm{s,r}} \cap \mathcal{S}_\mathrm{s}}, \tag{4.17}$$

where the system states $\mathbf{x}_\mathrm{s}^- = \Psi_\mathrm{s}^{-1}([\mathbf{0}^\top, \mathbf{0}^\top, (\boldsymbol{\xi}_\mathrm{s}^-)^\top]^\top)$ are derived from the diffeomorphism in (4.14). $\boldsymbol{\xi}_\mathrm{s}^+$ signifies the zero dynamics coordinates post-impact, thereby providing the initial conditions for the subsequent step period.
The formation of a periodic solution within the hybrid zero dynamics requires that the post-impact states $\boldsymbol{\xi}_\mathrm{s}^+ \in \mathcal{Z}_{\mathrm{s,r}}$ remain confined within the zero dynamics manifold $\mathcal{Z}_{\mathrm{s,r}}$, i.e., $\boldsymbol{\Delta}_{\mathrm{w,i}}^{\mathrm{HZD}}(\mathcal{Z}_{\mathrm{s,r}} \cap \mathcal{S}_\mathrm{s}) \in \mathcal{Z}_{\mathrm{s,r}}$, which exhibits discontinuous invariance upon impact. The impact surface is defined by the guard condition function $g_{-,\mathrm{HZD}}^+ : \mathcal{Z}_{\mathrm{s,r}} \to \mathbb{R}$ expressed as

$$g_{-,\mathrm{HZD}}^+(\boldsymbol{\xi}_\mathrm{s}) := g_-^+(\mathbf{x}_\mathrm{s}) \Big|_{\mathcal{Z}_{\mathrm{s,r}}} = 0, \tag{4.18}$$

obtained by assessing $g_-^+(\mathbf{x}_\mathrm{s})$ in the context of expression (3.38) on the zero dynamics manifold $\mathcal{Z}_{\mathrm{s,r}}$.
The resolution of the impact mapping (4.17), particularly the associated linear equation system (3.19), necessitates the application of a numerical factorization method, specifically LU decomposition, thereby precluding the acquisition of a closed-form solution. Considering that the generalized momentum $\xi_{\mathrm{s},2} = \sigma_\mathrm{s}$ relative to the stance foot serves as the second local coordinate within the zero dynamics framework, an alternative formulation of the impact mapping is consequently developed by utilizing

the conservation of generalized momentum with respect to the impact point during the impact, as indicated in [177, Section (3.5.5)].
In particular, the former swing foot collides with the rigid ground and thus serves as the impact pivot. Adopting the notation in Section 3.1.1, the angular momentum with respect to the impact point is indicated as $\sigma_{s,2}^-$ for before and $\sigma_{s,2}^+$ for after impact, respectively. $\sigma_{s,2}^-$ is determined by applying the equation [177, Equation (3.107)], yielding

$$\sigma_{s,2}^- = \sigma_{s,1}^- - m_{tot} \left((r_{2,z}(\mathbf{x}_s) - r_{1,z}(\mathbf{x}_s))\dot{x}_{CM}(\mathbf{x}_s) - (r_{2,x}(\mathbf{x}_s) - r_{1,x}(\mathbf{x}_s))\dot{z}_{CM}(\mathbf{x}_s) \right) \Big|_{\mathcal{Z}_{s,r} \cap \mathcal{S}_s} . \quad (4.19)$$

where m_{tot} is the total mass of the robot. Resulting from swapping the leading and trailing legs, the initial generalized momentum σ_s^+ for the new step period is determined by the angular momentum $\sigma_{s,2}$ around the impact point, i.e. $\sigma_s^+ = \sigma_{s,2}^+ = \sigma_{s,2}^-$.
Additionally, the remaining zero dynamics coordinate $\xi_{s,1} = \theta_{virt}$ is resolved in closed form through the relabeling of the coordinates.

Hybrid Invariant Zero Dynamics

Analogous to the methodology presented in [175, Equation (37)], the hybrid zero dynamics pertaining to gait with an instantaneous double support phase on rigid terrain are articulated within the state-space framework as comprehensively described in

$$\Sigma_{w,i}^{HZD} : \begin{cases} \dot{\xi}_s = \mathbf{f}_{s,ZD}(\xi_s) , & \xi_s^- \notin \mathcal{Z}_{s,r} \cap \mathcal{S}_s , \\ \xi_s^+ = \Delta_{w,i}^{HZD}(\xi_s^-) , & \xi_s^- \in \mathcal{Z}_{s,r} \cap \mathcal{S}_s , \end{cases} \quad (4.20)$$

with illustrations provided in Figure 4.3.

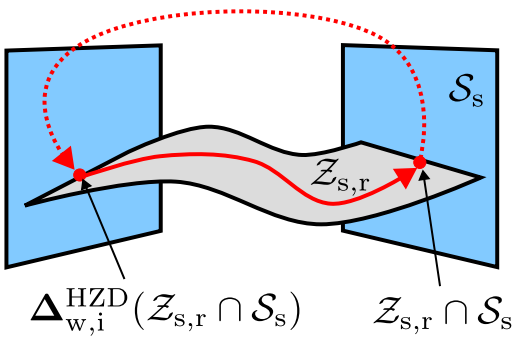

Figure 4.3: The zero dynamics manifold during the single support phase and the transition surface are depicted. A solid line represents the solution curve within the continuous domain, whereas a dashed line denotes the discrete transition mapping.

In accordance with the definition provided in [177, Section 4.1.2], the solution $\xi_s(t) = \mathbf{\Phi}_{w,i}(\xi_s^-, t)$ of the hybrid dynamical system (4.20), which encompasses impulsive effects, is represented as a trajectory within $\mathcal{Z}_{s,r}$, with its initial condition $\xi_s(t = 0) = \mathbf{\Phi}_{w,i}(\xi_s^-, t = 0) = \xi_s^-$ specified on the impact surface $\mathcal{S}_s$.
The discrete transition in the state variable, as induced by the impact mapping and denoted as $\xi_s^+ = \Delta_{w,i}^{HZD}(\xi_s^-)$, is initially executed. Subsequently, a right-continuous solution curve $\mathbf{\Phi}_{s,ZD}(\xi_s^+, t)$ of the vector field $\mathbf{f}_{s,ZD}(\xi_s)$ within the continuous dynamical domain is obtained through numerical integration, considering the initial condition ξ_s^+ post-impact.
The impact time t_s is characterized by the satisfaction of the guard condition referenced in (4.18), specifically $g_{-,HZD}^+(\xi_s(t_s)) = 0$. Given the assumption that the impact mapping occurs instantaneously, the impact time t_s is equivalent to the step duration specified in $t_{step} = t_s$. Periodic solutions that comply with condition $\mathbf{\Phi}_{w,i}(\xi_s^-, t) = \mathbf{\Phi}_{w,i}(\xi_s^-, t + t_s)$ are discerned through a multiple shooting technique analogous to the methodology outlined in [68].

4.1.3 Orbital Stability

In Chapter 7, numerical optimization is employed to ascertain periodic orbits within hybrid zero dynamics. As introduced in Section 2.4.3, the assessment of orbital stability is conducted using Floquet theory and the Poincaré return map.

Floquet Theory

Given a periodic orbit of the hybrid zero dynamics with period t_s obtained through optimization, the associated monodromy matrix $\mathbf{D}_{w,i}$ is articulated in compliance with [3] as

$$\mathbf{D}_{w,i} := \frac{\partial \mathbf{\Phi}_{w,i}(\xi_s^-, t_s)}{\partial \xi_s^-} = \underbrace{\left.\frac{\partial \mathbf{\Phi}_{s,ZD}(\xi_s^+, t)}{\partial \xi_s^+}\right|_{t=t_s}}_{\mathbf{F}_s(t_s)} \mathbf{C}_s(\xi_s^-) \ . \tag{4.21}$$

For a solution $\mathbf{\Phi}_{s,ZD}(\xi_s^+, t)$ with the specified initial condition ξ_s^+ within the continuous domain delineated in (4.20), the fundamental matrix solution $\mathbf{F}_s(t) = \partial \mathbf{\Phi}_{s,ZD}(\xi_s^+, t) / \partial \xi_s^+$ is computed via numerical integration of the variational equation $\dot{\mathbf{F}}_s = (\partial \mathbf{f}_{s,ZD} / \partial \xi_s) \mathbf{F}_s$, employing the initial condition $\mathbf{F}_s(t = 0) = \mathbf{I}_2$.
Alternatively, $\mathbf{F}_s(t_s)$ can be ascertained by computing the partial derivative of $\mathbf{\Phi}_{s,ZD}(\xi_s^+, t_s)$ with respect to the initial condition $\mathbf{\Phi}_{s,ZD}(\xi_s^+, 0) = \xi_s^+$ utilizing an Automatic Differentiation algorithm.

An additional factor to consider is that the state variation experiencing the discontinuous impact mapping $\xi_s^+ = \Delta_{w,i}^{HZD}(\xi_s^-)$ is approximated to the first order by the saltation matrix $\mathbf{C}_s(\xi_s^-)$, as defined according to [92] as

$$\mathbf{C}_s(\xi_s^-) = \frac{\partial \Delta_{w,i}^{HZD}(\xi_s^-)}{\partial \xi_s^-} + \frac{\left(\mathbf{f}_{s,ZD}(\xi_s^+) - \frac{\partial \Delta_{w,i}^{HZD}(\xi_s^-)}{\partial \xi_s^-}\mathbf{f}_{s,ZD}(\xi_s^-)\right)\frac{\partial g_{-,HZD}^+}{\partial \xi_s}\Big|_{\xi_s=\xi_s^-}}{\frac{\partial g_{-,HZD}^+}{\partial \xi_s}\Big|_{\xi_s=\xi_s^-}\mathbf{f}_{s,ZD}(\xi_s^-)}. \tag{4.22}$$

Taking into account the normal vector $\mathbf{n}_-^+(\xi_s) := (\partial g_{-,HZD}^+ \big/ \partial \xi_s)$ to the impact surface, the requirement $\mathbf{n}_-^+(\xi_s^-)\mathbf{f}_{s,ZD}(\xi_s^-) \neq 0$, $\xi_s^- \in \mathcal{Z}_{s,r} \cap \mathcal{S}_s$ within the expression (4.22) is met if the periodic solution $\xi_s(t)$ approaches the impact surface in a transverse fashion, a condition assumed in [177, Section 4.1] for bipedal locomotion.
According to Floquet theory, as expounded in [122, Section 3.2], the monodromy matrix $\mathbf{D}_{w,i}$ conveys the perturbations $\delta\xi_s$ in the system state ξ_s from the commencement of the period to its termination, i.e., $\delta\xi_s(t_s) = \mathbf{D}_{w,i}\,\delta\xi_s(0)$, as illustrated in Figure 4.4.

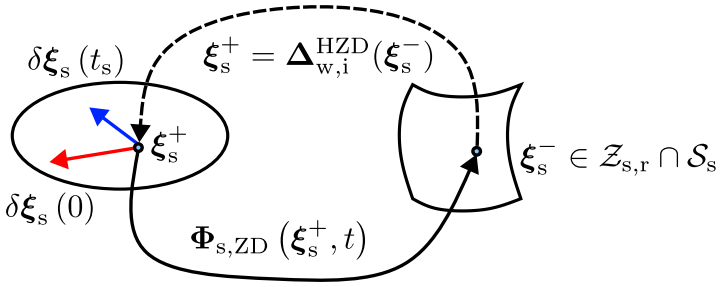

Figure 4.4: A periodic trajectory of the hybrid zero dynamics related to locomotion. The initial perturbation, denoted by the red arrow $\delta\xi_s(0)$, is applied to the state variables ξ_s^+ and subsequently mapped into the perturbation $\delta\xi_s(t_s)$ (indicated in blue) after the completion of one period t_s.

Analyzing the eigenvalues of the monodromy matrix $\mathbf{D}_{w,i}$, termed Floquet multipliers, elucidates the orbital stability of the periodic solution. Specifically, a $(n \times n)$-dimensional monodromy matrix encompasses n Floquet multipliers: one trivial multiplier $\Lambda_0 = 1$, which signifies the phase shift in the direction of the flow and does not influence orbital stability; and $n-1$ nontrivial multipliers, which signify perturbations perpendicular to the orbit and determine local orbital stability.
Given that the tangent vector $\mathbf{f}_{s,ZD}(\xi_s^-)$ of the solution curve serves as the eigenvector of $\mathbf{D}_{w,i}$ associated with the trivial multiplier $\Lambda_0 = 1$, the utilization of the projection

$$\hat{\mathbf{D}}_{w,i} = \mathbf{P}_{w,i}\mathbf{D}_{w,i}\mathbf{P}_{w,i} \tag{4.23}$$

facilitates the reduction of the monodromy matrix $\mathbf{D}_{\mathrm{w,i}}$ within the subspace orthogonal to the tangent vector $\mathbf{f}_{\mathrm{s,ZD}}(\xi_{\mathrm{s}}^{-})$ of the trajectory, thereby nullifying the influence of the trivial multiplier $\Lambda_0 = 1$. The symmetric orthogonal projector $\mathbf{P}_{\mathrm{w,i}}$, denoted by

$$\mathbf{P}_{\mathrm{w,i}} := \left(\mathbf{I}_2 - \frac{\mathbf{f}_{\mathrm{s,ZD}}(\xi_{\mathrm{s}}^{-}) \mathbf{f}_{\mathrm{s,ZD}}(\xi_{\mathrm{s}}^{-})^{\top}}{\mathbf{f}_{\mathrm{s,ZD}}(\xi_{\mathrm{s}}^{-})^{\top} \mathbf{f}_{\mathrm{s,ZD}}(\xi_{\mathrm{s}}^{-})} \right), \tag{4.24}$$

is thoroughly examined in [15, Chapter 7].
The projection transforms the (2×2)-dimensional matrix $\hat{\mathbf{D}}_{\mathrm{w,i}}$ into a structure of rank one, resulting in a nullity of one, which corresponds to the dimensionality of the matrix's nullspace (solutions to $\hat{\mathbf{D}}_{\mathrm{w,i}}\mathbf{x} = \mathbf{0}$). Consequently, one eigenvalue is zero, whereas the other [2], linked with the nontrivial multiplier Λ, characterizes the evolution of the state perturbations orthogonal to the flow. The periodic orbit remains stable provided that the magnitude of Λ is less than one, i.e., $|\Lambda| < 1$.

Poincaré Return Map

As introduced in [163, Section 8.7], the Poincaré return map $\mathcal{P}_{\mathrm{w}} : \mathcal{Z}_{\mathrm{s,r}} \cap \mathcal{S}_{\mathrm{s}} \to \mathcal{Z}_{\mathrm{s,r}} \cap \mathcal{S}_{\mathrm{s}}$; $\xi_{\mathrm{s}}^{-} \mapsto \mathcal{P}_{\mathrm{w}}(\xi_{\mathrm{s}}^{-})$ offers an alternative approach for calculating the Floquet multipliers of a periodic orbit. A fixed point $\xi_{\mathrm{s}}^{*} = \mathcal{P}_{\mathrm{w}}(\xi_{\mathrm{s}}^{*})$ denotes a periodic orbit.
Specifically, the Poincaré return map $\mathcal{P}_{\mathrm{w}}$ is determined through numerical integration using event detection techniques due to the impact. The associated Jacobian $\partial \mathcal{P}_{\mathrm{w}}(\xi_{\mathrm{s}}^{*}) / \partial \xi_{\mathrm{s}}^{*}$ of the Poincaré map is computed by employing an automatic differentiation algorithm, which requires extensive evaluations. Consequently, the Poincaré return map method is solely utilized to validate the resulting Floquet multiplier via the monodromy matrix and is not incorporated into the optimization framework for generating the reference gait.

4.2 Walking with Non-Instantaneous DSP

Consequent to the virtual actuator projection as delineated in (3.66), the overactuated non-instantaneous DSP is converted into a fully actuated model, wherein three degrees of freedom are regulated by three independent virtual actuators. In particular, two virtual actuators are applied to establish virtual constraints on the independent joints $\mathbf{q}_{\mathrm{di}}$, as detailed in Section 3.3.1, thereby aligning them with the reference trajectory $\mathbf{q}_{\mathrm{r,d}}(\theta_{\mathrm{virt}})$. The additional virtual actuator serves a supplementary control purpose aimed

[2] Considering that the matrix $\hat{\mathbf{D}}_{\mathrm{w,i}}$ is of dimension 2×2 and exhibits a nullity of one, the unique non-zero eigenvalue is equal to the trace $\mathrm{tr}(\hat{\mathbf{D}}_{\mathrm{w,i}})$ of $\hat{\mathbf{D}}_{\mathrm{w,i}}$.

at improving gait stability, which is developed in accordance with the methodology described in [177, Section 10.4].
The reference trajectory necessitates a vector-valued mapping $\mathbf{q}_{\mathrm{r,d}} : S^1 \to \mathbb{T}^2;\ \theta_{\mathrm{virt}} \mapsto \mathbf{q}_{\mathrm{r,d}}(\theta_{\mathrm{virt}})$ that articulates the intended angular progression through sixth-order Bézier polynomials. Specifically, the phase-dependent trajectory $\mathbf{q}_{\mathrm{r,d}}(\theta_{\mathrm{virt}})$ is constructed with respect to the orientation θ_{virt} of the virtual leg as its independent variable, due to θ_{virt} exhibiting a monotonic progression throughout the DSP.

4.2.1 Feedback Control in Fully Actuated DSP

Thereafter, the synchronization $\mathbf{h}_{\mathrm{d}}(\mathbf{q}_{\mathrm{d}})$ with $\mathbf{h}_{\mathrm{d}} : \mathcal{Q}_{\mathrm{d}} \to \mathbb{R}^2$ achieved through feedback control is regarded as holonomic virtual constraints, articulated as a function of the coordinates $\mathbf{q}_{\mathrm{d}} \in \mathcal{Q}_{\mathrm{d}}$. This approach concludes with the articulation of the control output $\mathbf{y}_{\mathrm{d}}$, as delineated by

$$\mathbf{y}_{\mathrm{d}} := \mathbf{h}_{\mathrm{d}}(\mathbf{q}_{\mathrm{d}}) = \mathbf{q}_{\mathrm{di}} - \mathbf{q}_{\mathrm{r,d}}(\theta_{\mathrm{virt}})\,. \tag{4.25}$$

In subsequent steps, two Lie derivatives are applied to control output (4.25) along the vector field $\tilde{X}_{\mathrm{d,f}}(\mathbf{x}_{\mathrm{d}}, \tilde{\mathbf{u}}_{(3)})$ of the virtually fully actuated DSP, as delineated in (3.71), resulting in

$$\dot{\mathbf{y}}_{\mathrm{d}} = \mathcal{L}_{\tilde{f},\mathrm{f}}\mathbf{h}_{\mathrm{d}}(\mathbf{q}_{\mathrm{d}}, \dot{\mathbf{q}}_{\mathrm{d}}) := \begin{bmatrix} -\frac{\partial \mathbf{q}_{\mathrm{r,d}}}{\partial \theta_{\mathrm{virt}}} & \mathbf{I}_2 \end{bmatrix} \dot{\mathbf{q}}_{\mathrm{d}}\,, \tag{4.26a}$$

$$\begin{aligned}\ddot{\mathbf{y}}_{\mathrm{d}} = {} & \underbrace{\left(-\frac{\partial^2 \mathbf{q}_{\mathrm{r,d}}}{\partial \theta_{\mathrm{virt}}^2} \dot{\theta}_{\mathrm{virt}}^2 - \begin{bmatrix} -\frac{\partial \mathbf{q}_{\mathrm{r,d}}}{\partial \theta_{\mathrm{virt}}} & \mathbf{I}_2 \end{bmatrix} \mathbf{M}_{\mathrm{d},(3)}^{-1} \boldsymbol{\Gamma}_{\mathrm{d},(3)} \right)}_{\mathcal{L}^2_{\tilde{f},\mathrm{f}}\mathbf{h}_{\mathrm{d}}(\mathbf{q}_{\mathrm{d}}, \dot{\mathbf{q}}_{\mathrm{d}})} \\ & + \underbrace{\left(\begin{bmatrix} -\frac{\partial \mathbf{q}_{\mathrm{r,d}}}{\partial \theta_{\mathrm{virt}}} & \mathbf{I}_2 \end{bmatrix} \mathbf{M}_{\mathrm{d},(3)}^{-1} \tilde{\mathbf{B}}_{(3)} \begin{bmatrix} \mathbf{I}_2 \\ \mathbf{0} \end{bmatrix} \right)}_{\mathcal{L}_{\tilde{g},\mathrm{f}}\mathcal{L}_{\tilde{f},\mathrm{f}}\mathbf{h}_{\mathrm{d}}(\mathbf{q}_{\mathrm{d}})} \tilde{\mathbf{u}}_{(3),12} + \underbrace{\left(\begin{bmatrix} -\frac{\partial \mathbf{q}_{\mathrm{r,d}}}{\partial \theta_{\mathrm{virt}}} & \mathbf{I}_2 \end{bmatrix} \mathbf{M}_{\mathrm{d},(3)}^{-1} \tilde{\mathbf{B}}_{(3)} \begin{bmatrix} \mathbf{0} \\ 1 \end{bmatrix} \right)}_{\mathcal{L}_{\tilde{h},\mathrm{f}}\mathcal{L}_{\tilde{f},\mathrm{f}}\mathbf{h}_{\mathrm{d}}(\mathbf{q}_{\mathrm{d}})} \tilde{u}_{(3),3}\,.\end{aligned} \tag{4.26b}$$

The structure in (4.26) elucidates a vector-valued relative degree $\{r_{\mathrm{d},1}, r_{\mathrm{d},2}\} = \{2, 2\}$ between the input $\tilde{\mathbf{u}}_{(3),12}$ and the output $\mathbf{y}_{\mathrm{d}}$.
It is crucial to acknowledge that the two-dimensional output $\mathbf{y}_{\mathrm{d}}$ is simultaneously affected by three distinct virtual actuators $\tilde{\mathbf{u}}_{(3)}$. Specifically, the exclusion of the redundant actuator $\tilde{u}_{(3),3}$ within expression (4.26b) results in a configuration equivalent to a virtually underactuated DSP, a topic not addressed within this thesis but explored in [194]. Consequently, the actuators $\tilde{\mathbf{u}}_{(3),12}$ are identified as those responsible for enforcing the

virtual constraints (4.25), while the redundant actuator $\tilde{u}_{(3),3}$ is employed for additional control objectives to improve gait stability.

State Feedback for Linearization

The linearizable subsystem is characterized by the dynamics intrinsic to a double integrator that establishes a connection between the newly introduced system input $\mathbf{v}_\mathrm{d} := \ddot{\mathbf{y}}_\mathrm{d} \in \mathbb{R}^2$ and the output $\mathbf{y}_\mathrm{d}$. The state feedback associated with the linearization is articulated in

$$\tilde{\mathbf{u}}_{(3),12} = \left(\mathcal{L}_{\tilde{g},\mathrm{f}}\mathcal{L}_{\tilde{f},\mathrm{f}}\mathbf{h}_\mathrm{d}(\mathbf{q}_\mathrm{d})\right)^{-1}\left(\mathbf{v}_\mathrm{d} - \mathcal{L}^2_{\tilde{f},\mathrm{f}}\mathbf{h}_\mathrm{d}(\mathbf{q}_\mathrm{d},\dot{\mathbf{q}}_\mathrm{d}) - \mathcal{L}_{\tilde{h},\mathrm{f}}\mathcal{L}_{\tilde{f},\mathrm{f}}\mathbf{h}_\mathrm{d}(\mathbf{q}_\mathrm{d})\tilde{u}_{(3),3}\right), \tag{4.27}$$

and it is pertinent within an open subset $\mathcal{Q}_{\mathrm{d},0} \subset \mathcal{Q}_\mathrm{d}$ located near the equilibrium point $\mathbf{y}_\mathrm{d} = \mathbf{0}$, especially in regions where the decoupling matrix $\mathcal{L}_{\tilde{g},\mathrm{f}}\mathcal{L}_{\tilde{f},\mathrm{f}}\mathbf{h}_\mathrm{d}(\mathbf{q}_\mathrm{d}) \in \mathbb{R}^{2\times 2}$ remains non-singular. Therefore, the stabilization of the equilibrium point is achieved through the use of a high-gain PD-feedback as described in

$$\mathbf{v}_\mathrm{d} = -\mathbf{K}_{\mathrm{p,d}}\mathbf{y}_\mathrm{d} - \mathbf{K}_{\mathrm{d,d}}\dot{\mathbf{y}}_\mathrm{d}\,. \tag{4.28}$$

The proportional and derivative gain constants are fulfilled by positive definite matrices $\mathbf{K}_{\mathrm{p,d}}$ and $\mathbf{K}_{\mathrm{d,d}}$, each having a dimensionality of (2×2).

Coordinate Transformation for Linearization

The articulation of the two-dimensional internal dynamics is enabled by the coordinates $\boldsymbol{\xi}_\mathrm{d} := [\xi_{\mathrm{d},1}, \xi_{\mathrm{d},2}]^\top$, which are deliberately chosen to remain invariant with respect to the input $\tilde{\mathbf{u}}_{(3),12}$ in (4.27), that is, $\mathcal{L}_{\tilde{g},\mathrm{f}}\xi_{\mathrm{d},1} = 0$, $\mathcal{L}_{\tilde{g},\mathrm{f}}\xi_{\mathrm{d},2} = 0$, considering that the actuators $\tilde{\mathbf{u}}_{(3),12}$ are solely tasked with the enforcement of the virtual constraints for the coordinates $\mathbf{q}_{\mathrm{di}}$ in (4.25).
Notably, the orientation $\xi_{\mathrm{d},1} = \theta_\mathrm{virt}$ of the virtual leg functions as an independent coordinate, determined through a linear scalar function $c_{\theta,\mathrm{d}} : \mathcal{Q}_\mathrm{d} \to \mathbb{R}$, which is expressed as

$$\theta_\mathrm{virt} = c_{\theta,\mathrm{d}}(\mathbf{q}_\mathrm{d}) := \begin{bmatrix}1 & \mathbf{0}\end{bmatrix}\mathbf{q}_\mathrm{d}\,. \tag{4.29}$$

The transformation matrix $\mathbf{H}_\mathrm{d}$, possessing full rank in expression (3.60), ensures the linear independence of the coordinate θ_virt with respect to the actuated joints $\mathbf{q}_{\mathrm{di}}$, and consequently, the output $\mathbf{h}_\mathrm{d}(\mathbf{q}_\mathrm{d})$.

The second coordinate pertaining to the internal dynamics, $\xi_{\mathrm{d},2} = \sigma_{\mathrm{d}}$, denotes the generalized momentum, as delineated in

$$\sigma_{\mathrm{d}} = c_{\sigma,\mathrm{d}}(\mathbf{q}_{\mathrm{d}}, \dot{\mathbf{q}}_{\mathrm{d}}) := \underbrace{\begin{bmatrix} 1 & \mathbf{0} \end{bmatrix} \mathbf{M}_{\mathrm{d},(3)}(\mathbf{q}_{\mathrm{d}})}_{\sigma_{\mathrm{d},0}(\mathbf{q}_{\mathrm{d}})} \dot{\mathbf{q}}_{\mathrm{d}} \,, \tag{4.30}$$

where $c_{\sigma,\mathrm{d}} : \mathcal{Q}_{\mathrm{d}} \times T_{\mathbf{q}_{\mathrm{d}}}\mathcal{Q}_{\mathrm{d}} \to \mathbb{R}$ constitutes a scalar function, and $\mathbf{M}_{\mathrm{d},(3)} = \mathbf{P}_{\tilde{\mathrm{G}},(3)}\mathbf{M}_{\mathrm{d}}$ refers to the inertia matrix as articulated in (3.66).
Consequently, the coordinate transformation Ψ_{d} elaborated in

$$\mathbf{z}_{\mathrm{d}} = \begin{bmatrix} \eta_{\mathrm{d},1} \\ \eta_{\mathrm{d},2} \\ \xi_{\mathrm{d},1} \\ \xi_{\mathrm{d},2} \end{bmatrix} = \Psi_{\mathrm{d}}(\mathbf{x}_{\mathrm{d}}) := \begin{bmatrix} \mathbf{h}_{\mathrm{d}}(\mathbf{q}_{\mathrm{d}}) \\ \mathcal{L}_{\tilde{f},\mathrm{f}}\mathbf{h}_{\mathrm{d}}(\mathbf{q}_{\mathrm{d}}, \dot{\mathbf{q}}_{\mathrm{d}}) \\ c_{\theta,\mathrm{d}}(\mathbf{q}_{\mathrm{d}}) \\ c_{\sigma,\mathrm{d}}(\mathbf{q}_{\mathrm{d}}, \dot{\mathbf{q}}_{\mathrm{d}}) \end{bmatrix} \,, \tag{4.31}$$

constitutes a diffeomorphism as per [2, p. 262], given that the Jacobian $\mathbf{J}_{\Psi,\mathrm{d}} := \partial\Psi_{\mathrm{d}}/\partial\mathbf{x}_{\mathrm{d}} = \begin{bmatrix} \partial\Psi_{\mathrm{d}}/\partial\mathbf{q}_{\mathrm{d}} \,, \partial\Psi_{\mathrm{d}}/\partial\dot{\mathbf{q}}_{\mathrm{d}} \end{bmatrix}$ is anticipated to maintain regularity as a result of the linear independence of the transformed coordinates, as evaluated in $\mathcal{Q}_{\mathrm{d},0}$.

Two-Stage Control Law

A comparable approach to zero the control output $\mathbf{y}_{\mathrm{d}}$ in (4.25) in the fully actuated DSP considers the acceleration $\mathbf{w}_{\mathrm{d}}$ as the system input. Consequently, the Lie derivatives of $\mathbf{y}_{\mathrm{d}}$ with respect to the vector field $X_{\mathrm{d,f}}(\mathbf{x}_{\mathrm{d}}, \mathbf{w}_{\mathrm{d}}, \tilde{u}_{(3),3})$ specified in (3.72) are executed, leading to

$$\dot{\mathbf{y}}_{\mathrm{d}} = \mathcal{L}_{f,\mathrm{f}}\mathbf{h}_{\mathrm{d}}(\mathbf{q}_{\mathrm{d}}, \dot{\mathbf{q}}_{\mathrm{d}}) := \begin{bmatrix} -\frac{\partial \mathbf{q}_{\mathrm{r,d}}}{\partial \theta_{\mathrm{virt}}} & \mathbf{I}_2 \end{bmatrix} \dot{\mathbf{q}}_{\mathrm{d}} \,, \tag{4.32a}$$

$$\ddot{\mathbf{y}}_{\mathrm{d}} = \underbrace{\left(-\frac{\partial \mathbf{q}_{\mathrm{r,d}}}{\partial \theta_{\mathrm{virt}}} M^{-1}_{\mathrm{d},(3),11} \tilde{B}_{(3),13} \right)}_{\mathcal{L}_{h,\mathrm{f}}\mathcal{L}_{f,\mathrm{f}}\mathbf{h}_{\mathrm{d}}(\mathbf{q}_{\mathrm{d}})} \tilde{u}_{(3),3} + \underbrace{\left(\mathbf{I}_2 + \frac{\partial \mathbf{q}_{\mathrm{r,d}}}{\partial \theta_{\mathrm{virt}}} M^{-1}_{\mathrm{d},(3),11} \mathbf{M}_{\mathrm{d},(3),12} \right)}_{\mathcal{L}_{g,\mathrm{f}}\mathcal{L}_{f,\mathrm{f}}\mathbf{h}_{\mathrm{d}}(\mathbf{q}_{\mathrm{d}})} \mathbf{w}_{\mathrm{d}}$$

$$+ \underbrace{\left(\frac{\partial \mathbf{q}_{\mathrm{r,d}}}{\partial \theta_{\mathrm{virt}}} M^{-1}_{\mathrm{d},(3),11} \Gamma_{\mathrm{d},(3),1} - \frac{\partial^2 \mathbf{q}_{\mathrm{r,d}}}{\partial \theta^2_{\mathrm{virt}}} \dot{\theta}^2_{\mathrm{virt}} \right)}_{\mathcal{L}^2_{f,\mathrm{f}}\mathbf{h}_{\mathrm{d}}(\mathbf{q}_{\mathrm{d}}, \dot{\mathbf{q}}_{\mathrm{d}})} \,. \tag{4.32b}$$

Feedback linearization is developed by implementing $\mathbf{v}_\mathrm{d} := \ddot{\mathbf{y}}_\mathrm{d}$ to establish a double-integrator behavior between $\mathbf{v}_\mathrm{d}$ and $\mathbf{y}_\mathrm{d}$, as delineated in

$$\mathbf{w}_\mathrm{d} = \left(\mathcal{L}_{g,\mathrm{f}}\mathcal{L}_{f,\mathrm{f}}\mathbf{h}_\mathrm{d}(\mathbf{q}_\mathrm{d})\right)^{-1}\left(\mathbf{v}_\mathrm{d} - \mathcal{L}_{f,\mathrm{f}}^2\mathbf{h}_\mathrm{d}(\mathbf{q}_\mathrm{d},\dot{\mathbf{q}}_\mathrm{d}) - \mathcal{L}_{h,\mathrm{f}}\mathcal{L}_{f,\mathrm{f}}\mathbf{h}_\mathrm{d}(\mathbf{q}_\mathrm{d})\tilde{u}_{(3),3}\right), \tag{4.33}$$

contingent upon the invertibility of the decoupling matrix $\mathcal{L}_{g,\mathrm{f}}\mathcal{L}_{f,\mathrm{f}}\mathbf{h}_\mathrm{d}(\mathbf{q}_\mathrm{d})$. The deployment of PD-feedback (4.28) facilitates asymptotic stability near the equilibrium point $\mathbf{y}_\mathrm{d} = \mathbf{0}$. The control methodology (4.39) prescribes the procedure for selecting the redundant actuator $\tilde{u}_{(3),3}$, which is integrated into the feedback configuration (4.33). Thereafter, inverse dynamics (3.68) are employed to ascertain the remaining virtual actuators $\tilde{\mathbf{u}}_{(3),12}$.

4.2.2 Zero Dynamics with Full Actuation

This section examines the internal dynamics and orbital stability of the fully actuated DSP. In particular, the employment of the redundant actuator $\tilde{u}_{(3),3}$ is crucial in modulating the internal zero dynamics of the fully actuated model, thereby improving the convergence rate of the periodic orbit generated for walking.

Continuous Invariance

The dynamics, constrained at the equilibrium point $\boldsymbol{\eta}_{\mathrm{d},1}^0 = \mathbf{0}$ as a consequence of the virtual constraints (4.25), form the zero dynamics manifold $\mathcal{Z}_\mathrm{d}$. This manifold is characterized by

$$\mathcal{Z}_\mathrm{d} := \{\mathbf{x}_\mathrm{d} \in T\mathcal{Q}_{\mathrm{d},0} \,|\, \mathbf{h}_\mathrm{d}(\mathbf{x}_\mathrm{d}) = \mathbf{0}, \mathcal{L}_{\tilde{f},\mathrm{f}}\mathbf{h}_\mathrm{d}(\mathbf{x}_\mathrm{d}) = \mathbf{0}\}, \tag{4.34}$$

and constitutes a two-dimensional submanifold embedded within $T\mathcal{Q}_{\mathrm{d},0}$. Considering the local coordinates $\boldsymbol{\xi}_\mathrm{d} := [\xi_{\mathrm{d},1}, \xi_{\mathrm{d},2}]^\top \in \mathcal{Z}_\mathrm{d}$, the system states $\mathbf{x}_\mathrm{d} \in T\mathcal{Q}_{\mathrm{d},0}$ within the DSP state space are determined via the inverse mapping Ψ_d^{-1} of the diffeomorphism, expressed as

$$\mathbf{x}_\mathrm{d}\Big|_{\mathcal{Z}_\mathrm{d}} = \begin{bmatrix}\mathbf{q}_\mathrm{d}\\ \dot{\mathbf{q}}_\mathrm{d}\end{bmatrix}\Bigg|_{\mathcal{Z}_\mathrm{d}} = \Psi_\mathrm{d}^{-1}\left(\begin{bmatrix}\boldsymbol{\eta}_{\mathrm{d},1} = \mathbf{0}\\ \boldsymbol{\eta}_{\mathrm{d},2} = \mathbf{0}\\ \boldsymbol{\xi}_\mathrm{d}\end{bmatrix}\right)\Bigg|_{\boldsymbol{\xi}_\mathrm{d}\in\mathcal{Z}_\mathrm{d}}. \tag{4.35}$$

The internal dynamics subsystem is delineated by the coordinates $\boldsymbol{\xi}_\mathrm{d} := [\xi_{\mathrm{d},1}, \xi_{\mathrm{d},2}]^\top$ and is regulated by the differential equations presented in

$$\dot{\xi}_{\mathrm{d},1} = \mathcal{L}_{\tilde{f},\mathrm{f}}\xi_{\mathrm{d},1} = \begin{bmatrix}1 & \mathbf{0}\end{bmatrix}\dot{\mathbf{q}}_\mathrm{d}\Big|_{\mathcal{Z}_\mathrm{d}}, \tag{4.36a}$$

$$\dot{\xi}_{\mathrm{d},2} = \underbrace{\left(\dot{\mathbf{q}}_{\mathrm{d}}^{\top} \frac{\partial \sigma_{\mathrm{d},0}(\mathbf{q}_{\mathrm{d}})^{\top}}{\partial \mathbf{q}_{\mathrm{d}}} \dot{\mathbf{q}}_{\mathrm{d}} - \Gamma_{\mathrm{d},(3),1}\right)\Big|_{\mathcal{Z}_{\mathrm{d}}}}_{\mathcal{L}_{\tilde{f},\mathrm{f}}\xi_{\mathrm{d},2}} + \underbrace{\tilde{B}_{(3),13}\Big|_{\mathcal{Z}_{\mathrm{d}}}}_{\mathcal{L}_{\tilde{h},\mathrm{f}}\xi_{\mathrm{d},2}} \tilde{u}_{(3),3} \,, \tag{4.36b}$$

which are derived through the application of the Lie derivative along the vector field $\tilde{X}_{\mathrm{d,f}}(\mathbf{x}_{\mathrm{d}}, \tilde{\mathbf{u}}_{(3)})$, as elucidated in (3.71). The impact of the actuators $\tilde{\mathbf{u}}_{(3),12} := [\tilde{u}_{(3),1}, \tilde{u}_{(3),2}]^{\top}$ is specifically nullified as a consequence of the stipulation $\mathcal{L}_{\tilde{g},\mathrm{f}}\xi_{\mathrm{d},1} = 0$, $\mathcal{L}_{\tilde{g},\mathrm{f}}\xi_{\mathrm{d},2} = 0$ during the selection of the coordinates $\boldsymbol{\xi}_{\mathrm{d}}$.

Control Law for Convergence Rate

The equations (4.36) that govern the partitioning of internal dynamics can be directly controlled by the redundant virtual actuator $\tilde{u}_{(3),3}$. Pursuant to the methodology presented in [177, Section 10.4.3], a supplementary control objective, besides that in (4.25), is formulated as

$$y_{\sigma_{\mathrm{d}}} = \sigma_{\mathrm{d}} - \sigma_{\mathrm{r,d}}(\theta_{\mathrm{virt}}) \,. \tag{4.37}$$

which is designed to influence the stability characteristics (convergence rate) of the periodic solution of the associated gait. In particular, the mapping $\sigma_{\mathrm{r,d}} : S^1 \to \mathbb{R}$; $\theta_{\mathrm{virt}} \mapsto \sigma_{\mathrm{r,d}}(\theta_{\mathrm{virt}})$ serves as a reference trajectory, with the purpose of modulating the generalized momentum σ_{d} as elucidated in (4.30) during the DSP. The reference trajectory treats the virtual leg angle θ_{virt} as an independent variable and is delineated through a sixth-order Bézier polynomial, whose parameters are regarded as optimization variables.

The objective of nullifying the control output $y_{\sigma_{\mathrm{d}}}$ can be effectively addressed by employing a simple proportional feedback mechanism,

$$\dot{y}_{\sigma_{\mathrm{d}}} = \dot{\sigma}_{\mathrm{d}} - \frac{\partial \sigma_{\mathrm{r,d}}}{\partial \theta_{\mathrm{virt}}} \dot{\theta}_{\mathrm{virt}} = -K_{\sigma_{\mathrm{d}}} y_{\sigma_{\mathrm{d}}} \,, \tag{4.38}$$

wherein $K_{\sigma_{\mathrm{d}}} > 0$ denotes the feedback gain characterized by a positive magnitude. This approach involves deriving the redundant virtual actuator $\tilde{u}_{(3),3}$ through the substitution of $\dot{\sigma}_{\mathrm{d}} = \dot{\xi}_{\mathrm{d},2}$ into the internal dynamics equation (4.36b), resulting in

$$\tilde{u}_{(3),3} = \left(\mathcal{L}_{\tilde{h},\mathrm{f}}\xi_{\mathrm{d},2}\right)^{-1} \left(\frac{\partial \sigma_{\mathrm{r,d}}}{\partial \theta_{\mathrm{virt}}} \dot{\theta}_{\mathrm{virt}} - K_{\sigma_{\mathrm{d}}} y_{\sigma_{\mathrm{d}}} - \mathcal{L}_{\tilde{f},\mathrm{f}}\xi_{\mathrm{d},2}\right) \,. \tag{4.39}$$

It is essential that the component $\mathcal{L}_{\tilde{h},\mathrm{f}}\xi_{\mathrm{d},2} := \tilde{B}_{(3),13}\big|_{\mathcal{Z}_{\mathrm{d}}}$ of the projection matrix $\tilde{\mathbf{B}}_{(3)}$, as delineated in (3.65), remains non-zero, thus guaranteeing the existence of a valid inverse in equation (4.39).

Consequently, upon substituting equation (4.36b) with the error dynamics in (4.38), the internal dynamics of the fully actuated DSP are governed by the ordinary differential equations $\dot{\boldsymbol{\xi}}_{\mathrm{d}} = \mathbf{f}_{\mathrm{d,ZD}}(\boldsymbol{\xi}_{\mathrm{d}})$, as evidenced in

$$\dot{\xi}_{\mathrm{d},1} = \begin{bmatrix} 1 & \mathbf{0} \end{bmatrix} \dot{\mathbf{q}}_{\mathrm{d}} \Big|_{\mathcal{Z}_{\mathrm{d}}} = \begin{bmatrix} 1 & \mathbf{0} \end{bmatrix} \begin{bmatrix} \frac{\partial \mathbf{h}_{\mathrm{d}}}{\partial \mathbf{q}_{\mathrm{d}}} \\ \boldsymbol{\sigma}_{\mathrm{d},0}(\mathbf{q}_{\mathrm{d}}) \end{bmatrix}^{-1} \Bigg|_{\mathcal{Z}_{\mathrm{d}}} \begin{bmatrix} \mathbf{0} \\ 1 \end{bmatrix} \xi_{\mathrm{d},2} \,, \tag{4.40a}$$

$$\dot{\xi}_{\mathrm{d},2} = \left(\frac{\partial \sigma_{\mathrm{r,d}}}{\partial \theta_{\mathrm{virt}}} \dot{\theta}_{\mathrm{virt}} - K_{\sigma_{\mathrm{d}}} y_{\sigma_{\mathrm{d}}} \right) \Big|_{\mathcal{Z}_{\mathrm{d}}} \,. \tag{4.40b}$$

Notably, the precise determination of the feedback gain value $K_{\sigma_{\mathrm{d}}}$ within equation (4.40b) significantly influences the solution curve.

Discontinuous Invariance

The discontinuous invariance is defined for both touch-down and lift-off events, as referenced in Section 3.3.2 and Section 3.3.3, respectively. In particular, the touch-down mapping (3.73) is defined on the surface $\mathcal{Z}_{\mathrm{s,r}} \cap \mathcal{S}_{\mathrm{s}}^{\mathrm{d}}$, which constitutes a one-dimensional submanifold embedded within $T\mathcal{Q}_{\mathrm{s},0}$. Utilizing the local coordinates $\boldsymbol{\xi}_{\mathrm{s}}^{-} \in \mathcal{Z}_{\mathrm{s,r}} \cap \mathcal{S}_{\mathrm{s}}^{\mathrm{d}}$, the mapping is articulated in the zero dynamics manifold as

$$\boldsymbol{\xi}_{\mathrm{d}}^{+} = \begin{bmatrix} c_{\theta,\mathrm{d}}\left(\mathbf{x}_{\mathrm{d}}^{+}\right) \\ c_{\sigma,\mathrm{d}}\left(\mathbf{x}_{\mathrm{d}}^{+}\right) \end{bmatrix} \Bigg|_{\mathcal{Z}_{\mathrm{d}}} = \boldsymbol{\Delta}_{\mathrm{TD}}^{\mathrm{HZD}}\left(\boldsymbol{\xi}_{\mathrm{s}}^{-}\right) := \begin{bmatrix} c_{\theta,\mathrm{d}}\left(\boldsymbol{\Delta}_{\mathrm{TD}}\left(\mathbf{x}_{\mathrm{s}}^{-}\right)\right) \\ c_{\sigma,\mathrm{d}}\left(\boldsymbol{\Delta}_{\mathrm{TD}}\left(\mathbf{x}_{\mathrm{s}}^{-}\right)\right) \end{bmatrix} \Bigg|_{\mathcal{Z}_{\mathrm{s,r}} \cap \mathcal{S}_{\mathrm{s}}^{\mathrm{d}}} \,, \tag{4.41}$$

where $\boldsymbol{\xi}_{\mathrm{d}}^{+} \in \mathcal{Z}_{\mathrm{d}}$ represents the local coordinates within the DSP zero dynamics submanifold, in accordance with the definitions in (4.29) and (4.30), respectively. Consequently, the condition $\boldsymbol{\Delta}_{\mathrm{TD}}^{\mathrm{HZD}}\left(\mathcal{Z}_{\mathrm{s,r}} \cap \mathcal{S}_{\mathrm{s}}^{\mathrm{d}}\right) \in \mathcal{Z}_{\mathrm{d}}$ evaluates the invariance of the solution to the touch-down mapping. The point at which the solution curve intersects the touch-down surface is ascertained by the guard function specified in (3.75), which is expressed in the zero dynamics coordinates $\boldsymbol{\xi}_{\mathrm{s}} \in \mathcal{Z}_{\mathrm{s,r}}$ as

$$g_{\mathrm{s,HZD}}^{\mathrm{d}}(\boldsymbol{\xi}_{\mathrm{s}}) := g_{\mathrm{s}}^{\mathrm{d}}(\mathbf{x}_{\mathrm{s}}) \Big|_{\mathcal{Z}_{\mathrm{s,r}}} = 0 \,. \tag{4.42}$$

Analogously, the lift-off mapping (3.74) is delineated on the surface $\mathcal{Z}_{\mathrm{d}} \cap \mathcal{S}_{\mathrm{d}}^{\mathrm{s}}$ at the termination of the DSP. The solution trajectory of the zero dynamics remains invariant with respect to the lift-off event under the condition $\boldsymbol{\Delta}_{\mathrm{LO}}^{\mathrm{HZD}}\left(\mathcal{Z}_{\mathrm{d}} \cap \mathcal{S}_{\mathrm{d}}^{\mathrm{s}}\right) \in \mathcal{Z}_{\mathrm{s,r}}$, where the

mapping $\Delta_{\mathrm{LO}}^{\mathrm{HZD}} : \mathcal{Z}_{\mathrm{d}} \cap \mathcal{S}_{\mathrm{d}}^{\mathrm{s}} \to \mathcal{Z}_{\mathrm{s,r}}$ is articulated using zero dynamics coordinates as described in

$$\xi_{\mathrm{s}}^{+} = \begin{bmatrix} c_\theta\left(\mathbf{x}_{\mathrm{s}}^{+}\right) \\ c_\sigma\left(\mathbf{x}_{\mathrm{s}}^{+}\right) \end{bmatrix}\Bigg|_{\mathcal{Z}_{\mathrm{s,r}}} = \Delta_{\mathrm{LO}}^{\mathrm{HZD}}\left(\xi_{\mathrm{d}}^{-}\right) := \begin{bmatrix} c_\theta\left(\Delta_{\mathrm{LO}}\left(\mathbf{x}_{\mathrm{d}}^{-}\right)\right) \\ c_\sigma\left(\Delta_{\mathrm{LO}}\left(\mathbf{x}_{\mathrm{d}}^{-}\right)\right) \end{bmatrix}\Bigg|_{\mathcal{Z}_{\mathrm{d}} \cap \mathcal{S}_{\mathrm{d}}^{\mathrm{s}}}, \tag{4.43}$$

The coordinates $\xi_{\mathrm{s}}^{+} \in \mathcal{Z}_{\mathrm{s,r}}$ are derived by assessing the transformation (4.5) and (4.6) on the zero dynamics manifold $\mathcal{Z}_{\mathrm{s,r}}$ within the SSP. The determination of whether the solution curve intersects the lift-off surface is accomplished through the application of the guard function defined in (3.76), as detailed in

$$g_{\mathrm{d,HZD}}^{\mathrm{s}}(\xi_{\mathrm{d}}) := g_{\mathrm{d}}^{\mathrm{s}}(\mathbf{x}_{\mathrm{d}})\Big|_{\mathcal{Z}_{\mathrm{d}}} = 0\,. \tag{4.44}$$

Hybrid Invariant Zero Dynamics

The hybrid zero dynamics model relevant to walking, characterized by a fully actuated non-instantaneous DSP, is constructed through the amalgamation of vector fields (4.16) and (4.40) within the zero dynamics manifolds of SSP and DSP, respectively. The transitions that maintain discontinuous invariance, as delineated in (4.41) and (4.43), are interposed between these two continuous phases. As a result, the comprehensive hybrid zero dynamics can be represented as follows:

$$\Sigma_{\mathrm{w,d}}^{\mathrm{HZD}} : \begin{cases} \dot{\xi}_{\mathrm{s}} = \mathbf{f}_{\mathrm{s,ZD}}(\xi_{\mathrm{s}})\,, & \xi_{\mathrm{s}}^{-} \notin \mathcal{Z}_{\mathrm{s,r}} \cap \mathcal{S}_{\mathrm{s}}^{\mathrm{d}}\,, \\ \xi_{\mathrm{d}}^{+} = \Delta_{\mathrm{TD}}^{\mathrm{HZD}}\left(\xi_{\mathrm{s}}^{-}\right)\,, & \xi_{\mathrm{s}}^{-} \in \mathcal{Z}_{\mathrm{s,r}} \cap \mathcal{S}_{\mathrm{s}}^{\mathrm{d}}\,, \\ \dot{\xi}_{\mathrm{d}} = \mathbf{f}_{\mathrm{d,ZD}}(\xi_{\mathrm{d}})\,, & \xi_{\mathrm{d}}^{-} \notin \mathcal{Z}_{\mathrm{d}} \cap \mathcal{S}_{\mathrm{d}}^{\mathrm{s}}\,, \\ \xi_{\mathrm{s}}^{+} = \Delta_{\mathrm{LO}}^{\mathrm{HZD}}\left(\xi_{\mathrm{d}}^{-}\right)\,, & \xi_{\mathrm{d}}^{-} \in \mathcal{Z}_{\mathrm{d}} \cap \mathcal{S}_{\mathrm{d}}^{\mathrm{s}}\,. \end{cases} \tag{4.45}$$

This system is defined as hybrid invariant if the zero dynamics ensure continuous invariance relative to the dynamics of the closed-loop system while demonstrating discontinuous invariance with respect to the transition mappings. The associated solution curve $\mathbf{\Phi}_{\mathrm{w,d}}\left(\xi_{\mathrm{s}}^{-}, t\right)$ consists of the trajectories $\mathbf{\Phi}_{\mathrm{s,ZD}}\left(\xi_{\mathrm{s}}^{+}, t\right)$ and $\mathbf{\Phi}_{\mathrm{d,ZD}}\left(\xi_{\mathrm{d}}^{+}, t\right)$ within the SSP and DSP domains, respectively.
Moreover, the intervals t_{s} within the SSP domain and t_{d} within the DSP domain are determined based on phase-dependent transition events. As a result, the step duration $t_{\mathrm{w,d}} = t_{\mathrm{s}} + t_{\mathrm{d}}$ is obtained by summing the intervals of these two domains. Periodic solutions that satisfy the condition $\mathbf{\Phi}_{\mathrm{w,d}}\left(\xi_{\mathrm{s}}^{-}, t\right) = \mathbf{\Phi}_{\mathrm{w,d}}\left(\xi_{\mathrm{s}}^{-}, t + t_{\mathrm{w,d}}\right)$ are identified through the employment of the multiple shooting method.

4.2.3 Orbital Stability with Full Actuation

The assessment of orbital stability for a periodic solution $\boldsymbol{\Phi}_{\mathrm{w,d}}(\xi_{\mathrm{s}}^{-}, t) = \boldsymbol{\Phi}_{\mathrm{w,d}}(\xi_{\mathrm{s}}^{-}, t + t_{\mathrm{w,d}})$ derived through optimization is conducted utilizing the monodromy matrix, as detailed in

$$\mathbf{D}_{\mathrm{w,d}} := \frac{\partial \boldsymbol{\Phi}_{\mathrm{w,d}}\left(\xi_{\mathrm{s}}^{-}, t_{\mathrm{w,d}}\right)}{\partial \xi_{\mathrm{s}}^{-}} = \mathbf{F}_{\mathrm{s}}\left(t_{\mathrm{s}}\right) \mathbf{C}_{\mathrm{d}}^{\mathrm{s}}\left(\xi_{\mathrm{d}}^{-}\right) \underbrace{\left.\frac{\partial \boldsymbol{\Phi}_{\mathrm{d,ZD}}\left(\xi_{\mathrm{d}}^{+}, t\right)}{\partial \xi_{\mathrm{d}}^{+}}\right|_{t=t_{\mathrm{d}}}}_{\mathbf{F}_{\mathrm{d}}(t_{\mathrm{d}})} \mathbf{C}_{\mathrm{s}}^{\mathrm{d}}\left(\xi_{\mathrm{s}}^{-}\right), \tag{4.46}$$

and demonstrated in Figure 4.5.

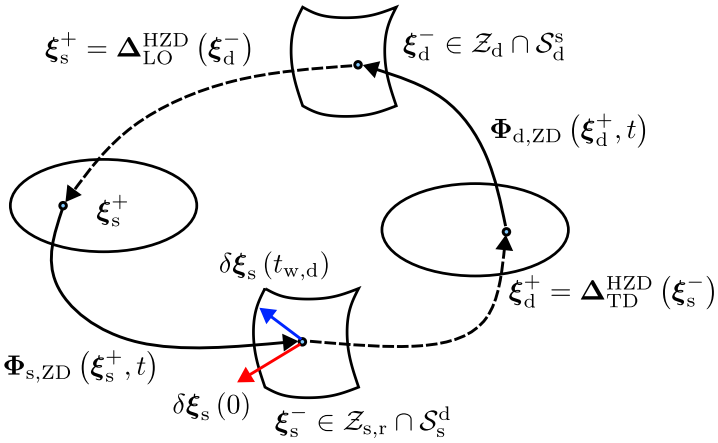

Figure 4.5: A periodic trajectory of the hybrid zero dynamics is depicted. The red and blue arrows represent the initial perturbation $\delta\xi_{\mathrm{s}}(0)$ at the touch-down surface and $\delta\xi_{\mathrm{s}}(t_{\mathrm{w,d}})$ following the completion of one period $t_{\mathrm{w,d}}$, respectively.

In this context, the fundamental matrix solution $\mathbf{F}_{\mathrm{s}}(t_{\mathrm{s}})$ is specified in equation (4.21). Analogously, $\mathbf{F}_{\mathrm{d}}(t) = \partial \boldsymbol{\Phi}_{\mathrm{d,ZD}}\left(\xi_{\mathrm{d}}^{+}, t\right) / \partial \xi_{\mathrm{d}}^{+}$ is ascertained via the variational equations $\dot{\mathbf{F}}_{\mathrm{d}} = (\partial \mathbf{f}_{\mathrm{d,ZD}} / \partial \xi_{\mathrm{d}}) \mathbf{F}_{\mathrm{d}}$, with initial conditions $\mathbf{F}_{\mathrm{d}}(t = 0) = \mathbf{I}_2$ applied in the DSP domain. The saltation matrices $\mathbf{C}_{\mathrm{d}}^{\mathrm{s}}\left(\xi_{\mathrm{d}}^{-}\right)$ and $\mathbf{C}_{\mathrm{s}}^{\mathrm{d}}\left(\xi_{\mathrm{s}}^{-}\right)$ are delineated as

$$\mathbf{C}_{\mathrm{d}}^{\mathrm{s}}\left(\xi_{\mathrm{d}}^{-}\right) := \frac{\partial \Delta_{\mathrm{LO}}^{\mathrm{HZD}}\left(\xi_{\mathrm{d}}^{-}\right)}{\partial \xi_{\mathrm{d}}^{-}} + \frac{\left(\mathbf{f}_{\mathrm{s,ZD}}\left(\xi_{\mathrm{s}}^{+}\right) - \frac{\partial \Delta_{\mathrm{LO}}^{\mathrm{HZD}}\left(\xi_{\mathrm{d}}^{-}\right)}{\partial \xi_{\mathrm{d}}^{-}} \mathbf{f}_{\mathrm{d,ZD}}(\xi_{\mathrm{d}}^{-})\right) \mathbf{n}_{\mathrm{d}}^{\mathrm{s}}(\xi_{\mathrm{d}}^{-})}{\mathbf{n}_{\mathrm{d}}^{\mathrm{s}}(\xi_{\mathrm{d}}^{-}) \mathbf{f}_{\mathrm{d,ZD}}(\xi_{\mathrm{d}}^{-})}, \tag{4.47a}$$

$$\mathbf{C}_{\mathrm{s}}^{\mathrm{d}}\left(\xi_{\mathrm{s}}^{-}\right) := \frac{\partial \Delta_{\mathrm{TD}}^{\mathrm{HZD}}\left(\xi_{\mathrm{s}}^{-}\right)}{\partial \xi_{\mathrm{s}}^{-}} + \frac{\left(\mathbf{f}_{\mathrm{d,ZD}}\left(\xi_{\mathrm{d}}^{+}\right) - \frac{\partial \Delta_{\mathrm{TD}}^{\mathrm{HZD}}\left(\xi_{\mathrm{s}}^{-}\right)}{\partial \xi_{\mathrm{s}}^{-}} \mathbf{f}_{\mathrm{s,ZD}}(\xi_{\mathrm{s}}^{-})\right) \mathbf{n}_{\mathrm{s}}^{\mathrm{d}}(\xi_{\mathrm{s}}^{-})}{\mathbf{n}_{\mathrm{s}}^{\mathrm{d}}(\xi_{\mathrm{s}}^{-}) \mathbf{f}_{\mathrm{s,ZD}}(\xi_{\mathrm{s}}^{-})}, \tag{4.47b}$$

wherein the normal vectors $\mathbf{n}_{\mathrm{d}}^{\mathrm{s}}(\xi_{\mathrm{d}}) := (\partial g_{\mathrm{d,HZD}}^{\mathrm{s}} \big/ \partial \xi_{\mathrm{d}})$ associated with the lift-off surface and $\mathbf{n}_{\mathrm{s}}^{\mathrm{d}}(\xi_{\mathrm{s}}) := (\partial g_{\mathrm{s,HZD}}^{\mathrm{d}} \big/ \partial \xi_{\mathrm{s}})$ related to the touch-down surface.
The singularity in the division mentioned in (4.47) is precluded when the trajectory $\mathbf{\Phi}_{\mathrm{w,d}}(\xi_{\mathrm{s}}^{-}, t)$ intersects the transition surfaces transversally, as articulated by

$$\mathbf{n}_{\mathrm{s}}^{\mathrm{d}}(\xi_{\mathrm{s}}^{-})\mathbf{f}_{\mathrm{s,ZD}}(\xi_{\mathrm{s}}^{-}) \neq 0, \qquad \xi_{\mathrm{s}}^{-} \in \mathcal{Z}_{\mathrm{s,r}} \cap \mathcal{S}_{\mathrm{s}}^{\mathrm{d}}\,, \tag{4.48a}$$

$$\mathbf{n}_{\mathrm{d}}^{\mathrm{s}}(\xi_{\mathrm{d}}^{-})\mathbf{f}_{\mathrm{d,ZD}}(\xi_{\mathrm{d}}^{-}) \neq 0, \qquad \xi_{\mathrm{d}}^{-} \in \mathcal{Z}_{\mathrm{d}} \cap \mathcal{S}_{\mathrm{d}}^{\mathrm{s}}\,. \tag{4.48b}$$

From a physical standpoint, condition (4.48a) stipulates that the velocity of the swing leg foot remains non-zero as it approaches ground contact. Furthermore, condition (4.48b) posits that the velocity $\dot{\theta}_{\mathrm{virt}}\big|_{\mathcal{Z}_{\mathrm{s,r}} \cap \mathcal{S}_{\mathrm{s}}^{\mathrm{d}}} \neq 0$ of the virtual leg does not reduce to zero when the controller initiates the lift-off of the trailing stance leg.
Owing to the inherent characteristics of the autonomous system, the eigenvector associated with the trivial eigenvalue $\Lambda_0 = 1$ is aligned with the tangent vector $\mathbf{f}_{\mathrm{s,ZD}}(\xi_{\mathrm{s}}^{-})$ of the trajectory. Consequently, the implementation of an orthogonal projection via the projector $\mathbf{P}_{\mathrm{w,d}}$, delineated as

$$\hat{\mathbf{D}}_{\mathrm{w,d}} = \mathbf{P}_{\mathrm{w,d}}\mathbf{D}_{\mathrm{w,d}}\mathbf{P}_{\mathrm{w,d}}\,, \text{ with } \quad \mathbf{P}_{\mathrm{w,d}} := \left(\mathbf{I}_2 - \frac{\mathbf{f}_{\mathrm{s,ZD}}(\xi_{\mathrm{s}}^{-})\mathbf{f}_{\mathrm{s,ZD}}(\xi_{\mathrm{s}}^{-})^{\top}}{\mathbf{f}_{\mathrm{s,ZD}}(\xi_{\mathrm{s}}^{-})^{\top}\mathbf{f}_{\mathrm{s,ZD}}(\xi_{\mathrm{s}}^{-})}\right)\,, \tag{4.49}$$

serves to effectively negate the impact of the trivial multiplier $\Lambda_0 = 1$. The remaining nontrivial multiplier $\Lambda = \mathrm{tr}(\hat{\mathbf{D}}_{\mathrm{w,d}})$ is associated with the trace of the projected monodromy matrix $\hat{\mathbf{D}}_{\mathrm{w,d}}$, attributable to the nullity of one. A periodic solution is classified as stable if the magnitude of the multiplier $|\Lambda| < 1$ is less than one.

5 Model for Bipedal Running

The periodic running gait of a bipedal robot model is articulated through a sequence of alternating single support and flight phases. Within prevailing scholarly discussions, as indicated in [177], the ground surface is conventionally presumed to be rigid. This presumption is employed to focus on the macroscopic dynamics of the robotic model during its running locomotion. The transition from the flight phase to the single support phase is thus described by a discontinuous, inelastic impact mapping. The assumption of no slipping during contact with the rigid ground allows for a reduction in the dimensionality of the equations of motion of the robot model, thereby streamlining the procedure for gait generation. Notably, the single support phase of running is analogous to that of walking, as elucidated in Chapter 3.

To accurately simulate running gaits on compliant surfaces, where ground deformation is pronounced and the contact period is extended, the contact procedure in the single support phase is augmented by implementing a compliant viscoelastic model, as succinctly introduced in Section 2.3.2.

The foundation of this chapter, rooted in the dynamical model of bipedal running on rigid surfaces as elucidated in Section 5.1, enables a thorough examination of the expanded model outlined in Section 5.2, which addresses running on compliant surfaces.

5.1 Running on Rigid Ground

As depicted in Figure 5.1, running gaits consist of two continuous dynamical phases and two discrete mappings. Specifically, the continuous single support phase (SSP) mirrors that of walking, as outlined in Section 3.2.1; the flight phase (FLP) is detailed in Section 5.1.1. Upon concluding the SSP, the system states transition to the FLP via the take-off event outlined in Section 5.1.2, which ends with the landing event discussed in Section 5.1.3; the state space expression is addressed in Section 5.1.4, regarding periodic running as alternating sequences: $\cdots \Rightarrow$ SSP $\Rightarrow$ take-off $\Rightarrow$ FLP $\Rightarrow$ landing $\Rightarrow \cdots$.

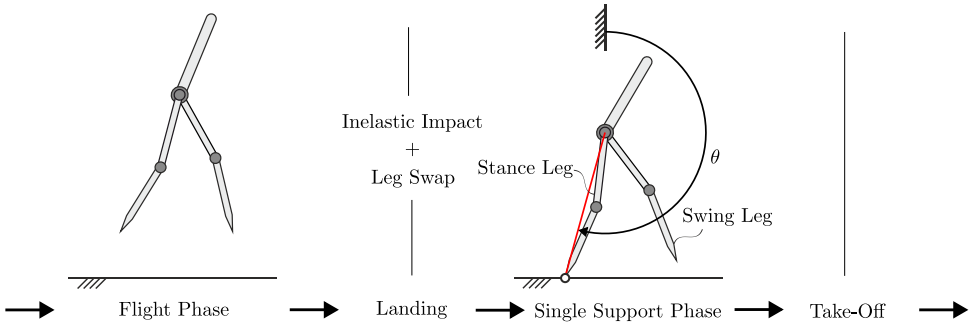

Figure 5.1: Periodic running gait on rigid ground. The red line delineates the virtual leg defined in the single support phase.

5.1.1 Flight Phase

In the FLP model, air drag is disregarded [1]. By setting the forces $\mathbf{F}_1$ and $\mathbf{F}_2$ in the free body dynamics equations (3.5) to zero, the equations of motion become

$$\mathbf{M}_{\mathrm{f}}(\mathbf{q}_{\mathrm{f}})\ddot{\mathbf{q}}_{\mathrm{f}} = -\boldsymbol{\Gamma}_{\mathrm{f}}(\mathbf{q}_{\mathrm{f}}, \dot{\mathbf{q}}_{\mathrm{f}}) + \mathbf{B}_{\mathrm{f}}\mathbf{u}\,. \tag{5.1}$$

The dynamics linked to $\mathbf{r}_{\mathrm{CM}}$ and θ_{HAT} cannot be controlled directly by the inputs $\mathbf{u}$. Decomposing the system of equations (5.1) yields

$$\mathbf{M}_{\mathrm{f},00}\ddot{\mathbf{r}}_{\mathrm{CM}} = m_{\mathrm{total}}\ddot{\mathbf{r}}_{\mathrm{CM}} = -\boldsymbol{\Gamma}_{\mathrm{f},0} = -\begin{bmatrix} 0 \\ m_{\mathrm{total}}g \end{bmatrix}\,, \tag{5.2a}$$

$$M_{\mathrm{f},11}\ddot{\theta}_{\mathrm{HAT}} + \mathbf{M}_{\mathrm{f},12}\ddot{\mathbf{q}}_{\mathrm{b}} = -\Gamma_{\mathrm{f},1}\,, \tag{5.2b}$$

$$\mathbf{M}_{\mathrm{f},21}\ddot{\theta}_{\mathrm{HAT}} + \mathbf{M}_{\mathrm{f},22}\ddot{\mathbf{q}}_{\mathrm{b}} = -\boldsymbol{\Gamma}_{\mathrm{f},2} + \mathbf{u}\,. \tag{5.2c}$$

Especially in (5.2a), the mass matrix $\mathbf{M}_{\mathrm{f},00} = m_{\mathrm{total}}\mathbf{I}_2$ represents the total mass of the robot, while $\boldsymbol{\Gamma}_{\mathrm{f},0}$ embodies the gravitational effects. By eliminating $\ddot{\theta}_{\mathrm{HAT}}$ from equations (5.2b) and (5.2c), the inverse dynamics,

$$\mathbf{u} = \underbrace{\left(\mathbf{M}_{\mathrm{f},22} - \mathbf{M}_{\mathrm{f},21}M_{\mathrm{f},11}^{-1}\mathbf{M}_{\mathrm{f},12}\right)}_{\bar{\mathbf{M}}_{\mathrm{f}}}\mathbf{w} + \underbrace{\left(\boldsymbol{\Gamma}_{\mathrm{f},2} - \mathbf{M}_{\mathrm{f},21}M_{\mathrm{f},11}^{-1}\Gamma_{\mathrm{f},1}\right)}_{\bar{\boldsymbol{\Gamma}}_{\mathrm{f}}}\,, \tag{5.3}$$

is deduced. Consequently, the acceleration $\mathbf{w} := \ddot{\mathbf{q}}_{\mathrm{b}}$ is regarded as an input to the system within the FLP.

[1] In the preceding chapters, air drag was not factored into the analyses of single and double support phases of walking.

5.1.2 Take-Off

Considering the system states represented by position $\hat{\mathbf{q}}_s^-$ and velocity $\dot{\hat{\mathbf{q}}}_s^-$ of the SSP model just before take-off, position $\mathbf{r}_{CM}(\hat{\mathbf{q}}_s^-)$ and velocity $\dot{\mathbf{r}}_{CM}(\hat{\mathbf{q}}_s^-, \dot{\hat{\mathbf{q}}}_s^-)$ of the center of mass of the robot are determined as functions of $\hat{\mathbf{q}}_s^-$ and $\dot{\hat{\mathbf{q}}}_s^-$, in accordance with the kinematic relation (3.13) in the SSP.
It is postulated that during the take-off event, state variables undergo a seamless transition, leading to the mapping

$$\mathbf{q}_{f,f}^+ = \mathbf{q}_{f,s}^- := \begin{bmatrix} \mathbf{r}_{CM}(\hat{\mathbf{q}}_s^-) \\ \hat{\mathbf{q}}_s^- \end{bmatrix}, \qquad \dot{\mathbf{q}}_{f,f}^+ = \dot{\mathbf{q}}_{f,s}^- := \begin{bmatrix} \dot{\mathbf{r}}_{CM}(\hat{\mathbf{q}}_s^-, \dot{\hat{\mathbf{q}}}_s^-) \\ \dot{\hat{\mathbf{q}}}_s^- \end{bmatrix} = \begin{bmatrix} \frac{\partial \mathbf{r}_{CM}}{\partial \hat{\mathbf{q}}_s}\Big|_{\hat{\mathbf{q}}_s = \hat{\mathbf{q}}_s^-} \\ \mathbf{I}_4 \end{bmatrix} \dot{\hat{\mathbf{q}}}_s^-, \tag{5.4}$$

where the position $\mathbf{q}_{f,f}^+$ and velocity $\dot{\mathbf{q}}_{f,f}^+$ denote the system states in the FLP immediately subsequent to take-off, thereby establishing the initial conditions for the subsequent FLP.
Taking into account coordinate transformations $\hat{\mathbf{q}}_s^- = \mathbf{H}_s^{-1}\mathbf{q}_s^-$ and $\dot{\hat{\mathbf{q}}}_s^- = \mathbf{H}_s^{-1}\dot{\mathbf{q}}_s^-$, alongside the matrix $\mathbf{H}_s^{-1}$ as outlined in (3.27), the take-off mapping (5.4) is specified by

$$\mathbf{q}_{f,f}^+ = \boldsymbol{\Delta}_{TO,\mathbf{q}_{f,f}}(\mathbf{q}_s^-) := \begin{bmatrix} \mathbf{r}_{CM}(\mathbf{H}_s^{-1}\mathbf{q}_s^-) \\ \mathbf{H}_s^{-1}\mathbf{q}_s^- \end{bmatrix}, \tag{5.5a}$$

$$\dot{\mathbf{q}}_{f,f}^+ = \boldsymbol{\Delta}_{TO,\dot{\mathbf{q}}_{f,f}}(\mathbf{q}_s^-)\,\dot{\mathbf{q}}_s^- := \begin{bmatrix} \frac{\partial \mathbf{r}_{CM}}{\partial \hat{\mathbf{q}}_s}\Big|_{\hat{\mathbf{q}}_s = \mathbf{H}_s^{-1}\mathbf{q}_s^-} \\ \mathbf{I}_4 \end{bmatrix} \mathbf{H}_s^{-1}\dot{\mathbf{q}}_s^-. \tag{5.5b}$$

5.1.3 Landing

The FLP is terminated once a swing leg touches the rigid ground surface, which is modeled as an inelastic impact between the point foot and the ground. For expressing the mapping, position $\mathbf{q}_{f,f}^-$ and velocity $\dot{\mathbf{q}}_{f,f}^-$ are assigned for the last instance of the FLP, and $\mathbf{q}_{f,s}^+ := [\mathbf{r}_{CM}(\hat{\mathbf{q}}_s^+)^\top, (\hat{\mathbf{q}}_s^+)^\top]^\top$ and $\dot{\mathbf{q}}_{f,s}^+ := [\dot{\mathbf{r}}_{CM}(\hat{\mathbf{q}}_s^+, \dot{\hat{\mathbf{q}}}_s^+)^\top, (\dot{\hat{\mathbf{q}}}_s^+)^\top]^\top$ at the beginning of the subsequent SSP after landing.
Following the inelastic collision, the position coordinates $\mathbf{q}_{f,f}^- = \mathbf{q}_{f,s}^+$ remain unchanged, while the velocity $\dot{\mathbf{r}}_2 = \mathbf{G}_2(\mathbf{q}_{f,s}^+)\dot{\mathbf{q}}_{f,s}^+ = \mathbf{0}$ of the stance foot [2] is reduced to zero, as delineated by equation (3.18) established for walking with an instantaneous double support phase.

[2] The stance leg after landing is the former swing leg in the FLP. Thus, following the notations announced in Section 3.1.1, the foot is denoted with the index "2".

Considering that the momentum equation (3.17) applicable to walking is also relevant to running, the impact mapping is expressed analogously to the system of equations (3.19) as follows:

$$\underbrace{\begin{bmatrix} \mathbf{M}_\mathrm{f}(\mathbf{q}_{\mathrm{f,f}}^-) & -\mathbf{G}_2^\top \\ \mathbf{G}_2 & \mathbf{0} \end{bmatrix}}_{\mathbf{\Pi}_{\mathrm{r,lhs}}(\mathbf{q}_{\mathrm{f,f}}^-)} \begin{bmatrix} \dot{\mathbf{q}}_{\mathrm{f,s}}^+ \\ \hat{\mathbf{F}}_2 \end{bmatrix} = \underbrace{\begin{bmatrix} \mathbf{M}_\mathrm{f}(\mathbf{q}_{\mathrm{f,f}}^-) \\ \mathbf{0} \end{bmatrix}}_{\mathbf{\Pi}_{\mathrm{r,rhs}}(\mathbf{q}_{\mathrm{f,f}}^-)} \dot{\mathbf{q}}_{\mathrm{f,f}}^- \,. \tag{5.6}$$

The integration of the impact mapping (5.6) with the exchange of the leading and trailing legs facilitates the simulation of single stride intervals within the formulation of periodic gaits. This process involves coordinate transformations $\mathbf{q}_\mathrm{s}^+ = \mathbf{H}_\mathrm{s}\hat{\mathbf{q}}_\mathrm{s}^+$ and $\dot{\mathbf{q}}_\mathrm{s}^+ = \mathbf{H}_\mathrm{s}\hat{\dot{\mathbf{q}}}_\mathrm{s}^+$ as defined in (3.26), resulting in

$$\mathbf{q}_\mathrm{s}^+ = \mathbf{H}_\mathrm{s}\begin{bmatrix}\mathbf{0} & \mathbf{R}_-^+(5)\end{bmatrix}\mathbf{q}_{\mathrm{f,f}}^- \,, \qquad \dot{\mathbf{q}}_\mathrm{s}^+ = \mathbf{H}_\mathrm{s}\begin{bmatrix}\mathbf{0} & \mathbf{R}_-^+(5) & \mathbf{0}\end{bmatrix}\mathbf{\Pi}_{\mathrm{r,lhs}}^{-1}\mathbf{\Pi}_{\mathrm{r,rhs}}\dot{\mathbf{q}}_{\mathrm{f,f}}^- \,, \tag{5.7}$$

The specification of the (5×5)-dimensional relabeling matrix $\mathbf{R}_-^+(5)$ can be found in (3.21). The impact force,

$$\hat{\mathbf{F}}_2 := \begin{bmatrix}\hat{F}_{2,x} \\ \hat{F}_{2,z}\end{bmatrix} = \begin{bmatrix}\mathbf{0} & \mathbf{I}_2\end{bmatrix}\mathbf{\Pi}_{\mathrm{r,lhs}}^{-1}\mathbf{\Pi}_{\mathrm{r,rhs}}\dot{\mathbf{q}}_{\mathrm{f,f}}^- \,, \tag{5.8}$$

satisfies the conditions of static friction (with friction coefficient $\mu = 0.6$) and unilateral contact, yielding the inequality constraints

$$\mu\hat{F}_{2,z} > \hat{F}_{2,x} > -\mu\hat{F}_{2,z} \,, \tag{5.9a}$$

$$\hat{F}_{2,z} > 0 \,. \tag{5.9b}$$

5.1.4 State Space Expression

The continuous FLP in Section 5.1.1 as well as the discontinuous take-off in Section 5.1.2 and landing in Section 5.1.3 are formulated in state space.

FLP in State Space

Considering the second-order characteristics of the FLP dynamics as referenced in (5.1), the state space

$$\mathcal{X}_\mathrm{f} = T\mathcal{Q}_\mathrm{f} := \left\{[\mathbf{q}_\mathrm{f}^\top, \dot{\mathbf{q}}_\mathrm{f}^\top]^\top \mid \mathbf{q}_\mathrm{f} \in \mathcal{Q}_\mathrm{f}, \dot{\mathbf{q}}_\mathrm{f} \in T_{\mathbf{q}_\mathrm{f}}\mathcal{Q}_\mathrm{f} \subset \mathbb{R}^7\right\} \tag{5.10}$$

is represented by the tangent bundle of the configuration space $\mathcal{Q}_\mathrm{f}$. The input to the system is provided by either the acceleration $\mathbf{w} := \ddot{\mathbf{q}}_\mathrm{b}$ of the actuated joints or by the actuators $\mathbf{u}$.
As per the equations of motion that regulate the FLP dynamics as described in (5.1), the vector field $\tilde{X}_{\mathrm{f,r}}(\mathbf{x}_\mathrm{f}, \mathbf{u}) := \tilde{\mathbf{f}}_{\mathrm{f,r}}(\mathbf{x}_\mathrm{f}) + \tilde{\mathbf{g}}_{\mathrm{f,r}}(\mathbf{x}_\mathrm{f})\mathbf{u}$ is articulated in correlation with the state variables $\mathbf{x}_\mathrm{f} \in T\mathcal{Q}_\mathrm{f}$ and the actuators $\mathbf{u}$, as referenced in

$$\underbrace{\begin{bmatrix}\dot{\mathbf{q}}_\mathrm{f}\\ \ddot{\mathbf{q}}_\mathrm{f}\end{bmatrix}}_{\dot{\mathbf{x}}_\mathrm{f}} = \begin{bmatrix}\dot{\mathbf{q}}_\mathrm{f}\\ \mathbf{M}_\mathrm{f}^{-1}\left(-\boldsymbol{\Gamma}_\mathrm{f} + \mathbf{B}_\mathrm{f}\mathbf{u}\right)\end{bmatrix} = \underbrace{\begin{bmatrix}\dot{\mathbf{q}}_\mathrm{f}\\ -\mathbf{M}_\mathrm{f}^{-1}\boldsymbol{\Gamma}_\mathrm{f}\end{bmatrix}}_{\tilde{\mathbf{f}}_{\mathrm{f,r}}(\mathbf{x}_\mathrm{f})} + \underbrace{\begin{bmatrix}\mathbf{0}\\ \mathbf{M}_\mathrm{f}^{-1}\mathbf{B}_\mathrm{f}\end{bmatrix}}_{\tilde{\mathbf{g}}_{\mathrm{f,r}}(\mathbf{x}_\mathrm{f})}\mathbf{u}\,. \tag{5.11}$$

In an alternative approach, the vector field $X_{\mathrm{f,r}}(\mathbf{x}_\mathrm{f}, \mathbf{w}) := \mathbf{f}_{\mathrm{f,r}}(\mathbf{x}_\mathrm{f}) + \mathbf{g}_{\mathrm{f,r}}(\mathbf{x}_\mathrm{f})\mathbf{w}$ is constructed by employing the acceleration $\mathbf{w}$ as system input, as illustrated in

$$\underbrace{\begin{bmatrix}\dot{\mathbf{q}}_\mathrm{f}\\ \ddot{\mathbf{r}}_\mathrm{CM}\\ \ddot{\theta}_\mathrm{HAT}\\ \mathbf{w}\end{bmatrix}}_{\dot{\mathbf{x}}_\mathrm{f}} = \underbrace{\begin{bmatrix}\dot{\mathbf{q}}_\mathrm{f}\\ -\mathbf{M}_{\mathrm{f},00}^{-1}\boldsymbol{\Gamma}_{\mathrm{f},0}\\ -M_{\mathrm{f},11}^{-1}\Gamma_{\mathrm{f},1}\\ \mathbf{0}\end{bmatrix}}_{\mathbf{f}_{\mathrm{f,r}}(\mathbf{x}_\mathrm{f})} + \underbrace{\begin{bmatrix}\mathbf{0}\\ \mathbf{0}\\ -M_{\mathrm{f},11}^{-1}\mathbf{M}_{\mathrm{f},12}\\ \mathbf{I}_4\end{bmatrix}}_{\mathbf{g}_{\mathrm{f,r}}(\mathbf{x}_\mathrm{f})}\mathbf{w}\,, \tag{5.12}$$

where $\ddot{\mathbf{r}}_\mathrm{CM}$ and $\ddot{\theta}_\mathrm{HAT}$ are obtained from equations (5.2a) and (5.2b), respectively.

Discrete Mappings

The discrete transition mappings defined for running on rigid ground are expressed using state variables $\mathbf{x}_\mathrm{s} \in T\mathcal{Q}_\mathrm{s}$ in the SSP (Section 3.2.3) and $\mathbf{x}_\mathrm{f} \in T\mathcal{Q}_\mathrm{f}$ in the FLP (Section 5.1.4). Specifically, the take-off mapping in (5.5) is rewritten as

$$\mathbf{x}_\mathrm{f}^+ = \boldsymbol{\Delta}_\mathrm{TO}\left(\mathbf{x}_\mathrm{s}^-\right) := \begin{bmatrix}\boldsymbol{\Delta}_{\mathrm{TO},\mathbf{q}_\mathrm{f,f}}\left(\mathbf{q}_\mathrm{s}^-\right)\\ \boldsymbol{\Delta}_{\mathrm{TO},\dot{\mathbf{q}}_\mathrm{f,f}}\left(\mathbf{q}_\mathrm{s}^-\right)\dot{\mathbf{q}}_\mathrm{s}^-\end{bmatrix}\,, \tag{5.13}$$

with states $\mathbf{x}_\mathrm{s}^- := [(\mathbf{q}_\mathrm{s}^-)^\top, (\dot{\mathbf{q}}_\mathrm{s}^-)^\top]^\top$ before and $\mathbf{x}_\mathrm{f}^+ := [(\mathbf{q}_\mathrm{f}^+)^\top, (\dot{\mathbf{q}}_\mathrm{f}^+)^\top]^\top$ after take-off. The landing event, expressed as

$$\mathbf{x}_\mathrm{s}^+ = \boldsymbol{\Delta}_\mathrm{LD}\left(\mathbf{x}_\mathrm{f}^-\right) := \left[\mathbf{H}_\mathrm{s}\begin{bmatrix}\mathbf{0} & \mathbf{R}_-^+(5)\end{bmatrix} \quad \mathbf{H}_\mathrm{s}\begin{bmatrix}\mathbf{0} & \mathbf{R}_-^+(5) & \mathbf{0}\end{bmatrix}\boldsymbol{\Pi}_{\mathrm{r,lhs}}^{-1}\boldsymbol{\Pi}_{\mathrm{r,rhs}}\right]\begin{bmatrix}\mathbf{q}_\mathrm{f,f}^-\\ \dot{\mathbf{q}}_\mathrm{f,f}^-\end{bmatrix}\,. \tag{5.14}$$

maps the last states $\mathbf{x}_\mathrm{f}^- := [(\mathbf{q}_\mathrm{f}^-)^\top, (\dot{\mathbf{q}}_\mathrm{f}^-)^\top]^\top$ of the FLP to the initial states $\mathbf{x}_\mathrm{s}^+ := [(\mathbf{q}_\mathrm{s}^+)^\top, (\dot{\mathbf{q}}_\mathrm{s}^+)^\top]^\top$ of the SSP, according to (5.7).

Hybrid Dynamics in State Space

The derivation of a hybrid dynamical system elucidating the periodic running gait on rigid ground is achieved through the integration of the flow within the SSP, governed by the vector field (3.34) and the take-off mapping (5.13),

$$\Sigma_{\mathrm{r,SSP}}: \begin{cases} \dot{\mathbf{x}}_{\mathrm{s}} = \tilde{\mathbf{f}}_{\mathrm{s}}(\mathbf{x}_{\mathrm{s}}) + \tilde{\mathbf{g}}_{\mathrm{s}}(\mathbf{x}_{\mathrm{s}})\mathbf{u}\,, & \mathbf{x}_{\mathrm{s}} \notin \mathcal{S}_{\mathrm{s}}^{\mathrm{f}}\,, \\ \mathbf{x}_{\mathrm{f}}^{+} = \boldsymbol{\Delta}_{\mathrm{TO}}\left(\mathbf{x}_{\mathrm{s}}^{-}\right)\,, & \mathbf{x}_{\mathrm{s}}^{-} \in \mathcal{S}_{\mathrm{s}}^{\mathrm{f}}\,, \\ \mathcal{S}_{\mathrm{s}}^{\mathrm{f}} := \{\mathbf{x}_{\mathrm{s}} \in T\mathcal{Q}_{\mathrm{s}} |\; g_{\mathrm{s}}^{\mathrm{f}}(\mathbf{x}_{\mathrm{s}}) = 0\}\,, \end{cases} \tag{5.15}$$

as well as the flow within the FLP, regulated by the vector field (5.11) alongside the discrete landing event (5.14),

$$\Sigma_{\mathrm{r,FLP}}: \begin{cases} \dot{\mathbf{x}}_{\mathrm{f}} = \tilde{\mathbf{f}}_{\mathrm{f,r}}(\mathbf{x}_{\mathrm{f}}) + \tilde{\mathbf{g}}_{\mathrm{f,r}}(\mathbf{x}_{\mathrm{f}})\mathbf{u}\,, & \mathbf{x}_{\mathrm{f}} \notin \mathcal{S}_{\mathrm{f}}^{\mathrm{s}}\,, \\ \mathbf{x}_{\mathrm{s}}^{+} = \boldsymbol{\Delta}_{\mathrm{LD}}\left(\mathbf{x}_{\mathrm{f}}^{-}\right)\,, & \mathbf{x}_{\mathrm{f}}^{-} \in \mathcal{S}_{\mathrm{f}}^{\mathrm{s}}\,, \\ \mathcal{S}_{\mathrm{f}}^{\mathrm{s}} := \{\mathbf{x}_{\mathrm{f}} \in T\mathcal{Q}_{\mathrm{f}} |\; g_{\mathrm{f}}^{\mathrm{s}}(\mathbf{x}_{\mathrm{f}}) = 0, r_{2,x}(\mathbf{x}_{\mathrm{f}}) - r_{1,x}(\mathbf{x}_{\mathrm{f}}) > 0\}\,. \end{cases} \tag{5.16}$$

Within the context of the SSP expression (5.15), the transition surface $\mathcal{S}_{\mathrm{s}}^{\mathrm{f}}$ is encountered through the assessment of the guard function $g_{\mathrm{s}}^{\mathrm{f}}(\mathbf{x}_{\mathrm{s}}) := \begin{bmatrix}1 & \mathbf{0}\end{bmatrix}\mathbf{x}_{\mathrm{s}} - \theta_{\mathrm{TO}} = \theta_{\mathrm{virt}} - \theta_{\mathrm{TO}}$ with $g_{\mathrm{s}}^{\mathrm{f}} : T\mathcal{Q}_{\mathrm{s}} \to \mathbb{R}$, which is influenced by a controller parameter θ_{TO} that determines the exact (phase-dependent) moment for the robot to transition into the FLP. Consequently, θ_{TO} is considered a gait parameter to be optimized. Furthermore, the reaction force $\mathbf{F}_1 := [F_{1,x}, F_{1,z}]^{\top}$ exerted on the stance foot by the ground, as specified in equation (3.8), must be nullified, a condition maintained through constraints implemented within the numerical optimization process.
In relation to the FLP expression (5.16), the transition surface $\mathcal{S}_{\mathrm{f}}^{\mathrm{s}}$ is delineated by the moment at which the front foot, having previously functioned as the swing foot in the preceding SSP, makes contact with the ground surface, as indicated in the guard function $g_{\mathrm{f}}^{\mathrm{s}}(\mathbf{x}_{\mathrm{f}}) := r_{2,z}(\mathbf{x}_{\mathrm{f}})$ with $g_{\mathrm{f}}^{\mathrm{s}} : T\mathcal{Q}_{\mathrm{f}} \to \mathbb{R}$. Moreover, the touchdown position is required to be situated anterior to the preceding stance foot of the last SSP, as enforced by the inequality condition $r_{2,x}(\mathbf{x}_{\mathrm{f}}) - r_{1,x}(\mathbf{x}_{\mathrm{f}}) > 0$.

5.2 Running on Compliant Ground

As illustrated in Figure 5.2, running gaits on compliant surfaces are structured by alternating sequences of single support and flight phases. Notably, the flight phase is analogous to the case of running on rigid ground. The single support phase, however, is distinguished by contact with the compliant ground.

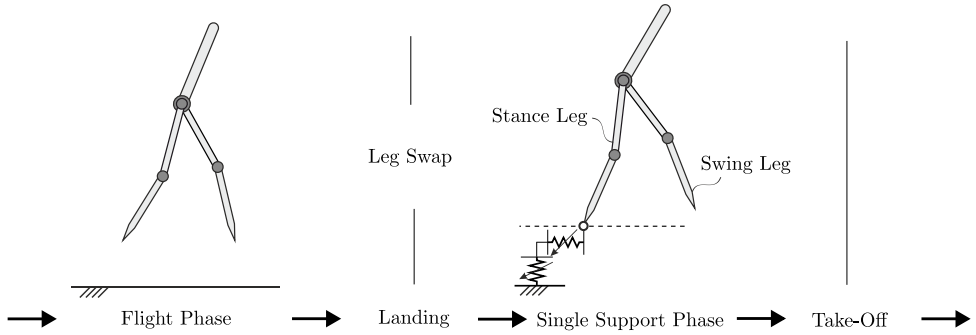

Figure 5.2: Periodic running gait on compliant ground.

In order to comprehensively address running gaits, this section is structured as follows: Section 5.2.1 delineates the contact model applicable to compliant ground surfaces; Section 5.2.2 elucidates the single support phase by considering the compliant contact at the stance foot; Section 5.2.3 examines the discrete take-off and landing events; Section 5.2.4 articulates the introduced models within a state space framework.

5.2.1 Compliant Contact Model

Section 2.3.2 provides a comprehensive overview of the formulation of compliant contact models found within the literature. For the purposes of the thesis study, two specific variations of the ground model are selected, in accordance with the investigations reported by Silva et al. in [155] and Carvalho et al. in [30]. Attributed to the kinematic relations inherent in the full-order system, the foot indentation $\boldsymbol{\delta}(\mathbf{q}_\mathrm{f})$ along with its time derivative $\dot{\boldsymbol{\delta}}(\mathbf{q}_\mathrm{f},\, \dot{\mathbf{q}}_\mathrm{f})$, are ascertained as functions reliant upon the state variables $\mathbf{q}_\mathrm{f}$ and $\dot{\mathbf{q}}_\mathrm{f}$, producing

$$F_{x,\mathrm{Silva}} := K_x \delta_x(\mathbf{q}_\mathrm{f}) + B_x \delta_z(\mathbf{q}_\mathrm{f}) \dot{\delta}_x(\mathbf{q}_\mathrm{f}, \dot{\mathbf{q}}_\mathrm{f}) \,, \tag{5.17a}$$

$$F_{z,\mathrm{Silva}} := K_z \delta_z(\mathbf{q}_\mathrm{f}) + B_z \left(\delta_z(\mathbf{q}_\mathrm{f})\right)^{0.9} \dot{\delta}_z(\mathbf{q}_\mathrm{f}, \dot{\mathbf{q}}_\mathrm{f}) \,, \tag{5.17b}$$

wherein, the nonlinear damping parameters B_x and B_z are accordingly derived from

$$B_x := \frac{\overline{B}_x}{\delta_{z,\max}} \,, \qquad B_z := \frac{\overline{B}_z}{(\delta_{z,\max})^{0.9}} \,, \tag{5.18}$$

serving as corrective terms to address nonlinear damping by employing linear damping parameters $\overline{B}_x = 625\,\mathrm{Nsm}^{-1}$ and $\overline{B}_z = 715\,\mathrm{Nsm}^{-1}$, in conjunction with stiffness $K_x = 43405\,\mathrm{Nm}^{-1}$ and $K_z = 56840\,\mathrm{Nm}^{-1}$, as specified for the material peat in [155, Table II]. $\delta_{z,\max}$ represents the maximum magnitude of the vertical indentation $\boldsymbol{\delta}_z$ occurring

within the contact period, ascertained through the application of the infinity-norm $\delta_{z,\max} = \|\boldsymbol{\delta}_z\|_\infty$.
As highlighted in [30], an intrinsic limitation of the normal force formulation as delineated in (5.17b) is its propensity to generate negative values. These values signify non-physical adhesive reaction forces emerging from the ground, predominantly attributable to numerical inaccuracies, especially when multiple forced contact points are simulated simultaneously. For the unilateral contact considered in this thesis, the issue of undesired adhesive forces is mitigated by employing the recommended formulation as proposed in [30, Equation (40)], given by

$$F_{z,\exp} := K_{\exp}\delta_z(\mathbf{q}_f)^\nu e^{\eta\,\dot{\delta}_z(\mathbf{q}_f,\dot{\mathbf{q}}_f)}\,, \tag{5.19}$$

wherein the exponential function ensures exclusively positive values. Parameters $K_{\exp}$, η, and ν are ascertained through the application of least-squares parameter fitting to align with the specified value in the model (5.17) and a nominal maximum magnitude $\delta_{z,\max}$ of ground penetration, as depicted in Figure 5.3.

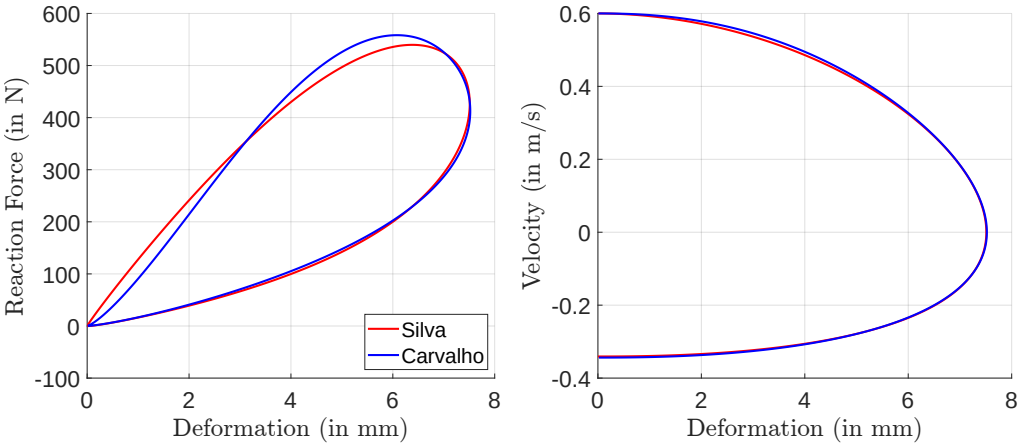

(a) Reaction force over deformation δ_z.

(b) Velocity $\dot{\delta}_z$ over deformation δ_z.

Figure 5.3: Parameter fitting to generate similar contact responces using models suggested by Silva in (5.17b) (in red) and by Carvalho in (5.19) (in blue).

5.2.2 Single Support Phase on Compliant Ground

The compliant contact law is derived from the models presented in Section 5.2.1, as articulated in

$$\mathbf{F}_1(\mathbf{q}_\mathrm{f}, \dot{\mathbf{q}}_\mathrm{f}) := \begin{bmatrix} F_{1,x}(\mathbf{q}_\mathrm{f}, \dot{\mathbf{q}}_\mathrm{f}) \\ F_{1,z}(\mathbf{q}_\mathrm{f}, \dot{\mathbf{q}}_\mathrm{f}) \end{bmatrix} = \begin{bmatrix} K_x \delta_x(\mathbf{q}_\mathrm{f}) + B_x \delta_z(\mathbf{q}_\mathrm{f}) \dot{\delta}_x(\mathbf{q}_\mathrm{f}, \dot{\mathbf{q}}_\mathrm{f}) \\ K_\mathrm{exp} \delta_z(\mathbf{q}_\mathrm{f})^\nu e^{\eta \dot{\delta}_z(\mathbf{q}_\mathrm{f}, \dot{\mathbf{q}}_\mathrm{f})} \end{bmatrix} , \tag{5.20}$$

concerning its application at the stance foot $\mathbf{r}_1(\mathbf{q}_\mathrm{f})$. In particular, the tangential and normal forces are derived from the formulations (5.17a) and (5.19), respectively, acknowledging that the tangential force may assume positive or negative values contingent upon the robot's motion, whereas the normal force is constrained to be positive.
By incorporating the reaction force $\mathbf{F}_1(\mathbf{q}_\mathrm{f}, \dot{\mathbf{q}}_\mathrm{f})$ of (5.20) into the free-body dynamics (3.5) via the principle of virtual work and eliminating the force $\mathbf{F}_2$ in the swing leg, the equations of motion are formulated as

$$\mathbf{M}_\mathrm{f}(\mathbf{q}_\mathrm{f})\ddot{\mathbf{q}}_\mathrm{f} = -\underbrace{\left(\boldsymbol{\Gamma}_\mathrm{f}(\mathbf{q}_\mathrm{f}, \dot{\mathbf{q}}_\mathrm{f}) - \mathbf{G}_1^\top \mathbf{F}_1(\mathbf{q}_\mathrm{f}, \dot{\mathbf{q}}_\mathrm{f})\right)}_{\boldsymbol{\Gamma}_\mathrm{cp}(\mathbf{q}_\mathrm{f}, \dot{\mathbf{q}}_\mathrm{f})} + \mathbf{B}_\mathrm{f}\mathbf{u} , \tag{5.21}$$

thereby resulting in an underactuated model. Specifically, three degrees of freedom, indicated by the coordinates $[\mathbf{r}_\mathrm{CM}^\top, \theta_\mathrm{HAT}]^\top$, are not directly governed by the actuators $\mathbf{u}$. The generalized forces $\boldsymbol{\Gamma}_\mathrm{f}$, along with the ground reaction $\mathbf{G}_1^\top \mathbf{F}_1$, are collectively represented using the abbreviation $\boldsymbol{\Gamma}_\mathrm{cp}(\mathbf{q}_\mathrm{f}, \dot{\mathbf{q}}_\mathrm{f})$, with the subscript "cp" indicating the compliant ground. The system of equations (5.21) is segmented into components as indicated in

$$\mathbf{M}_{\mathrm{f},00}\ddot{\mathbf{r}}_\mathrm{CM} = m_\mathrm{total}\ddot{\mathbf{r}}_\mathrm{CM} = -\begin{bmatrix} \mathbf{I}_2 & \mathbf{0} \end{bmatrix} \boldsymbol{\Gamma}_\mathrm{cp} , \tag{5.22a}$$

$$M_{\mathrm{f},11}\ddot{\theta}_\mathrm{HAT} + \mathbf{M}_{\mathrm{f},12}\ddot{\mathbf{q}}_\mathrm{b} = -\begin{bmatrix} \mathbf{0} & 1 & \mathbf{0} \end{bmatrix} \boldsymbol{\Gamma}_\mathrm{cp} , \tag{5.22b}$$

$$\mathbf{M}_{\mathrm{f},21}\ddot{\theta}_\mathrm{HAT} + \mathbf{M}_{\mathrm{f},22}\ddot{\mathbf{q}}_\mathrm{b} = -\begin{bmatrix} \mathbf{0} & \mathbf{I}_4 \end{bmatrix} \boldsymbol{\Gamma}_\mathrm{cp} + \mathbf{u} , \tag{5.22c}$$

wherein it elucidates the inverse dynamics of the SSP on compliant ground, as represented in

$$\mathbf{u} = \underbrace{\left(\mathbf{M}_{\mathrm{f},22} - \mathbf{M}_{\mathrm{f},21} M_{\mathrm{f},11}^{-1} \mathbf{M}_{\mathrm{f},12}\right)}_{\overline{\mathbf{M}}_\mathrm{cp}} \mathbf{w} + \underbrace{\left(\begin{bmatrix} \mathbf{0} & \mathbf{I}_4 \end{bmatrix} \boldsymbol{\Gamma}_\mathrm{cp} - \mathbf{M}_{\mathrm{f},21} M_{\mathrm{f},11}^{-1} \begin{bmatrix} \mathbf{0} & 1 & \mathbf{0} \end{bmatrix} \boldsymbol{\Gamma}_\mathrm{cp}\right)}_{\overline{\boldsymbol{\Gamma}}_\mathrm{cp}} . \tag{5.23}$$

Within this formulation, the actuator $\mathbf{u}$ is represented as a function of the acceleration $\mathbf{w} := \ddot{\mathbf{q}}_\mathrm{b}$, thereby serving as an alternative input to the system.

5.2.3 Take-Off and Landing on Compliant Ground

The interaction mechanism with a deformable ground surface is represented through the continuous dynamics of ground deformation, ensuring smooth transitions between system states during distinct take-off and landing events. In this context, simulation of a single step period exemplifies the periodic running gait, necessitating the interchange of roles between the front and trailing legs at the landing event.
The transition events are articulated with the following notation: the system states (position $\mathbf{q}_{\mathrm{f,f}}^{+}$ and velocity $\dot{\mathbf{q}}_{\mathrm{f,f}}^{+}$) are defined at the inception and ($\mathbf{q}_{\mathrm{f,f}}^{-}$, $\dot{\mathbf{q}}_{\mathrm{f,f}}^{-}$) at the conclusion of the FLP. Similarly, ($\mathbf{q}_{\mathrm{f,s}}^{+}$, $\dot{\mathbf{q}}_{\mathrm{f,s}}^{+}$) are defined at the commencement and ($\mathbf{q}_{\mathrm{f,s}}^{-}$, $\dot{\mathbf{q}}_{\mathrm{f,s}}^{-}$) at the termination of the SSP.
The continuous take-off event is delineated as

$$\mathbf{q}_{\mathrm{f,f}}^{+} = \mathbf{q}_{\mathrm{f,s}}^{-}\,, \qquad \dot{\mathbf{q}}_{\mathrm{f,f}}^{+} = \dot{\mathbf{q}}_{\mathrm{f,s}}^{-}\,, \tag{5.24}$$

and is followed by the exposition of the landing event as

$$\mathbf{q}_{\mathrm{f,s}}^{+} = \boldsymbol{\Delta}_{\mathrm{LD},\mathbf{q}_{\mathrm{f,s}}}(\mathbf{q}_{\mathrm{f,f}}^{-}) := \mathbf{R}_{-}^{+}(7)\mathbf{q}_{\mathrm{f,f}}^{-} - \begin{bmatrix} \mathbf{r}_{\mathrm{step}}(\mathbf{q}_{\mathrm{f,f}}^{-}) \\ \mathbf{0} \end{bmatrix}\,, \qquad \dot{\mathbf{q}}_{\mathrm{f,s}}^{+} = \mathbf{R}_{-}^{+}(7)\dot{\mathbf{q}}_{\mathrm{f,f}}^{-}\,. \tag{5.25}$$

The swapping of the front and trailing legs is achieved through the (7×7)-dimensional relabeling matrix $\mathbf{R}_{-}^{+}(7)$, defined as

$$\mathbf{R}_{-}^{+}(7) = \begin{bmatrix} \mathbf{I}_2 & \mathbf{0} \\ \mathbf{0} & \mathbf{R}_{-}^{+}(5) \end{bmatrix}\,, \tag{5.26}$$

with the (5×5)-dimensional $\mathbf{R}_{-}^{+}(5)$ as referenced in (3.21). The augmented matrix $\mathbf{R}_{-}^{+}(7)$ integrates two additional degrees of freedom, which are specified by the coordinates $\mathbf{r}_{\mathrm{CM}}$ of the center of mass. Furthermore, the displacement $\mathbf{r}_{\mathrm{step}}(\mathbf{q}_{\mathrm{f,f}}^{-})$ corresponding to one step period is deducted within the landing mapping to preserve periodic step sequences. Thus, more precisely, the expression "smooth transition" refers to the absence of sudden velocity variations during both the take-off and landing events. In the framework under consideration, discontinuities manifest as a result of the reset mechanism employed to maintain periodic gaits, as single step periods are simulated to generate the complete periodic gait. Conversely, when the simulation is arranged to accommodate sequences of multiple steps, the positional transitions display continuity across all discrete mappings.

5.2.4 State Space Expression

SSP in State Space

Within the state space manifold $\mathcal{X}_\mathrm{f} = T\mathcal{Q}_\mathrm{f}$, the equations of motion (5.21) define the vector field $\tilde{X}_\mathrm{cp}(\mathbf{x}_{\mathrm{f,s}}, \mathbf{u}) := \tilde{\mathbf{f}}_\mathrm{cp}(\mathbf{x}_{\mathrm{f,s}}) + \tilde{\mathbf{g}}_\mathrm{cp}(\mathbf{x}_{\mathrm{f,s}})\mathbf{u}$ in association with the state variables $\mathbf{x}_{\mathrm{f,s}} \in T\mathcal{Q}_\mathrm{f}$ and the actuators $\mathbf{u}$, as cited in

$$\underbrace{\begin{bmatrix}\dot{\mathbf{q}}_\mathrm{f}\\ \ddot{\mathbf{q}}_\mathrm{f}\end{bmatrix}}_{\dot{\mathbf{x}}_\mathrm{f}} = \begin{bmatrix}\dot{\mathbf{q}}_\mathrm{f}\\ \mathbf{M}_\mathrm{f}^{-1}\left(-\boldsymbol{\Gamma}_\mathrm{cp} + \mathbf{B}_\mathrm{f}\mathbf{u}\right)\end{bmatrix} = \underbrace{\begin{bmatrix}\dot{\mathbf{q}}_\mathrm{f}\\ -\mathbf{M}_\mathrm{f}^{-1}\boldsymbol{\Gamma}_\mathrm{cp}\end{bmatrix}}_{\tilde{\mathbf{f}}_\mathrm{cp}(\mathbf{x}_{\mathrm{f,s}})} + \underbrace{\begin{bmatrix}\mathbf{0}\\ \mathbf{M}_\mathrm{f}^{-1}\mathbf{B}_\mathrm{f}\end{bmatrix}}_{\tilde{\mathbf{g}}_\mathrm{cp}(\mathbf{x}_{\mathrm{f,s}})}\mathbf{u}\,. \tag{5.27}$$

Considering the acceleration $\mathbf{w} := \ddot{\mathbf{q}}_\mathrm{b}$ of the actuated joints as the input to the system, the vector field $X_\mathrm{cp}(\mathbf{x}_{\mathrm{f,s}}, \mathbf{w}) := \mathbf{f}_\mathrm{cp}(\mathbf{x}_{\mathrm{f,s}}) + \mathbf{g}_\mathrm{cp}(\mathbf{x}_{\mathrm{f,s}})\mathbf{w}$ is articulated as shown in

$$\underbrace{\begin{bmatrix}\dot{\mathbf{q}}_\mathrm{f}\\ \ddot{\mathbf{r}}_\mathrm{CM}\\ \ddot{\theta}_\mathrm{HAT}\\ \mathbf{w}\end{bmatrix}}_{\dot{\mathbf{x}}_{\mathrm{f,s}}} = X_\mathrm{cp}(\mathbf{x}_{\mathrm{f,s}}, \mathbf{w}) := \underbrace{\begin{bmatrix}\dot{\mathbf{q}}_\mathrm{f}\\ -\mathbf{M}_{\mathrm{f},00}^{-1}\begin{bmatrix}\mathbf{I}_2 & \mathbf{0}\end{bmatrix}\boldsymbol{\Gamma}_\mathrm{cp}\\ -M_{\mathrm{f},11}^{-1}\begin{bmatrix}\mathbf{0} & 1 & \mathbf{0}\end{bmatrix}\boldsymbol{\Gamma}_\mathrm{cp}\\ \mathbf{0}\end{bmatrix}}_{\mathbf{f}_\mathrm{cp}(\mathbf{x}_{\mathrm{f,s}})} + \underbrace{\begin{bmatrix}\mathbf{0}\\ \mathbf{0}\\ -M_{\mathrm{f},11}^{-1}\mathbf{M}_{\mathrm{f},12}\\ \mathbf{I}_4\end{bmatrix}}_{\mathbf{g}_\mathrm{cp}(\mathbf{x}_{\mathrm{f,s}})}\mathbf{w}\,, \tag{5.28}$$

wherein components $\ddot{\mathbf{r}}_\mathrm{CM}$ and $\ddot{\theta}_\mathrm{HAT}$ are derived following the expressions in equations (5.22a) and (5.22b), respectively.

Discrete Mappings

In state space representation, the take-off mapping in (5.24) is articulated as

$$\mathbf{x}_\mathrm{f}^+ = \mathbf{x}_{\mathrm{f,s}}^- := \begin{bmatrix}\mathbf{q}_{\mathrm{f,s}}^-\\ \dot{\mathbf{q}}_{\mathrm{f,s}}^-\end{bmatrix}\,, \tag{5.29}$$

where $\mathbf{x}_{\mathrm{f,s}}^-$ represents the states preceding take-off, and $\mathbf{x}_\mathrm{f}^+$ signifies the states in the FLP succeeding take-off. The process of landing, delineated in (5.25) and expressed as

$$\mathbf{x}_{\mathrm{f,s}}^+ = \tilde{\boldsymbol{\Delta}}_\mathrm{LD}\left(\mathbf{x}_\mathrm{f}^-\right) := \begin{bmatrix}\boldsymbol{\Delta}_{\mathrm{LD},\mathbf{q}_{\mathrm{f,s}}}(\mathbf{q}_{\mathrm{f,f}}^-)\\ \mathbf{R}_-^+(7)\dot{\mathbf{q}}_{\mathrm{f,f}}^-\end{bmatrix}\,, \tag{5.30}$$

facilitates the transition of the final states $\mathbf{x}_\mathrm{f}^-$ of the FLP to the initial states $\mathbf{x}_{\mathrm{f,s}}^+$ of the SSP.

Hybrid Dynamics in State Space

The hybrid dynamical model characterizing the running gait is synthesized by the flow within the SSP, as articulated by

$$\Sigma_{\text{cp,SSP}} : \begin{cases} \dot{\mathbf{x}}_{\text{f,s}} = \tilde{\mathbf{f}}_{\text{cp}}(\mathbf{x}_{\text{f,s}}) + \tilde{\mathbf{g}}_{\text{cp}}(\mathbf{x}_{\text{f,s}})\mathbf{u} \,, & \mathbf{x}_{\text{f,s}} \notin \tilde{\mathcal{S}}_{\text{s}}^{\text{f}} \,, \\ \mathbf{x}_{\text{f}}^{+} = \mathbf{x}_{\text{f,s}}^{-} \,, & \mathbf{x}_{\text{f,s}}^{-} \in \tilde{\mathcal{S}}_{\text{s}}^{\text{f}} \,, \\ \tilde{\mathcal{S}}_{\text{s}}^{\text{f}} := \{\mathbf{x}_{\text{f,s}} \in T\mathcal{Q}_{\text{f}} |\ \tilde{g}_{\text{s}}^{\text{f}}(\mathbf{x}_{\text{f,s}}) = 0\} \,, \end{cases} \tag{5.31}$$

and the FLP flow, delineated by

$$\Sigma_{\text{cp,FLP}} : \begin{cases} \dot{\mathbf{x}}_{\text{f}} = \tilde{\mathbf{f}}_{\text{f,r}}(\mathbf{x}_{\text{f}}) + \tilde{\mathbf{g}}_{\text{f,r}}(\mathbf{x}_{\text{f}})\mathbf{u} \,, & \mathbf{x}_{\text{f}} \notin \tilde{\mathcal{S}}_{\text{f}}^{\text{s}} \,, \\ \mathbf{x}_{\text{f,s}}^{+} = \tilde{\Delta}_{\text{LD}}\left(\mathbf{x}_{\text{f}}^{-}\right) \,, & \mathbf{x}_{\text{f}}^{-} \in \tilde{\mathcal{S}}_{\text{f}}^{\text{s}} \,, \\ \tilde{\mathcal{S}}_{\text{f}}^{\text{s}} := \{\mathbf{x}_{\text{f}} \in T\mathcal{Q}_{\text{f}} |\ \tilde{g}_{\text{f}}^{\text{s}}(\mathbf{x}_{\text{f}}) = 0, r_{2,x}(\mathbf{x}_{\text{f}}) - r_{1,x}(\mathbf{x}_{\text{f}}) > 0\} \,, \end{cases} \tag{5.32}$$

with state variables $\mathbf{x}_{\text{f}} \in T\mathcal{Q}_{\text{f}}$ in the FLP. Specifically, the switching surface $\tilde{\mathcal{S}}_{\text{s}}^{\text{f}}$ from the SSP to the FLP is attained when the normal reaction force during the unilateral contact phase becomes null. This event is represented by the guard function $\tilde{g}_{\text{s}}^{\text{f}}(\mathbf{x}_{\text{f,s}}) := F_{1,z}(\mathbf{x}_{\text{f,s}})$, which measures the magnitude of the normal reaction force on the compliant ground, as outlined in (5.20).
The other switching surface $\tilde{\mathcal{S}}_{\text{f}}^{\text{s}}$ transitioning from the FLP to the SSP is defined by the moment at which the swing foot contacts the ground surface, as determined by the guard function $\tilde{g}_{\text{f}}^{\text{s}}(\mathbf{x}_{\text{f}}) := r_{2,z}(\mathbf{x}_{\text{f}})$ with $\tilde{g}_{\text{f}}^{\text{s}} : T\mathcal{Q}_{\text{f}} \to \mathbb{R}$, closely resembling the event defined for running on rigid ground as depicted in (5.16).
While the system states are presumed to evolve in a continuous fashion, i.e., without abrupt jumps being pertinent, a hybrid dynamical model remains indispensable due to the variation of the vector fields across discrete transition events. As demonstrated in Section 6.2.3, this variability significantly affects the examination of the orbital stability of the resulting periodic solution.

6 Control Design for Running

The Hybrid Zero Dynamics (HZD) control approach, utilized for the development of periodic bipedal running gaits, has been rigorously investigated through simulation studies, as indicated in [35], and substantiated by experimental assessments as described in [109]. In these analyses, the ground is presumed to be perfectly rigid. The principal contribution of this chapter resides in extending the HZD control framework to incorporate compliant interactions with deformable ground surfaces.
The organization of this chapter is as follows: the design of the controller dedicated to the development of running gaits on rigid surfaces is thoroughly examined in Section 6.1, while the extension that accounts for compliant contact during the single support phase of running is explicated in Section 6.2.

6.1 Running on Rigid Ground

The periodic running gaits are delineated by the hybrid dynamical model as introduced in Section 5.1.4. The feedback controller utilized during the SSP for running is analogous to that specified in the SSP for walking, as described in Section 4.1.1. In the interest of completeness, the controller employed in the FLP is discussed in Section 6.1.1. Assuming that control errors in the SSP and FLP are negligible, the full-order system dynamics can be simplified to the zero dynamics of a reduced order, as demonstrated in Section 6.1.2. The orbital stability of periodic solutions arising from the resultant hybrid zero dynamics is assessed through the application of Floquet theory, as elaborated in Section 6.1.3.

6.1.1 Feedback Control in FLP

The feedback controller is engineered to eliminate the discrepancy between the actuated joints $\mathbf{q}_\mathrm{b}$ and the reference trajectory $\mathbf{q}_{\mathrm{r,f}}(x_\mathrm{CM})$, which necessitates a vector-valued mapping $\mathbf{q}_{\mathrm{r,f}} : \mathbb{R} \to \mathbb{T}^4; x_\mathrm{CM} \mapsto \mathbf{q}_{\mathrm{r,f}}(x_\mathrm{CM})$ that characterizes the desired angle progression through the utilization of high-order polynomials. In particular, the phase-dependent trajectory $\mathbf{q}_{\mathrm{r,f}}(x_\mathrm{CM})$ is organized with consideration of the horizontal position x_CM of the

center of mass as its independent phase variable, due to x_{CM} demonstrating a monotonic increase throughout the FLP.
Subsequently, the synchronization error $\mathbf{h}_{\mathrm{f}}(\mathbf{q}_{\mathrm{f}})$, where $\mathbf{h}_{\mathrm{f}} : \mathcal{Q}_{\mathrm{f}} \to \mathbb{R}^4$ is regarded as holonomic virtual constraints, is expressed as a function of the coordinates $\mathbf{q}_{\mathrm{f}} \in \mathcal{Q}_{\mathrm{f}}$. This process concludes with the derivation of the control output $\mathbf{y}_{\mathrm{f}}$, expressed as

$$\mathbf{y}_{\mathrm{f}} := \mathbf{h}_{\mathrm{f}}(\mathbf{q}_{\mathrm{f}}) = \mathbf{q}_{\mathrm{b}} - \mathbf{q}_{\mathrm{r,f}}(x_{\mathrm{CM}}) \,. \tag{6.1}$$

To facilitate the construction of state feedback intended to linearize the control task as specified in (6.1), the calculation advances with the Lie derivative of $\mathbf{y}_{\mathrm{f}}$ in relation to the vector field $\tilde{X}_{\mathrm{f,r}}(\mathbf{x}_{\mathrm{f}}, \mathbf{u}) := \tilde{\mathbf{f}}_{\mathrm{f,r}}(\mathbf{x}_{\mathrm{f}}) + \tilde{\mathbf{g}}_{\mathrm{f,r}}(\mathbf{x}_{\mathrm{f}})\mathbf{u}$ with state variables $\mathbf{x}_{\mathrm{f}} \in T\mathcal{Q}_{\mathrm{f}}$ as outlined in (5.11), resulting in

$$\dot{\mathbf{y}}_{\mathrm{f}} = \mathcal{L}_{\tilde{f}}\mathbf{h}_{\mathrm{f}}(\mathbf{q}_{\mathrm{f}}, \dot{\mathbf{q}}_{\mathrm{f}}) := \begin{bmatrix} -\frac{\partial \mathbf{q}_{\mathrm{r,f}}}{\partial x_{\mathrm{CM}}} & \mathbf{0} & \mathbf{I}_4 \end{bmatrix} \dot{\mathbf{q}}_{\mathrm{f}} \,. \tag{6.2}$$

Following this, the formulation of the second Lie derivative is delineated as

$$\ddot{\mathbf{y}}_{\mathrm{f}} = \underbrace{\left(-\frac{\partial^2 \mathbf{q}_{\mathrm{r,f}}}{\partial x_{\mathrm{CM}}^2} \dot{x}_{\mathrm{CM}}^2 - \begin{bmatrix} -\frac{\partial \mathbf{q}_{\mathrm{r,f}}}{\partial x_{\mathrm{CM}}} & \mathbf{0} & \mathbf{I}_4 \end{bmatrix} \mathbf{M}_{\mathrm{f}}^{-1} \boldsymbol{\Gamma}_{\mathrm{f}} \right)}_{\mathcal{L}_{\tilde{f}}^2 \mathbf{h}_{\mathrm{f}}(\mathbf{q}_{\mathrm{f}}, \dot{\mathbf{q}}_{\mathrm{f}})} + \underbrace{\left(\begin{bmatrix} -\frac{\partial \mathbf{q}_{\mathrm{r,f}}}{\partial x_{\mathrm{CM}}} & \mathbf{0} & \mathbf{I}_4 \end{bmatrix} \mathbf{M}_{\mathrm{f}}^{-1} \mathbf{B}_{\mathrm{f}} \right)}_{\mathcal{L}_{\tilde{g}} \mathcal{L}_{\tilde{f}} \mathbf{h}_{\mathrm{f}}(\mathbf{q}_{\mathrm{f}})} \mathbf{u} \,. \tag{6.3}$$

According to the notation outlined in [2, Definition 33], the vector-valued relative degree $\{r_{\mathrm{f},1}, r_{\mathrm{f},2}, r_{\mathrm{f},3}, r_{\mathrm{f},4}\} = \{2, 2, 2, 2\}$ is determined by the controller architecture, which engages input $\mathbf{u}$ and output $\mathbf{y}_{\mathrm{f}}$. The discrepancy between the total relative degree ($\sum_{i=1}^{4} r_{\mathrm{f},i} = 8$) and the system dimension ($\dim(\mathbf{x}_{\mathrm{f}}) = 14$) suggests the existence of a six-dimensional internal dynamical subsystem that remains uncontrollable by the input actuators $\mathbf{u}$.

State Feedback for Linearization

In addition to these nonlinear internal dynamics, the linearizable component of the system is characterized by a double integrator behavior between the newly defined system input $\mathbf{v}_{\mathrm{f}} := \ddot{\mathbf{y}}_{\mathrm{f}}$ and the output $\mathbf{y}_{\mathrm{f}}$. The linearization emerges as a result of the implementation of a static state feedback, denoted by

$$\mathbf{u} = \left(\mathcal{L}_{\tilde{g}} \mathcal{L}_{\tilde{f}} \mathbf{h}_{\mathrm{f}}(\mathbf{q}_{\mathrm{f}}) \right)^{-1} \left(\mathbf{v}_{\mathrm{f}} - \mathcal{L}_{\tilde{f}}^2 \mathbf{h}_{\mathrm{f}}(\mathbf{q}_{\mathrm{f}}, \dot{\mathbf{q}}_{\mathrm{f}}) \right) \,. \tag{6.4}$$

This feedback is predicated on the assumption that the decoupling matrix $\mathcal{L}_{\tilde{g}}\mathcal{L}_{\tilde{f}}\mathbf{h}_\mathrm{f}(\mathbf{q}_\mathrm{f})$ retains its invertibility within the vicinity of the equilibrium point $\mathbf{y}_\mathrm{f} = \mathbf{0}$, which is stabilized through high-gain PD-feedback as delineated in

$$\mathbf{v}_\mathrm{f} = -\mathbf{K}_{\mathrm{p,f}}\mathbf{y}_\mathrm{f} - \mathbf{K}_{\mathrm{d,f}}\dot{\mathbf{y}}_\mathrm{f}\,, \tag{6.5}$$

with positive definite matrices $\mathbf{K}_{\mathrm{p,f}}$ and $\mathbf{K}_{\mathrm{d,f}}$ functioning as proportional and derivative feedback gains, respectively.

Coordinate Transformation for Linearization

The system dynamics are divided into nonlinear internal dynamics and a linearizable subsystem, as illustrated via a coordinate transformation. Principally, the six-dimensional internal dynamics embody the three degrees of underactuation within the FLP. The six coordinates $\xi_\mathrm{f} := [\xi_{\mathrm{f},1}^\top, \xi_{\mathrm{f},2}^\top]^\top$ that characterize these internal dynamics may be selected arbitrarily, as referenced in [79, Section 5.1].
The implementation of condition $\mathcal{L}_{\tilde{g}}\xi_{\mathrm{f},1} = \mathcal{L}_{\tilde{g}}\xi_{\mathrm{f},2} = \mathbf{0}$ facilitates the formulation of the internal zero dynamics employing these coordinates ξ_f independent of the controller input $\mathbf{u}$. Subsequently, the solution, in conjunction with the inverse dynamics as delineated in (5.3), is utilized to ascertain the actuator torques $\mathbf{u}$. Thus, the coordinates ξ_f are defined by

$$\xi_{\mathrm{f},1} := \begin{bmatrix} \mathbf{r}_\mathrm{CM} \\ \theta_\mathrm{HAT} \end{bmatrix} = \mathbf{c}_{\xi,1}(\mathbf{q}_\mathrm{f}) := \begin{bmatrix} \mathbf{I}_3 & \mathbf{0} \end{bmatrix} \mathbf{q}_\mathrm{f}\,, \tag{6.6a}$$

$$\xi_{\mathrm{f},2} := \begin{bmatrix} \dot{\mathbf{r}}_\mathrm{CM} \\ \sigma_\mathrm{CM} \end{bmatrix} = \mathbf{c}_{\xi,2}(\mathbf{q}_\mathrm{f}, \dot{\mathbf{q}}_\mathrm{f}) := \begin{bmatrix} \mathbf{I}_2 & \mathbf{0} & \mathbf{0} \\ \mathbf{0} & M_{\mathrm{f},11}(\mathbf{q}_\mathrm{f}) & \mathbf{M}_{\mathrm{f},12}(\mathbf{q}_\mathrm{f}) \end{bmatrix} \dot{\mathbf{q}}_\mathrm{f}\,, \tag{6.6b}$$

with the mappings $\mathbf{c}_{\xi,1} : Q_\mathrm{f} \to \mathbb{R}^3$ and $\mathbf{c}_{\xi,2} : Q_\mathrm{f} \times T_{\mathbf{q}_\mathrm{f}}Q_\mathrm{f} \to \mathbb{R}^3$ serving as coordinate transformations for $\xi_{\mathrm{f},1}$ and $\xi_{\mathrm{f},2}$, respectively. In expression (6.6b), the angular momentum σ_CM with respect to the center of mass is conjugate to θ_HAT and remains conserved throughout the FLP, i.e., $\dot{\sigma}_\mathrm{CM} = 0$, due to the gravitational force being the only external influence exerted on the robot.
Furthermore, the coordinates pertinent to the linearizable subsystem are obtained via the Lie derivative, as demonstrated in (6.2), and are elucidated in

$$\begin{bmatrix} \eta_{\mathrm{f},1} \\ \eta_{\mathrm{f},2} \end{bmatrix} := \begin{bmatrix} \mathbf{h}_\mathrm{f}(\mathbf{q}_\mathrm{f}) \\ \mathcal{L}_{\tilde{f}}\mathbf{h}_\mathrm{f}(\mathbf{q}_\mathrm{f}, \dot{\mathbf{q}}_\mathrm{f}) \end{bmatrix}. \tag{6.7}$$

The extensive coordinate transformation $[\boldsymbol{\eta}_{\mathrm{f},1}^{\top}, \boldsymbol{\eta}_{\mathrm{f},2}^{\top}, \boldsymbol{\xi}_{\mathrm{f},1}^{\top}, \boldsymbol{\xi}_{\mathrm{f},2}^{\top}]^{\top} = \Psi_{\mathrm{f}}(\mathbf{x}_{\mathrm{f}})$ is delineated through the mapping $\Psi_{\mathrm{f}} : T\mathcal{Q}_{\mathrm{f}} \to \mathbb{R}^{14}$; $\mathbf{x}_{\mathrm{f}} \mapsto \Psi_{\mathrm{f}}(\mathbf{x}_{\mathrm{f}})$, which forms a diffeomorphism, attributable to an invertible Jacobian $\mathbf{J}_{\Psi,\mathrm{f}} := \partial\Psi_{\mathrm{f}}/\partial\mathbf{x}_{\mathrm{f}} = \left[\partial\Psi_{\mathrm{f}}/\partial\mathbf{q}_{\mathrm{f}} \, , \partial\Psi_{\mathrm{f}}/\partial\dot{\mathbf{q}}_{\mathrm{f}}\right]$.

Two-Stage Control Law

An alternative formulation to accomplish the virtual constraints in the FLP as referenced in (6.1) is achieved via the application of the Lie derivative to $\mathbf{y}_{\mathrm{f}}$ with respect to the vector field $X_{\mathrm{f,r}}(\mathbf{x}_{\mathrm{f}}, \mathbf{w})$ as described in (5.12), yielding

$$\dot{\mathbf{y}}_{\mathrm{f}} = \mathcal{L}_f \mathbf{h}_{\mathrm{f}}(\mathbf{q}_{\mathrm{f}}, \dot{\mathbf{q}}_{\mathrm{f}}) := \left[-\tfrac{\partial \mathbf{q}_{\mathrm{r,f}}}{\partial x_{\mathrm{CM}}} \quad \mathbf{0} \quad \mathbf{I}_4\right] \dot{\mathbf{q}}_{\mathrm{f}} \, . \tag{6.8}$$

Subsequently, the expression of the second Lie derivative is articulated as

$$\ddot{\mathbf{y}}_{\mathrm{f}} = \underbrace{\left(-\frac{\partial^2 \mathbf{q}_{\mathrm{r,f}}}{\partial x_{\mathrm{CM}}^2}\dot{x}_{\mathrm{CM}}^2 - \frac{\partial \mathbf{q}_{\mathrm{r,f}}}{\partial x_{\mathrm{CM}}}\ddot{x}_{\mathrm{CM}}\right)}_{\mathcal{L}_f^2 \mathbf{h}_{\mathrm{f}}(\mathbf{q}_{\mathrm{f}}, \dot{\mathbf{q}}_{\mathrm{f}})} + \underbrace{\mathbf{I}_4}_{\mathcal{L}_g \mathcal{L}_f \mathbf{h}_{\mathrm{f}}} \mathbf{w} \, . \tag{6.9}$$

with $\ddot{x}_{\mathrm{CM}} = 0$ in the expression $\mathcal{L}_f^2 \mathbf{h}_{\mathrm{f}}$ in (6.9), due to the absence of air drag during the flight. The system's linearizable component is delineated by a double integrator behavior connecting the newly defined system input $\mathbf{v}_{\mathrm{f}} := \ddot{\mathbf{y}}_{\mathrm{f}}$ and the output $\mathbf{y}_{\mathrm{f}}$. This linearization emerges as a result of the state feedback, as described in

$$\mathbf{w} = \mathbf{I}_4 \left(\mathbf{v}_{\mathrm{f}} - \mathcal{L}_f^2 \mathbf{h}_{\mathrm{f}}(\mathbf{q}_{\mathrm{f}}, \dot{\mathbf{q}}_{\mathrm{f}})\right) \, . \tag{6.10}$$

The decoupling matrix $\mathcal{L}_g \mathcal{L}_f \mathbf{h}_{\mathrm{f}} = \mathbf{I}_4$ is evidently non-singular and invertible within the neighborhood of the equilibrium point $\mathbf{y}_{\mathrm{f}} = \mathbf{0}$, which is stabilized via the PD-feedback as expounded in (6.5). Subsequently, the inverse dynamics depicted in (5.3) are employed to ascertain the actuator $\mathbf{u} = \overline{\mathbf{M}}_{\mathrm{f}}\mathbf{w} + \overline{\boldsymbol{\Gamma}}_{\mathrm{f}}$.

6.1.2 Zero Dynamics

The high-gain feedback (6.5) guarantees the presence of a stable equilibrium point $\mathbf{y}_{\mathrm{f}} = \mathbf{0}$, which corresponds to the linearizable partition of the full-order system. At this equilibrium point, the residual internal dynamics are considered as zero dynamics of the FLP, which are then combined with the zero dynamics of the SSP in Section 4.1.2 to construct the hybrid zero dynamics of running.

Continuous Invariance

At the equilibrium point $\mathbf{y}_\mathrm{f} = \mathbf{0}$, the zero dynamics manifold $\mathcal{Z}_\mathrm{f}$ is described as

$$\mathcal{Z}_\mathrm{f} := \{\mathbf{x}_\mathrm{f} \in TQ_\mathrm{f} | \, \mathbf{h}_\mathrm{f}(\mathbf{x}_\mathrm{f}) = \mathbf{0}, \mathcal{L}_{\tilde{f}}\mathbf{h}_\mathrm{f}(\mathbf{x}_\mathrm{f}) = \mathbf{0}\} \, , \tag{6.11}$$

forming a six-dimensional submanifold embedded within TQ_f. This submanifold is defined by the local coordinates ξ_f as established in (6.6), which are utilized for representing the system states $\mathbf{x}_\mathrm{f} \in TQ_\mathrm{f}$ within the FLP state space, articulated as

$$\mathbf{x}_\mathrm{f}\Big|_{\mathcal{Z}_\mathrm{f}} = \begin{bmatrix}\mathbf{q}_\mathrm{f} \\ \dot{\mathbf{q}}_\mathrm{f}\end{bmatrix}\Bigg|_{\mathcal{Z}_\mathrm{f}} = \Psi_\mathrm{f}^{-1}\left(\begin{bmatrix}\eta_{\mathrm{f},1} = \mathbf{0} \\ \eta_{\mathrm{f},2} = \mathbf{0} \\ \xi_{\mathrm{f},1} \\ \xi_{\mathrm{f},2}\end{bmatrix}\right)\Bigg|_{\xi_\mathrm{f} \in \mathcal{Z}_\mathrm{f}} \, , \tag{6.12}$$

where Ψ_f^{-1} signifies the inverse of the diffeomorphism Ψ_f. The elimination of the control error $\mathbf{y}_\mathrm{f} = \dot{\mathbf{y}}_\mathrm{f} = \mathbf{0}$ on the submanifold $\mathcal{Z}_\mathrm{f}$ converts the feedback (6.4) for linearization into

$$\mathbf{u}^0 = -\left(\mathcal{L}_{\tilde{g}}\mathcal{L}_{\tilde{f}}\mathbf{h}_\mathrm{f}(\mathbf{q}_\mathrm{f})\right)^{-1}\mathcal{L}_{\tilde{f}}^2\mathbf{h}_\mathrm{f}(\mathbf{q}_\mathrm{f}, \dot{\mathbf{q}}_\mathrm{f})\Big|_{\mathcal{Z}_\mathrm{f}} \, . \tag{6.13}$$

Furthermore, the invariance of FLP zero dynamics with respect to the dynamics of the closed-loop system utilizing state feedback $\mathbf{u}^0$ is consistently preserved. This occurrence is attributed to the vector $\dot{\mathbf{x}}_\mathrm{f}^0 = \tilde{\mathbf{f}}_{\mathrm{f,r}}(\mathbf{x}_\mathrm{f}^0) + \tilde{\mathbf{g}}_{\mathrm{f,r}}(\mathbf{x}_\mathrm{f}^0)\mathbf{u}^0$, which delineates the progression of the state variable $\mathbf{x}_\mathrm{f}^0 \in \mathcal{Z}_\mathrm{f}$, continuously maintaining tangency to the zero dynamics manifold $\mathcal{Z}_\mathrm{f}$, associated with the condition $\mathcal{L}_{\tilde{f}}\mathbf{h}_\mathrm{f}(\mathbf{x}_\mathrm{f}^0) = (\partial\mathbf{h}_\mathrm{f}/\partial\mathbf{x}_\mathrm{f})\big|_{\mathbf{x}_\mathrm{f}=\mathbf{x}_\mathrm{f}^0}\dot{\mathbf{x}}_\mathrm{f}^0 = \mathbf{0}$ in (6.11). The invariant zero dynamics delineated in $\mathcal{Z}_\mathrm{f}$ are ascertained through a system of ordinary differential equations, analogous to [177, Equation (9.18)]. The resultant zero dynamics $\dot{\xi}_\mathrm{f} = \mathbf{f}_{\mathrm{f,ZD}}(\xi_\mathrm{f})$ are articulated in coordinates $\xi_{\mathrm{f},1}$ and $\xi_{\mathrm{f},2}$, as delineated in

$$\dot{\xi}_{\mathrm{f},1} := \begin{bmatrix}\dot{\mathbf{r}}_\mathrm{CM} \\ \dot{\theta}_\mathrm{HAT}\end{bmatrix} = \mathcal{L}_{\tilde{f}}\xi_{\mathrm{f},1}\Big|_{\mathcal{Z}_\mathrm{f}} = \underbrace{\begin{bmatrix}1 & 0 & 0 \\ 0 & 1 & 0 \\ -M_{\mathrm{f},11}^{-1}\mathbf{M}_{\mathrm{f},12}\frac{\partial\mathbf{q}_{\mathrm{r,f}}}{\partial x_\mathrm{CM}} & 0 & M_{\mathrm{f},11}^{-1}\end{bmatrix}}_{\boldsymbol{\kappa}_{\mathrm{f},1}(\xi_{\mathrm{f},1})}\xi_{\mathrm{f},2} \, , \tag{6.14a}$$

$$\dot{\xi}_{\mathrm{f},2} := \begin{bmatrix}\ddot{\mathbf{r}}_\mathrm{CM} \\ \dot{\sigma}_\mathrm{CM}\end{bmatrix} = \mathcal{L}_{\tilde{f}}\xi_{\mathrm{f},2}\Big|_{\mathcal{Z}_\mathrm{f}} = \underbrace{\begin{bmatrix}0 \\ -g \\ 0\end{bmatrix}}_{\boldsymbol{\kappa}_{\mathrm{f},2}} \, . \tag{6.14b}$$

The term $\dot{\theta}_{\mathrm{HAT}}$, as mentioned in (6.14a), is deduced from equation (6.6b), considering the virtual constraints $\mathbf{q}_{\mathrm{b}}\big|_{\mathcal{Z}_{\mathrm{f}}} = \mathbf{q}_{\mathrm{r,f}}$ and $\dot{\mathbf{q}}_{\mathrm{b}}\big|_{\mathcal{Z}_{\mathrm{f}}} = (\partial \mathbf{q}_{\mathrm{r,f}}/\partial x_{\mathrm{CM}})\dot{x}_{\mathrm{CM}}$ that are consistently applicable to the zero dynamics manifold $\mathcal{Z}_{\mathrm{f}}$.

Discontinuous Invariance

The notion of discontinuous invariance is explicated with regard to both take-off and landing phenomena, as referenced in Section 5.1.2 and Section 5.1.3, respectively. Initially, the take-off mapping (5.13) is defined on the surface $\mathcal{Z}_{\mathrm{s,r}} \cap \mathcal{S}_{\mathrm{s}}^{\mathrm{f}}$, a one-dimensional submanifold embedded within $TQ_{\mathrm{s},0}$. Employing coordinates $\xi_{\mathrm{s}}^{-} \in \mathcal{Z}_{\mathrm{s,r}} \cap \mathcal{S}_{\mathrm{s}}^{\mathrm{f}}$ pertaining to the zero dynamics in the SSP, the take-off mapping is represented as

$$\xi_{\mathrm{f}}^{+} = \begin{bmatrix} \mathbf{c}_{\xi,1}\left(\mathbf{x}_{\mathrm{f}}^{+}\right) \\ \mathbf{c}_{\xi,2}\left(\mathbf{x}_{\mathrm{f}}^{+}\right) \end{bmatrix}\Bigg|_{\mathcal{Z}_{\mathrm{f}}} = \Delta_{\mathrm{TO}}^{\mathrm{HZD}}\left(\xi_{\mathrm{s}}^{-}\right) := \begin{bmatrix} \mathbf{c}_{\xi,1}\left(\Delta_{\mathrm{TO}}\left(\mathbf{x}_{\mathrm{s}}^{-}\right)\right) \\ \mathbf{c}_{\xi,2}\left(\Delta_{\mathrm{TO}}\left(\mathbf{x}_{\mathrm{s}}^{-}\right)\right) \end{bmatrix}\Bigg|_{\mathcal{Z}_{\mathrm{s,r}} \cap \mathcal{S}_{\mathrm{s}}^{\mathrm{f}}}, \tag{6.15}$$

where the system states $\mathbf{x}_{\mathrm{s}}^{-} = \Psi_{\mathrm{s}}^{-1}\left([\mathbf{0}^{\top}, \mathbf{0}^{\top}, (\xi_{\mathrm{s}}^{-})^{\top}]^{\top}\right)$ are obtained from the diffeomorphism described in (4.14) at the precise moment preceding take-off. Furthermore, discontinuous invariance at the take-off is established if, following the mapping, the system states remain on the zero dynamics manifold associated with the subsequent FLP, as demonstrated in $\Delta_{\mathrm{TO}}^{\mathrm{HZD}}\left(\mathcal{Z}_{\mathrm{s,r}} \cap \mathcal{S}_{\mathrm{s}}^{\mathrm{f}}\right) \in \mathcal{Z}_{\mathrm{f}}$.
The determination of whether a trajectory achieves intersection with the surface $\mathcal{Z}_{\mathrm{s,r}} \cap \mathcal{S}_{\mathrm{s}}^{\mathrm{f}}$ is facilitated through the assessment of the guard function $g_{\mathrm{s}}^{\mathrm{f}}(\mathbf{x}_{\mathrm{s}})$ in accordance with (5.15); this process is executed on the zero dynamics manifold $\mathcal{Z}_{\mathrm{s,r}}$ as

$$g_{\mathrm{s,HZD}}^{\mathrm{f}}(\xi_{\mathrm{s}}) := g_{\mathrm{s}}^{\mathrm{f}}(\mathbf{x}_{\mathrm{s}})\Big|_{\mathcal{Z}_{\mathrm{s,r}}} = 0\,. \tag{6.16}$$

Furthermore, the landing mapping (5.14) is defined on the surface $\mathcal{Z}_{\mathrm{f}} \cap \mathcal{S}_{\mathrm{f}}^{\mathrm{s}}$, which constitutes a one-dimensional submanifold embedded within TQ_{f}. The zero dynamics coordinates $\xi_{\mathrm{f}}^{-} \in \mathcal{Z}_{\mathrm{f}} \cap \mathcal{S}_{\mathrm{f}}^{\mathrm{s}}$ in the FLP articulate the landing as

$$\xi_{\mathrm{s}}^{+} = \begin{bmatrix} c_{\theta}\left(\mathbf{x}_{\mathrm{s}}^{+}\right) \\ c_{\sigma}\left(\mathbf{x}_{\mathrm{s}}^{+}\right) \end{bmatrix}\Bigg|_{\mathcal{Z}_{\mathrm{s,r}}} = \Delta_{\mathrm{LD}}^{\mathrm{HZD}}\left(\xi_{\mathrm{f}}^{-}\right) := \begin{bmatrix} c_{\theta}\left(\Delta_{\mathrm{LD}}\left(\mathbf{x}_{\mathrm{f}}^{-}\right)\right) \\ c_{\sigma}\left(\Delta_{\mathrm{LD}}\left(\mathbf{x}_{\mathrm{f}}^{-}\right)\right) \end{bmatrix}\Bigg|_{\mathcal{Z}_{\mathrm{f}} \cap \mathcal{S}_{\mathrm{f}}^{\mathrm{s}}}, \tag{6.17}$$

where $\xi_{\mathrm{s}}^{+} \in \mathcal{Z}_{\mathrm{s,r}}$ signifies the initial states for the SSP following the impact. Thus, the landing is considered a discontinuous invariance if condition $\Delta_{\mathrm{LD}}^{\mathrm{HZD}}\left(\mathcal{Z}_{\mathrm{f}} \cap \mathcal{S}_{\mathrm{f}}^{\mathrm{s}}\right) \in \mathcal{Z}_{\mathrm{s,r}}$ is

consistently fulfilled. The guard function $g_{\mathrm{f}}^{\mathrm{s}}(\mathbf{x}_{\mathrm{f}})$ delineated in (5.16) is articulated within the FLP zero dynamics coordinates $\xi_{\mathrm{f}} \in \mathcal{Z}_{\mathrm{f}}$ as

$$g_{\mathrm{f,HZD}}^{\mathrm{s}}(\xi_{\mathrm{f}}) := g_{\mathrm{f}}^{\mathrm{s}}(\mathbf{x}_{\mathrm{f}})\Big|_{\mathcal{Z}_{\mathrm{f}}} = 0\,. \tag{6.18}$$

Hybrid Invariant Zero Dynamics

The formulation of the hybrid zero dynamics pertaining to periodic running gaits is accomplished through the combination of the vector fields within the zero dynamics manifolds of the continuous SSP (specified in equation (4.16)) and FLP (described in equation (6.14)), alongside the discrete transition mappings given in the equations (6.15) and (6.17). Therefore, the formulation of the hybrid zero dynamics is presented in

$$\Sigma_{\mathrm{run,r}}^{\mathrm{HZD}}: \begin{cases} \dot{\xi}_{\mathrm{s}} = \mathbf{f}_{\mathrm{s,ZD}}(\xi_{\mathrm{s}})\,, & \xi_{\mathrm{s}}^{-} \notin \mathcal{Z}_{\mathrm{s,r}} \cap \mathcal{S}_{\mathrm{s}}^{\mathrm{f}}\,, \\ \xi_{\mathrm{f}}^{+} = \Delta_{\mathrm{TO}}^{\mathrm{HZD}}(\xi_{\mathrm{s}}^{-})\,, & \xi_{\mathrm{s}}^{-} \in \mathcal{Z}_{\mathrm{s,r}} \cap \mathcal{S}_{\mathrm{s}}^{\mathrm{f}}\,, \\ \dot{\xi}_{\mathrm{f}} = \mathbf{f}_{\mathrm{f,ZD}}(\xi_{\mathrm{f}})\,, & \xi_{\mathrm{f}}^{-} \notin \mathcal{Z}_{\mathrm{f}} \cap \mathcal{S}_{\mathrm{f}}^{\mathrm{s}}\,, \\ \xi_{\mathrm{s}}^{+} = \Delta_{\mathrm{LD}}^{\mathrm{HZD}}(\xi_{\mathrm{f}}^{-})\,, & \xi_{\mathrm{f}}^{-} \in \mathcal{Z}_{\mathrm{f}} \cap \mathcal{S}_{\mathrm{f}}^{\mathrm{s}}\,, \end{cases} \tag{6.19}$$

accompanied by graphical representations in Figure 6.1.

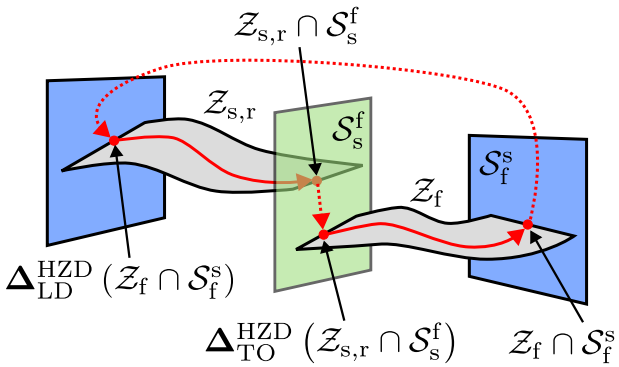

Figure 6.1: The zero dynamics manifolds for running are depicted. A solid line represents the solution curve within the continuous domain, whereas a dashed line denotes the discrete transition mapping.

This system is defined as hybrid invariant if the zero dynamics ensure continuous invariance relative to the dynamics of the closed-loop system while demonstrating discontinuous invariance with respect to the transition mappings. In such an invariant system, the solution $\mathbf{\Phi}_{\mathrm{run,r}}(\xi_{\mathrm{s}}^{-}, t)$ involves the integration of both discrete impulsive jumps and continuous trajectories $\mathbf{\Phi}_{\mathrm{s,ZD}}(\xi_{\mathrm{s}}^{+}, t)$ and $\mathbf{\Phi}_{\mathrm{f,ZD}}(\xi_{\mathrm{f}}^{+}, t)$ within the SSP and FLP domains, respectively.

In a more precise manner, the right-continuous trajectory, referred to as the solution curve $\mathbf{\Phi}_{\mathrm{s,ZD}}\left(\xi_{\mathrm{s}}^{+}, t\right)$ of vector field $\mathbf{f}_{\mathrm{s,ZD}}(\xi_{\mathrm{s}})$, is delineated within the SSP domain, whereas the solution curve $\mathbf{\Phi}_{\mathrm{f,ZD}}\left(\xi_{\mathrm{f}}^{+}, t\right)$ of vector field $\mathbf{f}_{\mathrm{f,ZD}}(\xi_{\mathrm{f}})$ is delineated within the FLP domain. The initial condition $\mathbf{\Phi}_{\mathrm{run,r}}\left(\xi_{\mathrm{s}}^{-}, t=0\right)=\xi_{\mathrm{s}}^{-} \in \mathcal{Z}_{\mathrm{s,r}} \cap \mathcal{S}_{\mathrm{s}}^{\mathrm{f}}$ of the overall solution $\mathbf{\Phi}_{\mathrm{run,r}}\left(\xi_{\mathrm{s}}^{-}, t\right)$ is prescribed on the transition surface before take-off. Subsequently, the states $\xi_{\mathrm{f}}^{+}=\mathbf{\Delta}_{\mathrm{TO}}^{\mathrm{HZD}}\left(\xi_{\mathrm{s}}^{-}\right) \in \mathcal{Z}_{\mathrm{f}}$ are employed to initialize the solution curve $\mathbf{\Phi}_{\mathrm{f,ZD}}\left(\xi_{\mathrm{f}}^{+}, t\right)$. Similarly, the landing event facilitates the transition of the states at the conclusion of the FLP to SSP, as represented by $\xi_{\mathrm{s}}^{+}=\mathbf{\Delta}_{\mathrm{LD}}^{\mathrm{HZD}}\left(\xi_{\mathrm{f}}^{-}\right) \in \mathcal{Z}_{\mathrm{s,r}}$.
Furthermore, the intervals t_{s} and t_{f} within the SSP and FLP domains, respectively, are ascertained according to phase-dependent transition events. Consequently, the step duration $t_{\mathrm{run,r}}=t_{\mathrm{s}}+t_{\mathrm{f}}$ is derived by aggregating the intervals of these two domains. Periodic solutions that fulfill the condition $\mathbf{\Phi}_{\mathrm{run,r}}\left(\xi_{\mathrm{s}}^{-}, t\right)=\mathbf{\Phi}_{\mathrm{run,r}}\left(\xi_{\mathrm{s}}^{-}, t+t_{\mathrm{run,r}}\right)$ are identified via the multiple shooting method.

6.1.3 Orbital Stability

Upon obtaining a periodic solution $\mathbf{\Phi}_{\mathrm{run,r}}\left(\xi_{\mathrm{s}}^{-}, t\right)=\mathbf{\Phi}_{\mathrm{run,r}}\left(\xi_{\mathrm{s}}^{-}, t+t_{\mathrm{run,r}}\right)$ through optimization, its orbital stability is evaluated by determining the monodromy matrix [1], as articulated in

$$\mathbf{D}_{\mathrm{run,r}}:=\frac{\partial \mathbf{\Phi}_{\mathrm{run,r}}\left(\xi_{\mathrm{s}}^{-}, t_{\mathrm{run,r}}\right)}{\partial \xi_{\mathrm{s}}^{-}}=\mathbf{F}_{\mathrm{s}}\left(t_{\mathrm{s}}\right) \mathbf{C}_{\mathrm{f}}^{\mathrm{s}}\left(\xi_{\mathrm{f}}^{-}\right) \underbrace{\left.\frac{\partial \mathbf{\Phi}_{\mathrm{f,ZD}}\left(\xi_{\mathrm{f}}^{+}, t\right)}{\partial \xi_{\mathrm{f}}^{+}}\right|_{t=t_{\mathrm{f}}}}_{\mathbf{F}_{\mathrm{r,f}}\left(t_{\mathrm{f}}\right)} \mathbf{C}_{\mathrm{s}}^{\mathrm{f}}\left(\xi_{\mathrm{s}}^{-}\right) . \tag{6.20}$$

Specifically, the fundamental matrix solution $\mathbf{F}_{\mathrm{s}}\left(t_{\mathrm{s}}\right)$ in the SSP corresponds exactly to that established for the walking gait as delineated in equation (4.21). In the FLP, $\mathbf{F}_{\mathrm{r,f}}(t)=\partial \mathbf{\Phi}_{\mathrm{f,ZD}}\left(\xi_{\mathrm{f}}^{+}, t\right) / \partial \xi_{\mathrm{f}}^{+}$ is deduced from the variational equation $\dot{\mathbf{F}}_{\mathrm{r,f}}=\left(\partial \mathbf{f}_{\mathrm{f,ZD}} / \partial \xi_{\mathrm{f}}\right) \mathbf{F}_{\mathrm{r,f}}$, employing the initial conditions $\mathbf{F}_{\mathrm{r,f}}\left(t=0\right)=\mathbf{I}_{6}$.
The saltation matrices $\mathbf{C}_{\mathrm{f}}^{\mathrm{s}}\left(\xi_{\mathrm{f}}^{-}\right)$ and $\mathbf{C}_{\mathrm{s}}^{\mathrm{f}}\left(\xi_{\mathrm{s}}^{-}\right)$ are delineated as

$$\mathbf{C}_{\mathrm{f}}^{\mathrm{s}}\left(\xi_{\mathrm{f}}^{-}\right):=\frac{\partial \mathbf{\Delta}_{\mathrm{LD}}^{\mathrm{HZD}}\left(\xi_{\mathrm{f}}^{-}\right)}{\partial \xi_{\mathrm{f}}^{-}}+\frac{\left(\mathbf{f}_{\mathrm{s,ZD}}\left(\xi_{\mathrm{s}}^{+}\right)-\frac{\partial \mathbf{\Delta}_{\mathrm{LD}}^{\mathrm{HZD}}\left(\xi_{\mathrm{f}}^{-}\right)}{\partial \xi_{\mathrm{f}}^{-}} \mathbf{f}_{\mathrm{f,ZD}}\left(\xi_{\mathrm{f}}^{-}\right)\right) \mathbf{n}_{\mathrm{f}}^{\mathrm{s}}\left(\xi_{\mathrm{f}}^{-}\right)}{\mathbf{n}_{\mathrm{f}}^{\mathrm{s}}\left(\xi_{\mathrm{f}}^{-}\right) \mathbf{f}_{\mathrm{f,ZD}}\left(\xi_{\mathrm{f}}^{-}\right)}, \tag{6.21a}$$

[1] It should be noted that the choice of the hyperplane for evaluating the monodromy matrix is arbitrary as long as the solution trajectory intersects the hyperplane transversally. Pertaining to running on rigid ground, the FLP features three unactuated degrees of freedom, whereas the SSP has only one. Consequently, the dimension of the monodromy matrix evaluated within the FLP is (6×6), while in the SSP, it is (2×2). Despite both resulting in the same magnitude of the largest Floquet multiplier, considering system states in the SSP streamlines the process of determining the resultant eigenvalues.

$$\mathbf{C}_{\mathrm{s}}^{\mathrm{f}}\left(\boldsymbol{\xi}_{\mathrm{s}}^{-}\right) := \frac{\partial \boldsymbol{\Delta}_{\mathrm{TO}}^{\mathrm{HZD}}\left(\boldsymbol{\xi}_{\mathrm{s}}^{-}\right)}{\partial \boldsymbol{\xi}_{\mathrm{s}}^{-}} + \frac{\left(\mathbf{f}_{\mathrm{f,ZD}}\left(\boldsymbol{\xi}_{\mathrm{f}}^{+}\right) - \frac{\partial \boldsymbol{\Delta}_{\mathrm{TO}}^{\mathrm{HZD}}(\boldsymbol{\xi}_{\mathrm{s}}^{-})}{\partial \boldsymbol{\xi}_{\mathrm{s}}^{-}} \mathbf{f}_{\mathrm{s,ZD}}(\boldsymbol{\xi}_{\mathrm{s}}^{-})\right) \mathbf{n}_{\mathrm{s}}^{\mathrm{f}}(\boldsymbol{\xi}_{\mathrm{s}}^{-})}{\mathbf{n}_{\mathrm{s}}^{\mathrm{f}}(\boldsymbol{\xi}_{\mathrm{s}}^{-}) \mathbf{f}_{\mathrm{s,ZD}}(\boldsymbol{\xi}_{\mathrm{s}}^{-})}\,, \tag{6.21b}$$

characterized by normal vectors $\mathbf{n}_{\mathrm{f}}^{\mathrm{s}}(\boldsymbol{\xi}_{\mathrm{f}}) := \left(\partial g_{\mathrm{f,HZD}}^{\mathrm{s}} \middle/ \partial \boldsymbol{\xi}_{\mathrm{f}}\right)$ associated with the landing surface and $\mathbf{n}_{\mathrm{s}}^{\mathrm{f}}(\boldsymbol{\xi}_{\mathrm{s}}) := \left(\partial g_{\mathrm{s,HZD}}^{\mathrm{f}} \middle/ \partial \boldsymbol{\xi}_{\mathrm{s}}\right)$ related to the take-off surface. In particular, conditions

$$\mathbf{n}_{\mathrm{s}}^{\mathrm{f}}(\boldsymbol{\xi}_{\mathrm{s}}^{-}) \mathbf{f}_{\mathrm{s,ZD}}(\boldsymbol{\xi}_{\mathrm{s}}^{-}) \neq 0, \qquad \boldsymbol{\xi}_{\mathrm{s}}^{-} \in \mathcal{Z}_{\mathrm{s,r}} \cap \mathcal{S}_{\mathrm{s}}^{\mathrm{f}}\,, \tag{6.22a}$$

$$\mathbf{n}_{\mathrm{f}}^{\mathrm{s}}(\boldsymbol{\xi}_{\mathrm{f}}^{-}) \mathbf{f}_{\mathrm{f,ZD}}(\boldsymbol{\xi}_{\mathrm{f}}^{-}) \neq 0, \qquad \boldsymbol{\xi}_{\mathrm{f}}^{-} \in \mathcal{Z}_{\mathrm{f}} \cap \mathcal{S}_{\mathrm{f}}^{\mathrm{s}}\,, \tag{6.22b}$$

hold true provided that the trajectory $\boldsymbol{\Phi}_{\mathrm{run,r}}\left(\boldsymbol{\xi}_{\mathrm{s}}^{-}, t\right)$ intersects the transition surfaces transversely, according to [177, Section 9.4]. With respect to the running gait, the condition (6.22a) implies that the angular velocity $\dot{\theta}_{\mathrm{virt}}\big|_{\mathcal{Z}_{\mathrm{s,r}} \cap \mathcal{S}_{\mathrm{s}}^{\mathrm{f}}} \neq 0$ of the robot's body remains non-zero upon approaching the take-off surface $g_{\mathrm{s}}^{\mathrm{f}}(\mathbf{x}_{\mathrm{s}}) := \begin{bmatrix} 1 & \mathbf{0} \end{bmatrix} \mathbf{x}_{\mathrm{s}} - \theta_{\mathrm{TO}}$. Furthermore, the condition (6.22b) is satisfied when the vertical velocity of the contacting foot is non-zero.

The monodromy matrix $\mathbf{D}_{\mathrm{run,r}}$ characterizes the evolution of an initial deviation $\delta \boldsymbol{\xi}_{\mathrm{f}}(0)$ in the system states along the trajectory after one period cycle $t_{\mathrm{run,r}}$. This phenomenon is represented by the monodromy matrix $\mathbf{D}_{\mathrm{run,r}}$ as $\delta \boldsymbol{\xi}_{\mathrm{s}}\left(t_{\mathrm{run,r}}\right) = \mathbf{D}_{\mathrm{run,r}}\, \delta \boldsymbol{\xi}_{\mathrm{s}}(0)$. The determination of whether the deviation $\delta \boldsymbol{\xi}_{\mathrm{s}}(0)$ diverges from or converges towards zero is defined as orbital stability, which is assessed through the eigenvalues, known as Floquet multipliers, of the (2×2)-dimensional monodromy matrix $\mathbf{D}_{\mathrm{run,r}}$.

Notably, a trivial multiplier $\Lambda_0 = 1$ emerges due to the inherent autonomous nature of the hybrid dynamical system; the other nontrivial multiplier is indicative of the stability of the solution curve. The tangent vector $\mathbf{f}_{\mathrm{s,ZD}}(\boldsymbol{\xi}_{\mathrm{s}}^{-})$ of the trajectory functions as the eigenvector associated with the trivial eigenvalue $\Lambda_0 = 1$. An orthogonal projection of the monodromy matrix $\mathbf{D}_{\mathrm{run,r}}$ is achieved through the application of a symmetric orthogonal projector $\mathbf{P}_{\mathrm{run,r}}$, denoted as

$$\hat{\mathbf{D}}_{\mathrm{run,r}} = \mathbf{P}_{\mathrm{run,r}} \mathbf{D}_{\mathrm{run,r}} \mathbf{P}_{\mathrm{run,r}}\,, \text{ with } \quad \mathbf{P}_{\mathrm{run,r}} := \left(\mathbf{I}_2 - \frac{\mathbf{f}_{\mathrm{s,ZD}}(\boldsymbol{\xi}_{\mathrm{s}}^{-}) \mathbf{f}_{\mathrm{s,ZD}}(\boldsymbol{\xi}_{\mathrm{s}}^{-})^{\top}}{\mathbf{f}_{\mathrm{s,ZD}}(\boldsymbol{\xi}_{\mathrm{s}}^{-})^{\top} \mathbf{f}_{\mathrm{s,ZD}}(\boldsymbol{\xi}_{\mathrm{s}}^{-})}\right)\,, \tag{6.23}$$

which effectively nullifies the effect of the trivial multiplier $\Lambda_0 = 1$. Consequently, the nontrivial multiplier $\Lambda = \mathrm{tr}(\hat{\mathbf{D}}_{\mathrm{run,r}})$ corresponds to the trace of the projected monodromy matrix $\hat{\mathbf{D}}_{\mathrm{run,r}}$, due to the nullity of one. The constraint on the solution space for the optimization of stable running gaits is established as an inequality, represented by $|\Lambda| < 1$.

6.2 Running on Compliant Ground

The Hybrid Zero Dynamics (HZD) control framework is implemented for the running model on compliant ground as delineated in Section 5.2.4. Fundamentally, the controller shares similarities with that formulated for running on rigid ground, as presented in Section 6.1. The primary distinction between these environmental scenarios lies in the augmented degrees of freedom, which remain unaffected by the actuators $\mathbf{u}$ in the joints. Consequently, the controller within the SSP is elaborated in Section 6.2.1, and it is integrated with the previously established controller in the FLP in Section 6.1.1 to construct a hybrid zero dynamics model of reduced order as detailed in Section 6.2.2. The orbital stability of the periodic solution trajectory of the resulting hybrid zero dynamics is examined in Section 6.2.3.

6.2.1 Feedback Control in SSP

The feedback controller is constructed to enforce virtual constraints on the actuated joints $\mathbf{q}_\mathrm{b}$, thus synchronizing them with the reference trajectory $\mathbf{q}_{\mathrm{r,cp}}(x_\mathrm{CM})$. In particular, the vector-valued mapping $\mathbf{q}_{\mathrm{r,cp}} : \mathbb{R} \to \mathbb{T}^4; x_\mathrm{CM} \mapsto \mathbf{q}_{\mathrm{r,cp}}(x_\mathrm{CM})$ is delineated by high-order polynomials that consider the center of mass position x_CM as the independent phase variable, necessitated by the monotonic progression of x_CM during the SSP. Subsequently, the synchronization error $\mathbf{h}_\mathrm{cp}(\mathbf{q}_\mathrm{f})$ with $\mathbf{h}_\mathrm{cp} : \mathcal{Q}_\mathrm{f} \to \mathbb{R}^4$ is identified as the control output $\mathbf{y}_\mathrm{cp}$, articulated as

$$\mathbf{y}_\mathrm{cp} := \mathbf{h}_\mathrm{cp}(\mathbf{q}_\mathrm{f}) = \mathbf{q}_\mathrm{b} - \mathbf{q}_{\mathrm{r,cp}}(x_\mathrm{CM}) \,. \tag{6.24}$$

Feedback linearization is achieved by differentiating the nonlinear control output $\mathbf{y}_\mathrm{cp}$ twice utilizing the Lie derivative along the vector field $\tilde{X}_\mathrm{cp}(\mathbf{x}_{\mathrm{f,s}}, \mathbf{u})$, as described in (5.27), with the state variables $\mathbf{x}_{\mathrm{f,s}} \in T\mathcal{Q}_\mathrm{f}$, thereby yielding

$$\dot{\mathbf{y}}_\mathrm{cp} = \mathcal{L}_{\tilde{f}} \mathbf{h}_\mathrm{cp}(\mathbf{q}_\mathrm{f}, \dot{\mathbf{q}}_\mathrm{f}) := \begin{bmatrix} -\frac{\partial \mathbf{q}_{\mathrm{r,cp}}}{\partial x_\mathrm{CM}} & \mathbf{0} & \mathbf{I}_4 \end{bmatrix} \dot{\mathbf{q}}_\mathrm{f} \,, \tag{6.25a}$$

$$\ddot{\mathbf{y}}_\mathrm{cp} = \underbrace{\left(-\frac{\partial^2 \mathbf{q}_{\mathrm{r,f}}}{\partial x_\mathrm{CM}^2} \dot{x}_\mathrm{CM}^2 - \begin{bmatrix} -\frac{\partial \mathbf{q}_{\mathrm{r,f}}}{\partial x_\mathrm{CM}} & \mathbf{0} & \mathbf{I}_4 \end{bmatrix} \mathbf{M}_\mathrm{f}^{-1} \boldsymbol{\Gamma}_\mathrm{cp} \right)}_{\mathcal{L}_{\tilde{f}}^2 \mathbf{h}_\mathrm{cp}(\mathbf{q}_\mathrm{f}, \dot{\mathbf{q}}_\mathrm{f})} + \underbrace{\left(\begin{bmatrix} -\frac{\partial \mathbf{q}_{\mathrm{r,f}}}{\partial x_\mathrm{CM}} & \mathbf{0} & \mathbf{I}_4 \end{bmatrix} \mathbf{M}_\mathrm{f}^{-1} \mathbf{B}_\mathrm{f} \right)}_{\mathcal{L}_{\tilde{g}} \mathcal{L}_{\tilde{f}} \mathbf{h}_\mathrm{cp}(\mathbf{q}_\mathrm{f})} \mathbf{u} \,, \tag{6.25b}$$

Owing to $\mathcal{L}_{\tilde{g}} \mathbf{h}_\mathrm{cp} = \mathbf{0}$ and $\mathcal{L}_{\tilde{g}} \mathcal{L}_{\tilde{f}} \mathbf{h}_\mathrm{cp} \neq \mathbf{0}$, the characterization of the vector-valued relative degree $\{r_{\mathrm{f},1}, r_{\mathrm{f},2}, r_{\mathrm{f},3}, r_{\mathrm{f},4}\} = \{2, 2, 2, 2\}$ is determined by the controller architecture with respect to the control input $\mathbf{u}$ and output $\mathbf{y}_\mathrm{cp}$.

State Feedback for Linearization

The disparity between the total relative degree ($\sum_{i=1}^{4} r_{\mathrm{f},i} = 8$) and the system dimension ($\dim(\mathbf{x}_{\mathrm{f,s}}) = 14$) indicates the presence of a six-dimensional internal dynamical subsystem that remains invariant to the input $\mathbf{u}$. Moreover, apart from these nonlinear internal dynamics, the linearizable aspect of the system exhibits a double integrator behavior between the newly defined system input $\mathbf{v}_{\mathrm{cp}} := \ddot{\mathbf{y}}_{\mathrm{cp}}$ and the output $\mathbf{y}_{\mathrm{cp}}$. This linearization arises consequent to the application of state feedback, denoted by

$$\mathbf{u} = \left(\mathcal{L}_{\tilde{g}}\mathcal{L}_{\tilde{f}}\mathbf{h}_{\mathrm{cp}}(\mathbf{q}_{\mathrm{f}})\right)^{-1}\left(\mathbf{v}_{\mathrm{cp}} - \mathcal{L}_{\tilde{f}}^{2}\mathbf{h}_{\mathrm{cp}}(\mathbf{q}_{\mathrm{f}}, \dot{\mathbf{q}}_{\mathrm{f}})\right) , \tag{6.26}$$

on the premise that the decoupling matrix $\mathcal{L}_{\tilde{g}}\mathcal{L}_{\tilde{f}}\mathbf{h}_{\mathrm{cp}}(\mathbf{q}_{\mathrm{f}})$ maintains its invertibility in the neighborhood of the equilibrium point $\mathbf{y}_{\mathrm{f}} = \mathbf{0}$. The equilibrium point is stabilized through the implementation of a high-gain PD-feedback, specified as

$$\mathbf{v}_{\mathrm{cp}} = -\mathbf{K}_{\mathrm{p,cp}}\mathbf{y}_{\mathrm{cp}} - \mathbf{K}_{\mathrm{d,cp}}\dot{\mathbf{y}}_{\mathrm{cp}} . \tag{6.27}$$

In this context, positive definite matrices $\mathbf{K}_{\mathrm{p,cp}}$ and $\mathbf{K}_{\mathrm{d,cp}}$ function as the proportional and derivative gain constants, respectively.

Coordinate Transformation for Linearization

In relation to the control task (6.24), the system is decomposed into the nonlinear internal dynamics of six dimensions and the eight-dimensional linearizable subsystem via state feedback. Specifically, the internal dynamics are associated with three degrees of underactuation occurring within the SSP on compliant ground. The coordinates $\xi_{\mathrm{cp}} := [\xi_{\mathrm{cp},1}^{\top}, \xi_{\mathrm{cp},2}^{\top}]^{\top}$ are selected to ensure the condition $\mathcal{L}_{\tilde{g}}\xi_{\mathrm{cp},1} = \mathcal{L}_{\tilde{g}}\xi_{\mathrm{cp},2} = \mathbf{0}$, consistent with the rationale detailed in Section 6.1.1. The coordinates ξ_{cp} are expressed as

$$\xi_{\mathrm{cp},1} := \begin{bmatrix} \mathbf{r}_{\mathrm{CM}} \\ \theta_{\mathrm{HAT}} \end{bmatrix} = \tilde{\mathbf{c}}_{\xi,1}(\mathbf{q}_{\mathrm{f}}) := \begin{bmatrix} \mathbf{I}_3 & \mathbf{0} \end{bmatrix} \mathbf{q}_{\mathrm{f}} , \tag{6.28a}$$

$$\xi_{\mathrm{cp},2} := \begin{bmatrix} \mathbf{p}_{\mathrm{CM}} \\ \sigma_{\mathrm{CM}} \end{bmatrix} = \tilde{\mathbf{c}}_{\xi,2}(\mathbf{q}_{\mathrm{f}}, \dot{\mathbf{q}}_{\mathrm{f}}) := \underbrace{\begin{bmatrix} \mathbf{I}_3 & \mathbf{0} \end{bmatrix} \mathbf{M}_{\mathrm{f}}(\mathbf{q}_{\mathrm{f}})}_{\sigma_{\mathrm{cp},0}(\mathbf{q}_{\mathrm{f}})} \dot{\mathbf{q}}_{\mathrm{f}} , \tag{6.28b}$$

with mappings $\tilde{\mathbf{c}}_{\xi,1} : Q_{\mathrm{f}} \to \mathbb{R}^3$ and $\tilde{\mathbf{c}}_{\xi,2} : Q_{\mathrm{f}} \times T_{\mathbf{q}_{\mathrm{f}}}Q_{\mathrm{f}} \to \mathbb{R}^3$ serving as coordinate transformations for $\xi_{\mathrm{cp},1}$ and $\xi_{\mathrm{cp},2}$, respectively. In this context, $\xi_{\mathrm{cp},2}$ encompasses the translational momentum $\mathbf{p}_{\mathrm{CM}}$ and the angular momentum σ_{CM} relative to the position $\mathbf{r}_{\mathrm{CM}}$ of the center of mass. Moreover, the coordinates relevant to the linearizable

subsystem are derived through the application of Lie derivatives, as demonstrated in (6.25), and are comprehensively elucidated in

$$\begin{bmatrix} \eta_{\mathrm{cp},1} \\ \eta_{\mathrm{cp},2} \end{bmatrix} := \begin{bmatrix} \mathbf{h}_{\mathrm{cp}}(\mathbf{q}_{\mathrm{f}}) \\ \mathcal{L}_{\tilde{f}} \mathbf{h}_{\mathrm{cp}}(\mathbf{q}_{\mathrm{f}}, \dot{\mathbf{q}}_{\mathrm{f}}) \end{bmatrix} . \tag{6.29}$$

The coordinate transformation $[\eta_{\mathrm{cp},1}^{\top}, \eta_{\mathrm{cp},2}^{\top}, \xi_{\mathrm{cp},1}^{\top}, \xi_{\mathrm{cp},2}^{\top}]^{\top} = \Psi_{\mathrm{cp}}(\mathbf{x}_{\mathrm{f,s}})$ is characterized by the mapping $\Psi_{\mathrm{cp}} : TQ_{\mathrm{f}} \to \mathbb{R}^{14}$; $\mathbf{x}_{\mathrm{f,s}} \mapsto \Psi_{\mathrm{cp}}(\mathbf{x}_{\mathrm{f,s}})$, which constitutes a diffeomorphism due to the presence of a non-singular Jacobian $\mathbf{J}_{\Psi,\mathrm{cp}} := \partial \Psi_{\mathrm{cp}} / \partial \mathbf{x}_{\mathrm{f,s}} = \left[\partial \Psi_{\mathrm{cp}} / \partial \mathbf{q}_{\mathrm{f}} \, , \partial \Psi_{\mathrm{cp}} / \partial \dot{\mathbf{q}}_{\mathrm{f}} \right]$.

Two-Stage Control Law

An alternative methodology involves linearizing the control output $\mathbf{y}_{\mathrm{cp}}$ by applying two Lie derivatives along the vector field $X_{\mathrm{cp}}(\mathbf{x}_{\mathrm{f,s}}, \mathbf{w}) := \mathbf{f}_{\mathrm{cp}}(\mathbf{x}_{\mathrm{f,s}}) + \mathbf{g}_{\mathrm{cp}}(\mathbf{x}_{\mathrm{f,s}})\mathbf{w}$, as delineated in (5.28), thereby resulting in

$$\dot{\mathbf{y}}_{\mathrm{cp}} = \mathcal{L}_f \mathbf{h}_{\mathrm{cp}}(\mathbf{q}_{\mathrm{f}}, \dot{\mathbf{q}}_{\mathrm{f}}) := \begin{bmatrix} -\frac{\partial \mathbf{q}_{\mathrm{r,cp}}}{\partial x_{\mathrm{CM}}} & \mathbf{0} & \mathbf{I}_4 \end{bmatrix} \dot{\mathbf{q}}_{\mathrm{f}} \, , \tag{6.30a}$$

$$\ddot{\mathbf{y}}_{\mathrm{cp}} = \left(-\frac{\partial^2 \mathbf{q}_{\mathrm{r,cp}}}{\partial x_{\mathrm{CM}}^2} \dot{x}_{\mathrm{CM}}^2 - \frac{\partial \mathbf{q}_{\mathrm{r,cp}}}{\partial x_{\mathrm{CM}}} \ddot{x}_{\mathrm{CM}} \right) + \mathbf{I}_4 \mathbf{w} \tag{6.30b}$$

$$= \underbrace{\left(-\frac{\partial^2 \mathbf{q}_{\mathrm{r,cp}}}{\partial x_{\mathrm{CM}}^2} \dot{x}_{\mathrm{CM}}^2 + \frac{\partial \mathbf{q}_{\mathrm{r,cp}}}{\partial x_{\mathrm{CM}}} \begin{bmatrix} \frac{1}{m_{\mathrm{total}}} & \mathbf{0} \end{bmatrix} \boldsymbol{\Gamma}_{\mathrm{cp}} \right)}_{\mathcal{L}_f^2 \mathbf{h}_{\mathrm{cp}}(\mathbf{q}_{\mathrm{f}}, \dot{\mathbf{q}}_{\mathrm{f}})} + \underbrace{\mathbf{I}_4}_{\mathcal{L}_g \mathcal{L}_f \mathbf{h}_{\mathrm{cp}}} \mathbf{w} \, , \tag{6.30c}$$

where $\ddot{x}_{\mathrm{CM}} = - \begin{bmatrix} 1/m_{\mathrm{total}} & \mathbf{0} \end{bmatrix} \boldsymbol{\Gamma}_{\mathrm{cp}}$ within (6.30b) is deduced from the equation (5.22a). Furthermore, the aspect of the system that can be linearized demonstrates a double integrator dynamic between the newly defined system input $\mathbf{v}_{\mathrm{cp}} := \ddot{\mathbf{y}}_{\mathrm{cp}}$ and the output $\mathbf{y}_{\mathrm{cp}}$. This linearization arises as a consequence of the state feedback, as articulated in

$$\mathbf{w} = \mathbf{I}_4 \left(\mathbf{v}_{\mathrm{cp}} - \mathcal{L}_f^2 \mathbf{h}_{\mathrm{cp}}(\mathbf{q}_{\mathrm{f}}, \dot{\mathbf{q}}_{\mathrm{f}}) \right) . \tag{6.31}$$

It is apparent that the decoupling matrix $\mathcal{L}_g \mathcal{L}_f \mathbf{h}_{\mathrm{cp}} = \mathbf{I}_4$ maintains its invertibility near the equilibrium point $\mathbf{y}_{\mathrm{f}} = \mathbf{0}$. The stabilization of this equilibrium point is achieved through the application of a high-gain PD feedback, as detailed in (6.27). Subsequently, the inverse dynamics described in (5.23) are utilized to determine the actuator $\mathbf{u} = \overline{\mathbf{M}}_{\mathrm{cp}} \mathbf{w} + \overline{\boldsymbol{\Gamma}}_{\mathrm{cp}}$.

6.2.2 Zero Dynamics

The application of high-gain feedback (6.27) enables the achievement of an asymptotically stable equilibrium point $\mathbf{y}_\mathrm{f} = \mathbf{0}$, where the residual internal dynamics manifest as the zero dynamics of the SSP on compliant ground. These dynamics are then combined with the zero dynamics of the FLP, as detailed for running on rigid ground in Section 6.1.1, to construct the hybrid zero dynamics relevant to running on compliant ground.

Continuous Invariance

At the equilibrium point $\mathbf{y}_\mathrm{f} = \mathbf{0}$, the zero dynamics manifold $\mathcal{Z}_\mathrm{cp}$ is established as

$$\mathcal{Z}_\mathrm{cp} := \{\mathbf{x}_{\mathrm{f,s}} \in TQ_\mathrm{f} | \, \mathbf{h}_\mathrm{cp}(\mathbf{x}_{\mathrm{f,s}}) = \mathbf{0}, \mathcal{L}_{\tilde{f}}\mathbf{h}_\mathrm{cp}(\mathbf{x}_{\mathrm{f,s}}) = \mathbf{0}\} \,, \tag{6.32}$$

which is a six-dimensional submanifold embedded within TQ_f. The coordinates ξ_cp elucidated in (6.28) facilitate the representation of the system states $\mathbf{x}_{\mathrm{f,s}} \in \mathcal{Z}_\mathrm{cp}$ within the submanifold, as given by

$$\mathbf{x}_{\mathrm{f,s}}\Big|_{\mathcal{Z}_\mathrm{cp}} = \begin{bmatrix}\mathbf{q}_\mathrm{f} \\ \dot{\mathbf{q}}_\mathrm{f}\end{bmatrix}\Big|_{\mathcal{Z}_\mathrm{cp}} = \Psi_\mathrm{cp}^{-1}\left(\begin{bmatrix}\eta_{\mathrm{cp},1} = 0 \\ \eta_{\mathrm{cp},2} = 0 \\ \xi_{\mathrm{cp},1} \\ \xi_{\mathrm{cp},2}\end{bmatrix}\right)\Bigg|_{\xi_\mathrm{cp} \in \mathcal{Z}_\mathrm{cp}} . \tag{6.33}$$

This representation employs the inverse Ψ_cp^{-1} of the diffeomorphism coordinate transformation Ψ_cp. In particular, within transformation (6.33), the velocity component $\dot{\mathbf{q}}_\mathrm{f}$ presented in $\mathcal{Z}_\mathrm{cp}$ is expressed as

$$\dot{\mathbf{q}}_\mathrm{f}\Big|_{\mathcal{Z}_\mathrm{cp}} = \begin{bmatrix}\frac{\partial \mathbf{h}_\mathrm{cp}}{\partial \mathbf{q}_\mathrm{f}} \\ \sigma_{\mathrm{cp},0}(\mathbf{q}_\mathrm{f})\end{bmatrix}^{-1}\begin{bmatrix}\eta_{\mathrm{cp},2} = 0 \\ \xi_{\mathrm{cp},2}\end{bmatrix}\Bigg|_{\mathcal{Z}_\mathrm{cp}} = \begin{bmatrix}\frac{\partial \mathbf{h}_\mathrm{cp}}{\partial \mathbf{q}_\mathrm{f}} \\ \sigma_{\mathrm{cp},0}(\mathbf{q}_\mathrm{f})\end{bmatrix}^{-1}\Bigg|_{\mathcal{Z}_\mathrm{cp}}\begin{bmatrix}\mathbf{0} \\ \mathbf{I}_3\end{bmatrix}\xi_{\mathrm{cp},2} \,, \tag{6.34}$$

making use of $\sigma_{\mathrm{cp},0}(\mathbf{q}_\mathrm{f})$ as delineated in equation (6.28b). Assuming a vanishing control error $\mathbf{y}_\mathrm{f} = \dot{\mathbf{y}}_\mathrm{f} = \mathbf{0}$ converts the feedback (6.26) for linearization on the submanifold $\mathcal{Z}_\mathrm{cp}$ into

$$\mathbf{u}^0 = -\left(\mathcal{L}_{\tilde{g}}\mathcal{L}_{\tilde{f}}\mathbf{h}_\mathrm{cp}(\mathbf{q}_\mathrm{f})\right)^{-1}\mathcal{L}_{\tilde{f}}^2\mathbf{h}_\mathrm{cp}(\mathbf{q}_\mathrm{f}, \dot{\mathbf{q}}_\mathrm{f})\Big|_{\mathcal{Z}_\mathrm{cp}} \,, \tag{6.35}$$

which provides the invariance of the SSP zero dynamics with respect to the closed-loop system.

The zero dynamics corresponding to $\dot{\xi}_{cp} = \mathbf{f}_{cp,ZD}(\xi_{cp})$ as described in $\mathcal{Z}_{cp}$ are articulated in the form of a system of ordinary differential equations, as specified in

$$\dot{\xi}_{cp,1} = \begin{bmatrix} \mathbf{I}_3 & \mathbf{0} \end{bmatrix} \dot{\mathbf{q}}_f \Big|_{\mathcal{Z}_{cp}} = \underbrace{\begin{bmatrix} \mathbf{I}_3 & \mathbf{0} \end{bmatrix} \begin{bmatrix} \frac{\partial \mathbf{h}_{cp}}{\partial \mathbf{q}_f} \\ \sigma_{cp,0}(\mathbf{q}_f) \end{bmatrix}^{-1} \Bigg|_{\mathcal{Z}_{cp}} \begin{bmatrix} \mathbf{0} \\ \mathbf{I}_3 \end{bmatrix}}_{\kappa_{cp,1}(\xi_{cp,1})} \xi_{cp,2} \,, \tag{6.36a}$$

$$\dot{\xi}_{cp,2} = \mathcal{L}_{\tilde{f}} \xi_{cp,2} \Big|_{\mathcal{Z}_{cp}} = \underbrace{\left(\dot{\mathbf{q}}_f^\top \frac{\partial \sigma_{cp,0}(\mathbf{q}_f)^\top}{\partial \mathbf{q}_f} \dot{\mathbf{q}}_f - \begin{bmatrix} \mathbf{I}_3 & \mathbf{0} \end{bmatrix} \Gamma_{cp} \right) \Big|_{\mathcal{Z}_{cp}}}_{\kappa_{cp,2}(\xi_{cp,1}, \xi_{cp,2})} \,, \tag{6.36b}$$

with $\dot{\mathbf{q}}_f \big|_{\mathcal{Z}_{cp}}$ in equation (6.36a) deduced from equation (6.34).

Discontinuous Invariance

The discontinuous invariance of the solution curve with respect to the transition mappings of take-off and landing, as described in Section 5.2.3, is examined. Specifically, it is hypothesized that the transition of state variables during take-off, from interaction with the compliant ground to the flight phase, is smooth, as articulated in equation (5.29). The discontinuity refers to the fact that the vector field differs before and after the transition.

Utilizing zero dynamics coordinates as outlined in $\xi_{cp} \in \mathcal{Z}_{cp}$ within the SSP and $\xi_f \in \mathcal{Z}_f$ within the FLP facilitates the articulation of the take-off as expressed in

$$\xi_f^+ = \begin{bmatrix} \mathbf{c}_{\xi,1}\left(\mathbf{x}_f^+\right) \\ \mathbf{c}_{\xi,2}\left(\mathbf{x}_f^+\right) \end{bmatrix} \Bigg|_{\mathcal{Z}_f} = \tilde{\Delta}_{TO}^{HZD}\left(\xi_{cp}^-\right) := \begin{bmatrix} \mathbf{c}_{\xi,1}\left(\mathbf{x}_{f,s}^-\right) \\ \mathbf{c}_{\xi,2}\left(\mathbf{x}_{f,s}^-\right) \end{bmatrix} \Bigg|_{\mathcal{Z}_{cp} \cap \tilde{\mathcal{S}}_s^f} . \tag{6.37}$$

The states of the system, $\mathbf{x}_{f,s}^- = \Psi_{cp}^{-1}\left([\mathbf{0}^\top, \mathbf{0}^\top, (\xi_{cp}^-)^\top]^\top\right)$, $\xi_{cp}^- \in \mathcal{Z}_{cp} \cap \tilde{\mathcal{S}}_s^f$, are determined in accordance with the transformation delineated in (6.33). The discontinuous invariance relative to the take-off is established through the condition specified in $\tilde{\Delta}_{TO}^{HZD}\left(\mathcal{Z}_{cp} \cap \tilde{\mathcal{S}}_s^f\right) \in \mathcal{Z}_f$.

The guard function $\tilde{g}_s^f(\mathbf{x}_{f,s})$, responsible for assessing whether the trajectory intercepts the switching surface $\tilde{\mathcal{S}}_s^f$ specified in (5.31), is formulated on the zero dynamics manifold $\mathcal{Z}_{cp}$, as delineated in

$$\tilde{g}_{s,HZD}^f(\xi_{cp}) := \tilde{g}_s^f(\mathbf{x}_{f,s}) \Big|_{\mathcal{Z}_{cp}} = 0 \,. \tag{6.38}$$

Similarly, the landing event as outlined in (5.30) is articulated within the zero dynamics manifolds $\mathcal{Z}_{\text{cp}}$ and $\mathcal{Z}_{\text{f}}$ of the SSP and FLP, respectively, as

$$\xi_{\text{cp}}^{+} = \begin{bmatrix} \tilde{\mathbf{c}}_{\xi,1}\left(\mathbf{x}_{\text{f,s}}^{+}\right) \\ \tilde{\mathbf{c}}_{\xi,2}\left(\mathbf{x}_{\text{f,s}}^{+}\right) \end{bmatrix}\Bigg|_{\mathcal{Z}_{\text{cp}}} = \tilde{\boldsymbol{\Delta}}_{\text{LD}}^{\text{HZD}}\left(\xi_{\text{f}}^{-}\right) := \begin{bmatrix} \tilde{\mathbf{c}}_{\xi,1}\left(\tilde{\boldsymbol{\Delta}}_{\text{LD}}\left(\mathbf{x}_{\text{f}}^{-}\right)\right) \\ \tilde{\mathbf{c}}_{\xi,2}\left(\tilde{\boldsymbol{\Delta}}_{\text{LD}}\left(\mathbf{x}_{\text{f}}^{-}\right)\right) \end{bmatrix}\Bigg|_{\mathcal{Z}_{\text{f}} \cap \tilde{\mathcal{S}}_{\text{f}}^{\text{s}}}, \tag{6.39}$$

wherein the system states $\mathbf{x}_{\text{f}}^{-} = \Psi_{\text{f}}^{-1}\left([\mathbf{0}^{\top}, \mathbf{0}^{\top}, (\xi_{\text{f}}^{-})^{\top}]^{\top}\right)$, $\xi_{\text{f}}^{-} \in \mathcal{Z}_{\text{f}} \cap \tilde{\mathcal{S}}_{\text{f}}^{\text{s}}$ are established in accordance with the transformation described in (6.12).
The discontinuous invariance pertaining to landing is characterized by condition $\tilde{\boldsymbol{\Delta}}_{\text{LD}}^{\text{HZD}}\left(\mathcal{Z}_{\text{f}} \cap \tilde{\mathcal{S}}_{\text{f}}^{\text{s}}\right) \in \mathcal{Z}_{\text{cp}}$. In this context, the interaction on the switching surface $\tilde{\mathcal{S}}_{\text{f}}^{\text{s}}$ defined in (5.32) is evaluated on the zero dynamics manifold $\mathcal{Z}_{\text{f}}$ as

$$\tilde{g}_{\text{f,HZD}}^{\text{s}}(\xi_{\text{f}}) := \tilde{g}_{\text{f}}^{\text{s}}(\mathbf{x}_{\text{f}})\Big|_{\mathcal{Z}_{\text{f}}} = 0\,. \tag{6.40}$$

Hybrid Invariant Zero Dynamics

The formulation of hybrid zero dynamics related to periodic running gaits on compliant ground is achieved by integrating the vector fields within the zero dynamics manifolds of the continuous SSP (as specified in equation (6.36)) and FLP (detailed in equation (6.14)), in conjunction with the discrete transition mappings outlined in equations (6.37) and (6.39). Consequently, the hybrid zero dynamics can be delineated as follows:

$$\Sigma_{\text{run,cp}}^{\text{HZD}} : \begin{cases} \dot{\xi}_{\text{cp}} = \mathbf{f}_{\text{cp,ZD}}(\xi_{\text{cp}})\,, & \xi_{\text{cp}}^{-} \notin \mathcal{Z}_{\text{cp}} \cap \tilde{\mathcal{S}}_{\text{s}}^{\text{f}}\,, \\ \xi_{\text{f}}^{+} = \tilde{\boldsymbol{\Delta}}_{\text{TO}}^{\text{HZD}}\left(\xi_{\text{cp}}^{-}\right)\,, & \xi_{\text{cp}}^{-} \in \mathcal{Z}_{\text{cp}} \cap \tilde{\mathcal{S}}_{\text{s}}^{\text{f}}\,, \\ \dot{\xi}_{\text{f}} = \mathbf{f}_{\text{f,ZD}}(\xi_{\text{f}})\,, & \xi_{\text{f}}^{-} \notin \mathcal{Z}_{\text{f}} \cap \tilde{\mathcal{S}}_{\text{f}}^{\text{s}}\,, \\ \xi_{\text{cp}}^{+} = \tilde{\boldsymbol{\Delta}}_{\text{LD}}^{\text{HZD}}\left(\xi_{\text{f}}^{-}\right)\,, & \xi_{\text{f}}^{-} \in \mathcal{Z}_{\text{f}} \cap \tilde{\mathcal{S}}_{\text{f}}^{\text{s}}\,. \end{cases} \tag{6.41}$$

The hybrid invariance of the zero dynamics is characterized by the continuous invariance of the overall solution curve $\boldsymbol{\Phi}_{\text{run,cp}}\left(\xi_{\text{f}}^{-}, t\right)$ with respect to the closed-loop system, alongside its discontinuous invariance concerning the discrete transition events.
Specifically, trajectories $\boldsymbol{\Phi}_{\text{cp,ZD}}\left(\xi_{\text{cp}}^{+}, t\right)$ and $\boldsymbol{\Phi}_{\text{f,ZD}}\left(\xi_{\text{f}}^{+}, t\right)$ constitute the solutions to the vector field within the continuous SSP and FLP domains, respectively. These trajectories are interconnected to compose the comprehensive solution curve $\boldsymbol{\Phi}_{\text{run,cp}}\left(\xi_{\text{f}}^{-}, t\right)$, facilitated through the discrete transitions of the system state variables as elucidated in (6.41).
The differential equations governing the SSP are identified as stiff due to the contact interactions with the compliant ground. Consequently, minor adjustments in the

gait trajectory through numerical optimization can result in significant variations in the ground reaction force, complicating the optimization convergence to a feasible minimum. Conversely, the differential equations in the FLP exhibit less stiffness, primarily defining a parabolic trajectory for the center of the mass position. To enhance optimization performance, the initial condition for the overall solution trajectory $\mathbf{\Phi}_{\text{run,cp}}\left(\xi_{\text{f}}^{-}, t\right)$ is determined at the conclusion of the FLP, specifically at the landing surface $\xi_{\text{f}}^{-} \in \mathcal{Z}_{\text{f}} \cap \tilde{\mathcal{S}}_{\text{f}}^{\text{s}}$. Moreover, the intervals t_{s} and t_{f} within the SSP and FLP domains, respectively, are determined in accordance with phase-dependent transition events. As a result, the duration of the step $t_{\text{run,cp}} = t_{\text{s}} + t_{\text{f}}$ is obtained by the summation of the intervals from these two domains. Periodic solutions that satisfy condition $\mathbf{\Phi}_{\text{run,cp}}\left(\xi_{\text{f}}^{-}, t\right) = \mathbf{\Phi}_{\text{run,cp}}\left(\xi_{\text{f}}^{-}, t + t_{\text{run,cp}}\right)$ are identified through the application of the multiple shooting method.

6.2.3 Orbital Stability

Considering a periodic solution $\mathbf{\Phi}_{\text{run,cp}}\left(\xi_{\text{f}}^{-}, t\right) = \mathbf{\Phi}_{\text{run,cp}}\left(\xi_{\text{f}}^{-}, t + t_{\text{run,cp}}\right)$ with period $t_{\text{run,cp}}$ for the hybrid zero dynamics system (6.41), the assessment of orbital stability is conducted through the computation of the monodromy matrix, as articulated by

$$\mathbf{D}_{\text{run,cp}} := \frac{\partial \mathbf{\Phi}_{\text{run,cp}}\left(\xi_{\text{f}}^{-}, t_{\text{run,cp}}\right)}{\partial \xi_{\text{f}}^{-}} = \mathbf{F}_{\text{r,f}}\left(t_{\text{f}}\right) \tilde{\mathbf{C}}_{\text{s}}^{\text{f}}\left(\xi_{\text{cp}}^{-}\right) \underbrace{\left.\frac{\partial \mathbf{\Phi}_{\text{cp,ZD}}\left(\xi_{\text{cp}}^{+}, t\right)}{\partial \xi_{\text{cp}}^{+}}\right|_{t=t_{\text{s}}}}_{\mathbf{F}_{\text{r,cp}}(t_{\text{s}})} \tilde{\mathbf{C}}_{\text{f}}^{\text{s}}\left(\xi_{\text{f}}^{-}\right) , \tag{6.42}$$

with the fundamental matrix solution $\mathbf{F}_{\text{r,f}}\left(t\right)$ adopted from the FLP in the monodromy matrix in (6.20). Analogously, $\mathbf{F}_{\text{r,cp}}\left(t_{\text{s}}\right)$ represents the fundamental matrix solution within the SSP domain. The saltation matrices, denoted by $\tilde{\mathbf{C}}_{\text{s}}^{\text{f}}\left(\xi_{\text{cp}}^{-}\right)$ and $\tilde{\mathbf{C}}_{\text{f}}^{\text{s}}\left(\xi_{\text{f}}^{-}\right)$, are defined as

$$\tilde{\mathbf{C}}_{\text{f}}^{\text{s}}\left(\xi_{\text{f}}^{-}\right) := \frac{\partial \tilde{\mathbf{\Delta}}_{\text{LD}}^{\text{HZD}}\left(\xi_{\text{f}}^{-}\right)}{\partial \xi_{\text{f}}^{-}} + \frac{\left(\mathbf{f}_{\text{cp,ZD}}\left(\xi_{\text{cp}}^{+}\right) - \frac{\partial \tilde{\mathbf{\Delta}}_{\text{LD}}^{\text{HZD}}(\xi_{\text{f}}^{-})}{\partial \xi_{\text{f}}^{-}} \mathbf{f}_{\text{f,ZD}}(\xi_{\text{f}}^{-})\right) \tilde{\mathbf{n}}_{\text{f}}^{\text{s}}(\xi_{\text{f}}^{-})}{\tilde{\mathbf{n}}_{\text{f}}^{\text{s}}(\xi_{\text{f}}^{-}) \mathbf{f}_{\text{f,ZD}}(\xi_{\text{f}}^{-})} , \tag{6.43a}$$

$$\tilde{\mathbf{C}}_{\text{s}}^{\text{f}}\left(\xi_{\text{cp}}^{-}\right) := \frac{\partial \tilde{\mathbf{\Delta}}_{\text{TO}}^{\text{HZD}}\left(\xi_{\text{cp}}^{-}\right)}{\partial \xi_{\text{cp}}^{-}} + \frac{\left(\mathbf{f}_{\text{f,ZD}}\left(\xi_{\text{f}}^{+}\right) - \frac{\partial \tilde{\mathbf{\Delta}}_{\text{TO}}^{\text{HZD}}(\xi_{\text{cp}}^{-})}{\partial \xi_{\text{cp}}^{-}} \mathbf{f}_{\text{cp,ZD}}(\xi_{\text{cp}}^{-})\right) \tilde{\mathbf{n}}_{\text{s}}^{\text{f}}(\xi_{\text{cp}}^{-})}{\tilde{\mathbf{n}}_{\text{s}}^{\text{f}}(\xi_{\text{cp}}^{-}) \mathbf{f}_{\text{cp,ZD}}(\xi_{\text{cp}}^{-})} , \tag{6.43b}$$

wherein the normal vectors $\tilde{\mathbf{n}}_{\mathrm{f}}^{\mathrm{s}}(\boldsymbol{\xi}_{\mathrm{f}}) := (\partial \tilde{g}_{\mathrm{f,HZD}}^{\mathrm{s}} \big/ \partial \boldsymbol{\xi}_{\mathrm{f}})$ pertain to the landing surface and $\tilde{\mathbf{n}}_{\mathrm{s}}^{\mathrm{f}}(\boldsymbol{\xi}_{\mathrm{cp}}) := (\partial \tilde{g}_{\mathrm{s,HZD}}^{\mathrm{f}} \big/ \partial \boldsymbol{\xi}_{\mathrm{cp}})$ correspond to the take-off surface. Notably, the conditions specified in

$$\tilde{\mathbf{n}}_{\mathrm{s}}^{\mathrm{f}}(\boldsymbol{\xi}_{\mathrm{cp}}^{-})\mathbf{f}_{\mathrm{cp,ZD}}(\boldsymbol{\xi}_{\mathrm{cp}}^{-}) \neq 0, \qquad \boldsymbol{\xi}_{\mathrm{cp}}^{-} \in \mathcal{Z}_{\mathrm{cp}} \cap \tilde{\mathcal{S}}_{\mathrm{s}}^{\mathrm{f}}, \tag{6.44a}$$

$$\tilde{\mathbf{n}}_{\mathrm{f}}^{\mathrm{s}}(\boldsymbol{\xi}_{\mathrm{f}}^{-})\mathbf{f}_{\mathrm{f,ZD}}(\boldsymbol{\xi}_{\mathrm{f}}^{-}) \neq 0, \qquad \boldsymbol{\xi}_{\mathrm{f}}^{-} \in \mathcal{Z}_{\mathrm{f}} \cap \tilde{\mathcal{S}}_{\mathrm{f}}^{\mathrm{s}}, \tag{6.44b}$$

are satisfied given that the trajectory $\boldsymbol{\Phi}_{\mathrm{run,cp}}\left(\boldsymbol{\xi}_{\mathrm{f}}^{-}, t\right)$ intersects the transition surfaces in a transverse manner.

The (6×6)-dimensional monodromy matrix $\mathbf{D}_{\mathrm{run,cp}}$ is characterized by six eigenvalues, commonly referred to as Floquet multipliers. As expounded by the Abel–Ruffini theorem in [80, Section 4], it is generally impractical to solve equations of degree higher than four by radicals [2]. Since the eigenvalue problem involves determining the roots of the characteristic polynomial, the resolution of these six eigenvalues necessitates the utilization of iterative algorithms. Indeed, the orthogonal projection described in (6.23) produces a matrix of equivalent dimension with a nullity of one. This suggests that the trivial multiplier $\Lambda_0 = 1$ becomes zero following the projection, even though it still necessitates iterative determination, which requires considerable computational resources.

Nonetheless, to reduce computational effort and enhance convergence behavior, it is crucial to minimize the number of eigenvalues requiring computation. Consequently, an alternative methodology has been formulated to directly reduce the dimensionality of the monodromy matrix by utilizing orthogonal projection. A (6×5)-dimensional matrix $\mathbf{Q}_{\perp}$, composed of five basis vectors forming its columns, is constructed through the application of Algorithm 1 in Appendix B. These basis vectors establish the orthogonal complement to the specified eigenvector $\mathbf{f}_{\mathrm{f,ZD}}(\boldsymbol{\xi}_{\mathrm{f}}^{-})$ associated with the trivial eigenvalue $\Lambda_0 = 1$, which symbolizes the tangent vector of the solution curve at the landing surface. Subsequently, the (6×6)-dimensional monodromy matrix $\mathbf{D}_{\mathrm{run,cp}}$ is projected onto the orthogonal subspace, as outlined in

$$\hat{\mathbf{D}}_{\mathrm{run,cp}} = \mathbf{Q}_{\perp}^{\top} \mathbf{D}_{\mathrm{run,cp}} \mathbf{Q}_{\perp}, \tag{6.45}$$

where the five eigenvalues of the projected monodromy matrix $\hat{\mathbf{D}}_{\mathrm{run,cp}} \in \mathbb{R}^{5\times5}$ are determined through the iterative Algorithm 2 in Appendix B.

It is generally observed that the eigenvalues of the orthogonal complement to an eigenvector of a given matrix may differ from those of the original matrix. In specific cases

[2] A solution expressed in radicals constitutes a closed-form expression that incorporates algebraic operations including addition, subtraction, multiplication, and division.

such as symmetric matrices, the eigenvalues of the orthogonal complement coincide with those of the original matrix, except for the eigenvalue associated with the particular eigenvector used for projection. The primary objective of the eigenvalue problem addressed herein is to determine the orbital stability of the periodic solution curve rather than to compute the exact eigenvalues. Employing orthogonal projection as a coordinate transformation for the fundamental matrix solution facilitates a deeper understanding of the subspace orthogonal to the flow direction, thereby elucidating the convergence or divergence behavior of state perturbations.
Consequently, the eigenvalues of the projected monodromy matrix $\hat{\mathbf{D}}_{\text{run,cp}}$ are identified as the nontrivial Floquet multipliers Λ, which are evaluated according to the criterion for orbital stability. Specifically, the periodic solution curve is considered stable provided that the magnitude of the largest multiplier satisfies $|\Lambda| < 1$.

7 Numerical Optimization

The process of generating highly energy-efficient walking and running gaits for the examined biped model is conceptualized as an optimization problem, with the ultimate objective of minimizing energy consumption during locomotion. Constraints of physical feasibility and gait stability in the simulation are incorporated into the optimization framework. This constrained optimization problem is addressed using a Sequential Quadratic Programming (SQP) algorithm.

Specifically, the previously developed Hybrid Zero Dynamics (HZD) controller ensures synchronization of the robot's movement with reference motion, which is parameterized through high-order polynomials. The associated polynomial parameters are considered as gait parameters subject to optimization. Additionally, to maintain flexibility in redesigning the mechanical system post the production phase of a biped robot, elastic compliant mechanisms are employed to connect adjacent rigid body segments. The characteristics of these elastic couplings are deemed mutable mechanical parameters that can also be optimized.

The formulated optimization problem seeks to simultaneously optimize these gait parameters of the controller and the elastic coupling parameters to enhance the energy efficiency across varying gaits and environments. Evidently, a salient advantage of the simultaneous optimization formulation is that it ensures the optimized gait aligns closely with the mechanical system's resonance behavior, thereby minimizing actuator efforts required for locomotion across diverse scenarios.

This chapter expounds upon an optimization problem structured as follows: in Section 7.1, the objective function subject to minimization is articulated; in Section 7.2, the configuration of elastic couplings among the robot's rigid body segments is delineated; in Section 7.3, the incorporation of Bézier curves as high-order polynomial reference trajectories into the controller design is outlined; in Section 7.4, optimization-targeted gait parameters for bipedal walking and running are derived; in Section 7.5, optimization constraints ensuring physically feasible and stable periodic gaits are described; and in Section 7.6, a synopsis of the formulation as a nonlinear constrained optimization problem is presented.

7.1 Objective Function of Optimization

The goal of the optimization is to enhance the energy efficiency of locomotion, which is assessed using the dimensionless metric known as the cost of transport (CoT). The CoT is conceptualized as the ratio of the aggregate energy consumption to the product of the travel distance and the robot's total mass. In simulation scenarios, periodic gaits are treated as repetitions of singular step periods; consequently, the energy expenditure during a single step is utilized to assess the CoT, as expressed in

$$f_{\text{obj}}(\xi_{\text{opt}}) = \text{CoT} := \frac{\sum_{i=1}^{4} \int_0^{t_{\text{step}}} \max\left(0, P_{\text{mech},i}\right) \mathrm{d}t}{m_{\text{total}} g \ell_{\text{step}}} , \tag{7.1}$$

while the total mass m_{total} is described in (3.3). The exhaustive array of optimization parameters, as elucidated in ξ_{opt}, includes both the mechanical design parameters of the compliant mechanisms operating as elastic couplings, as specified in Section 7.2, and the gait parameters relevant to walking or running, as outlined in Section 7.4.
The mechanical power $P_{\text{mech},i} := u_i \dot{q}_{\text{b},i}$, $i \in [1, 4]$ is ascertained from the torque $u_i \in \mathbf{u}$ generated by the electric drivetrain in conjunction with the angular velocity $\dot{q}_{\text{b},i} \in \dot{\mathbf{q}}_{\text{b}}$ of the joint. The recuperation of electrical energy during actuator deceleration is disregarded, thereby excluding negative mechanical power, which signals the motor operating in generator mode, through the application of the max$(\cdot)$ operator. Furthermore, in this preliminary analysis, Ohmic losses are omitted based on the presumption $I^2R \ll P_{\text{mech},i}$, $i \in [1, 4]$, wherein I denotes the electric current and R represents the electrical resistance.

7.2 Parallel Elastic Couplings

The studies presented in [17, 18] have investigated improvements in the energy efficiency of bipedal locomotion facilitated by parallel elastic couplings. These researches particularly focus on the walking gait of robotic models with three and five segments operating on a rigid, flat surface. Building on their findings, the present thesis extends the framework to include a range of complex gaits and varied environmental conditions, as previously elaborated in the earlier chapters.
Acknowledging the dependency of elastic potential energy $V_{\text{f,e}}(\mathbf{q}_{\text{f}})$ on the configuration $\mathbf{q}_{\text{f}}$, the equations of motion (3.5) are augmented by the generalized force $\boldsymbol{\Gamma}_{\text{e}}(\mathbf{q}_{\text{f}}) := \partial V_{\text{f,e}}(\mathbf{q}_{\text{f}})/\partial \mathbf{q}_{\text{f}}$ resulting from the elastic couplings, as delineated in

$$\mathbf{M}_{\text{f}}\ddot{\mathbf{q}}_{\text{f}} + \underbrace{\boldsymbol{\Gamma}_{\text{f}}(\mathbf{q}_{\text{f}}, \dot{\mathbf{q}}_{\text{f}}) + \boldsymbol{\Gamma}_{\text{e}}(\mathbf{q}_{\text{f}})}_{\boldsymbol{\Gamma}_{\text{gen}}(\mathbf{q}_{\text{f}}, \dot{\mathbf{q}}_{\text{f}})} = \mathbf{B}_{\text{f}}\mathbf{u} + \mathbf{G}_1^{\top}\mathbf{F}_1 + \mathbf{G}_2^{\top}\mathbf{F}_2 . \tag{7.2}$$

It is noteworthy that the integration of all generalized forces, particularly the recently introduced elastic coupling as referenced in $\mathbf{\Gamma}_{\text{gen}}(\mathbf{q}_{\text{f}}, \dot{\mathbf{q}}_{\text{f}})$, does not alter the derivation process of the control design nor the resultant hybrid zero dynamics pertaining to walking and running, as previously discussed. Consequently, the control design employed is derived from scenarios wherein elastic coupling is absent. Of greater significance is the parameterization of the elastic coupling, which is introduced as mechanical design parameters that require optimization.
In practical applications, parallel elastic coupling is achieved through the utilization of torsional springs, which serve to interconnect multiple rigid body segments. These torsional springs are implemented via compliant mechanisms, exhibiting nonlinear torque-angular displacement characteristics [187]. Within the framework of simulation-based efficiency analysis, these properties are modeled using cubic splines [1] characterized by $n_{\text{sp}} = 9$ independent control points. In particular, one of the control points is located at the neutral angle, corresponding to zero elastic torque, whereas the remaining $n_{\text{sp}} - 1 = 8$ control points modulate the nonlinear characteristics of the spline, namely, $\boldsymbol{\alpha}_k \in \mathbb{R}^8$.
The optimization process involves the simultaneous optimization of both the design parameters of the compliant mechanisms and the gait parameters in the controller, seeking to harmonize the gait with the mechanical system, thereby enhancing energy efficiency across various scenarios.

7.2.1 Configuration of Parallel Elastic Couplings

Theoretically, any pair of segments exhibiting relative rotational motion can be elastically coupled. However, the principal aim of this research is to demonstrate the feasibility of elastic coupling within a robotic prototype via empirical experimentation. To ensure practical applicability, this investigation is confined to the elastic coupling of adjacent segments, resulting in three distinct configurations, as specified in

- Upper body - Thigh (UT): Coupling between upper-body and thighs through two identical mechanisms in Figure 7.1a;
- Thigh - Thigh (TT): Coupling between thighs through a single symmetric mechanism in Figure 7.1b;
- Thigh - Shank (TS): Coupling between thighs and shanks through two identical mechanisms in Figure 7.1c.

and depicted in Figure 7.1.

[1] Cubic splines provide smooth, C^2-continuous curves that interpolate all given data points, making them ideal for applications requiring high smoothness, such as data fitting. Their piecewise definition allows for efficient representation of long, complex curves, while local control ensures that changes to one segment

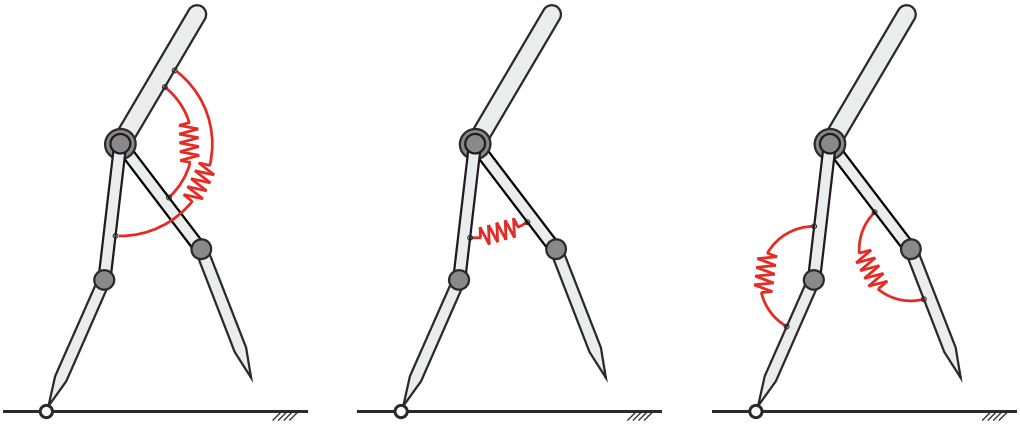

(a) Elastic coupling between the upper body and both thighs.

(b) Elastic coupling between the thighs.

(c) Elastic coupling between the thigh and the shank.

Figure 7.1: Configurations of elastic couplings between the neighboring rigid body segments.

Earlier investigations in [17, 18] indicate that the integration of elastic couplings between the thighs and shanks (TS) at the knee joints results in merely negligible improvements in energy efficiency. Hence, this aspect is excluded from the scope of this thesis. Owing to the symmetry intrinsic to the robot model, the UT configuration permits the integration of two identical compliant mechanisms within both left and right legs. The neutral angle $\varphi_{\mathrm{UT},0}$, defined as the position where the elastic torque vanishes, can be modified through specific design and assembly procedures. Accordingly, these angles are considered as parameters for optimization. The design parameters are formulated as

$$\boldsymbol{\alpha}_{\mathrm{UT}} := [\varphi_{\mathrm{UT},0}, \boldsymbol{\alpha}_{k,\mathrm{UT}}^{\top}]^{\top} \in \mathbb{R}^{n_{\mathrm{sp}}} , \tag{7.3}$$

with $\boldsymbol{\alpha}_{k,\mathrm{UT}}$ serving as the control points to define a cubic spline.
In contrast, to achieve symmetry, a singular coupling is employed between the two thighs. In particular, the relative angle of zero between the thighs coincides with the neutral angle $\varphi_{\mathrm{TT},0} = 0$ of the elastic compliant mechanisms, characterized by an absence of elastic torque. Furthermore, the characteristic curve exhibits rotational symmetry with respect to the neutral angle. Consequently, the design parameters are constituted by the control points of the cubic spline, specifically

$$\boldsymbol{\alpha}_{\mathrm{TT}} := \boldsymbol{\alpha}_{k,\mathrm{TT}} \in \mathbb{R}^{(n_{\mathrm{sp}}-1)/2} . \tag{7.4}$$

affect only nearby sections. Flexible boundary conditions (e.g., natural or clamped) further enhance their adaptability to various scenarios.

7.3 Reference Trajectory in Controller

The reference trajectory is integral to the specification of holonomic virtual constraints within the framework of HZD control. Essentially, the implementation of these virtual constraints is linearized through the application of feedback linearization. This methodology is supported by coordinate transformations that operate as local diffeomorphisms. To achieve this, high-order, smooth (C^∞) Bézier curves, as characterized in Appendix C are utilized to delineate the reference trajectories.
As per the controller specified in Section 4.1.1, the parameter set [2] $\boldsymbol{\alpha}_\mathrm{s} \in \mathbb{R}^{4\times(n+1)}$ is employed to define four independent Bézier curves of order n, which function as the reference trajectory $\mathbf{q}_\mathrm{r}(s, \boldsymbol{\alpha}_\mathrm{s}) \in \mathbb{T}^4$ during the single support phase. Given that the optimization determines both the initial θ^+_virt and terminal orientation θ^-_virt of the virtual leg, the independent variable $\theta_\mathrm{virt} \in [\theta^+_\mathrm{virt}, \theta^-_\mathrm{virt}]$, which demonstrates monotonically increasing behavior, is subjected to normalization via the mapping $s : S^1 \to \mathbb{R}$, as outlined by

$$s = s(\theta_\mathrm{virt}) := \frac{\theta_\mathrm{virt} - \theta^+_\mathrm{virt}}{\theta^-_\mathrm{virt} - \theta^+_\mathrm{virt}} \in [0, 1] \,, \tag{7.5}$$

which is utilized for defining the reference $\mathbf{q}_{\mathrm{r},s}(\theta_\mathrm{virt}) = \mathbf{q}_\mathrm{r}(s(\theta_\mathrm{virt}), \boldsymbol{\alpha}_\mathrm{s})$ of the virtual constraint (4.1). An analogous formulation, which accounts for the differentiation relationship $\mathrm{d}\theta_\mathrm{virt} = (\theta^-_\mathrm{virt} - \theta^+_\mathrm{virt})\mathrm{d}s$ resulting from the normalization (7.5), is employed for the partial derivatives $\partial\mathbf{q}_{\mathrm{r},s}/\partial\theta_\mathrm{virt}$ and $\partial^2\mathbf{q}_{\mathrm{r},s}/\partial\theta^2_\mathrm{virt}$ in equations (4.2) and (4.3), respectively. Particularly, the evaluation of the reference trajectory $\mathbf{q}_{\mathrm{r},s}$ at the initial ($\theta_\mathrm{virt} = \theta^+_\mathrm{virt}$) and terminal points ($\theta_\mathrm{virt} = \theta^-_\mathrm{virt}$) is presented as

$$\mathbf{q}_{\mathrm{r},s}(\theta^+_\mathrm{virt}) = \mathbf{q}_\mathrm{r}(s, \boldsymbol{\alpha}_\mathrm{s})\Big|_{s=0} = \boldsymbol{\alpha}_{\mathrm{s},0} \,, \qquad \mathbf{q}_{\mathrm{r},s}(\theta^-_\mathrm{virt}) = \mathbf{q}_\mathrm{r}(s, \boldsymbol{\alpha}_\mathrm{s})\Big|_{s=1} = \boldsymbol{\alpha}_{\mathrm{s},n} \,, \tag{7.6}$$

followed by the corresponding partial derivatives,

$$\frac{\partial\mathbf{q}_{\mathrm{r},s}(\theta_\mathrm{virt})}{\partial\theta_\mathrm{virt}}\bigg|_{\theta^+_\mathrm{virt}} = \frac{1}{\theta^-_\mathrm{virt} - \theta^+_\mathrm{virt}} \frac{\partial\mathbf{q}_\mathrm{r}(s, \boldsymbol{\alpha}_\mathrm{s})}{\partial s}\bigg|_{s=0} = n\frac{\boldsymbol{\alpha}_{\mathrm{s},1} - \boldsymbol{\alpha}_{\mathrm{s},0}}{\theta^-_\mathrm{virt} - \theta^+_\mathrm{virt}} \,, \tag{7.7a}$$

$$\frac{\partial\mathbf{q}_{\mathrm{r},s}(\theta_\mathrm{virt})}{\partial\theta_\mathrm{virt}}\bigg|_{\theta^-_\mathrm{virt}} = \frac{1}{\theta^-_\mathrm{virt} - \theta^+_\mathrm{virt}} \frac{\partial\mathbf{q}_\mathrm{r}(s, \boldsymbol{\alpha}_\mathrm{s})}{\partial s}\bigg|_{s=1} = n\frac{\boldsymbol{\alpha}_{\mathrm{s},n} - \boldsymbol{\alpha}_{\mathrm{s},n-1}}{\theta^-_\mathrm{virt} - \theta^+_\mathrm{virt}} \,. \tag{7.7b}$$

[2] While the reference trajectory $\mathbf{q}_\mathrm{r}$ is specified within the configuration space $\mathcal{Q}_\mathrm{b} \subset \mathbb{T}^4$ of the actuated joints $\mathbf{q}_\mathrm{b} \in \mathcal{Q}_\mathrm{b}$, which exists as an open subset of a four-dimensional torus $\mathbb{T}^4 = (S^1)^4$, it is imperative to recognize that the control points α_s may be positioned outside the unit circle. This occurs because the resultant Bézier curve is confined within the convex hull of these control points, without necessarily intersecting the control points themselves, as elucidated in Figure C.1 in Appendix C. Consequently, $\alpha_\mathrm{s} \in \mathbb{R}$ is presumed, and the resultant reference $\mathbf{q}_\mathrm{r} \in \mathcal{Q}_\mathrm{b}$ is restricted through optimization constraints.

As the parameterization of the reference trajectory pertaining to the virtual constraints in the other continuous phases is applied in a comparable manner, a detailed description is deemed unnecessary.

7.4 Optimization Parameter for Gait

To enhance clarity, the optimization parameters are delineated for the introduced gait scenarios. Specifically, Section 7.4.1 provides a summary of the gait parameters characterizing walking with an instantaneous double support phase on rigid ground; Section 7.4.2 examines walking with a non-instantaneous double support phase; Section 7.4.3 and Section 7.4.4 explicate running on rigid and compliant ground surfaces, respectively.

7.4.1 Walking with Instantaneous DSP

The objective of parameter specification is to establish a periodic solution on the zero dynamics manifold, which epitomizes a periodic walking gait. Fundamentally, the zero dynamics manifold is formulated by reference trajectory parameters $\boldsymbol{\alpha}_\mathrm{s} \in \mathbb{R}^{4\times(n+1)}$ with $n = 6$, which are instrumental in defining the virtual constraints (4.1) during the SSP. Alterations in reference trajectory parameters $\boldsymbol{\alpha}_\mathrm{s}$ lead to variations in the corresponding gait, thereby influencing energy efficiency.
Subsequently, the initial conditions $\boldsymbol{\xi}_\mathrm{s}^- := [\xi_{\mathrm{s},1}^-, \xi_{\mathrm{s},2}^-]^\top \in \mathcal{Z}_{\mathrm{s,r}} \cap \mathcal{S}_\mathrm{s}$ on the impact surface, alongside the period duration t_s, constitute essential parameters for ensuring a periodic solution that fulfills condition $\boldsymbol{\Phi}_{\mathrm{w,i}}(\boldsymbol{\xi}_\mathrm{s}^-, t) = \boldsymbol{\Phi}_{\mathrm{w,i}}(\boldsymbol{\xi}_\mathrm{s}^-, t + t_\mathrm{s})$ on the zero dynamics manifold $\mathcal{Z}_{\mathrm{s,r}}$.
For a simpler expression of the equality constraints which will be discussed in Section 7.5.3, it is equivalent to regard the angle θ_virt^- and velocity $\dot{\theta}_\mathrm{virt}^-$ of the virtual leg immediately before impact as optimization parameters, instead of $\boldsymbol{\xi}_\mathrm{s}^-$. This equivalence is provided by the boundary characteristics of the Bézier curve at $\xi_{\mathrm{s},1}^- = \theta_\mathrm{virt}^-$, as specified in (7.6) and (7.7b). This yields the state space variables $\mathbf{x}_\mathrm{s}^- := [(\mathbf{q}_\mathrm{s}^-)^\top, (\dot{\mathbf{q}}_\mathrm{s}^-)^\top]^\top \in \mathcal{S}_\mathrm{s}$ before impact evaluated as

$$\mathbf{q}_\mathrm{s}^-\Big|_{\mathcal{Z}_{\mathrm{s,r}}} = \begin{bmatrix}\theta_\mathrm{virt}\\ \mathbf{q}_\mathrm{b}\end{bmatrix}\Big|_{\mathcal{Z}_{\mathrm{s,r}}\cap\mathcal{S}_\mathrm{s}} = \begin{bmatrix}\theta_\mathrm{virt}^-\\ \mathbf{q}_{\mathrm{r,s}}(\theta_\mathrm{virt}^-)\end{bmatrix} = \begin{bmatrix}\theta_\mathrm{virt}^-\\ \boldsymbol{\alpha}_{\mathrm{s},n}\end{bmatrix}, \tag{7.8a}$$

$$\dot{\mathbf{q}}_\mathrm{s}^-\Big|_{\mathcal{Z}_{\mathrm{s,r}}} = \begin{bmatrix}\dot{\theta}_\mathrm{virt}\\ \dot{\mathbf{q}}_\mathrm{b}\end{bmatrix}\Big|_{\mathcal{Z}_{\mathrm{s,r}}\cap\mathcal{S}_\mathrm{s}} = \begin{bmatrix}1\\ \frac{\partial \mathbf{q}_{\mathrm{r,s}}(\theta_\mathrm{virt})}{\partial\theta_\mathrm{virt}}\Big|_{\theta_\mathrm{virt}^-}\end{bmatrix}\dot{\theta}_\mathrm{virt}^- = \begin{bmatrix}1\\ n\frac{\boldsymbol{\alpha}_{\mathrm{s},n}-\boldsymbol{\alpha}_{\mathrm{s},n-1}}{\theta_\mathrm{virt}^- - \theta_\mathrm{virt}^+}\end{bmatrix}\dot{\theta}_\mathrm{virt}^-. \tag{7.8b}$$

Ultimately, by substituting the expressions (7.8) into the definitions provided for the virtual leg angle $\xi_{\mathrm{s},1} = \theta_\mathrm{virt}$ and the conjugate generalized momentum $\xi_{\mathrm{s},2} = \sigma_\mathrm{s}$ within

the contexts of (4.5) and (4.6), respectively, one can derive the local coordinates $\xi_s := [\xi_{s,1}, \xi_{s,2}]^\top \in \mathcal{Z}_{s,r}$ on the zero dynamics manifold $\mathcal{Z}_{s,r}$.
Notably, the initial virtual leg angle θ^+_{virt} at the commencement of the SSP is included within the expression (7.8b) and is thus considered an additional optimization parameter. In summary, the optimization parameters pertinent to walking with an instantaneous double support phase are elucidated as [3]

$$\xi_{opt,w} := [\theta^+_{virt}, \theta^-_{virt}, \dot{\theta}^-_{virt}, t_s, \mathrm{vec}(\boldsymbol{\alpha}_s)^\top]^\top \in \mathbb{T}^2 \times \mathbb{R}^2 \times \mathbb{R}^{28} . \tag{7.9}$$

7.4.2 Walking with Non-Instantaneous DSP

Walking gaits that include a non-instantaneous DSP are characterized by periodic solutions that progress through continuous single and double support phases. For the hybrid zero dynamics system (4.45), periodic solutions that satisfy the condition $\boldsymbol{\Phi}_{w,d}(\xi^-_s, t) = \boldsymbol{\Phi}_{w,d}(\xi^-_s, t + t_{w,d})$ include solution curves $\boldsymbol{\Phi}_{s,ZD}(\xi^+_s, t)$ and $\boldsymbol{\Phi}_{d,ZD}(\xi^+_d, t)$ within the SSP and DSP domains, respectively. In this study, the discontinuous mappings $\xi^+_s = \boldsymbol{\Delta}^{HZD}_{LO}(\xi^-_d)$ and $\xi^+_d = \boldsymbol{\Delta}^{HZD}_{TD}(\xi^-_s)$ are utilized to ascertain the state variables at the commencement of the SSP and DSP, respectively.
Subsequently, ξ^-_s is parameterized in a way analogous to the approach detailed in Section 7.4.1. Similarly, the state variables $\xi^-_d := [\xi^-_{d,1}, \xi^-_{d,2}]^\top \in \mathcal{Z}_d \cap \mathcal{S}^s_d$ on the lift-off surface are deduced from the associated configuration $\mathbf{q}^-_d$ and velocity $\dot{\mathbf{q}}^-_d$, through the application of coordinate transformations (4.29) and (4.30).
Furthermore, these variables are determined with respect to the angle $\theta^-_{virt,d}$ and velocity $\dot{\theta}^-_{virt,d}$ of the virtual leg, together with the reference trajectory $\mathbf{q}_{r,d}(\theta_{virt,d})$, as demonstrated in

$$\mathbf{q}^-_d\Big|_{\mathcal{Z}_d} = \begin{bmatrix} \theta_{virt,d} \\ \mathbf{q}_{di} \end{bmatrix}\Big|_{\mathcal{Z}_d \cap \mathcal{S}^s_d} = \begin{bmatrix} \theta^-_{virt,d} \\ \mathbf{q}_{r,d}(\theta^-_{virt,d}) \end{bmatrix} = \begin{bmatrix} \theta^-_{virt,d} \\ \boldsymbol{\alpha}_{d,n} \end{bmatrix} , \tag{7.10a}$$

$$\dot{\mathbf{q}}^-_d\Big|_{\mathcal{Z}_d} = \begin{bmatrix} \dot{\theta}_{virt,d} \\ \dot{\mathbf{q}}_{di} \end{bmatrix}\Big|_{\mathcal{Z}_d \cap \mathcal{S}^s_d} = \begin{bmatrix} 1 \\ \frac{\partial \mathbf{q}_{r,d}(\theta_{virt,d})}{\partial \theta_{virt,d}}\Big|_{\theta^-_{virt,d}} \end{bmatrix} \dot{\theta}^-_{virt,d} = \begin{bmatrix} 1 \\ n \frac{\boldsymbol{\alpha}_{d,n} - \boldsymbol{\alpha}_{d,n-1}}{\theta^-_{virt,d} - \theta^+_{virt,d}} \end{bmatrix} \dot{\theta}^-_{virt,d} . \tag{7.10b}$$

The overall duration $t_{w,d} = t_s + t_d$ of the step is determined by aggregating the intervals from these two domains, which are considered additional optimization parameters subject to discrete transition events.
Furthermore, the controller in a fully actuated DSP exerts a direct influence on the convergence rate by ensuring the synchronization of the generalized momentum σ_d

[3] The vectorization transformation, represented by operator vec(·), reorganizes a matrix with a dimension of $n \times m$ into a column vector with a dimension of nm.

with its reference trajectory $\sigma_{\mathrm{r,d}}(\theta_{\mathrm{virt}})$, as explicated in (4.37). This reference trajectory is characterized by a sixth-order Bézier curve involving parameters $\boldsymbol{\alpha}_\sigma \in \mathbb{R}^7$.
Nonetheless, as the zero dynamics are delineated by the dynamics of the feedback error, as defined in (4.38), the solution space of the reference trajectory $\sigma_{\mathrm{r,d}}(\theta_{\mathrm{virt}})$ becomes indefinitely large. Notably, owing to the high gain feedback $K_{\sigma_{\mathrm{d}}}$, the generalized momentum $\sigma_{\mathrm{d}}(t_{\mathrm{d}})$ eventually aligns with the reference $\sigma_{\mathrm{r,d}}(\theta_{\mathrm{virt}})$ at the conclusion of a step, irrespective of the magnitude of the initial error. This results in challenges in the numerical optimization, as the solution may oscillate between various parameterizations of the reference $\sigma_{\mathrm{r,d}}(\theta_{\mathrm{virt}})$, thereby causing poor convergence.
To confine the solution space of the reference trajectory $\sigma_{\mathrm{r,d}}(\theta_{\mathrm{virt}})$, the initial Bézier parameter $\alpha_{\sigma,0} \in \boldsymbol{\alpha}_\sigma$ is determined by the initial generalized momentum $\sigma_{\mathrm{d}}(t_{\mathrm{d}} = 0)$ at the commencement of the DSP, specifically $\alpha_{\sigma,0} = \sigma_{\mathrm{r,d}}(\theta^+_{\mathrm{virt,d}}) = \sigma_{\mathrm{d}}(t_{\mathrm{d}} = 0)$, by employing the boundary property of the Bézier curve as demonstrated in (7.6). Thus, the remaining Bézier parameters $\tilde{\boldsymbol{\alpha}}_\sigma \in \mathbb{R}^6 \in \boldsymbol{\alpha}_\sigma$ are then positioned for optimization. Furthermore, the projection matrix $\mathbf{P}_{\mathbf{u},(3)} \in \mathbb{R}^{4\times3}$, as delineated in (3.63), constitutes the residual optimization parameters, which are encapsulated as

$$\begin{aligned}\boldsymbol{\xi}_{\mathrm{opt,d}} := [&\theta^+_{\mathrm{virt,s}}, \theta^-_{\mathrm{virt,s}}, \dot{\theta}^-_{\mathrm{virt,s}}, t_{\mathrm{s}}, \mathrm{vec}(\boldsymbol{\alpha}_{\mathrm{s}})^\top, \theta^+_{\mathrm{virt,d}}, \theta^-_{\mathrm{virt,d}}, \dot{\theta}^-_{\mathrm{virt,d}}, t_{\mathrm{d}},\\ &\mathrm{vec}(\boldsymbol{\alpha}_{\mathrm{d}})^\top, \tilde{\boldsymbol{\alpha}}_\sigma^\top, \mathrm{vec}(\mathbf{P}_{\mathbf{u},(3)})^\top]^\top\\ &\in \mathbb{T}^2 \times \mathbb{R}^2 \times \mathbb{R}^{28} \times \mathbb{T}^2 \times \mathbb{R}^2 \times \mathbb{R}^{14} \times \mathbb{R}^6 \times \mathbb{R}^{12}\,.\end{aligned} \tag{7.11}$$

7.4.3 Running on Rigid Ground

The parameters of the reference trajectory $\boldsymbol{\alpha}_{\mathrm{s}} \in \mathbb{R}^{4\times(n+1)}$ in the SSP and $\boldsymbol{\alpha}_{\mathrm{f}} \in \mathbb{R}^{4\times(n+1)}$ in the FLP are crucial for formulating a periodic solution for biped running. To ensure uniformity, two specifications are delineated through identical polynomial orders $n = 6$. Specifically, the SSP parameters $\boldsymbol{\alpha}_{\mathrm{s}}$ mirror those utilized in walking with instantaneous DSP; meanwhile, the FLP parameters are instrumental in defining the reference trajectory $\mathbf{q}_{\mathrm{r,f}}(x_{\mathrm{CM}})$ within the virtual constraints, as defined in (6.1). The differentiation between the two trajectories is attributed to the employment of the virtual leg angle θ_{virt} as the independent phase variable in the SSP, whereas the robot's center of mass position x_{CM} serves as the independent variable in the FLP.
In accordance with the hybrid zero dynamics delineated in (6.19), a periodic solution is delineated by the condition $\boldsymbol{\Phi}_{\mathrm{run,r}}(\boldsymbol{\xi}^-_{\mathrm{s}}, t) = \boldsymbol{\Phi}_{\mathrm{run,r}}(\boldsymbol{\xi}^-_{\mathrm{s}}, t + t_{\mathrm{run,r}})$, which comprises the solution trajectories $\boldsymbol{\Phi}_{\mathrm{s,ZD}}(\boldsymbol{\xi}^+_{\mathrm{s}}, t)$ in the SSP and $\boldsymbol{\Phi}_{\mathrm{f,ZD}}(\boldsymbol{\xi}^+_{\mathrm{f}}, t)$ in the FLP. For each trajectory, initial conditions $\boldsymbol{\xi}^+_{\mathrm{s}}$ and $\boldsymbol{\xi}^+_{\mathrm{f}}$ are identified as optimization parameters. Notably, $\boldsymbol{\xi}^+_{\mathrm{s}} := [\xi^+_{\mathrm{s},1}, \xi^+_{\mathrm{s},2}]^\top \in \mathcal{Z}_{\mathrm{s,r}}$ in the SSP is defined analogously to walking with instantaneous DSP; specifically, the angle θ^+_{virt} and velocity $\dot{\theta}^+_{\mathrm{virt}}$ of the virtual leg serve as the optimization parameters.

In the FLP, initial condition $\boldsymbol{\xi}_{\mathrm{f}}^{+}$ is defined in accordance with the expressions in (6.6), where the state space variables $\mathbf{q}_{\mathrm{f}}^{+}$ and $\dot{\mathbf{q}}_{\mathrm{f}}^{+}$ post-take-off are evaluated utilizing the reference trajectory $\mathbf{q}_{\mathrm{r,f}}(x_{\mathrm{CM}})$ at x_{CM}^{+}, presented as

$$\mathbf{q}_{\mathrm{f}}^{+}\Big|_{\mathcal{Z}_{\mathrm{f}}} = \begin{bmatrix} \mathbf{r}_{\mathrm{CM}} \\ \theta_{\mathrm{HAT}} \\ \mathbf{q}_{\mathrm{b}} \end{bmatrix}\Bigg|_{\Delta_{\mathrm{TO}}^{\mathrm{HZD}}(\mathcal{Z}_{\mathrm{s,r}} \cap \mathcal{S}_{\mathrm{s}}^{\mathrm{f}}) \in \mathcal{Z}_{\mathrm{f}}} = \begin{bmatrix} \mathbf{r}_{\mathrm{CM}}^{+} \\ \theta_{\mathrm{HAT}}^{+} \\ \mathbf{q}_{\mathrm{r,f}}(x_{\mathrm{CM}}^{+}) \end{bmatrix} = \begin{bmatrix} \mathbf{r}_{\mathrm{CM}}^{+} \\ \theta_{\mathrm{HAT}}^{+} \\ \boldsymbol{\alpha}_{\mathrm{f},0} \end{bmatrix}, \tag{7.12a}$$

$$\dot{\mathbf{q}}_{\mathrm{f}}^{+}\Big|_{\mathcal{Z}_{\mathrm{f}}} = \begin{bmatrix} \dot{\mathbf{r}}_{\mathrm{CM}} \\ \dot{\theta}_{\mathrm{HAT}} \\ \dot{\mathbf{q}}_{\mathrm{b}} \end{bmatrix}\Bigg|_{\Delta_{\mathrm{TO}}^{\mathrm{HZD}}(\mathcal{Z}_{\mathrm{s,r}} \cap \mathcal{S}_{\mathrm{s}}^{\mathrm{f}}) \in \mathcal{Z}_{\mathrm{f}}} = \begin{bmatrix} \dot{\mathbf{r}}_{\mathrm{CM}}^{+} \\ \dot{\theta}_{\mathrm{HAT}}^{+} \\ \frac{\partial \mathbf{q}_{\mathrm{r,f}}(x_{\mathrm{CM}})}{\partial x_{\mathrm{CM}}}\Big|_{x_{\mathrm{CM}}^{+}} \dot{x}_{\mathrm{CM}}^{+} \end{bmatrix} = \begin{bmatrix} \dot{\mathbf{r}}_{\mathrm{CM}}^{+} \\ \dot{\theta}_{\mathrm{HAT}}^{+} \\ n \frac{\boldsymbol{\alpha}_{\mathrm{f},1} - \boldsymbol{\alpha}_{\mathrm{f},0}}{x_{\mathrm{CM}}^{-} - x_{\mathrm{CM}}^{+}} \dot{x}_{\mathrm{CM}}^{+} \end{bmatrix}. \tag{7.12b}$$

Thus, configuration $[(\mathbf{r}_{\mathrm{CM}}^{+})^{\top}, \theta_{\mathrm{HAT}}^{+}]$ and velocity $[(\dot{\mathbf{r}}_{\mathrm{CM}}^{+})^{\top}, \dot{\theta}_{\mathrm{HAT}}^{+}]$ are considered optimization parameters. Duration of the step $t_{\mathrm{run,r}} = t_{\mathrm{s}} + t_{\mathrm{f}}$ is ascertained by the sum of the SSP time t_{s} and the FLP time t_{f}. Although t_{s} is recognized as an optimization parameter, the flight time $t_{\mathrm{f}} = (x_{\mathrm{CM}}^{-} - x_{\mathrm{CM}}^{+})/\dot{x}_{\mathrm{CM}}^{+}$ is governed by the flight distance and the constant velocity $\dot{x}_{\mathrm{CM}}^{+}$.
To conclude, the optimization parameters relevant to running on rigid ground surfaces are expounded as

$$\begin{aligned} \boldsymbol{\xi}_{\mathrm{opt,r}} := [&\theta_{\mathrm{virt}}^{+}, \theta_{\mathrm{virt}}^{-}, \dot{\theta}_{\mathrm{virt}}^{+}, t_{\mathrm{s}}, \mathrm{vec}(\boldsymbol{\alpha}_{\mathrm{s}})^{\top}, (\mathbf{r}_{\mathrm{CM}}^{+})^{\top}, \theta_{\mathrm{HAT}}^{+}, (\dot{\mathbf{r}}_{\mathrm{CM}}^{+})^{\top}, \dot{\theta}_{\mathrm{HAT}}^{+}, \\ &x_{\mathrm{CM}}^{-}, \mathrm{vec}(\boldsymbol{\alpha}_{\mathrm{f}})^{\top}]^{\top} \\ &\in \mathbb{R}^{4} \times \mathbb{R}^{28} \times \mathbb{R}^{7} \times \mathbb{R}^{28}. \end{aligned} \tag{7.13}$$

7.4.4 Running on Compliant Ground

In the context of running on compliant surfaces, the center of mass position x_{CM} is treated as an independent variable in both the SSP and the FLP. Correspondingly, the reference trajectory is defined by parameter sets $\boldsymbol{\alpha}_{\mathrm{s}} \in \mathbb{R}^{4\times(n+1)}$ in the SSP and $\boldsymbol{\alpha}_{\mathrm{f}} \in \mathbb{R}^{4\times(n+1)}$ in the FLP, with $n = 6$ indicating the Bézier curve order.
Given the similarity in the specification of optimization parameters to those utilized for running on rigid surfaces, these parameters are collectively represented as

$$\begin{aligned} \boldsymbol{\xi}_{\mathrm{opt,r}} := [&(\mathbf{r}_{\mathrm{CM,s}}^{+})^{\top}, \theta_{\mathrm{HAT,s}}^{+}, (\dot{\mathbf{r}}_{\mathrm{CM,s}}^{+})^{\top}, \dot{\theta}_{\mathrm{HAT,s}}^{+}, x_{\mathrm{CM,s}}^{-}, t_{\mathrm{s}}, \mathrm{vec}(\boldsymbol{\alpha}_{\mathrm{s}})^{\top}, \\ &(\mathbf{r}_{\mathrm{CM,f}}^{+})^{\top}, \theta_{\mathrm{HAT,f}}^{+}, (\dot{\mathbf{r}}_{\mathrm{CM,f}}^{+})^{\top}, \dot{\theta}_{\mathrm{HAT,f}}^{+}, x_{\mathrm{CM,f}}^{-}, \mathrm{vec}(\boldsymbol{\alpha}_{\mathrm{f}})^{\top}]^{\top} \\ &\in \mathbb{R}^{8} \times \mathbb{R}^{28} \times \mathbb{R}^{7} \times \mathbb{R}^{28}, \end{aligned} \tag{7.14}$$

without elaborate descriptions.

7.5 Optimization Constraints

Equality and inequality constraints [4] play a crucial role in maintaining the feasibility and stability of the simulated periodic walking and running gaits. Specifically, the simulation feasibility of these dynamical models during continuous phases is enhanced by the inequality constraints elucidated in Section 7.5.1. These constraints are integrated with the constraints for discrete transitions to construct periodic walking and running gaits, as elucidated in Section 7.5.2. Furthermore, the utilization of the multiple shooting method to determine periodic solutions is bolstered by the enforcement of equality constraints, as described in Section 7.5.3.

7.5.1 Feasible Continuous Phases

The characterization of periodic walking and running gaits is accomplished through hybrid dynamical models, which encompass both continuous dynamic domains and discrete transition events. The constraints presented in this section pertain to ensuring feasibility within a particular continuous phase. Specifically, these constraints apply to the single support and double support phases on rigid ground, the single support phase on compliant ground, and the flight phase.

It is important to recognize that the i-th inequality constraint $h_i(t_k) < 0$ in conjunction with $i, k \in \mathbb{Z}$ is formulated at a designated time step $t_k \in [0, t_{\text{end}}]$ during the phase of an overall duration t_{end}. These time steps are estimated numerically through ODE solvers within the framework of multiple shooting. Consequently, the aggregate number of constraints depends on the step size of the numerical solution. Despite the potentially substantial total number of constraints, sophisticated nonlinear optimization algorithms exploit the activity properties of the inequality constraints to enhance convergence speed.

In nonlinear optimization, "active" inequality constraints are those that equate at a certain point, thus defining the local feasible region, whereas "inactive" constraints are strictly satisfied and presently do not impact the solution. Sequential Quadratic Programming (SQP) algorithms adeptly tackle large-scale problems by directly integrating these active constraints into a quadratic subproblem, thereby circumventing cumbersome penalties and more effectively utilizing structural features, as outlined in [125, Section 18.2]. To maintain clarity and simplicity in definition, the time steps are excluded from the constraints' expression.

[4] In this context, equality constraints are denoted as g, while inequality constraints are indicated by h.

Single Support Phase (SSP) on Rigid Ground

A crucial prerequisite for the reduction of the robot's system dynamics, from seven degrees of freedom to those in the single support phase with five degrees of freedom, is the non-slippage of the contacting stance foot on the ground. This is governed by the static friction condition as described in (3.10) and the unilateral contact condition detailed in (3.11), which culminate in the formulation of inequality constraints,

$$h_1 := -F_{1,z} \,, \qquad h_2 := -\mu F_{1,z} - F_{1,x} \,, \qquad h_3 := -\mu F_{1,z} + F_{1,x} \,. \tag{7.15}$$

Subsequently, the orientation of the upper body θ_{HAT} is constrained to an upward direction. The range of the knee joint angle is constrained to values akin to those typical of a human, which notably diverges from the morphology observed in avian species. Specifically, this implies that when the knee joint is in full extension, the knee joint angle is approximately zero degrees; it can bend to approximately 135°–140° in a deep squat posture [146]. These configurations are enforced by the inequality constraints,

$$h_4 := -\theta_{\mathrm{HAT}} - \frac{\pi}{2} \,, \qquad h_5 := \theta_{\mathrm{HAT}} - \frac{\pi}{2} \,, \qquad h_6 := -\theta_{\mathrm{K1}} \,, \tag{7.16a}$$

$$h_7 := -\theta_{\mathrm{K2}} \,, \qquad h_8 := \theta_{\mathrm{K1}} - \pi \,, \qquad h_9 := \theta_{\mathrm{K2}} - \pi \,. \tag{7.16b}$$

In addition, to prevent the swing foot from coming into contact with the ground surface, the position $\mathbf{r}_2 := [r_{2,x}, r_{2,z}]^\top$ is constrained to remain above the ground level, leading to the inequality constraint,

$$h_{10} := -r_{2,z} \,. \tag{7.17}$$

Double Support Phase (DSP) on Rigid Ground

Throughout the continuous DSP, both stance feet maintain unilateral contact on the ground without slippage, a condition facilitated by static friction at the foot's point of contact, as detailed in (3.43) and (3.44). Consequently, this leads to the establishment of inequality constraints,

$$h_{11} := -F_{1,z} \,, \qquad h_{12} := -\mu F_{1,z} - F_{1,x} \,, \qquad h_{13} := -\mu F_{1,z} + F_{1,x} \,, \tag{7.18a}$$

$$h_{14} := -F_{2,z} \,, \qquad h_{15} := -\mu F_{2,z} - F_{2,x} \,, \qquad h_{16} := -\mu F_{2,z} + F_{2,x} \,. \tag{7.18b}$$

In order to produce motion that resembles human behavior, the body configuration constrained by the inequality restrictions (7.16) is applicable within the continuous DSP. As per the definition (3.45) of the configuration space $\hat{\boldsymbol{Q}}_{\mathrm{d}}$ of the non-instantaneous DSP, the two stance feet are prohibited from occupying the same spatial position. Therefore, it

is imperative that the step length $\ell_{\text{step}} = \|\mathbf{r}_2 - \mathbf{r}_1\|_2$ remains non-zero, which necessitates the establishment of an inequality constraint,

$$h_{17} := -\ell_{\text{step}} = -\|\mathbf{r}_2 - \mathbf{r}_1\|_2 \,. \tag{7.19}$$

Single Support Phase (SSP) on Compliant Ground

In the SSP on a compliant ground surface, as outlined in Section 5.2.2, the condition of the static friction cone at the stance foot is preserved. Furthermore, the unilateral contact condition mandates that the normal reaction force exerted by the ground onto the stance foot must remain positive. This requirement is implicitly fulfilled through the implementation of the force law of component $F_{1,z}$, as detailed in (5.20), given that the position $\mathbf{r}_1 := [r_{1,x}, r_{1,z}]^\top$ of the stance foot is situated below the undeformed ground level. These considerations are encapsulated within the inequality constraints,

$$h_{18} := r_{1,z} \,, \qquad h_{19} := -\mu F_{1,z} - F_{1,x} \,, \qquad h_{20} := -\mu F_{1,z} + F_{1,x} \,. \tag{7.20}$$

Moreover, the inequality constraint (7.17) is utilized to ensure that the swing foot $\mathbf{r}_2 := [r_{2,x}, r_{2,z}]^\top$ does not come into contact with the ground surface. The geometry of the deformable ground is intentionally omitted in this constraint formulation, as the deformation is negligible relative to the trajectory of the swing foot. This simplification substantially enhances the efficiency of numerical computations.

Flight Phase (FLP)

To generate motion that emulates human movement, the body configuration is subject to inequality constraints (7.16) within the FLP. Furthermore, the positions of both feet are restricted to remain above ground level, resulting in the inequality constraints,

$$h_{21} := -r_{1,z} \,, \qquad h_{22} := -r_{2,z} \,. \tag{7.21}$$

7.5.2 Feasible Walking and Running Gaits

In order to address discontinuous transition events and ensure comprehensive gait stability, this section delineates equality and inequality constraints relevant to completing the periodic gait cycles. These constraints are integrated with those described for each continuous phase in Section 7.5.1 to enable the generation of highly efficient and stable gaits through numerical optimization. Additionally, the constraints in this section are defined either exclusively for the transition instance or for the entire periodic gait, meaning that the number of constraints remains unaffected by the step size of the numerical solutions.

Initially, the consistent average speed v_{avg} of locomotion, as articulated in (3.1), must align with the desired average speed v_{d}, thereby leading to the equality constraint,

$$g_v := v_{\text{d}} - v_{\text{avg}} = v_{\text{d}} - \frac{\ell_{\text{step}}}{t_{\text{step}}} \,. \tag{7.22}$$

An overarching condition pertinent to both walking and running is the requirement for the orbital stability of the periodic solution to be fulfilled. In accordance with Floquet theory, the stability is assured when the magnitude of the resultant Floquet multiplier Λ remains below unity, as denoted by $|\Lambda| < 1$. This is considered an inequality constraint,

$$h_\Lambda := |\Lambda| - 1 \,. \tag{7.23}$$

Walking with Instantaneous DSP

The walking pattern encompassing an instantaneous DSP incorporates a continuous SSP and an inelastic impact mapping within the DSP, as delineated in Section 3.2.2. In particular, the impact surface $\mathcal{S}_{\text{s}}$ expressed within the state space in (3.38) is defined by the guard function $g_-^+(\mathbf{x}_{\text{s}}) := r_{2,z}(\mathbf{x}_{\text{s}})$, indicating the precise moment at which the swing foot contacts the ground surface. This circumstance is expressed as an equality constraint,

$$g_1 := g_-^+(\mathbf{x}_{\text{s}}^-) \,, \qquad \mathbf{x}_{\text{s}}^- \in \mathcal{S}_{\text{s}} \,, \tag{7.24}$$

enforced at the conclusion of the SSP. The corresponding impact force $\hat{\mathbf{F}}_2 := [\hat{F}_{2,x}, \hat{F}_{2,z}]^\top$ derived in (3.22) is subject to the condition of the friction cone and unilateral contact as specified in (3.23) and (3.24), respectively. These are formulated as inequality constraints,

$$h_{23} := -\hat{F}_{2,z} \,, \qquad h_{24} := -\mu\hat{F}_{2,z} - \hat{F}_{2,x} \,, \qquad h_{25} := -\mu\hat{F}_{2,z} + \hat{F}_{2,x} \,. \tag{7.25}$$

Walking with Non-Instantaneous DSP

Two distinct transition mappings, namely touch-down as referenced in Section 3.3.2 and lift-off as referenced in Section 3.3.3, are incorporated within the periodic walking gait featuring a non-instantaneous DSP. The initial condition under which the touch-down event surface $\mathcal{S}_{\text{s}}^{\text{d}}$ is attained is defined within the state space expression (3.75), contingent upon the fulfillment of the guard function $g_{\text{s}}^{\text{d}}(\mathbf{x}_{\text{s}}) := r_{2,z}(\mathbf{x}_{\text{s}}) = 0$. This denotes the instance where the swing foot makes contact with the ground surface.
Subsequently, the assessment of the lift-off event surface is based on the state space expression (3.76), evaluated in the guard function $g_{\text{d}}^{\text{s}}(\mathbf{x}_{\text{d}}) := \theta_{\text{virt}} - \theta_{\text{LO}} = 0$. In this

context, the phase variable $\theta_{\mathrm{LO}} = \theta^{-}_{\mathrm{virt,d}} \in \boldsymbol{\xi}_{\mathrm{opt,d}}$ is delineated in (7.11) as an optimization parameter. The specified criteria are articulated as equality constraints,

$$g_2 := g^{\mathrm{d}}_{\mathrm{s}}(\mathbf{x}^{-}_{\mathrm{s}}) = r_{2,z}(\mathbf{x}^{-}_{\mathrm{s}}) \,, \quad \mathbf{x}^{-}_{\mathrm{s}} \in \mathcal{S}^{\mathrm{d}}_{\mathrm{s}} \,, \quad g_3 := g^{\mathrm{s}}_{\mathrm{d}}(\mathbf{x}^{-}_{\mathrm{d}}) = \theta^{-}_{\mathrm{virt}} - \theta_{\mathrm{LO}} \,, \quad \mathbf{x}^{-}_{\mathrm{d}} \in \mathcal{S}^{\mathrm{s}}_{\mathrm{d}} \,, \tag{7.26}$$

and an inequality constraint,

$$h_{26} := -r_{2,x}(\mathbf{x}^{-}_{\mathrm{s}}) \,, \quad \mathbf{x}^{-}_{\mathrm{s}} \in \mathcal{S}^{\mathrm{d}}_{\mathrm{s}} \,, \tag{7.27}$$

which stipulates that the swing foot makes ground contact anterior to the stance foot. During the touch-down event, the impact forces $\hat{\mathbf{F}}_1$ and $\hat{\mathbf{F}}_2$ at both stance feet adhere to the conditions of static friction (3.56) and unilateral contact (3.57), which are expressed as inequality constraints,

$$h_{27} := -\hat{F}_{1,z} \,, \qquad h_{28} := -\mu\hat{F}_{1,z} - \hat{F}_{1,x} \,, \qquad h_{29} := -\mu\hat{F}_{1,z} + \hat{F}_{1,x} \,, \tag{7.28a}$$

$$h_{30} := -\hat{F}_{2,z} \,, \qquad h_{31} := -\mu\hat{F}_{2,z} - \hat{F}_{2,x} \,, \qquad h_{32} := -\mu\hat{F}_{2,z} + \hat{F}_{2,x} \,. \tag{7.28b}$$

While designing virtually independent actuators, the projection matrix $\mathbf{P}_{\mathbf{u},(3)}$ in (3.63) is restricted to prevent any scaling of the virtual inputs by the projection. Additionally, the projection onto the four physical actuators retains mutual independence. At the outset, the projection matrix is presented via its column vectors, as illustrated in the form

$$\mathbf{P}_{\mathbf{u},(3)} := \begin{bmatrix} \mathbf{P}_{\mathbf{u},(3),1} & \mathbf{P}_{\mathbf{u},(3),2} & \mathbf{P}_{\mathbf{u},(3),3} \end{bmatrix} \,, \tag{7.29}$$

which are further formulated as equality constraints,

$$g_4 := \left\| \mathbf{P}_{\mathbf{u},(3),1} \right\|_2 - 1 \,, \qquad g_5 := \left\| \mathbf{P}_{\mathbf{u},(3),2} \right\|_2 - 1 \,, \qquad g_6 := \left\| \mathbf{P}_{\mathbf{u},(3),3} \right\|_2 - 1 \,, \tag{7.30a}$$

$$g_7 := \mathbf{P}_{\mathbf{u},(3),1} \cdot \mathbf{P}_{\mathbf{u},(3),2} \,, \qquad g_8 := \mathbf{P}_{\mathbf{u},(3),1} \cdot \mathbf{P}_{\mathbf{u},(3),3} \,, \qquad g_9 := \mathbf{P}_{\mathbf{u},(3),2} \cdot \mathbf{P}_{\mathbf{u},(3),3} \,. \tag{7.30b}$$

Running on Rigid Ground

As presented in the state space in (5.15) and (5.16), running gaits include two transition events, namely take-off as described in Section 5.1.2 and landing as described in Section 5.1.3. The surface $\mathcal{S}^{\mathrm{f}}_{\mathrm{s}}$ of the take-off event is defined by the guard function $g^{\mathrm{f}}_{\mathrm{s}}(\mathbf{x}_{\mathrm{s}}) := \theta_{\mathrm{virt}} - \theta_{\mathrm{TO}} = 0$, wherein the phase variable $\theta_{\mathrm{TO}} = \theta^{-}_{\mathrm{virt}} \in \boldsymbol{\xi}_{\mathrm{opt,r}}$ is considered as a controller parameter to be optimized as outlined in (7.13). The initiation of the take-off event is consequently triggered by event-based control, contingent upon this parameter θ_{TO}. Moreover, from a physical perspective, the reaction force $\mathbf{F}_1 := [F_{1,x}, F_{1,z}]^{\top}$ exerted

by the ground on the stance foot, as described in equation (3.8), is required to be nullified at the take-off event. These conditions are represented as equality constraints,

$$g_{10} := g_{\mathrm{s}}^{\mathrm{f}}(\mathbf{x}_{\mathrm{s}}^{-}) = \theta_{\mathrm{virt}}^{-} - \theta_{\mathrm{TO}}\,, \quad g_{11} := F_{1,x}(\mathbf{x}_{\mathrm{s}}^{-})\,, \quad g_{12} := F_{1,z}(\mathbf{x}_{\mathrm{s}}^{-})\,, \quad \mathbf{x}_{\mathrm{s}}^{-} \in \mathcal{S}_{\mathrm{s}}^{\mathrm{f}}\,. \tag{7.31}$$

Furthermore, the determination of the landing event surface $\mathcal{S}_{\mathrm{f}}^{\mathrm{s}}$ is governed by the guard function $g_{\mathrm{f}}^{\mathrm{s}}(\mathbf{x}_{\mathrm{f}}) := r_{2,z}(\mathbf{x}_{\mathrm{f}}) = 0$, which is distinguished by the foot's position. This is further complemented by the prerequisite that the prior swing leg from the preceding SSP makes contact with the ground in advance of the other leg, thus enabling a running motion analogous to that seen in human locomotion. These parameters are articulated as the equality g_{13} and inequality constraint h_{33}, as elaborated in

$$g_{13} := g_{\mathrm{f}}^{\mathrm{s}}(\mathbf{x}_{\mathrm{f}}^{-}) = r_{2,z}(\mathbf{x}_{\mathrm{f}}^{-})\,, \quad h_{33} := r_{1,x}(\mathbf{x}_{\mathrm{f}}^{-}) - r_{2,x}(\mathbf{x}_{\mathrm{f}}^{-})\,, \quad \mathbf{x}_{\mathrm{f}}^{-} \in \mathcal{S}_{\mathrm{f}}^{\mathrm{s}}\,. \tag{7.32}$$

The impact force $\hat{\mathbf{F}}_2 := [\hat{F}_{2,x}, \hat{F}_{2,z}]^{\top}$ conforms to the conditions of static friction and unilateral contact as delineated in (5.9). These conditions are structured as inequality constraints analogous to those presented in (7.25) for walking with instantaneous DSP.

Running on Compliant Ground

The state space formulations in (5.31) and (5.32) pertaining to running on compliant ground reflect the take-off and landing events analogously to those observed on rigid ground. Notably, the landing event is equivalent to those specified for rigid ground, as delineated in the constraints (7.32), which are therefore not elaborated upon.
The occurrence of the take-off event is contingent upon the normal reaction force $\mathbf{F}_1(\mathbf{q}_{\mathrm{f}}, \dot{\mathbf{q}}_{\mathrm{f}})$ from the ground, as delineated in (5.20), diminishing to zero. This phenomenon does not result from direct actuation by the controller. It is articulated through the guard function $\tilde{g}_{\mathrm{s}}^{\mathrm{f}}(\mathbf{x}_{\mathrm{f,s}}) := F_{1,z}(\mathbf{x}_{\mathrm{f,s}})$, which is subsequently treated as equality constraints, [5]

$$g_{14} := F_{1,x}(\mathbf{x}_{\mathrm{f}}^{-})\,, \quad g_{15} := F_{1,z}(\mathbf{x}_{\mathrm{f}}^{-})\,, \quad \mathbf{x}_{\mathrm{f}}^{-} \in \tilde{\mathcal{S}}_{\mathrm{s}}^{\mathrm{f}}\,. \tag{7.33}$$

7.5.3 Multiple Shooting

The multiple shooting method is a numerical strategy designed for solving boundary value problems in the context of ordinary differential equations. This technique offers an improvement over the more basic single shooting method, specifically designed to enhance numerical stability and robustness in the presence of stiff equations, sensitive

[5] The guard function requires only the nullification of the vertical component $F_{1,z}$ of the force. Due to the condition of the friction cone, the tangential component $F_{1,x}$ is implicitly rendered null. Nevertheless, to enhance the local convergence of the optimization, both components are incorporated within the equality constraints.

initial conditions, or large integration intervals. Essentially, the boundary value problem is reformulated as an initial value problem, where the satisfaction of boundary conditions is transformed into a nonlinear system of equations. This system is then approximately solved using numerical techniques such as Newton's method. Alternatively, solving the resulting system of equations can be achieved through equality constraints of optimization, as illustrated in [68].
Fundamentally, the periodic gaits explored in this thesis are characterized through hybrid dynamical models that encompass both continuous dynamics and discontinuous transition events. The continuous phases are independently simulated from the adjoining phases using suitable numerical solvers provided by the library *DifferentialEquations.jl* in the programming language *Julia*. Discontinuities, along with the conditions for periodic gaits, are expressed as equality constraints within the optimization process. A clear advantage of this approach is the ability to employ various advanced ODE or DAE solvers to manage different stiff numerical problems. This versatility is particularly crucial for accurately simulating the running gait on compliant surfaces. In this context, the contact phase is approximated by a stiff ordinary differential equations system necessitating meticulous numerical methods, whereas during the flight phase, the use of an efficient numerical solver is beneficial for enhancing evaluation efficiency, since the movement is described by a parabolic trajectory of the robot's center of mass.

Walking with Instantaneous DSP

To formulate a periodic solution for walking incorporating an instantaneous DSP, the optimization parameters $\xi_{\text{opt,w}}$ in (7.9) are utilized in the expression (7.8) that encompasses the boundary characteristics of the Bézier curve, expressing the state space variables $\mathbf{x}_{\text{s}}^{-,0} := [(\mathbf{q}_{\text{s}}^{-,0})^{\top}, (\dot{\mathbf{q}}_{\text{s}}^{-,0})^{\top}]^{\top} \in \mathcal{Z}_{\text{s,r}} \cap \mathcal{S}_{\text{s}}$ on the impact surface. Following this, the transition mapping $\mathbf{x}_{\text{s}}^{+} = \boldsymbol{\Delta}_{\text{w,i}}(\mathbf{x}_{\text{s}}^{-,0})$, as delineated in (3.37), establishes the initial condition $\mathbf{x}_{\text{s}}^{+}$ for the subsequent SSP post-impact. Thereafter, the solution curve $\boldsymbol{\Phi}_{\text{s,ZD}}(\xi_{\text{s}}^{+}, t)$ of the vector field $\mathbf{f}_{\text{s,ZD}}(\xi_{\text{s}})$ within the hybrid zero dynamics model (4.20) is derived through a numerical ODE solver.
At the final temporal instance $t_{\text{s}} \in \xi_{\text{opt,w}}$, which is regarded as an optimization parameter, it is imperative that the state variables $\mathbf{x}_{\text{s}}^{-}$ correspond precisely with the initial configuration $\mathbf{x}_{\text{s}}^{-,0}$, as depicted in the equality constraints,

$$\mathbf{g}_{16} := \mathbf{x}_{\text{s}}^{-,0} - \mathbf{x}_{\text{s}}^{-} \in \mathbb{R}^{10}\,, \quad \mathbf{x}_{\text{s}}^{-,0}, \mathbf{x}_{\text{s}}^{-} \in \mathcal{Z}_{\text{s,r}} \cap \mathcal{S}_{\text{s}}\,. \tag{7.34}$$

Walking with Non-Instantaneous DSP

In the scenario where the DSP is non-instantaneous, the optimization parameters $\xi_{\text{opt,d}}$ as delineated in (7.11) are utilized within the boundary expressions (7.10) of the

Bézier curve to ascertain the state variables $\mathbf{x}_{\mathrm{d}}^{-,0} := [(\mathbf{q}_{\mathrm{d}}^{-,0})^\top, (\dot{\mathbf{q}}_{\mathrm{d}}^{-,0})^\top]^\top \in \mathcal{Z}_{\mathrm{d}} \cap \mathcal{S}_{\mathrm{d}}^{\mathrm{s}}$ at the conclusion of the DSP. Concurrently, the states $\mathbf{x}_{\mathrm{s}}^{-,0} := [(\mathbf{q}_{\mathrm{s}}^{-,0})^\top, (\dot{\mathbf{q}}_{\mathrm{s}}^{-,0})^\top]^\top \in \mathcal{Z}_{\mathrm{s,r}} \cap \mathcal{S}_{\mathrm{s}}^{\mathrm{d}}$ at the termination of the SSP on the impact surface are specified according to the parameter set $\xi_{\mathrm{opt,d}}$. Subsequently, the transitions $\mathbf{x}_{\mathrm{d}}^{+} = \boldsymbol{\Delta}_{\mathrm{TD}}(\mathbf{x}_{\mathrm{s}}^{-})$ and $\mathbf{x}_{\mathrm{s}}^{+} = \boldsymbol{\Delta}_{\mathrm{LO}}\left(\mathbf{x}_{\mathrm{d}}^{-}\right)$ delineated in (3.73) and (3.74), respectively, are implemented to derive the initial conditions for the continuous SSP and DSP zero dynamics, which are independently resolved using suitable ODE solvers.
At the final time step $t_{\mathrm{s}} \in \xi_{\mathrm{opt,d}}$ in the SSP and $t_{\mathrm{d}} \in \xi_{\mathrm{opt,d}}$ in the DSP, the ultimate state variables $\mathbf{x}_{\mathrm{s}}^{-}$ in the SSP and $\mathbf{x}_{\mathrm{d}}^{-}$ in the DSP must correspond with the respective initial configurations, resulting in the equality constraints,

$$\mathbf{g}_{17} := \mathbf{x}_{\mathrm{s}}^{-,0} - \mathbf{x}_{\mathrm{s}}^{-} \in \mathbb{R}^{10}\,, \quad \mathbf{x}_{\mathrm{s}}^{-,0}, \mathbf{x}_{\mathrm{s}}^{-} \in \mathcal{Z}_{\mathrm{s,r}} \cap \mathcal{S}_{\mathrm{s}}^{\mathrm{d}}\,, \tag{7.35a}$$

$$\mathbf{g}_{18} := \mathbf{x}_{\mathrm{d}}^{-,0} - \mathbf{x}_{\mathrm{d}}^{-} \in \mathbb{R}^{6}\,, \quad \mathbf{x}_{\mathrm{d}}^{-,0}, \mathbf{x}_{\mathrm{d}}^{-} \in \mathcal{Z}_{\mathrm{d}} \cap \mathcal{S}_{\mathrm{d}}^{\mathrm{s}}\,. \tag{7.35b}$$

Running on Rigid and Compliant Grounds

The methodology for determining periodic solutions pertaining to running on both rigid and compliant surfaces is analogous; however, a principal distinction is that running on compliant terrain entails a larger number of degrees of freedom, thereby augmenting the quantity of equality constraints. To eliminate unnecessary repetition, the specific details of the running gait are exclusively discussed in the context of rigid ground.
Initially, the optimization parameters $\xi_{\mathrm{opt,r}}$, as defined in (7.13), are utilized to articulate the state space variables $\mathbf{x}_{\mathrm{s}}^{+,0} := [(\mathbf{q}_{\mathrm{s}}^{+,0})^\top, (\dot{\mathbf{q}}_{\mathrm{s}}^{+,0})^\top]^\top \in \mathcal{Z}_{\mathrm{s,r}}$ and $\mathbf{x}_{\mathrm{f}}^{+,0} := [(\mathbf{q}_{\mathrm{f}}^{+,0})^\top, (\dot{\mathbf{q}}_{\mathrm{f}}^{+,0})^\top]^\top \in \mathcal{Z}_{\mathrm{f}}$ at the outset of the SSP and FLP, respectively. Importantly, the boundary characteristics of the Bézier curve, as delineated in (7.8) [6] and (7.12), are employed to ascertain these states on the zero dynamics manifold.
Subsequently, the solution curves for the SSP and FLP are independently derived utilizing numerical ODE solvers. The terminal state variables $\mathbf{x}_{\mathrm{s}}^{-} \in \mathcal{Z}_{\mathrm{s,r}}$ and $\mathbf{x}_{\mathrm{f}}^{-} \in \mathcal{Z}_{\mathrm{f}}$ are subjected to transition events, such as take-off $\mathbf{x}_{\mathrm{f}}^{+} = \boldsymbol{\Delta}_{\mathrm{TO}}(\mathbf{x}_{\mathrm{s}}^{-})$ and landing $\mathbf{x}_{\mathrm{s}}^{+} = \boldsymbol{\Delta}_{\mathrm{LD}}(\mathbf{x}_{\mathrm{f}}^{-})$, as illustrated in the mappings (5.13) and (5.14). Post-transition, the alignment of state variables with the initial configuration is imperative, resulting in the equality constraints,

$$\mathbf{g}_{19} := \mathbf{x}_{\mathrm{s}}^{+,0} - \mathbf{x}_{\mathrm{s}}^{+} \in \mathbb{R}^{10}\,, \quad \mathbf{x}_{\mathrm{s}}^{+,0}, \mathbf{x}_{\mathrm{s}}^{+} \in \mathcal{Z}_{\mathrm{s,r}}\,, \tag{7.36a}$$

$$\mathbf{g}_{20} := \mathbf{x}_{\mathrm{f}}^{+,0} - \mathbf{x}_{\mathrm{f}}^{+} \in \mathbb{R}^{14}\,, \quad \mathbf{x}_{\mathrm{f}}^{+,0}, \mathbf{x}_{\mathrm{f}}^{+} \in \mathcal{Z}_{\mathrm{f}}\,. \tag{7.36b}$$

[6] Notably, expression (7.8) is assessed at the concluding position $\theta_{\mathrm{virt}}^{-}$ of the SSP. Owing to the analogous formulation of the partial derivatives as articulated in (7.7), this expression is readily adapted to the initial position $\theta_{\mathrm{virt}}^{+}$ of the SSP.

7.6 Constrained Optimization Problem

In conclusion, a constrained optimization problem is established to derive stable periodic walking or running gaits characterized by high energy efficiency, as delineated in

$$\begin{aligned} \min_{\boldsymbol{\xi}_{\text{opt}}} \quad & f_{\text{obj}}(\boldsymbol{\xi}_{\text{opt}}) \\ \text{subject to} \quad & g_v = 0\,, \\ & \mathbf{g}_{\text{opt}} = \mathbf{0}\,, \\ & \mathbf{h}_{\text{opt}} < \mathbf{0}\,, \\ & h_\Lambda < 0\,, \end{aligned} \tag{7.37}$$

The objective function delineated in (7.1) evaluates energy consumption and is minimized through optimization. The selection of equality $\mathbf{g}_{\text{opt}} = \mathbf{0}$ and inequality constraints $\mathbf{h}_{\text{opt}} < \mathbf{0}$ from the aforementioned descriptions is contingent upon the specific gait considered. Additionally, two universally applicable conditions are maintained: the equality constraint $g_v = 0$, outlined in (7.22), which governs the average speed, and the inequality constraint $h_\Lambda < 0$, prescribed in (7.23), which ensures the orbital stability of the periodic solution.
During the analysis of elastic couplings, the configuration parameters, as specified in Section 7.2.1, are incorporated alongside the gait parameters to constitute the complete set of optimization parameters $\boldsymbol{\xi}_{\text{opt}}$. This methodology enables the optimization problem articulated in (7.37) to simultaneously optimize both the gait trajectory and the mechanical design (elastic coupling) within a unified framework, thereby ensuring high energy efficiency. This synergy is attained by aligning the gait with the mechanical design such that the robot's locomotion occurs in close proximity to the mechanical system's resonance, significantly diminishing the energy requirements of the actuator.
The optimization problem is tackled through the application of a SQP algorithm, as provided in *Artelys Knitro*, which constitutes a commercial software package tailored for addressing large-scale nonlinear optimization challenges. The associated derivatives are obtained through the employment of Automatic Differentiation algorithms.

8 Simulation without Elastic Coupling

This chapter investigates periodic walking and running patterns derived from the optimization procedure previously presented, with an emphasis on examining the impact of gait and environmental variations on energy efficiency and stability. The analysis encompasses four different scenarios: two kinds of walking gait on rigid surfaces and running on both rigid and compliant surfaces. Such periodic gaits are generated across a range of average speeds, while elastic couplings are not yet incorporated into the study.
The chapter is organized as follows: Section 8.1 delineates the model parameters of the robot and offers an overview of the variations in both gaits and environments; Section 8.2 describes the optimal walking gaits featuring an instantaneous double support phase on rigid ground; Section 8.3 presents the optimized walking gaits incorporating a non-instantaneous double support phase on rigid ground; whereas Section 8.4 and Section 8.5 elucidate the optimal running gaits on rigid and compliant grounds, respectively. Section 8.6 concludes the study, omitting consideration of elastic coupling within this chapter.

8.1 Simulation Setup

The walking and running gaits examined in this thesis are characterized by periodicity at a constant average speed. To address the gait efficiency and stability, periodic walking gaits are analyzed at $v \in [0.5, 0.6, \ldots, 1.5]$ m/s, while running gaits are assessed at $v \in [1.8, 1.9, \ldots, 2.8]$ m/s. This section delineates the parameters pertaining to the robot model as presented in Section 8.1.1, followed by an exposition on the variations in environmental conditions and gaits as elaborated in Section 8.1.2.

8.1.1 Model Parameters

The mechanical design of the robot is symmetric, with parameters of the mechanical components included in Table 8.1. These parameters are determined through a parameter identification method based on the homotopy optimization approach, which is

introduced in [173] and implemented on a robot prototype presently under development, as detailed in the study [191].

	upper body	thigh	shank
mass moment of inertia (in 10^{-3} kg m^2)	40.53	25.28	8.78
mass (in kg)	7.00	2.69	1.33
length (in m)	0.23	0.30	0.30
center of mass position (in m)	0.14	0.16	0.09

Table 8.1: The configuration parameters for the robot model comprising five rigid body segments.

8.1.2 Variation of Gaits and Ground Compliance

The present investigation delves into walking and running gaits, which are generated through the application of the Hybrid Zero Dynamics (HZD) control methodology. Walking gaits, in particular, are delineated by the alternation between single support (SSP) and double support phases (DSP). Two distinct categories of walking gaits are identified by configuring the DSP as either instantaneous or non-instantaneous. In contrast, running gaits are characterized by alternations between single support and flight phases (FLP). Running gaits on both rigid and compliant ground surfaces are differentiated by the SSP model, while the FLP remains consistent across these running gaits.

8.2 Walking with Instantaneous DSP on Rigid Ground

Walking with instantaneous DSP on rigid surfaces has been extensively studied within the academic literature. For comparison with alternative gaits, energy efficiency and gait stability are detailed in Section 8.2.1 and Section 8.2.2, respectively.

8.2.1 Efficiency Study

The efficiency analysis encompasses two primary perspectives: cost of transport (CoT) and energy losses. Within this framework, the periodic gaits are conceptualized as limit cycles within the hybrid zero dynamics of reduced dimensionality, resulting in a constant system energy level. At a stationary operating velocity of the periodic motion, the energy input, assessed through the CoT, equates to the cumulative energy losses. These losses comprise motor loss during the actuator's deceleration phase and the losses related to the ground contact. Figure 8.1 illustrates this energy level across varying speeds $v \in [0.5, 0.6, \ldots, 1.5]$ m/s.

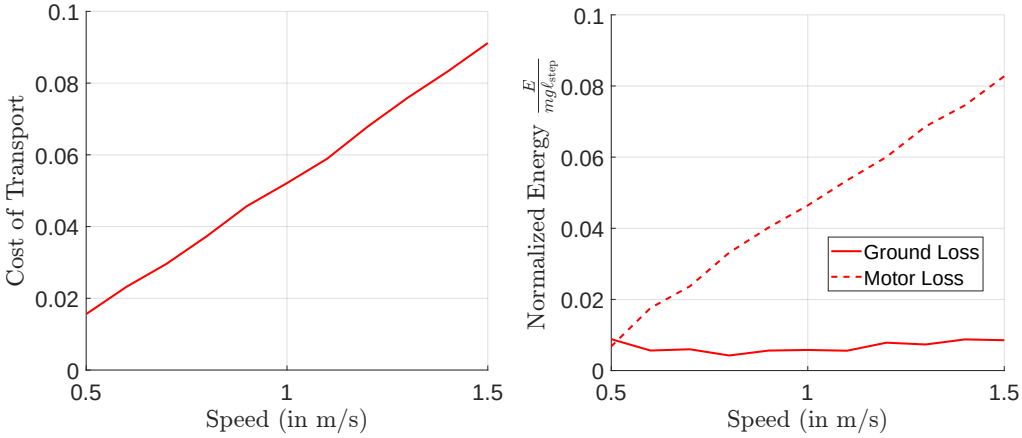

(a) Optimized cost of transport.

(b) Normalized energy losses, with ground losses shown in solid lines and motor losses shown in dashed lines.

Figure 8.1: Illustration of optimized cost of transport and the corresponding energy losses.

Cost of Transport and Energy Loss

As characterized in (7.1), the CoT quantifies the total input energy from the actuators, which is normalized by travel distance and robot weight, resulting in a dimensionless metric for assessing the energy efficiency of locomotion. The CoT demonstrates an approximately linear correlation with operating speed, as emphasized in Figure 8.1a. Notably, an augmentation in walking speed corresponds to a reduction in the efficiency of locomotion. For comparative purposes, the energy losses incurred during one step period are normalized by the weight of the robot and the distance traveled (step length), which aligns with the calculation of the CoT as presented in equation (7.1).
As illustrated in Figure 8.1b, actuator deceleration constitutes a substantial portion of the total energy loss. During the deceleration phase, the actuator generates negative mechanical power, indicating that kinetic energy is converted into electrical energy. This regenerative process often leads to significant increases in voltage within the motor controller, potentially damaging the electrical circuit. Consequently, most direct current controllers are equipped with a "brake chopper" to monitor the voltage within the controller. When the voltage unexpectedly surpasses a certain threshold, the brake chopper activates, redirecting the surplus energy to a braking resistor, thereby converting the electrical energy into thermal energy losses.
According to the observations documented in the Bachelor's thesis [201], the low transfer efficiency suggests that no electrical energy is reused for battery recharging. Thus, negative mechanical power represents a considerable portion of the total energy loss

that occurs during locomotion. As walking speeds increase, the loss incurred during the deceleration phase follows almost linearly.
Conversely, the phenomenon of contact loss with the ground is also illustrated in Figure 8.1b. In particular, an inelastic impact is modeled at the end of the single support phase when the swing foot makes contact with the rigid ground. The impact loss is mitigated by optimizing the walking gait across the examined speeds, thereby maintaining a nearly constant magnitude. Specifically, the optimized gait strategy involves decelerating the motion just prior to contacting the ground surface in order to diminish the impact loss. Consequently, there is an increase in deceleration-related energy loss in the motor, but a reduction in impact loss. At lower walking speeds, the impact loss exerts a more considerable effect on the overall energy loss, as minimal actuation is required to facilitate the forward motion.

Step Length and Frequency

Figure 8.2 presents step length and step frequency of optimized walking gaits across various speeds. Notably, the product of step length and step frequency determines the operational speed, indicating an interdependence between these two variables. However, Figure 8.2a demonstrates that at lower speeds (below 0.9 m/s), the robot tends to markedly increase the step length while maintaining nearly constant step frequencies to achieve increased speed with minimal energy expenditure. Once the walking speed exceeds 1.0 m/s, it becomes advantageous to enhance the step frequency to accommodate a higher speed.

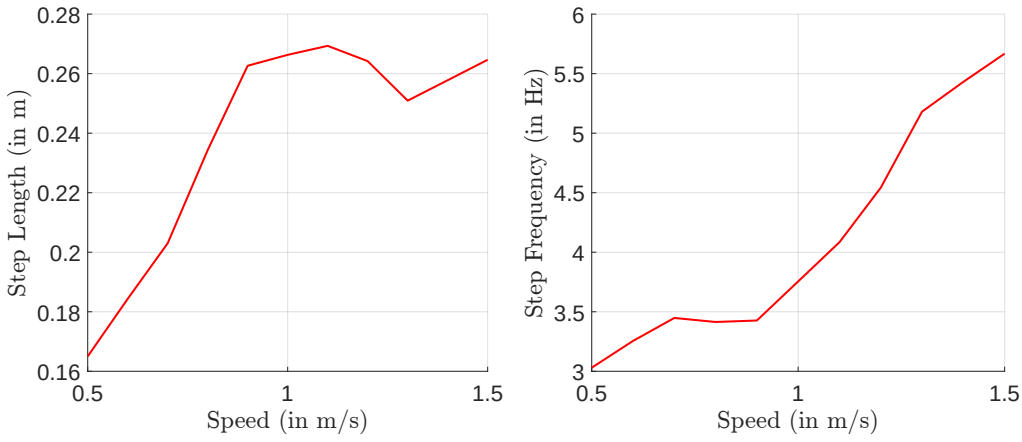

(a) Step length of the optimized gaits.

(b) Step frequency of the optimized gaits.

Figure 8.2: Illustration of step length and frequency of the optimized walking gaits at varying speeds.

Optimal Gait and Posture

The optimized posture of the walking motion is depicted in Figure 8.3, Figure 8.4, and Figure 8.5 corresponding to the speeds $v = 0.5$, $v = 1.0$, and $v = 1.5$ m/s, respectively. Specifically, the torque requirements of the actuators are represented by the intensity of color within the actuated joints.

Upon analyzing the speeds presented, it becomes apparent that the optimal gait at lower speed ($v = 0.5$ m/s) is characterized by minimal segmental movement. Notably, the relative movement of the thighs is insignificantly small, with the walking motion primarily relying on the free oscillation of the shanks, thereby necessitating minimal actuator work while achieving high energy efficiency, as illustrated in Figure 8.3.

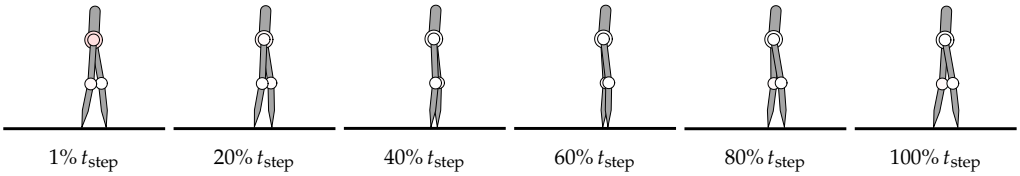

Figure 8.3: Snapshots of the optimized walking gaits at speed $v = 0.5$ m/s.

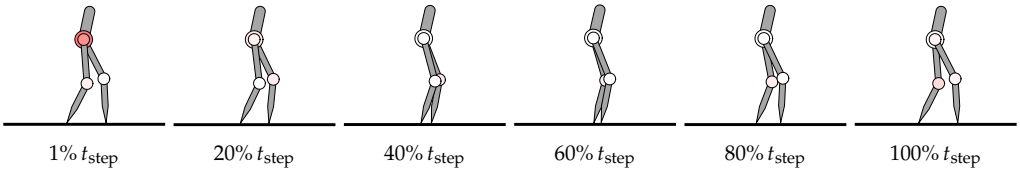

Figure 8.4: Snapshots of the optimized walking gaits at speed $v = 1.0$ m/s.

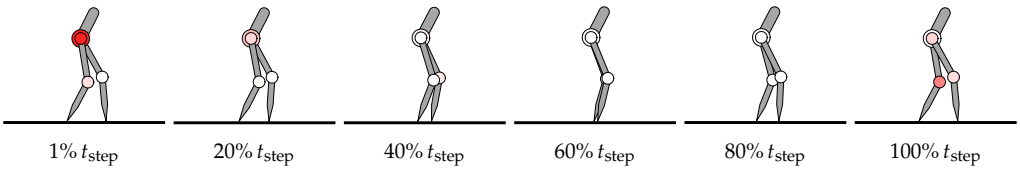

Figure 8.5: Snapshots of the optimized walking gaits at speed $v = 1.5$ m/s.

At high velocities, as demonstrated in Figure 8.4 and Figure 8.5, significant actuation is required at both the initiation and termination of the single support phase. Specifically, the hip actuator is critical in maintaining upper body orientation after impact and in accelerating the swing leg for the subsequent step period at the beginning of the single support phase. Just prior to the contact event, the actuators are tasked with decelerating the motion to reduce the approach velocity of the swing foot towards the ground,

thus mitigating impact loss. Mid-step period observations reveal that the actuators predominantly remain inactive, as the robot exploits the segments' free oscillation to facilitate forward motion.

8.2.2 Gait Stability

The stability of the periodic walking gait encompasses two perspectives: first, the asymptotic stability of the high-gain feedback controller, which is crucial for ensuring that the robot's motion remains constrained within the zero dynamics manifold, is imperative. Secondly, the stability properties of the periodic solution of the hybrid zero dynamics are assessed by examining the magnitude of the nontrivial Floquet multiplier, as discussed in this section. The verification of the ensuing gait stability is performed by evaluating initial perturbations in closed-loop simulations.

Floquet Multiplier

The two-dimensional characteristics of the zero dynamics linked with walking on rigid ground result in a single nontrivial Floquet multiplier, as demonstrated in Figure 8.6 across varying speeds. In particular, the magnitude of this nontrivial multiplier is constrained to be less than one, a requirement that is formulated as an inequality constraint within the optimization framework. Consequently, it is evident that the periodic solutions remain stable within the considered speed range.

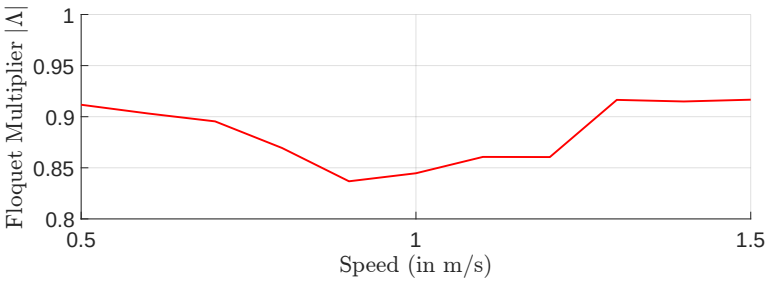

Figure 8.6: Magnitude of the nontrivial Floquet multiplier over different walking speeds.

Closed-Loop Simulation

To evaluate the stability attributes of the resultant walking gaits, initial perturbations in the system state variables are analyzed within the closed-loop simulations. As illustrated in Figure 8.7, 20 % deviations are introduced into the initial velocities of the robot with respect to the reference velocity $\dot{\mathbf{q}}_{\mathrm{ref,s}}$, i.e., $\dot{\mathbf{q}}_{\mathrm{s}}(t = 0) = 80\,\% \, \dot{\mathbf{q}}_{\mathrm{ref,s}}(t = 0)$. For the PD-feedback in the simulation, the gain parameters are set at $K_{\mathrm{p}} = 1000$ and

$K_d = 100$. The stability of the walking gaits at velocities $v = 0.5$ and $v = 1.5$ m/s is corroborated by the Floquet multiplier as described in Figure 8.6, wherein the simulated trajectories (represented by dotted lines) progressively converge to the reference limit cycle (depicted by solid lines). In other words, the perturbed gait invariably converges to the stable periodic reference walking motion ascertained through optimization.

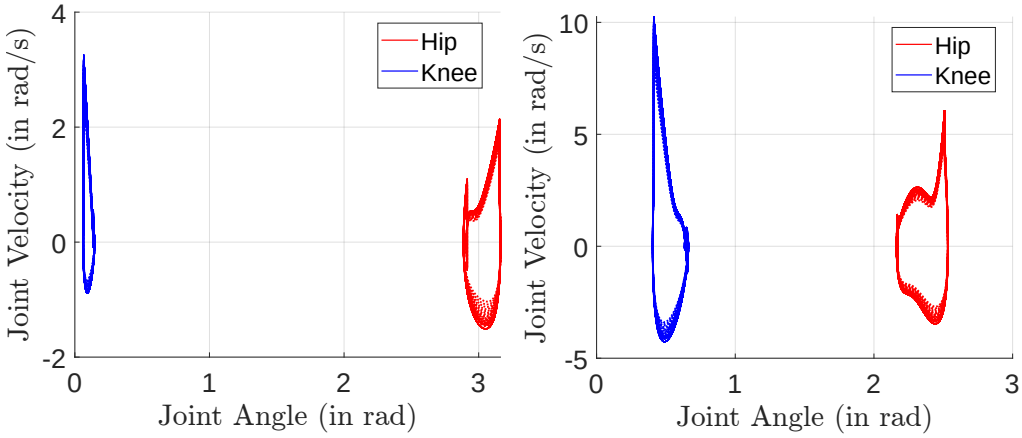

(a) Walking speed $v = 0.5$ m/s.

(b) Walking speed $v = 1.5$ m/s.

Figure 8.7: Illustration of the simulated joint configurations $\mathbf{q}_b$ and angular velocities $\dot{\mathbf{q}}_b$ denoted by dotted lines, considering initial deviations. The reference trajectory is depicted using solid lines.

Furthermore, the Floquet multiplier also signifies the convergence rate of the perturbed periodic solution. A smaller magnitude of the Floquet multiplier indicates a faster convergence rate. As the associated Floquet multipliers in Figure 8.6 for walking are generally slightly less than one, numerous step periods are required for the perturbation to converge close enough to zero.

8.3 Walking with Non-Instantaneous DSP on Rigid Ground

In comparison to locomotion with an instantaneous DSP, the full actuation during a continuous DSP enables the controller to actively improve gait stability. Nonetheless, this enhancement is accompanied by reduced energy efficiency. To address this issue, an efficiency analysis is undertaken in Section 8.3.1, and stability is examined in Section 8.3.2.

8.3.1 Efficiency Study

Gait patterns with a non-instantaneous DSP are examined within the same speed range $v \in [0.5, 0.6, \ldots, 1.5]$ m/s as those incorporating an instantaneous DSP, as documented

in Section 8.2.1. For the purpose of comparison, both instantaneous (represented in blue lines) and non-instantaneous DSP (represented in red lines) assumptions are depicted in Figure 8.8.

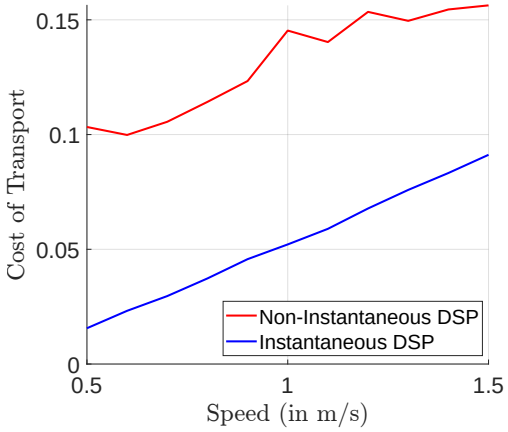

(a) Optimized cost of transport.

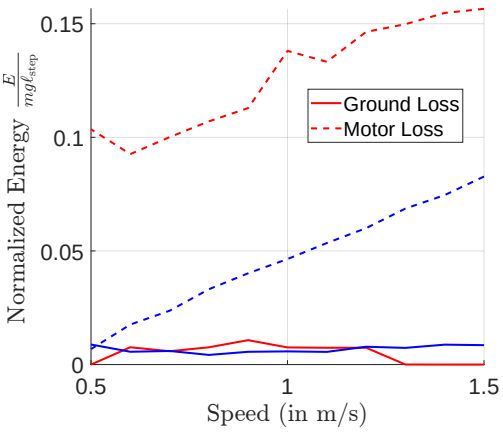

(b) Normalized energy losses, with ground losses shown in solid lines and motor losses shown in dashed lines.

Figure 8.8: Depiction of the optimized cost of transport alongside the associated energy loss for walking with non-instantaneous DSP, represented in red, and instantaneous DSP, represented in blue.

Cost of Transport and Energy Loss

The CoT presented in Figure 8.8a demonstrates an approximately linear relationship with the target average walking speed, indicating that an increase in walking velocity reduces the energy efficiency of locomotion. Moreover, compared with the gait featuring instantaneous DSP (illustrated in blue), a consistent discrepancy exists in the optimized CoT. To elucidate the underlying reasons for this disparity, the research detailed in [194] considers various strategies to modify the walking gait with instantaneous DSP. Specifically, the effects of step length and touch-down conditions are examined between gaits employing diverse DSP formulations. One of the primary distinctions between the two gaits is that both stance feet must remain in contact with the ground without slipping, thereby forming a closed kinematic chain during the DSP. In scenarios where the DSP is instantaneous, the preceding stance foot is lifted immediately following the impact of the swing leg with the ground.
The hypothesis from the study is that the key factor in the efficiency gap is the adoption of a point foot model. Consequently, maintaining the closed chain configuration within the DSP results in decreased efficiency, as the robot is unable to exploit the natural dynamics of the system for locomotion. In contrast, human walking gaits can achieve

high energy efficiency in a non-instantaneous DSP due to the employment of a rolling foot geometry. Therefore, future research should examine robot models with non-point foot geometry to assess their effectiveness during the non-instantaneous DSP to test the hypothesis.

Analysis of energy dissipation across diverse gait patterns yields critical insights into variations in resultant energy efficiency. As demonstrated in Figure 8.8b, the impact energy loss on rigid terrain displays similar magnitudes across both gait configurations. Notably, at elevated velocities, particularly at $v > 1.3$ m/s, the enforcement of a non-instantaneous DSP results in diminished impact loss, primarily attributed to the actuators' propensity to decelerate the motion immediately prior to impact to mitigate such losses. Moreover, decreasing the velocity of the swing foot as it nears the ground is essential to uphold the condition preventing the stance feet from slipping post-impact, a prerequisite for forming a closed kinematic chain configuration in the DSP. Nonetheless, this deceleration necessitates substantial effort from the actuator operating in generator mode, which is associated with the marked deceleration loss depicted by the dotted lines in Figure 8.8b.

Step Frequency and Proportion of SSP

A notable feature of the walking gait characterized by non-instantaneous DSP is that the step length remains approximately constant across varying speeds, particularly within the range $\ell_{\text{step}} \in [0.33, 0.43]$ m. This behavior markedly contrasts with observations of the gait exhibiting instantaneous DSP, as illustrated in Figure 8.2a, where the optimal step length exhibits a near-linear dependence on the target speed.

However, the step frequency of the optimal gaits demonstrates a comparable dependence on the walking velocity, as indicated in Figure 8.9a. Specifically, the step frequency associated with the gait characterized by non-instantaneous DSP is generally lower than that of the instantaneous DSP configuration across the range of speeds examined. A primary factor contributing to the enhanced energy efficiency of the gait incorporating instantaneous DSP is the robot's ability to exploit the natural oscillation of its segments during motion. This means the optimal step frequency is matched with the system's free oscillation frequency, thereby necessitating only minimal actuation.

Particularly, due to the utilization of a point foot model, the closed kinematic chain inherent in the non-instantaneous DSP constrains the controller's capability to fully leverage the natural oscillation to produce a feasible gait. Consequently, substantial actuator effort is required to prevent slippage of the point foot on the substrate, which degrades energy efficiency.

To enhance efficiency, the optimization process adjusts the distribution of the DSP duration relative to the step period as the walking speed varies. As illustrated in

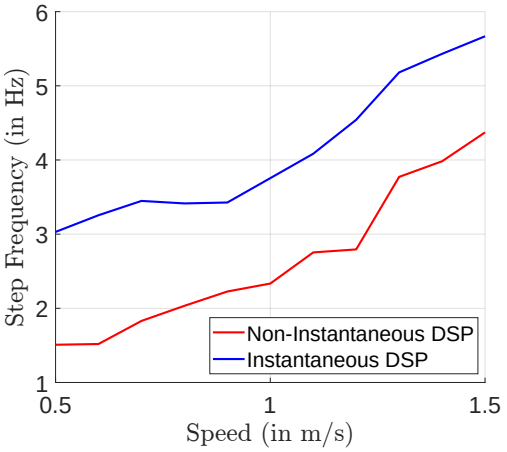

(a) Step frequency of the optimized walking with instantaneous (in blue) and non-instantaneous (in red) DSP.

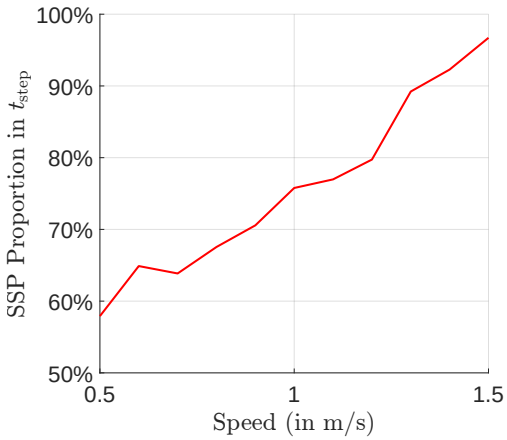

(b) Proportional allocation of SSP within step duration t_{step}.

Figure 8.9: Illustration of step frequency and proportion of the SSP of the optimized walking gaits.

Figure 8.9b, the significance of the SSP increases with greater walking speeds. The contact constraints in the SSP are more readily satisfied compared to those in the DSP, thereby allowing the substantial amplitude of the robot segments' free oscillation to be harnessed for improved efficiency.

Optimal Gait and Posture

The optimized posture of the walking motion is illustrated in Figure 8.10, Figure 8.11, and Figure 8.12, corresponding to the speeds $v = 0.5$, $v = 1.0$, and $v = 1.5$ m/s, respectively. The step length of the walking gaits with non-instantaneous DSP exhibits minimal variation with respect to speed, as depicted in these snapshots.

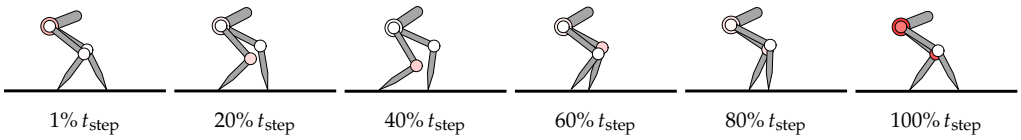

Figure 8.10: Snapshots of the optimized walking gaits at speed $v = 0.5$ m/s.

Compared to gaits with instantaneous DSP, those with non-instantaneous DSP typically exhibit a lower center of mass position. This characteristic is crucial for the controller to uphold the constraints defined at the contact foot during the non-instantaneous DSP, encompassing unilateral contact and static friction conditions. Even during the SSP, the

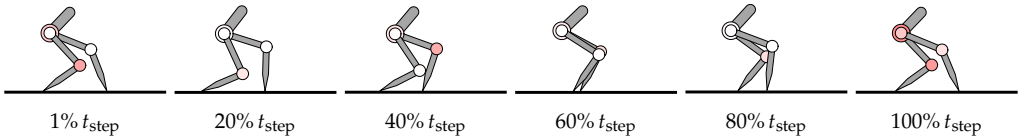

Figure 8.11: Snapshots of the optimized walking gaits at speed $v = 1.0$ m/s.

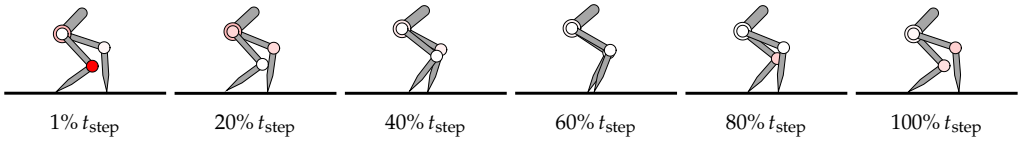

Figure 8.12: Snapshots of the optimized walking gaits at speed $v = 1.5$ m/s.

swing leg is slightly elevated from the ground to ensure that the vertical velocity of approach towards the ground before impact remains minimal. The marked difference in optimal gaits underscores the fact that the natural dynamics are not harnessed in the gait with a non-instantaneous DSP, resulting in reduced energy efficiency compared to the instantaneous DSP gait.

Figure 8.13 elucidates the torque requirements for the four physical actuators integral to producing optimal walking gaits at a uniform velocity of $v = 0.5$ m/s. Owing to the optimal projection of virtual actuators in the DSP, the actuators positioned at the knee joint of the trailing leg and the hip joint of the leading leg are pivotal for propelling forward motion, while the other two actuators remain inactive, as illustrated in Figure 8.13a. Subsequent to the lift-off event, both hip joint actuators become critical, particularly at the commencement and conclusion of the SSP. Specifically, substantial actuation is imperative to maintain the orientation of the upper body at the start of the SSP and to decelerate movement to mitigate impact loss at the SSP's conclusion. Midway through the SSP, all actuators exert comparatively minimal torque as the robot predominantly exploits the segment's free oscillation for motion. Conversely, the instantaneous DSP gait, as portrayed in Figure 8.13b, demands considerably reduced torque from all actuators, as the resulting walking gait is chiefly derived from the segment's free oscillation with high energy efficiency, as demonstrated by the body posture exhibited in Figure 8.3.

Figure 8.14 presents the actuator torques resulting from two walking gaits at an increased speed of $v = 1.5$ m/s, where the proportional share of the DSP is diminished to 3.3% of the complete step duration t_{step}, in accordance with Figure 8.9b. In the simulations, as actuator saturation is not accounted for, the optimal gait configuration relies on a notably large actuator torque within the knee joint of the trailing leg during the DSP to avert the breach of constraints at the stance feet, as illustrated in Figure 8.14a. Nevertheless, during the SSP, the actuator magnitudes exhibit behavior akin to that observed in gaits with

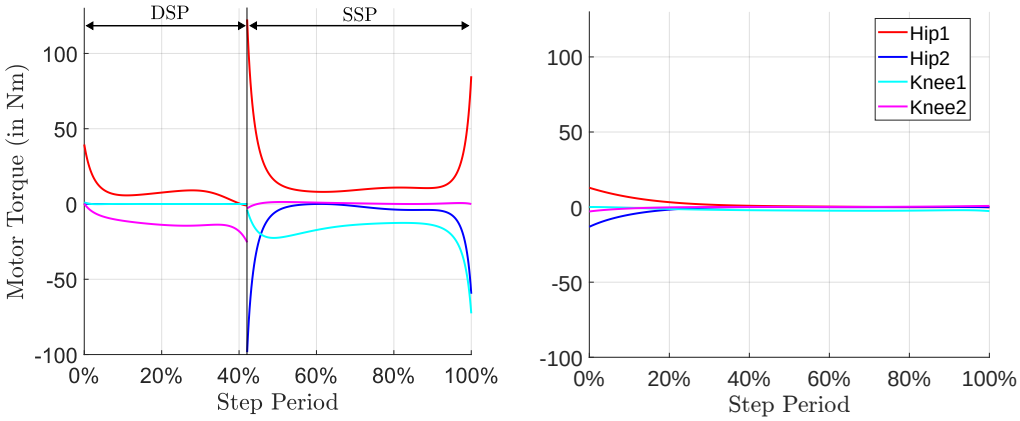

(a) Walking with non-instantaneous DSP.

(b) Walking with instantaneous DSP.

Figure 8.13: Illustration of the four actuators **u** for walking at speed $v = 0.5$ m/s.

an instantaneous DSP, as illustrated in Figure 8.14b. This indicates that the diminution in energy efficiency is chiefly attributable to the non-instantaneous character of the DSP, wherein the natural dynamics of the closed kinematic chain cannot be effectively harnessed for locomotion.

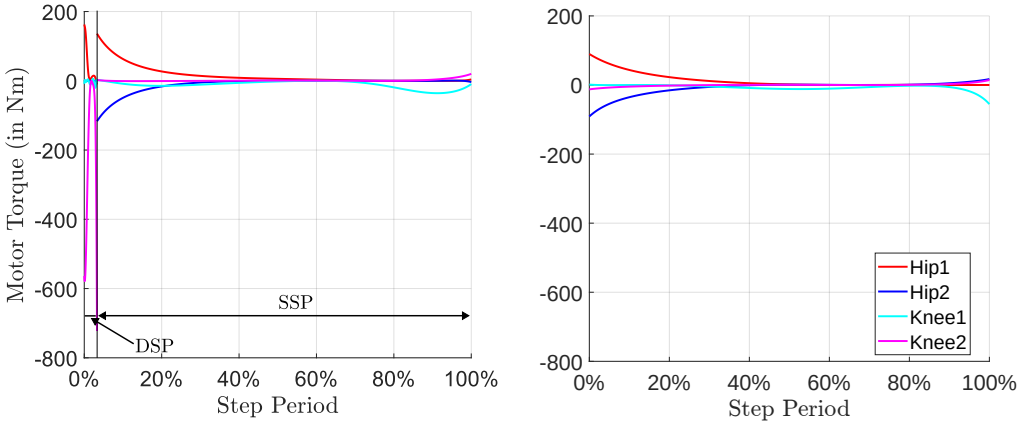

(a) Walking with non-instantaneous DSP.

(b) Walking with instantaneous DSP.

Figure 8.14: Illustration of the four actuators **u** for walking at speed $v = 1.5$ m/s.

Furthermore, a primary discrepancy between the optimal body postures presented in Figure 8.5 and Figure 8.12 lies in the foot-ground contact condition: both stance feet remain on the ground without slippage under a non-instantaneous DSP. In contrast,

should the DSP be regarded as instantaneous, the formerly trailing stance leg is immediately lifted off, leading to a non-zero foot velocity; this scenario aligns more closely with the free oscillation of the body segments, yielding enhanced efficiency.

8.3.2 Gait Stability

One of the principal advantages of considering the DSP as non-instantaneous is the enhanced stability of the periodic gait. In contrast to the conventional walking gait with instantaneous DSP, the fully actuated DSP is employed to exert an influence on the perturbations in the periodic solution, even though the SSP remains invariant across both gaits. Crucially, minor deviations from the periodic orbit are mitigated to zero through the control law that is directly formulated on the zero dynamics coordinate, as delineated in Section 4.2.1. In this section, the augmented stability is evidenced by the Floquet multiplier and validated through closed-loop simulations.

Floquet Multiplier

For comparative purposes, two distinct feedback gains K_{σ_d} within the scope of control design (4.40b) are examined in the assessment of the Floquet multiplier, as illustrated in Figure 8.15. In light of the fully actuated nature of the DSP, the magnitude of the nontrivial Floquet multiplier pertaining to the periodic gait is adjusted to approach zero upon the selection of a substantial gain K_{σ_d}.

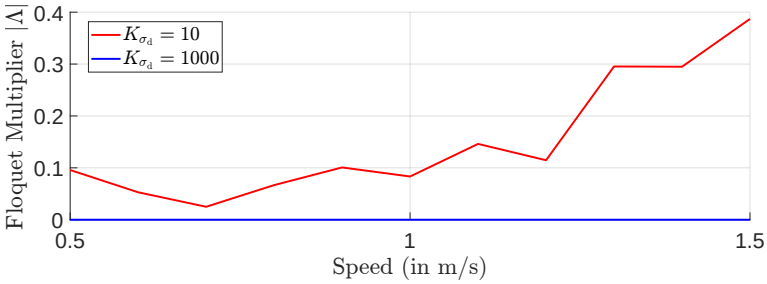

Figure 8.15: Magnitude of the nontrivial Floquet multiplier for different feedback gains K_{σ_d}.

Closed-Loop Simulation

Owing to the enhanced stability characteristics observed in walking with non-instantaneous DSP, a greater initial error is accounted for in the velocity of the robot's segments, specifically $\dot{\mathbf{q}}_\mathrm{d}(t = 0) = 60\,\% \, \dot{\mathbf{q}}_{\mathrm{ref,d}}(t = 0)$, where $\dot{\mathbf{q}}_{\mathrm{ref,d}}(t = 0)$ represents the reference initial velocities in the DSP of the periodic gait. For the PD-feedback in the simulation, the gain parameters are set at $K_{\sigma_\mathrm{d}} = 10$, $K_\mathrm{p} = 1000$ and $K_\mathrm{d} = 100$. As illustrated in

Figure 8.16, the steady periodic limit cycle is attained after fewer steps in comparison to the gait employing instantaneous DSP, as shown in Figure 8.7.

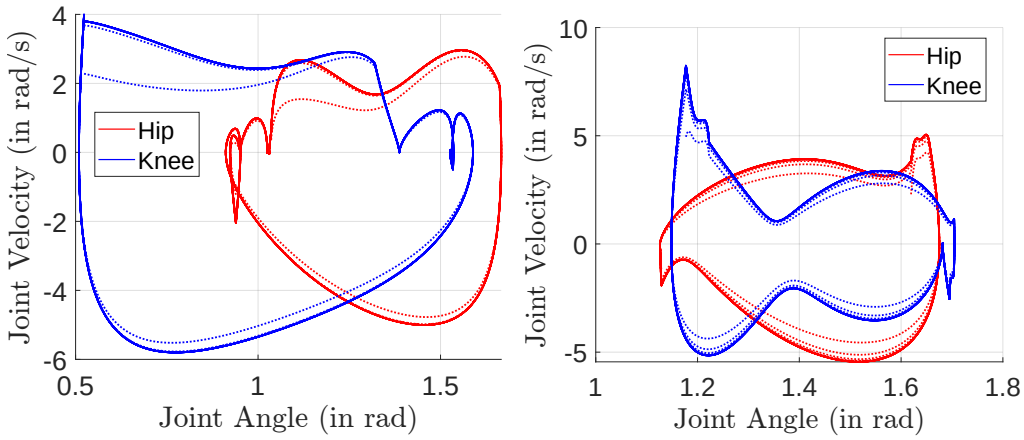

(a) Walking speed $v = 0.5$ m/s. **(b)** Walking speed $v = 1.5$ m/s.

Figure 8.16: Illustration of the simulated joint configurations $\mathbf{q}_b$ and angular velocities $\dot{\mathbf{q}}_b$ denoted by dotted lines, considering initial deviations. The reference trajectory is depicted using solid lines.

The augmented convergence behavior facilitated by the implementation of a non-instantaneous DSP may be employed in experimental investigations involving biped robots. Particularly, in the context of initializing locomotion, the effort required for adjusting the initial conditions of the coordinates and velocity of the segments can be significantly reduced if the initiation of the gait occurs during the DSP. Once the robot attains a steady walking motion incorporating a non-instantaneous DSP, transient steps can be effectively executed by refining the reference gait within the controller, thereby ultimately achieving a periodic gait characterized by less optimal convergence behavior. Owing to the uniform HZD control framework, the reference gait can be effortlessly reprogrammed in real-time within the controller. Furthermore, the improved stability attributes associated with the non-instantaneous DSP gait can be leveraged in scenarios where environmental conditions pose substantial challenges.

8.4 Running on Rigid Ground

Periodic running gaits on rigid ground surfaces are demonstrated with regard to their energy efficiency and stability attributes, as examined in Section 8.4.1 and Section 8.4.2, respectively.

8.4.1 Efficiency Study

The analysis of the efficiency study focuses on the CoT and energy losses, as illustrated in Figure 8.17. Specifically, this analysis is performed within the running speed range of $v \in [1.8, 1.9, \ldots, 2.8]$ m/s. In order to enable a comparison between walking and running on rigid surfaces, the speed range for walking, which includes an instantaneous DSP, is extended to $v \in [1.8, 1.9, \ldots, 2.3]$ m/s, thereby illustrating the intersection of the CoT between running and walking.
The speed range can indeed be extended to align with the running speed range. However, for the investigated robot model, which possesses a height of 0.83 m, the extended walking speeds exceed the realizable limits. For example, reference [25] denotes that individuals of average height, measured at 1.77 m, generally achieve a maximum walking speed of less than 2.5 m/s. The utilization of this extended speed range is confined to academic investigations, enabling a comparative analysis of walking and running within simulation settings, particularly concerning the transitional speed between these gaits.

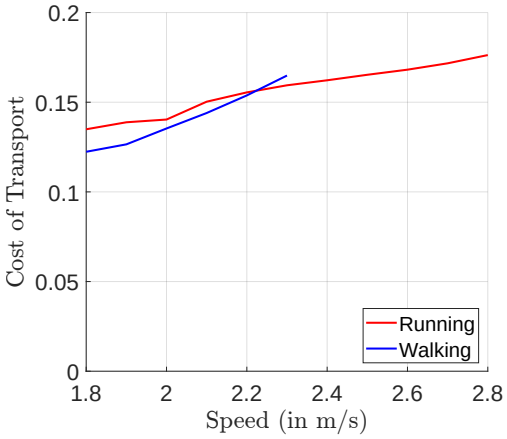

(a) Optimized cost of transport.

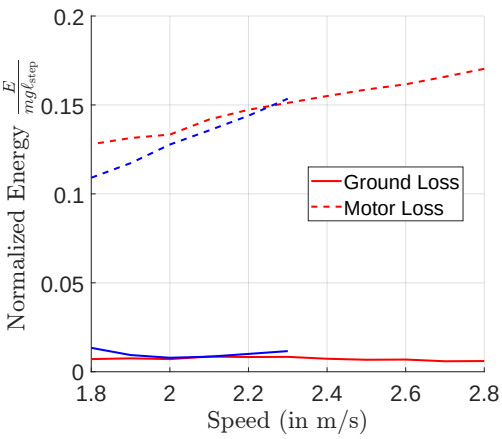

(b) Normalized energy losses, with ground losses shown in solid lines and motor losses shown in dashed lines.

Figure 8.17: Depiction of the optimized CoT alongside the associated energy loss for running (illustrated in red) and walking (depicted in blue).

Cost of Transport and Energy Loss

Figure 8.17a suggests a nearly linear relationship between the optimized CoT and running speed. The intersection point of the CoT for walking and running occurs at

approximately 2.2 m/s, indicating that below 2.2 m/s, walking is more energy-efficient, while above this threshold, running exhibits greater efficiency.
The representation of normalized energy loss in Figure 8.17b illustrates that the loss of impact energy during walking and running is significantly less than the energy loss experienced by the actuator when functioning in generator mode during deceleration. Specifically, an increase in locomotion speed leads to an augmentation in the actuator's energy loss. Furthermore, although running gaits incur a higher per-step impact loss compared to walking, the normalization process, taking into account the robot's weight and the significantly greater step length in running as detailed in Figure 8.18a, renders the normalized impact loss to be of comparable magnitude and nearly invariant across the range of speeds examined.

Step Length and Frequency

As illustrated in Figure 8.18a, achieving high energy efficiency in running necessitates a substantial adjustment of step length in accordance with the average running speed. Conversely, the step frequency of running remains largely unaffected by speed, contrasting markedly with observations in walking gaits. Specifically, Figure 8.9a demonstrates that walking, with either instantaneous or non-instantaneous double support phases, adjusts the step frequency to correspond with variations in walking speed. This discrepancy arises because running gaits incorporate a flight phase, which facilitates higher speeds with minimal actuator effort.

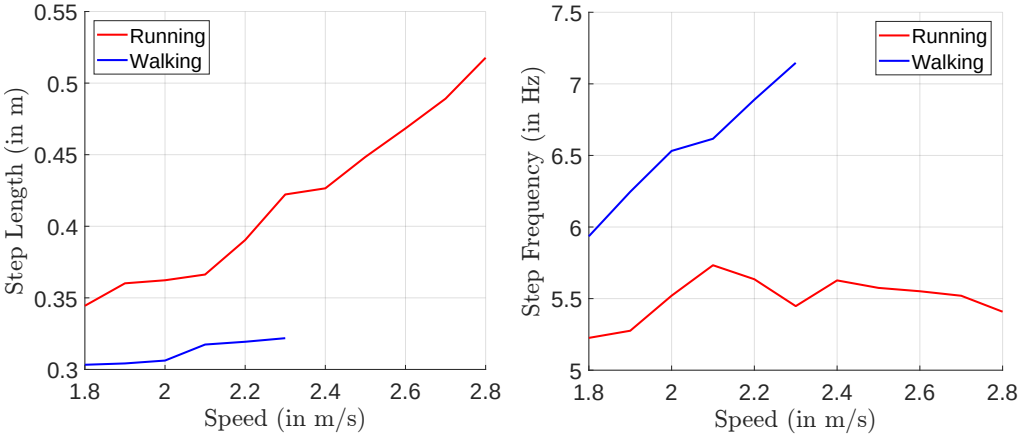

(a) Step length of the optimized gaits.

(b) Step frequency of the optimized gaits.

Figure 8.18: Illustration of the step length and frequency of the optimized running gaits.

Optimal Gait and Posture

The optimized posture of running motion at speeds $v = 1.8$, $v = 2.3$, and $v = 2.8$ m/s is illustrated in Figure 8.19, Figure 8.20, and Figure 8.21, respectively. Initial observations suggest that the orientation of the upper body remains relatively constant regardless of speed variations. Notably, the approach angle of the swing leg's foot is adjusted to be nearly vertical to the ground surface immediately prior to landing, thereby aiding in the reduction of impact loss.

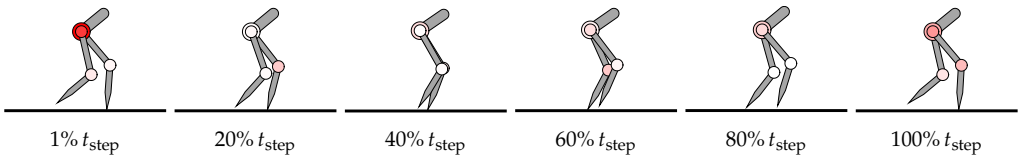

Figure 8.19: Snapshots of the optimized running gaits at speed $v = 1.8$ m/s.

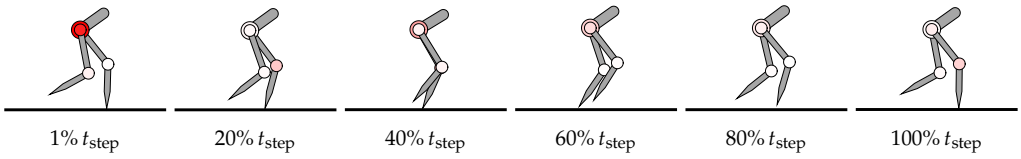

Figure 8.20: Snapshots of the optimized running gaits at speed $v = 2.3$ m/s.

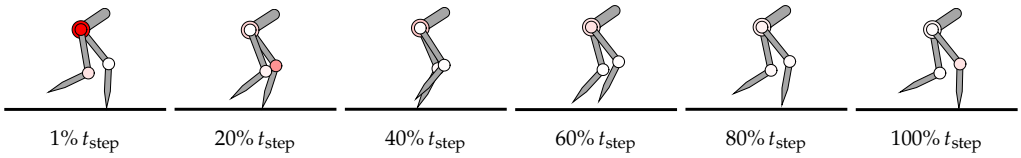

Figure 8.21: Snapshots of the optimized running gaits at speed $v = 2.8$ m/s.

To accommodate the increase in speed, both the step length and the relative duration of the flight phase within a step cycle are augmented. Specifically, as the effect of energy dissipation due to air resistance during the flight phase is neglected, the trajectory of the robot's center of mass is characterized by a parabolic path. Consequently, a longer flight duration results in an increased distance between the robot and the ground surface, as evidenced by the presented gaits.

8.4.2 Gait Stability

The stability of gait is assessed using the Floquet multiplier, which is employed for both walking and running on rigid ground for comparative analysis, as illustrated

in Figure 8.22a. Both gaits are generated by utilizing the inequality constraint (7.23), which requires the magnitude of the nontrivial multiplier to remain below one. Upon optimization, it is noted that the nontrivial Floquet multiplier for running consistently remains slightly below one across all tested speeds, although it exceeds that observed in walking.

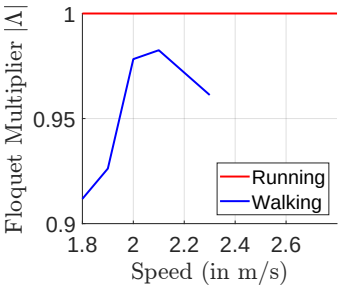

(a) Magnitude of the nontrivial Floquet multiplier.

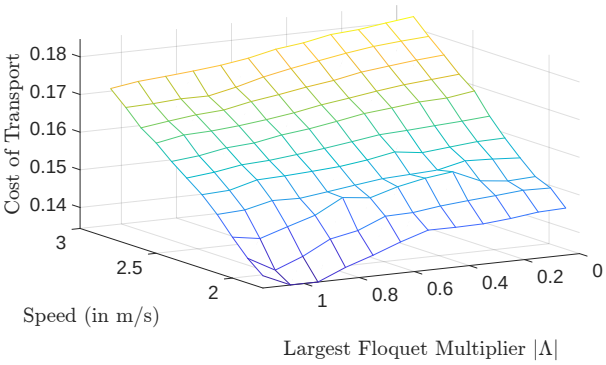

(b) Cost of tranport at varying running speed and nontrivial Floquet multipliers.

Figure 8.22: The nontrivial Floquet multiplier and its impact on the cost of transport.

The parameter study outlined in Figure 8.22b provides valuable insights into the relationship between the CoT and the stability characteristics of running gaits. In particular, modifications to the posture during the underactuated flight phase can readily influence the stability of the running gait, resulting in a diverse array of distinct Floquet multipliers. A reduction in the Floquet multiplier corresponds to an increase in the CoT, implying that enhancing gait stability diminishes energy efficiency. Given that efficiency is regarded as the optimization objective, solutions characterized by a Floquet multiplier slightly less than one invariably represent the optimization minimum.

8.5 Running on Compliant Ground

Periodic running gaits on compliant ground surfaces are evaluated concerning their attributes of energy efficiency and stability, as investigated in Section 8.5.1 and Section 8.5.2, respectively. Furthermore, these gaits are compared to running on rigid ground, as documented in Section 8.4.

8.5.1 Efficiency Study

An efficiency analysis of running on both compliant and rigid ground surfaces is performed over a speed range of $v \in [1.8, 1.9, \ldots, 2.8]$ m/s, as depicted in Figure 8.23.

This examination encompasses an evaluation of the CoT and the energy dissipation associated with the periodic gaits. In the tangential force (5.17a), the damping coefficient B_x is set to 69440 Nsm^{-1}, and the stiffness K_x is 43405 Nm^{-1}. For the vertical force (5.19), the parameters are $K_{\mathrm{exp}} = 152042\,\mathrm{Nm}^{-1}$, $\nu = 1.5$, and $\eta = 1.2$.

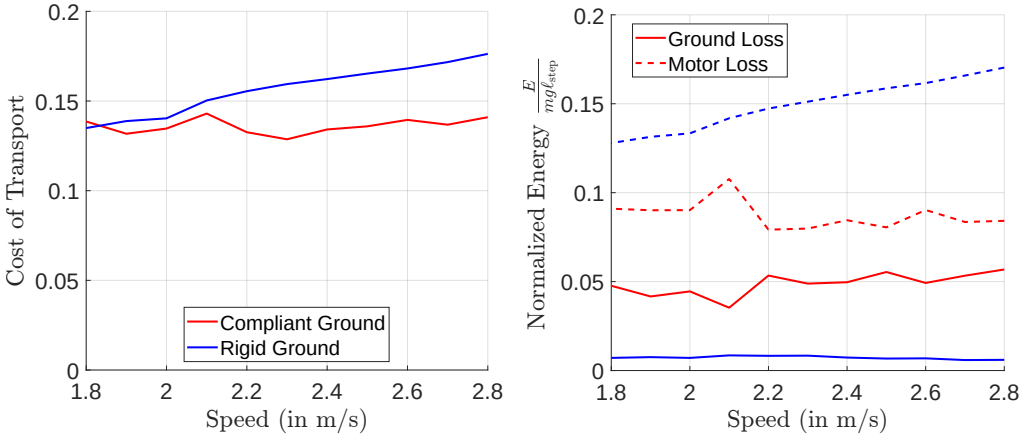

(a) Optimized cost of transport.

(b) Normalized energy losses, with ground losses shown in solid lines and motor losses shown in dashed lines.

Figure 8.23: Depiction of the optimized CoT alongside the associated energy loss for running on compliant (illustrated in red) and rigid ground (depicted in blue).

Cost of Transport and Energy Loss

As demonstrated in Figure 8.23a, in contrast to running on rigid surfaces, the optimal CoT displays minimal dependency across the assessed running velocities. Therefore, at speed $v = 1.8$ m/s, the efficiency of running on both types of surfaces is comparable. However, as velocity increases, the gaits on compliant surfaces exhibit greater efficiency than those on rigid ground.

Figure 8.23b illustrates that the impact loss experienced on rigid ground is significantly less than the energy dissipation caused by damping on compliant ground. Conversely, the energy loss linked to actuator deceleration is diminished when operating on compliant ground. In addition, this motor loss remains almost unchanged with varying running speeds. In essence, the robot's motion on compliant ground more closely resembles its natural oscillation, allowing it to effectively utilize the elastic energy temporarily stored due to the ground's elasticity for the running motion. Consequently, despite the higher damping dissipation, running on compliant ground proves to be more energy-efficient.

Step Length and Frequency

The step length and frequency while running on both rigid and compliant ground surfaces are illustrated in Figure 8.24. Essentially, step length exhibits an increase with the augmentation of running speed across both ground types, whereas step frequency demonstrates minimal responsiveness to speed variations.

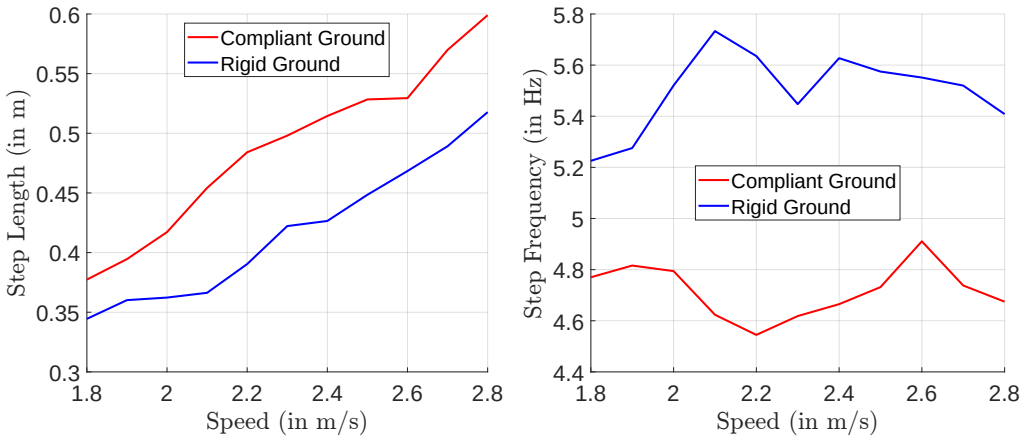

(a) Step length of the optimized gaits.

(b) Step frequency of the optimized gaits.

Figure 8.24: Illustration of the step length and frequency of the optimized running gaits.

Notably, running on compliant ground is characterized by an extended step length coupled with a reduced frequency. The variation in optimal step frequency stems from leveraging the stiffness of the compliant ground to minimize the effort required for locomotion. Since rigid ground can be represented with an infinitely large stiffness parameter, a gradual increase in the stiffness parameter may result in a higher optimal step frequency, situated between the cases illustrated in Figure 8.24b.
Additionally, Figure 8.25 elucidates the relative distribution of flight phase duration within a step period t_{step} and the allocation of the cost of transport CoT_s, that is assessed during the single support phase, in relation to the overall CoT of the periodic gait. Notably, Figure 8.25a identifies that the optimal running gait on compliant surfaces is associated with a substantially large proportion of the flight phase relative to the total step period. In the absence of air dissipation considerations, an extended flight phase contributes to minimizing the actuator's effort in facilitating locomotion.
Concerning energy consumption, Figure 8.25b demonstrates that a significant portion of the total energy expended during locomotion on a rigid surface occurs during the SSP, i.e., over 97 %. Conversely, the act of running on compliant ground, which leverages the elasticity of the deformable ground, results in a reduction of relative energy consumption to approximately 85 %. This phenomenon can be explained by the transient conversion

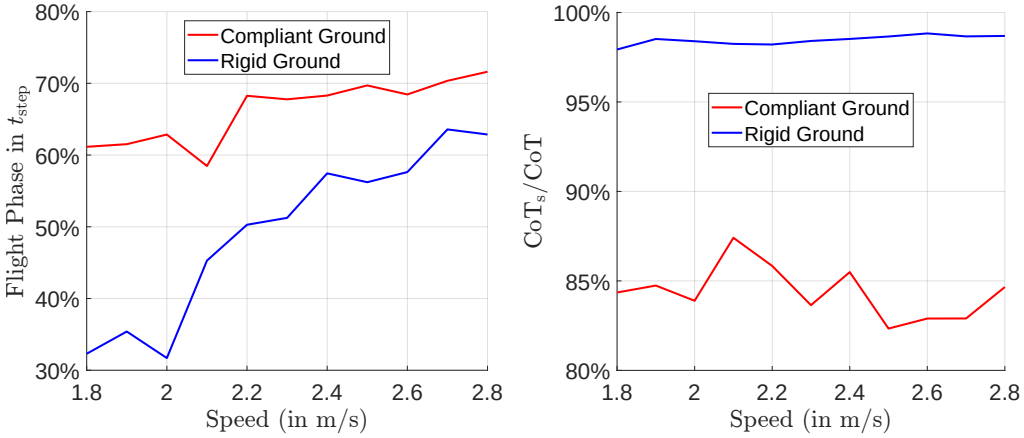

(a) Distribution of flight phase duration.

(b) CoT_s in SSP to total CoT.

Figure 8.25: The relative duration of the flight phase with respect to t_{step}, and the allocation of CoT_s during the SSP in relation to the total CoT.

of kinetic energy into elastic energy stored within the ground substrate. Despite considerable damping dissipation, this stored elastic energy is subsequently released during the phase of contact separation, facilitating the robot's lift-off from the ground. Consequently, the overall energy efficiency is enhanced when contrasted with movement on rigid ground.

Actuator and Reaction Force in Ground

Additional insights into the contact mechanics can be gleaned from the analysis of actuator power and torque, as depicted in Figure 8.26 and Figure 8.27, respectively. In particular, Figure 8.26 illustrates the mechanical power $P_{\text{mech},i} := u_i \dot{q}_{\text{b},i}$, $i \in \{1, 2, 3, 4\}$ that is generated by four actuators. The CoT is calculated by integrating the positive mechanical power, while the deceleration loss, as depicted in Figure 8.23b, is determined by integrating the negative mechanical power.

In the context of running on compliant ground, as illustrated in Figure 8.26a, the mechanical power exhibits a gradual increase during the restitution phase, followed by a gentle decrease during the separation phase of the contact period. During the mid-contact phase, substantial actuation, predominantly from the hip joints, is necessitated for the stabilization of the body. Furthermore, at the commencement of the flight phase, significant deceleration (negative mechanical power) in the hip of the former stance leg is essential for preserving an optimal body configuration during flight.

Conversely, running on rigid ground, as depicted in Figure 8.26b, demands considerable deceleration in the hip of the stance leg immediately following the inelastic impact at the

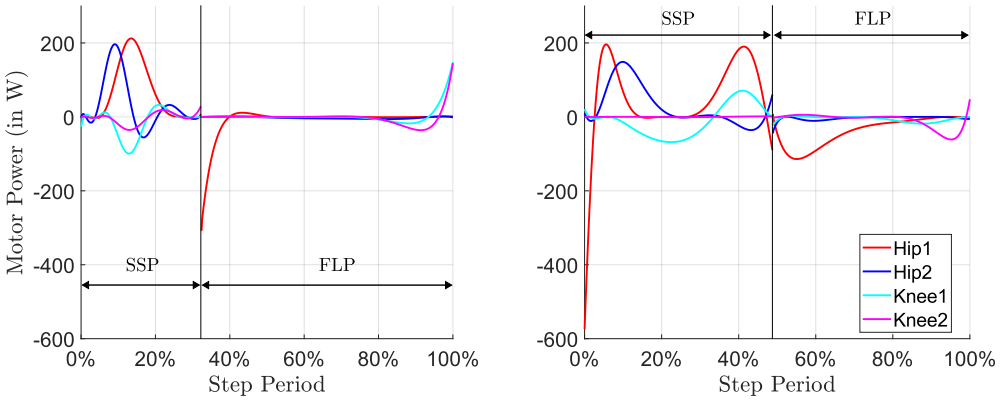

(a) Running on compliant ground.

(b) Running on rigid ground.

Figure 8.26: Actuator's mechanical power for running at 2.3 m/s on both compliant and rigid ground surfaces.

onset of the SSP, to absorb the impact and retain upper body orientation. Subsequent to this marked deceleration, positive mechanical power is imperative for re-accelerating the segments for the subsequent step period. During the mid-point of the SSP, the actuators operate with minimal activity. Towards the conclusion of the SSP, both the hip and knee actuators in the stance leg are required to exert considerable positive work to propel the body off the ground, owing to the absence of recoverable elastic energy from the rigid surface.

It is characteristic that the actuators remain largely inactive during the flight phase. However, towards the conclusion of the flight, actuation becomes necessary to adjust body configurations in order to achieve optimal landing, thereby minimizing contact loss, whether in the form of damping dissipation on compliant surfaces or impact loss on rigid surfaces.

Subsequently, Figure 8.27 demonstrates the torque produced by the actuators under the same conditions. In a comparable manner, Figure 8.27a illustrates that the actuator torque experiences a gradual increase and decrease throughout the contact phase while running on compliant ground. Conversely, Figure 8.27b suggests that a substantial jump occurs in the hip actuators following the inelastic impact on rigid ground. Consequently, from a perspective focused on reducing potential harm to the actuators and transmissions, running on compliant ground offers a significant benefit.

The reaction force during the SSP on compliant and rigid ground is illustrated in Figure 8.28. Similar to the behavior of the actuator torque, the reaction force for running on compliant ground, as shown in Figure 8.28a, also demonstrates a gradual increase

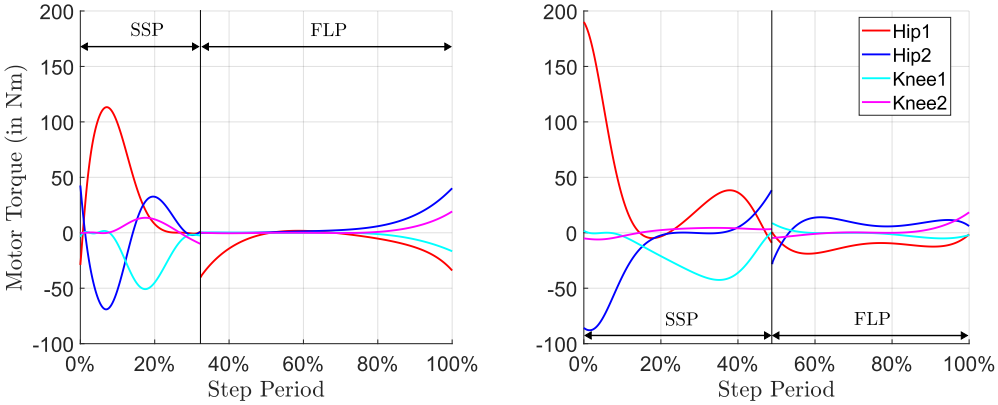

(a) Running on compliant ground. **(b)** Running on rigid ground.

Figure 8.27: Torque generated by the actuator for running at 2.3 m/s on both compliant and rigid ground surfaces.

and decrease during the contact period, differing from that on rigid ground, as depicted in Figure 8.28b.

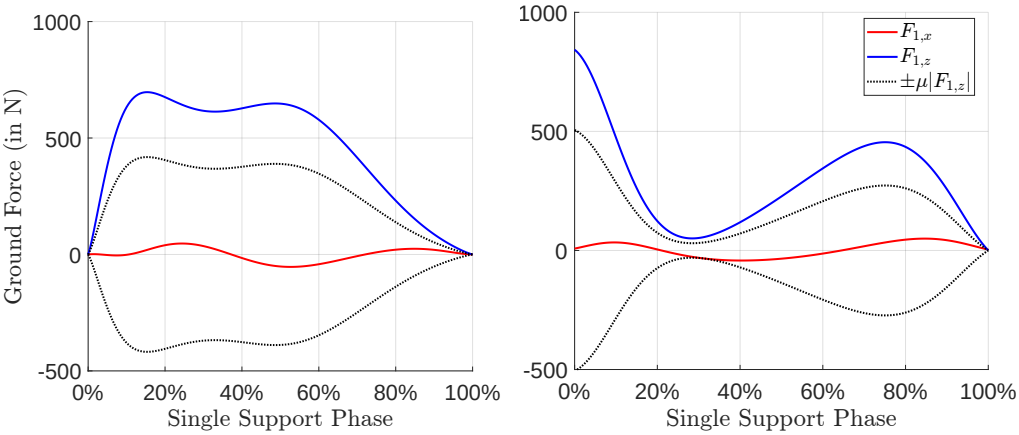

(a) Running on compliant ground. **(b)** Running on rigid ground.

Figure 8.28: Solid lines indicate reaction forces $\mathbf{F}_1 := [F_{1,x}, F_{1,z}]^\top$ on both rigid and compliant ground during the SSP of running at 2.3 m/s. Dashed lines show the maximum horizontal force without slippage, per $\mu = 0.6$.

In the realm of optimization, the static friction cone condition, as discussed in (7.15) and (7.20) for rigid and compliant surfaces respectively, defines the maximum permissible horizontal force magnitude $F_{1,x}$ (depicted as red lines) in relation to the vertical force $F_{1,z}$ (represented by blue lines) to guarantee a non-slipping contact. With regard to

running on compliant surfaces in Figure 8.28a, the occurrence of critical slippage is predominantly constrained to the initial and terminal phases of the contact interaction, attributable to the consideration of a soft material, particularly in the vertical direction. Conversely, on rigid surfaces, slippage occurring midway through the contact phase is of elevated concern, thereby potentially complicating the control strategy due to the necessity for the controller to perpetually assess the contact conditions. Moreover, a reduced running velocity contributes to the mitigation of the critical slippage condition during the mid-contact phase, as demonstrated in Figure 8.29 for a speed of 1.8 m/s.

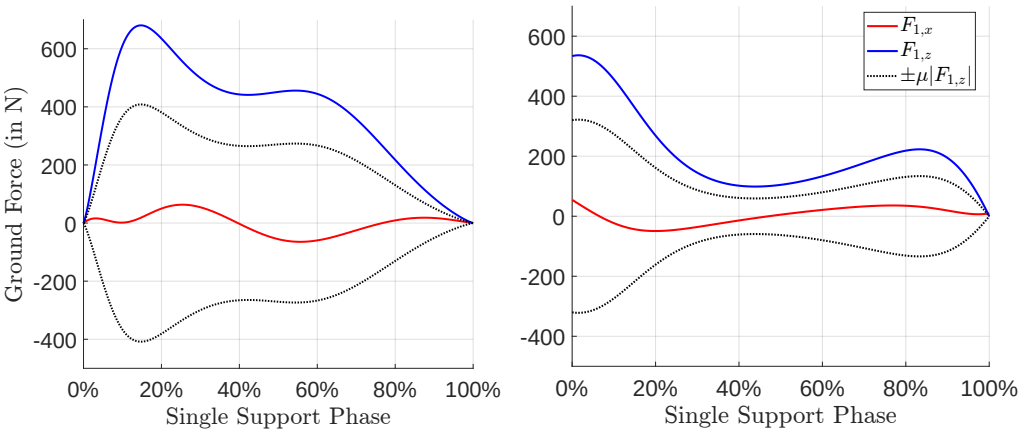

(a) Running on compliant ground.

(b) Running on rigid ground.

Figure 8.29: Solid lines indicate reaction forces $\mathbf{F}_1 := [F_{1,x}, F_{1,z}]^\top$ on both rigid and compliant ground during the SSP of running at 1.8 m/s. Dashed lines show the maximum horizontal force without slippage, per $\mu = 0.6$.

Furthermore, the investigations illustrated in Figure 8.28 and Figure 8.29 reveal that the peak magnitudes of reaction forces generated by both compliant and rigid surfaces are comparable. This implies that while the surface elasticity does not diminish the maximum magnitude of the reaction force, it effectively mitigates abrupt variations in reaction force and actuator torque during transitional events.

Optimal Gait and Posture

The optimized running posture at velocities of $v = 1.8$, $v = 2.3$, and $v = 2.8$ m/s is depicted in Figure 8.30, Figure 8.31, and Figure 8.32, respectively. In contrast to those observed on rigid ground, the running patterns on compliant ground exhibit a notable division of the flight phase, resulting in an increased maximum distance between the robot's body and the ground during flight. Furthermore, the postures remain consistent across varying speeds. As previously discussed, adaptation to different speeds is

primarily accomplished through the elongation of the flight phase and the extension of step length.

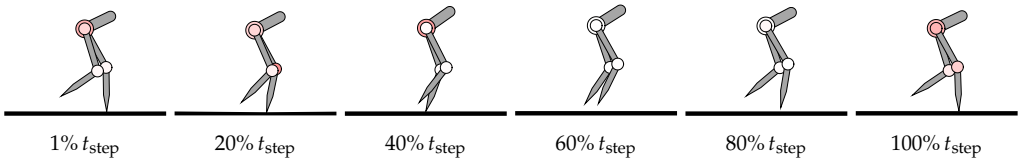

Figure 8.30: Snapshots of the optimized running gaits at speed $v = 1.8$ m/s.

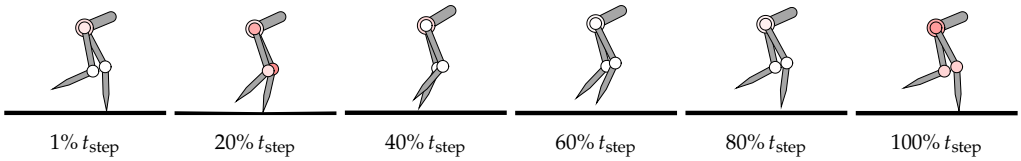

Figure 8.31: Snapshots of the optimized running gaits at speed $v = 2.3$ m/s.

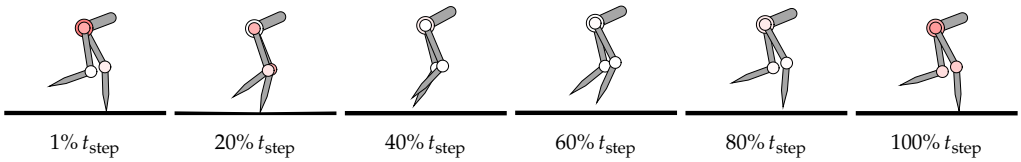

Figure 8.32: Snapshots of the optimized running gaits at speed $v = 2.8$ m/s.

8.5.2 Gait Stability

Nontrivial Floquet multipliers are computed for locomotion over both rigid and compliant surfaces, with the objective of evaluating the stability of periodic running gaits. Subsequently, closed-loop simulations are conducted to confirm the stability of these running gaits when exposed to initial disturbances.

Floquet Multiplier

Figure 8.33 elucidates the magnitude of the largest Floquet multiplier associated with running on rigid and compliant surfaces. Through optimization, these multipliers are deliberately restricted to values slightly below unity. Specifically, a singular nontrivial multiplier pertains to running on a rigid surface, which is precisely determined through the orthogonal projection of the monodromy matrix, as documented in Section 6.1.3.

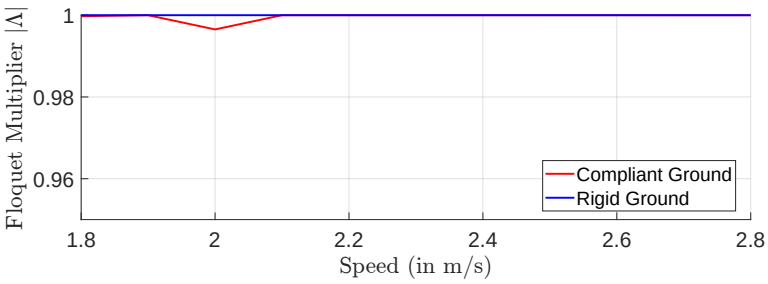

Figure 8.33: Magnitude of the nontrivial Floquet multiplier for running on compliant and rigid grounds.

Conversely, the scenario of running on compliant surfaces results in the determination of five nontrivial multipliers via an iterative QR-algorithm, as delineated in Section 6.2.3. Consequently, the multipliers derived for the compliant ground case exhibit minor fluctuations attributed to numerical inaccuracies. Crucially, the orthogonal projection is indispensable for forming stable running gaits on compliant ground, owing to the stiff differential equations system imposed by the compliant contact within the hybrid zero dynamics.

Closed-Loop Simulation

Figure 8.34 presents closed-loop simulations of running on both rigid and compliant surfaces, incorporating initial perturbations in the velocities of the robot's segments. To enhance the visualization of convergence behavior, the magnitude $|\Lambda|$ of the largest nontrivial Floquet multiplier is constrained to a value smaller than 0.9. Additionally, a minimal initial deviation is incorporated, attributed to the sensitivity of the numerical ODE solver. For the PD-feedback in the simulation, the gain parameters are set at $K_\mathrm{p} = 1000$ and $K_\mathrm{d} = 1000$.
The inelastic impact on rigid ground results in significant discontinuities in the simulated trajectories of the actuated joints at the moment of landing, as illustrated in Figure 8.34b. In contrast, simulating the ground as compliant leads to smoother transitions in the trajectories.

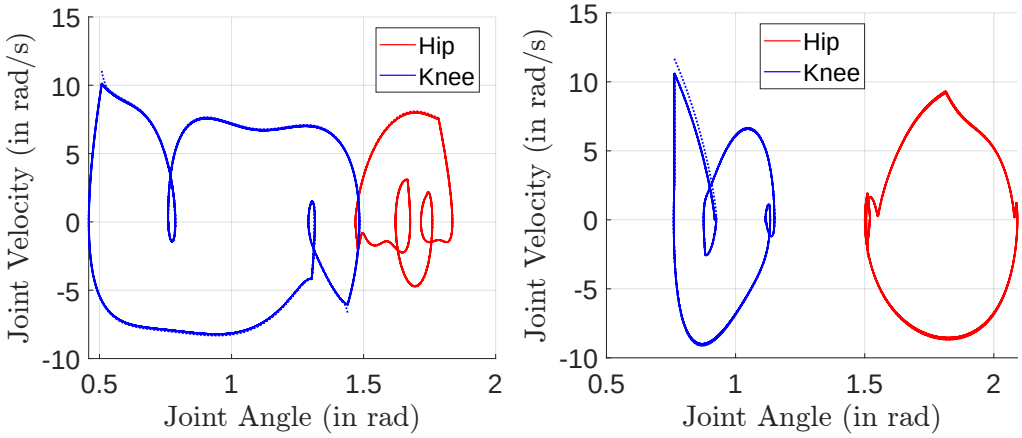

(a) Running at speed $v = 2.0$ m/s on compliant ground.

(b) Running at speed $v = 2.0$ m/s on rigid ground.

Figure 8.34: Illustration of the simulated joint configurations $\mathbf{q}_b$ and angular velocities $\dot{\mathbf{q}}_b$ denoted by dotted lines, considering initial deviations. The reference trajectory is depicted using solid lines.

8.6 Concluding Remarks

This chapter rigorously assesses periodic walking and running gaits across a range of speeds and diverse environmental conditions, with a primary emphasis on efficiency and stability. Notably, both walking and running motions are optimized on rigid ground, while running is additionally investigated on a compliant surface. The principal findings and insights obtained from this chapter are outlined below:

- **Walking with Instantaneous DSP on Rigid Ground:**
  - The optimized walking gaits rely predominantly on the natural swing of the leg and require relatively small actuator effort, particularly in mid-stance.
  - As walking speed increases, the CoT grows approximately linearly, indicating a decline in energy efficiency. At higher speeds, deceleration immediately before impact helps curb inelastic losses but raises deceleration losses in the actuators.
  - Stability is confirmed by Floquet multipliers slightly less than one. Perturbation studies in closed-loop simulations show slow, but eventual, convergence to the steady walking limit cycle.
- **Walking with Non-Instantaneous DSP on Rigid Ground:**
  - Fully actuated double support phases enable faster perturbation convergence and simplify the initialization of robot at the cost of increased actuator

effort and thus higher CoT across all investigated speeds. Compared to instantaneous DSP, the robot exploits fewer natural oscillations due to the closed kinematic chain constraints, which reduces efficiency.

  - To develop highly efficient walking gaits that include a non-instantaneous DSP, it is imperative to use advanced foot models. These models facilitate the exploitation of the foot's rolling motion, thereby harnessing the inherent dynamics of the system to minimize energy consumption [112].
  - The numerical findings indicate that utilizing a non-instantaneous DSP in walking may provide advantages under challenging conditions, such as significant disturbances or when rapid management of initial gait conditions is required.

- **Running on Rigid Ground:**
  - Periodic running motions are optimized over a range of speeds from 1.8 m/s to 2.8 m/s. Similar to walking, CoT increased nearly linearly with speed.
  - An intersection speed around 2.2 m/s is observed, beyond which running proved more energy-efficient than walking.
  - Floquet multipliers remain below one, confirming asymptotic stability. However, aggressive deceleration occurs in the hip immediately after foot impact, resulting in torque spikes.

- **Running on Compliant Ground:**
  - Despite higher damping losses, running on compliant ground achieved lower overall CoT at increased speeds because the robot effectively harnesses elastic energy stored in the substrate.
  - The reaction force, actuator torque, and power profiles are smoother compared to rigid-ground running, mitigating impact spikes and possibly reducing mechanical stress on components.
  - Numerical simulations, however, are more sensitive on compliant terrain due to stiff ground-contact dynamics. Minor deviations in the reduced-order dynamics can grow if not carefully managed with robust numerical methods and projection schemes.

The process for generating stable running gaits on compliant ground using the presented framework demonstrates extreme sensitivity to minor variations in gait parameters and initial conditions during the single support phase. This sensitivity arises from the stiff nature of the reduced dynamics during the contact period with the compliant ground. Specifically, the force law depends on the position and velocity of the stance foot, which are further expressed as functions of the virtual constraints in the actuated joints.

Although the virtual constraints are theoretically substituted into the full-order dynamics, numerical errors accumulate during the integration of the resulting ordinary differential equations system of reduced order, eventually leading to minor unphysical violations of the constraint manifold. Particularly, the constraint surface is not explicitly stabilized. These minor violations, in turn, significantly affect the ground force, precisely due to the large stiffness parameter, thus impacting the resultant running gait. Notwithstanding the numerical challenges, the proposed optimization technique, employing the multiple shooting method, exploits sophisticated ODE and DAE solvers to identify stable running gaits. To augment numerical stability further, it is recommended to exercise enhanced control over the constraint surface, such as the potential future implementation of the stabilization methods introduced in Section 2.2.2.
Despite this, the present chapter underscores the importance of fundamental solutions in locomotion, specifically in walking and running. It provides a benchmark for future comparative analyses as elastic couplings are incorporated.

9 Efficiency Study of Elastic Coupling

Building on the exhaustive analysis of diverse gaits and environmental conditions as described in Chapter 8, this chapter examines the incorporation of elastic couplings within the structural architecture of the bipedal robot, which comprises rigid body segments, to improve the energy efficiency of bipedal locomotion, including both walking and running. The resulting optimal nonlinear properties of the elastic couplings are considered.

The structure of this chapter is delineated as follows: Section 9.1 elucidates the optimization framework aimed at the simultaneous optimization of gait parameters and elastic couplings. Section 9.2 and Section 9.3 examine the enhanced energy efficiency in walking, ascribed to elastic couplings, employing both instantaneous and non-instantaneous double support phase (DSP) formulations, respectively. Section 9.4 and Section 9.5 explore the improved energy efficiency of running enabled by elastic couplings on rigid and compliant ground surfaces, respectively; Section 9.6 concludes the analysis presented in this chapter.

9.1 Setups of Optimization Framework

To realize the full potential of elastic couplings in augmenting energy efficiency, both the reference gait trajectory and the characteristics of elastic coupling are optimized simultaneously at a specified speed. Especially within the context of biped walking with overactuation and running, the application of elastic coupling remains a topic that has yet to be systematically examined in the literature. The methodology presented in this chapter asserts that the elastic properties are precisely customized for each distinct locomotion speed, signifying that, for each particular speed, both the reference gait parameter and the elastic coupling parameter are subjected to optimization.

Nevertheless, it is noteworthy that for each individual operational speed, the elastic properties necessitate modification via an auxiliary actuator, such as the variable stiffness actuators discussed in [44]. The associate collaborator on this research project is exploring the practical application of the intended nonlinear, adjustable stiffness

behavior through the utilization of compliant mechanisms [187]. Therefore, this method diverges from the one proposed in [147], which assumes the constancy of elastic coupling across varying locomotion velocities.

9.2 Walking with Instantaneous DSP

Two configurations of attaching elastic couplings in the mechanical design of the robot are presented, namely coupling the upper body to each thigh (noted as "UT"), and coupling both thighs (noted as "TT"). It is noteworthy that the investigation into the enhanced energy efficiency of a biped walking robot featuring an instantaneous DSP has been methodically conducted in [17]. To ensure comprehensiveness and facilitate comparisons with alternative gaits, the outcomes have been replicated in this section utilizing the proposed optimization framework in conjunction with the multiple shooting method.
This section delineates the enhancement in energy efficiency attributable to the implementation of elastic couplings as discussed in Section 9.2.1, subsequently followed by an examination of the consequent gait stability as analyzed in Section 9.2.2.

9.2.1 Improvement of Energy Efficiency

Figure 9.1 illustrates the diminished CoT and energy loss resulting from the implementation of optimal nonlinear elastic couplings between the rigid segments of the robot's structure. Specifically, Figure 9.1a demonstrates that mean energy reductions of 74.2 % and 75.9 % are achieved via the optimal elastic couplings positioned between the thighs and between the upper body and thighs, respectively.
The enhancement in energy efficiency is primarily ascribed to a marked decrease in deceleration losses within the actuator. This is achieved through two specific strategies: 75.9 % via the coupling of the thighs, and 76.5 % via the coupling of the upper body and thighs, as illustrated by the dashed lines in Figure 9.1b. By employing elastic torques for the deceleration of movement, there is a reduced need for actuator-based deceleration. Consequently, locomotion primarily arises from the inherent free oscillation of the mechanical system, which is adjusted by the optimal elastic couplings, thereby reducing the exertion required from the actuators.
Furthermore, as indicated by Figure 9.1b, the reduction in impact loss can be attributed to the effects of elastic coupling. Specifically, the contributions to diminished impact losses, namely 62.3 % and 72.0 %, arise from the elastic couplings between the thighs and between the upper body and thighs, respectively. This attenuation can be ascribed to a reduction in step length, as illustrated in Figure 9.2a, which results in a decreased approach velocity of the swing foot toward the ground surface immediately prior to

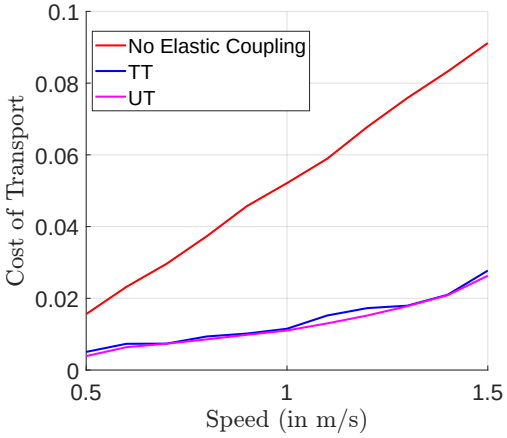

(a) Cost of transport of walking.

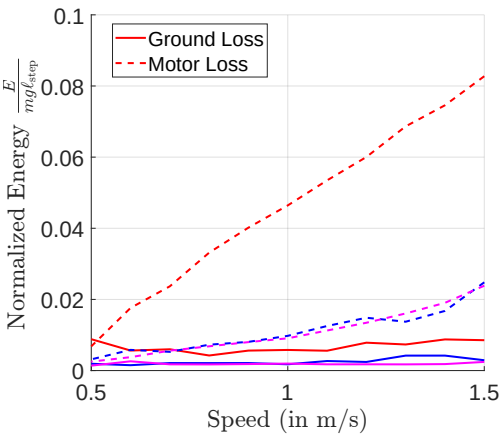

(b) Normalized energy losses, with ground losses shown in solid lines and motor losses shown in dashed lines.

Figure 9.1: Cost of transport and energy losses of walking with or without elastic couplings.

impact. Notably, when the post-impact velocity is reduced to zero following an inelastic collision, a lower pre-impact velocity consequently leads to diminished impact loss.

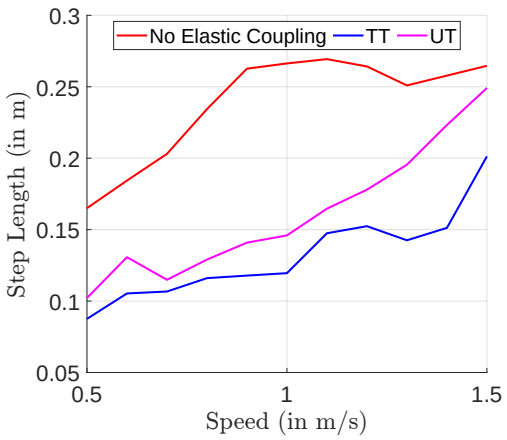

(a) Step length of the optimized gaits.

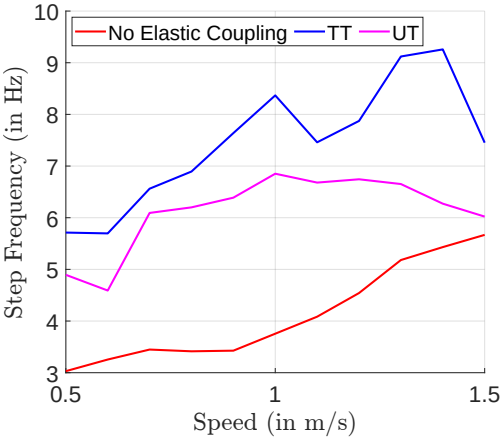

(b) Step frequency of the optimized gaits.

Figure 9.2: Step length and frequency of optimized walking with or without elastic couplings.

Step Length and Frequency

Implementing elastic couplings in accordance with both examined configurations results in an elevated step frequency, as shown in Figure 9.2b. Consequently, the optimal step length diminishes when compared to the system without elastic couplings, as depicted in Figure 9.2a. The investigation presented in [193] employs a simplified pendulum model to elucidate that the optimal double step frequency aligns with the robot's natural oscillation frequency, attributed to the elastic coupling between the thighs. This suggests that the robot operates near system resonance, thereby enhancing energy efficiency. This phenomenon similarly applies to the coupling of the upper body and thighs, as it also leads to an increased step frequency due to the positive stiffness parameter.

Optimal Gait and Posture

The optimal gaits featuring optimal elastic couplings between the thighs are illustrated in Figure 9.3, Figure 9.4, and Figure 9.5 for the respective speeds of $v = 0.5$, $v = 1.0$, and $v = 1.5$ m/s.

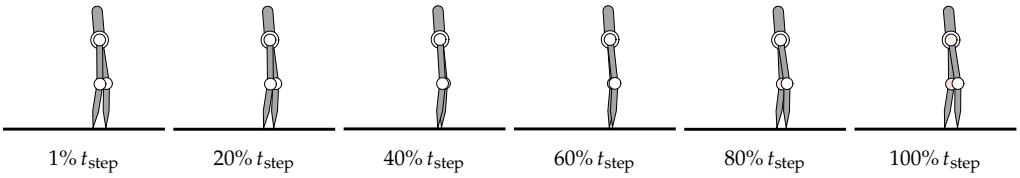

Figure 9.3: Walking with optimal elastic couplings between thighs (TT) at speed $v = 0.5$ m/s.

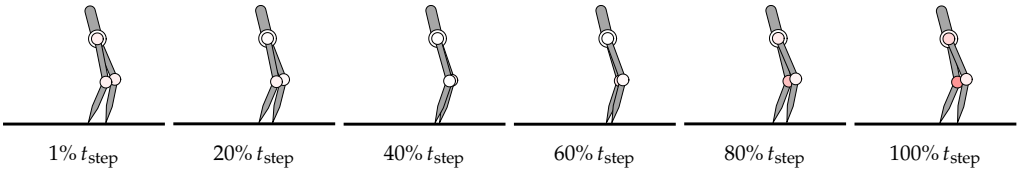

Figure 9.4: Walking with optimal elastic couplings between thighs (TT) at speed $v = 1.0$ m/s.

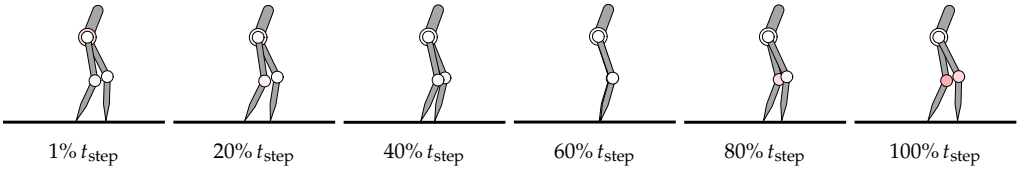

Figure 9.5: Walking with optimal elastic couplings between thighs (TT) at speed $v = 1.5$ m/s.

In comparison with the gait without elastic couplings, as demonstrated in Section 8.2.1, these movements are characterized by a notably reduced step length. Additionally, the actuator torques, denoted by the intensity of the joint color, diminish significantly, particularly at the commencement and conclusion of the single support phase.
The gaits characterized by optimal elastic coupling between the upper body and thighs are illustrated in Figure 9.6, Figure 9.7, and Figure 9.8 for speeds of $v = 0.5$, $v = 1.0$, and $v = 1.5$ m/s, respectively.

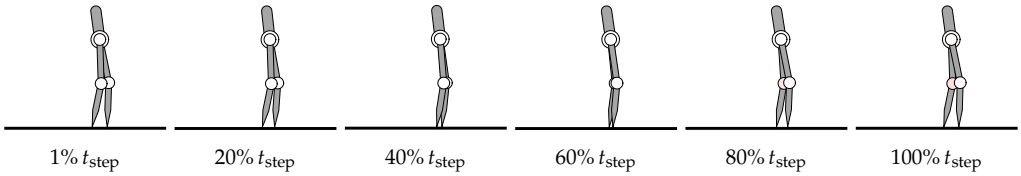

Figure 9.6: Walking with optimal elastic coupling between the upper body and thighs (UT) at speed $v = 0.5$ m/s.

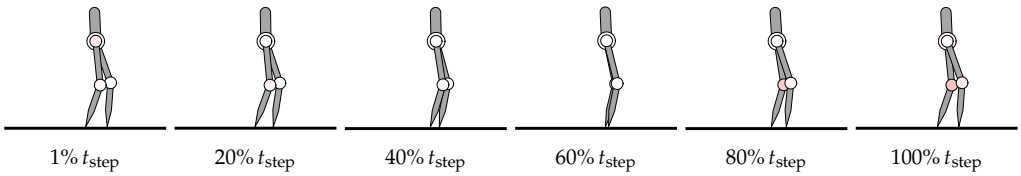

Figure 9.7: Walking with optimal elastic coupling between the upper body and thighs (UT) at speed $v = 1.0$ m/s.

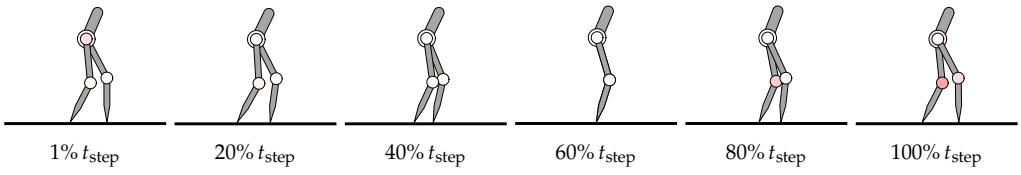

Figure 9.8: Walking with optimal elastic coupling between the upper body and thighs (UT) at speed $v = 1.5$ m/s.

In contrast to the elastic characteristics present between the thighs, optimizing the neutral angle $\varphi_{\text{UT},0}$ of the elastic coupling between the upper body and thighs leads to an optimal upper body orientation across varying speeds, leading to less deceleration loss. In particular, Figure 9.9 provides a comparative analysis of the mechanical power contributed by the actuators during ambulation both without and with elastic couplings at the velocity of $v = 1.5$ m/s. As demonstrated in Figure 9.9a, the robot without elastic couplings requires a substantial deceleration, observed as negative mechanical power in

both hip joints. This deceleration is crucial for sustaining the optimal orientation of the upper body immediately following the impact. Subsequent to this deceleration phase, the actuator imparts significant positive power to accelerate the segments for the ensuing step period. During the mid-section of the single support phase, the actuator remains largely inactive, allowing the robot to exploit the inherent oscillation of the swing leg for locomotion. As the swing phase concludes, actuation is necessary to modify the body configuration in preparation for ground contact, aiming to minimize impact loss.

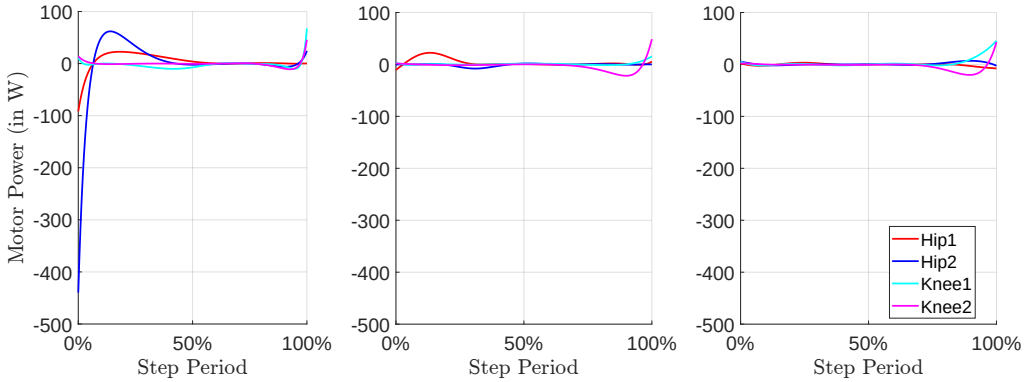

(a) Without elastic coupling.

(b) Elastic coupling between thighs (TT).

(c) Elastic coupling between upper body and thighs (UT).

Figure 9.9: Mechanical power in the actuators for the configuration without or with elastic couplings at walking speed $v = 1.5\,\mathrm{m/s}$.

As indicated in Figure 9.9b and Figure 9.9c, elastic couplings lead to a marked reduction in deceleration losses at the onset of the single support phase. This phenomenon suggests that the kinetic energy present during deceleration is temporarily converted into elastic energy immediately following impact, as illustrated in Figure 9.10a. To enhance clarity, the potential energy, encompassing both gravitational and elastic energy, is normalized to zero at the initiation of a step period. Subsequently, this stored elastic energy is utilized to accelerate the segments during the new step period, thereby diminishing positive mechanical power in the mid-step period. Notably, the optimal neutral angle $\varphi_{\mathrm{UT},0}$ of the elastic coupling between the upper body and thighs results in a substantial decrease in deceleration using the actuator.

9.2.2 Gait Stability

Moreover, as demonstrated by Figure 9.10b, the introduction of elastic couplings adversely affects gait stability, as evidenced by the magnitude of the nontrivial Floquet multiplier. While the gaits remain stable, the rate of convergence deteriorates due to the

increased step frequency required for walking with elastic couplings, rendering it more susceptible to minor perturbations around the reference limit cycle.

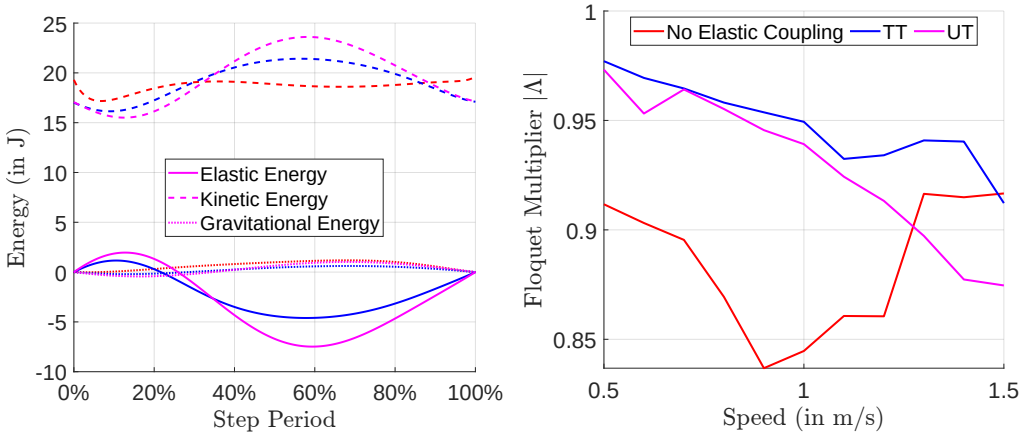

(a) Energy throughout one step period.

(b) Magnitude of the nontrivial Floquet multiplier.

Figure 9.10: Depiction of kinetic and potential energy in walking at speed $v = 1.5$ m/s, and the gait stability without or with elastic couplings.

9.3 Walking with Non-Instantaneous DSP

The concept of walking with a non-instantaneous DSP is characterized by the existence of a closed kinematic chain within the continuous DSP, which is enabled by the static friction at the contact points of the feet. Preliminary efficiency studies reveal that the integration of elastic couplings between the thighs leads to an elevated cost of transport, as the actuator must exert additional effort to oppose the coupling in order to preserve the closed kinematic chain's integrity. Consequently, the investigation does not consider the coupling between the thighs within the presented efficiency analysis.
On the other hand, positioning the elastic coupling between the upper body and the thighs outside the closed kinematic chain enhances energy efficiency. This section undertakes an analysis of both linear and nonlinear elastic properties, optimized for distinct average walking speeds, to elucidate the effect of the nonlinearity of the elastic coupling, especially between the upper body and thighs.
This section elucidates the improvement in energy efficiency resulting from the integration of elastic couplings as detailed in Section 9.3.1, followed by an analysis of the resulting gait stability as examined in Section 9.3.2.

9.3.1 Improvement of Energy Efficiency

As illustrated in Figure 9.11a, the implementation of elastic couplings with optimized nonlinear characteristics between the upper body and thighs results in a reduction of up to 62.5 % in energy consumption within the investigated speed range. Comparatively, elastic couplings with optimal linear characteristics lead to a reduction of 43.0 % in energy consumption. It is noteworthy that the decreased CoT achieved through the nonlinear elastic couplings closely approximates the CoT observed when walking with an instantaneous DSP in the absence of elastic couplings.

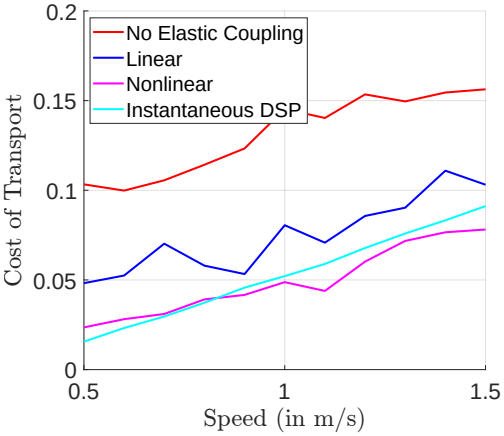

(a) Cost of transport of walking.

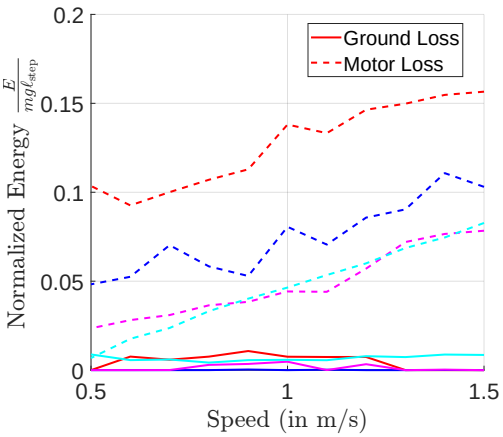

(b) Normalized energy losses, with ground losses shown in solid lines and motor losses shown in dashed lines.

Figure 9.11: Cost of transport and energy losses of walking with or without elastic couplings.

The diminution of energy losses is elucidated in Figure 9.11b. It is noteworthy that the impact loss is reduced to nearly negligible levels owing to the presence of both linear and nonlinear elastic couplings. Due to its predominant influence, the minimization of deceleration loss emerges as the principal contributor to the improved efficiency attributable to elastic couplings. In essence, the presence of elastic couplings necessitates reduced deceleration by the actuator, which otherwise leads to considerable heat dissipation.

Step Frequency and SSP Duration

The optimized step frequency of walking with non-instantaneous DSP and optimal elastic couplings is illustrated in Figure 9.12a. Significantly, the incorporation of elastic couplings into the rigid body model does not augment the optimal step frequency when the DSP is considered continuous. While the total step duration remains constant, the

presence of elastic coupling slightly extends the relative duration of the DSP, thereby reducing the relative duration of the SSP within a step period, as observed in Figure 9.12b.

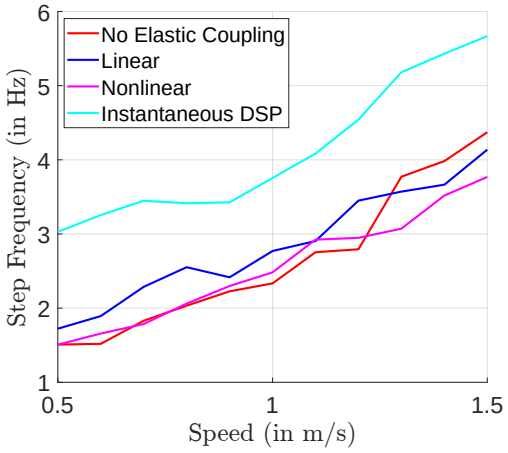

(a) Step frequency of the optimized gaits.

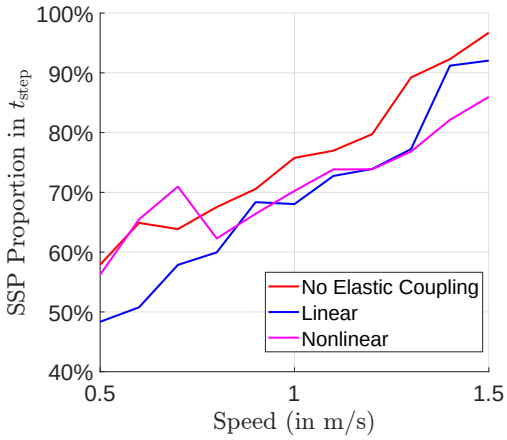

(b) Relative duration of the single support phase in one step period.

Figure 9.12: Step frequency of the optimized walking gaits and the proportion of the single support phase within each step period.

While the resultant CoT exhibits a comparable magnitude as observed in Figure 9.11a, Figure 9.12a highlights a marked difference in the optimal step frequency between walking with an instantaneous DSP and walking with a non-instantaneous DSP when optimal elastic couplings are employed. It is of particular interest that the considerable efficiency observed in walking with an instantaneous DSP is attributable to a high step frequency that nearly coincides with the system's natural oscillation frequency. Conversely, when the DSP is continuous, the integration of the elastic coupling is inclined to regulate the distribution between the DSP and SSP to match with the free oscillation frequency of the underactuated SSP.

Optimal Gait and Posture

Figure 9.13, Figure 9.14, and Figure 9.15 illustrate the postures of optimized gaits with elastic couplings exhibiting linear characteristics corresponding to speeds of $v = 0.5$, $v = 1.0$, and $v = 1.5$ m/s, respectively.
At higher speeds, the posture remains comparable to the gait observed in the absence of elastic coupling as illustrated in Figure 8.11 and Figure 8.12; however, at a reduced velocity of $v = 0.5$ m/s, a considerable distinction becomes apparent. Specifically, Figure 9.13 illustrates that the upper body tends to orient vertically, as its equilibrium

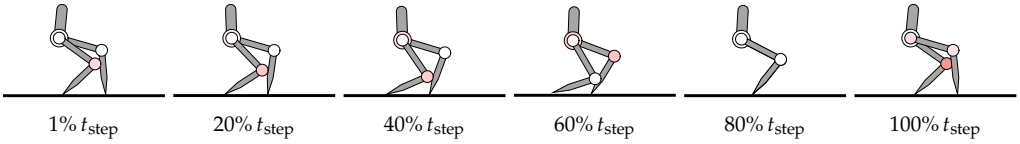

Figure 9.13: Walking with optimal linear elastic coupling between the upper body and thighs at speed $v = 0.5$ m/s.

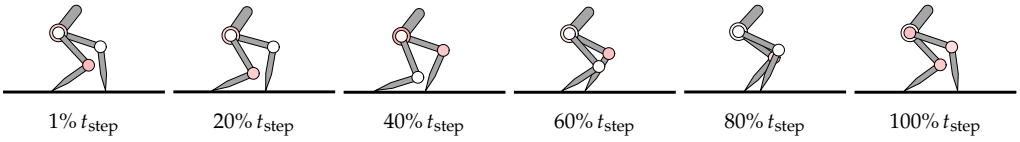

Figure 9.14: Walking with optimal linear elastic coupling between the upper body and thighs at speed $v = 1.0$ m/s.

position is modulated by the neutral angle $\varphi_{\text{UT},0}$ of the elastic coupling between the upper body and thighs. At low speeds, as noted in Figure 9.12b, the DSP exhibits a prolonged relative duration within each gait cycle. An optimal vertical alignment of the upper body, which is chiefly maintained by the influence of elastic torque, markedly reduces the actuator's exertion needed to support the upper body's load.
Analogously, Figure 9.16, Figure 9.17, and Figure 9.18 depict the postures of optimized gaits with elastic couplings that exhibit nonlinear characteristics, corresponding to velocities of $v = 0.5$, $v = 1.0$, and $v = 1.5$ m/s, respectively.
Irrespective of the presence of elastic coupling, the formulation of a non-instantaneous DSP results in a decreased center of mass position. This phenomenon is attributed to the complex contact constraints inherent to the point foot, which are essential for constituting the closed kinematic chain within the DSP. Nevertheless, the elasticity in the multibody system facilitates an optimal distribution of the durations of both the DSP and the SSP, which further enables the exploitation of free oscillation, particularly in the underactuated SSP, thereby achieving heightened efficiency.

Optimal Elastic Characteristics

In accordance with the gaits presented, the optimal elastic couplings exhibiting both linear and nonlinear characteristics are illustrated in Figure 9.19. Specifically, these characteristics are displayed within the active operating range of the spring. Given the pronounced differences among the presented gaits at different average speeds, it is plausible to expect considerable variability in the corresponding optimal elastic couplings. Notably, for a low speed of $v = 0.5$ m/s, a multistable characteristic is preferred, whereas for other speeds, a monostable configuration suffices. These nonlinear characteristics are implemented through compliant mechanisms, as exemplified in [197].

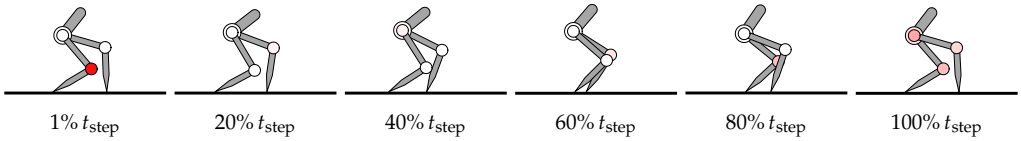

Figure 9.15: Walking with optimal linear elastic coupling between the upper body and thighs at speed $v = 1.5$ m/s.

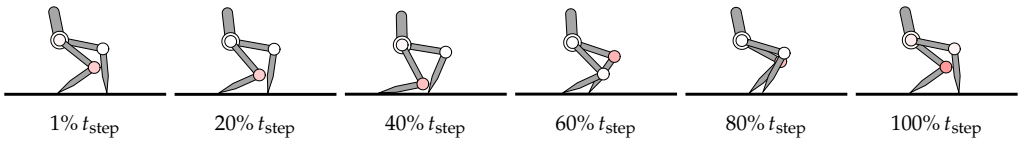

Figure 9.16: Walking with optimal nonlinear elastic coupling between the upper body and thighs at speed $v = 0.5$ m/s.

Figure 9.19 demonstrates that the optimized neutral angle $\varphi_{\text{UT},0}$ for both linear and nonlinear elastic couplings is relatively consistent. This angle signifies a position where the elastic torque is nullified, thereby playing a critical role in determining the optimal equilibrium position of the upper body. The primary aim is to reduce the effort needed by the actuator to maintain the upper body's weight.

Energy in Periodic Gait

The assessment of potential energy (encompassing both elastic and gravitational components) in conjunction with kinetic energy is conducted for locomotion involving non-instantaneous DSP at a velocity of $v = 0.5$ m/s, as illustrated in Figure 9.20. Notably, during the normalized DSP, as delineated in Figure 9.20a, there is a monotonic increase in elastic energy, signifying that the elastic torque is responsible for generating negative mechanical work. Conversely, the descent of the center of mass results in a diminution of gravitational energy. Subsequently, in the ensuing SSP, as shown in Figure 9.20b, the stored elastic energy is released to assist the actuator in accelerating the segment and elevating the center of mass.

At an elevated speed of $v = 1.5$ m/s, as depicted in Figure 9.21, the gravitational and kinetic energies remain nearly constant due to the brevity of the corresponding DSP and the insubstantial movement involved, as stated in Figure 9.12b. Nevertheless, the elastic energy, particularly within the nonlinear elastic coupling, rises notably in a monotonic fashion. The stored elastic energy is subsequently released during the ensuing SSP to facilitate movement, as illustrated in Figure 9.21b.

A comparative analysis of the optimal linear and nonlinear elastic characteristics reveals that the nonlinear characteristic is more congruent with the natural oscillation of the system in the underactuated SSP, given that acceleration occurs solely at the

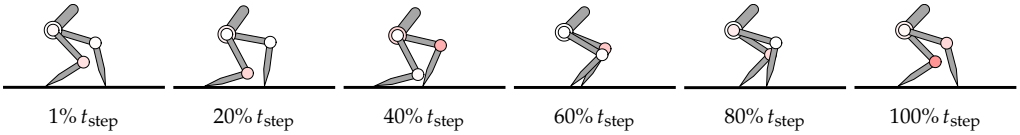

Figure 9.17: Walking with optimal nonlinear elastic coupling between the upper body and thighs at speed $v = 1.0$ m/s.

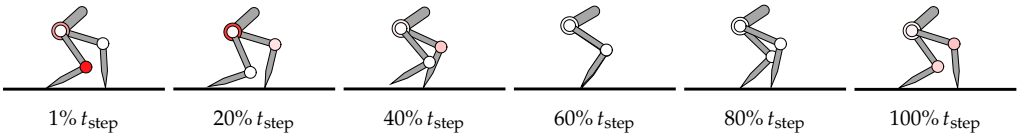

Figure 9.18: Walking with optimal nonlinear elastic coupling between the upper body and thighs at speed $v = 1.5$ m/s.

commencement of the SSP. Specifically, the elastic potential energy is predominantly converted into kinetic energy. Following the initial phase of acceleration, the elastic potential energy gradually diminishes to zero. Conversely, the linear elastic spring demonstrates significantly larger oscillations in the depicted energy, leading to a slightly higher step frequency in contrast to the nonlinear elastic coupling at $v = 1.5$ m/s, as detailed in Figure 9.12a. Therefore, due to the elastic coupling, the non-instantaneous DSP is employed to accumulate elastic potential energy, which is subsequently released during the underactuated SSP. Particularly during the SSP, the system's free oscillation is harnessed to enhance the overall energy efficiency of the gait.

9.3.2 Gait Stability

Figure 9.22 presents the resultant magnitude of the single nontrivial Floquet multiplier with controller gain parameter $K_{\sigma_d} = 10$ when both linear and nonlinear elastic couplings between the upper body and thighs are considered. Clearly, introducing elasticity into the multibody system does not adversely affect gait stability, given that the non-instantaneous DSP is fully actuated. Conversely, incorporating elastic coupling into the underactuated gait with an instantaneous DSP detrimentally affects stability, as the resulting Floquet multiplier increases, as demonstrated in Figure 9.10b.

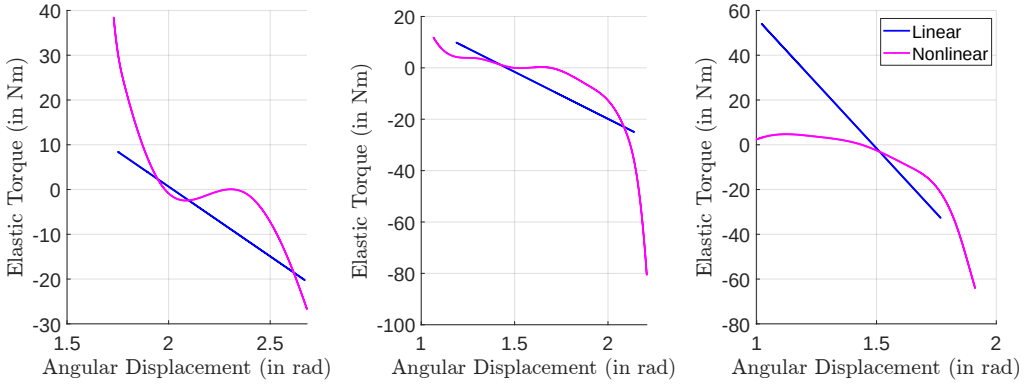

(a) Walking speed $v = 0.5$ m/s. **(b)** Walking speed $v = 1.0$ m/s. **(c)** Walking speed $v = 1.5$ m/s.

Figure 9.19: Optimized linear and nonlinear elastic characteristics across varying walking speeds.

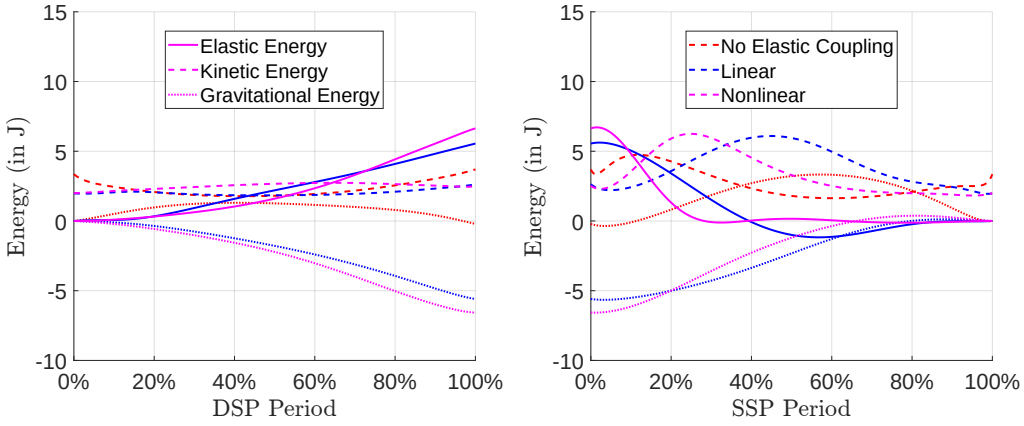

(a) Energy in normalized DSP. **(b)** Energy in normalized SSP.

Figure 9.20: Energy profiles during DSP and SSP for locomotion at $v = 0.5$ m/s without elastic coupling (in red), with linear elastic couplings (in blue), and with nonlinear elastic couplings (in magenta).

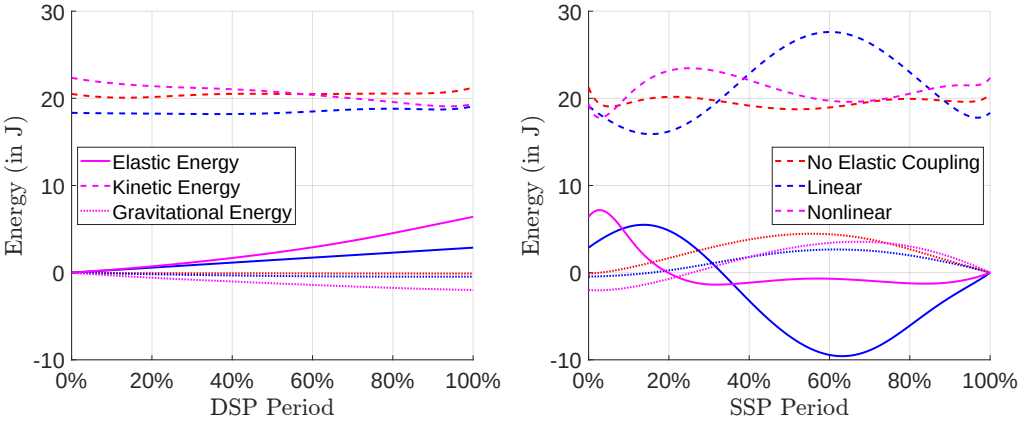

(a) Energy in normalized DSP.

(b) Energy in normalized SSP.

Figure 9.21: Energy during DSP and SSP for locomotion at $v = 1.5$ m/s without elastic coupling (in red), with linear elastic couplings (in blue), and with nonlinear elastic couplings (in magenta).

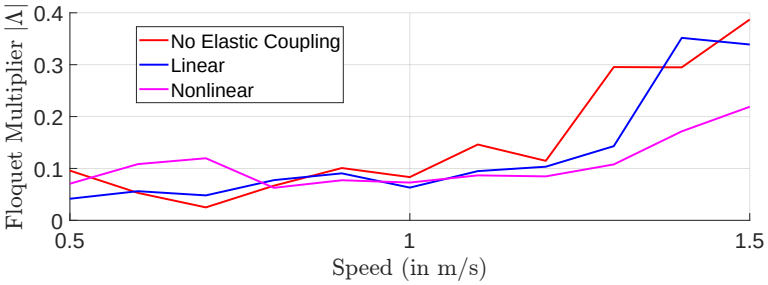

Figure 9.22: Magnitude of the nontrivial Floquet multiplier of the gait without or with elastic couplings.

9.4 Running on Rigid Ground

The study examines two configurations of elastic couplings in the robotic system: the coupling between the upper body and both thighs (denoted as "UT"), and the coupling between the thighs (denoted as "TT"), for applications involving running on rigid surfaces. Both elastic coupling configurations are characterized through nonlinear elastic properties and are optimized for each distinct running speed $v \in [1.8, 1.9, \ldots, 2.8]$ m/s. This section encompasses the discourse on the enhancement of energy efficiency attributed to elastic couplings, as explicated in Section 9.4.1, alongside the examination of gait stability as investigated in Section 9.4.2.

9.4.1 Improvement of Energy Efficiency

Figure 9.23 presents an analysis of the CoT and the associated energy dissipation in bipedal running on rigid surfaces, with considerations for elastic couplings. As indicated by Figure 9.23a, connecting the thighs leads to a reduction of 52.2 % in the mean energy expenditure, while coupling both the upper body and the thighs results in a reduction of 59.0 % in average energy consumption across various speeds.

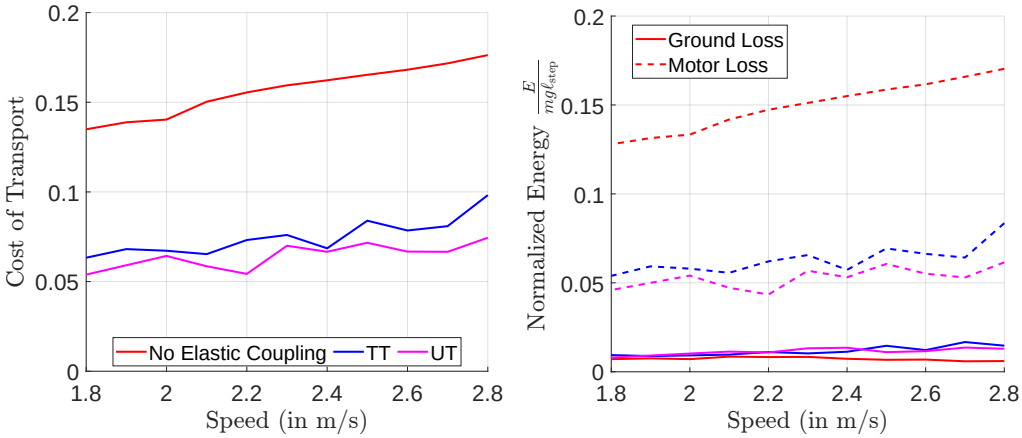

(a) Cost of transport of running.

(b) Normalized energy losses, with ground losses shown in solid lines and motor losses shown in dashed lines.

Figure 9.23: Cost of transport and energy losses of running on rigid ground with or without elastic couplings.

The CoT without elastic coupling exhibits an approximately linear relationship with running speed. In contrast, the CoT resulting from the utilization of optimal elastic couplings demonstrates slightly reduced dependence on speed. Elastic components function by storing energy during the deceleration of the robot's leg and subsequently

releasing this stored energy to facilitate acceleration, thereby substantially mitigating energy loss during deceleration using actuators, as observed in Figure 9.23b. Furthermore, while Figure 9.23b reports an increase in impact loss attributed to elastic coupling, the aggregate efficiency is enhanced because the impact loss is relatively insignificant.

Step Frequency

Figure 9.24a demonstrates that running gaits devoid of elastic coupling typically maintain a nearly constant step frequency across various speeds. The implementation of elastic coupling in the thighs (TT) appreciably elevates the optimal step frequency at all speeds due to the presence of positive stiffness. The interaction between the upper body and the thighs (UT) chiefly influences frequencies at moderate and low speeds. In order to accommodate a broad spectrum of running speeds with heightened energy efficiency, the flight phase duration in diverse gaits, irrespective of elastic coupling, is adjusted in a similar manner, as elucidated in Figure 9.24b. Specifically, as the running gait increases in speed, the flight phase becomes more predominant within a step period, contributing to a reduction in energy expenditure. Given that the implementation of elastic coupling in the thighs (TT) leads to an increase in optimal step frequency, and that the utilization of free oscillation during the single support phase contributes to a reduction in energy consumption, the alteration in flight phase duration is comparatively less pronounced than in the other two scenarios.

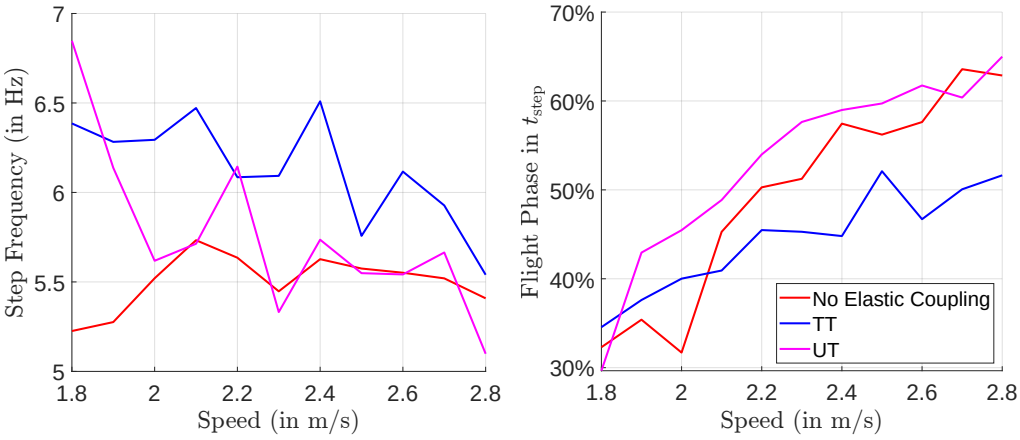

(a) Optimal step frequency of running.

(b) Relative flight duration in each step period.

Figure 9.24: Optimized step frequency and relative flight duration with respect to entire step period on rigid ground.

Furthermore, a notable modification attributed to the elastic coupling is evident in the distribution of energy consumption within the SSP CoT_s relative to the total CoT over a step period, evaluated through the ratio CoT_s/CoT as illustrated in Figure 9.25a.

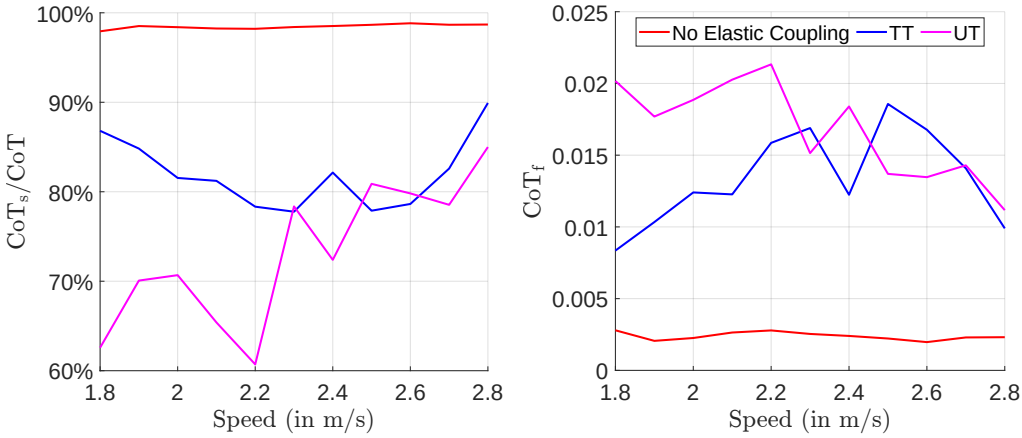

(a) Relative energy consumption within the SSP. **(b)** Normalized energy consumption during flight.

Figure 9.25: Relative energy consumption in the SSP with respect to total cost of transport of the gait, and the normalized cost of transport during FLP.

The simulation omits air dissipation, rendering the energy consumption during the flight phase negligibly small for all investigated gaits when juxtaposed with the overall cost of transport associated with the running gait as reported in Figure 9.23a. As depicted in Figure 9.25b, although the addition of elastic coupling increases the energy consumption during flight, the negligible minor magnitude has a small influence on overall CoT. Moreover, the relative allocation of the energy consumption in the SSP is significantly reduced due to the elastic coupling, indicating that the natural free oscillation in the SSP is utilized for reducing the overall CoT.

Optimal Gait and Posture

The optimized running posture with elastic coupling between the thighs, observed at velocities of $v = 1.8$, $v = 2.3$, and $v = 2.8$ m/s, is illustrated in Figure 9.26, Figure 9.27, and Figure 9.28, respectively. Compared to running gaits without elastic couplings as shown in Section 8.4.1, gaits incorporating elastic coupling exhibit appreciably reduced step lengths, thus leading to a decrease in the relative motion of the segments and consequently reduced actuation.
The optimized running posture, characterized by an elastic coupling between the upper body and thighs at speeds of $v = 1.8$, $v = 2.3$, and $v = 2.8$ m/s, is illustrated in Figure 9.29, Figure 9.30, and Figure 9.31, respectively. These gaits are produced even

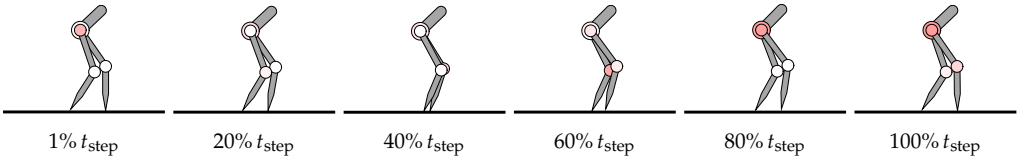

Figure 9.26: Optimized running with elastic coupling between thighs (TT) at speed $v = 1.8$ m/s.

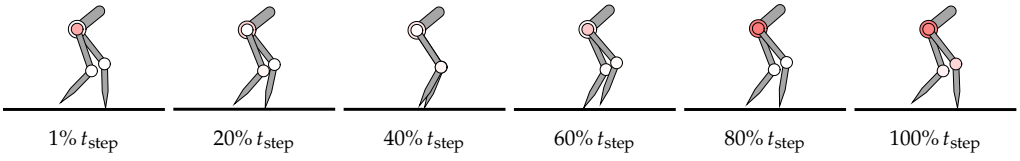

Figure 9.27: Optimized running with elastic coupling between thighs (TT) at speed $v = 2.3$ m/s.

using smaller relative movement between the legs in comparison to the gait with elastic coupling between the thighs.

Energy in Periodic Gait

An additional analysis of the enhanced efficiency is performed with a focus on energy considerations. Specifically, Figure 9.32 illustrates the kinetic and potential energy within the SSP and the FLP at a running speed of $v = 2.3$ m/s.
In the absence of elastic coupling, kinetic energy initially diminishes at the commencement of the SSP due to the deceleration of actuators to achieve an optimal post-impact posture. As the SSP progresses towards its conclusion, kinetic energy attains its peak value, facilitating preparation for take-off. Throughout the ensuing flight phase, kinetic energy decreases monotonically, while gravitational energy exhibits a parabolic trajectory.
Owing to the additional elasticity, the deceleration immediately after impact is harnessed for the accumulation of elastic potential energy, which is subsequently released midway through the SSP to facilitate the acceleration of the segments. The apex of kinetic energy is achieved prior to take-off. Concurrently, the robot initiates the reloading of elastic potential energy through the use of actuators and a portion of the kinetic energy. Furthermore, in the FLP, elastic potential energy is accumulated in a nearly monotonic fashion.
In summary, elasticity is predominantly utilized to expedite the acceleration of the segments exclusively during the initial phase of the SSP. In other phases, particularly during the flight, the elastic couplings function as interim energy storage mechanisms.

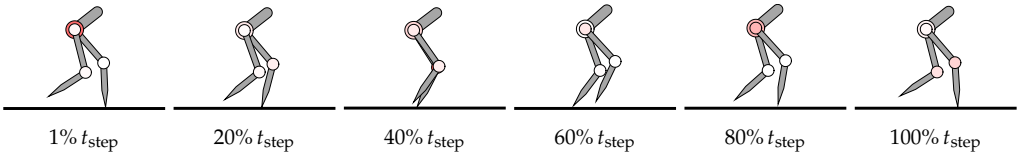

Figure 9.28: Optimized running with elastic coupling between thighs (TT) at speed $v = 2.8$ m/s.

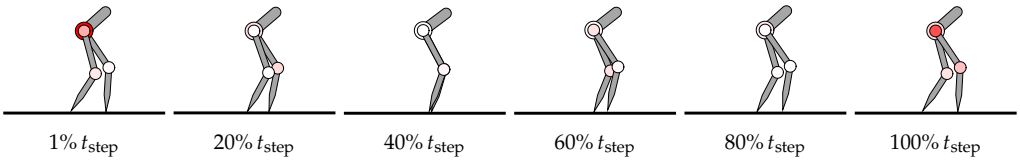

Figure 9.29: Optimized running with elastic coupling between upper body and thighs (UT) at speed $v = 1.8$ m/s.

Mechanical Power in Actuator

At a running speed of $v = 2.3$ m/s, Figure 9.33 presents the mechanical power output from the four actuators across various configurations of elastic coupling. To be precise, Figure 9.33a illustrates that a considerable amount of negative mechanical power is necessary at the hip joint of the stance leg at the commencement of the SSP, to maintain body posture after the inelastic impact. Subsequently, both hip joints contribute significant positive mechanical power to propel the segment, thereby accumulating the momentum necessary for the take-off. In the following FLP, the hip joint associated with the former stance foot decelerates the swing leg to ensure an optimal posture for landing.

Upon the attachment of elastic couplings between the thighs or between the upper body and thighs, as illustrated in Figure 9.33b and Figure 9.33c respectively, it is no longer necessary for the actuator to decelerate the movement post-impact. Instead, elasticity absorbs the deceleration motion, as evidenced by the increase in elastic energy observed in Figure 9.32a. Since the movement in the SSP is predominantly generated by free oscillation, modulated by the elastic coupling, there is a resultant decrease in the positive mechanical power required by the actuator, thereby enhancing efficiency.

Fundamentally, only the knee joint in the stance leg provides significant actuation to meet the contact condition at the stance foot. Particularly in the FLP, the actuators tend to produce negligible power. It should be noted that the static actuator torque is exceptionally high, as indicated by the color intensity in the postures, for instance, depicted in Figure 9.27 and Figure 9.30 for the same speed $v = 2.3$ m/s. In fact, the velocity of the joint nearly reaches zero, leading to minimal mechanical power output.

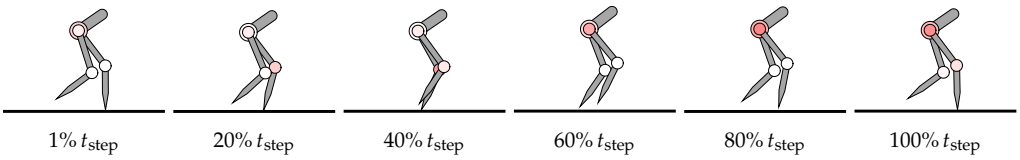

Figure 9.30: Optimized running with elastic coupling between upper body and thighs (UT) at speed $v = 2.3$ m/s.

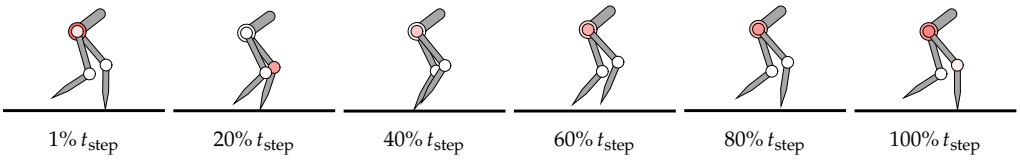

Figure 9.31: Optimized running with elastic coupling between upper body and thighs (UT) at speed $v = 2.8$ m/s.

Consequently, the static actuator torque is crucial for maintaining an optimal posture during flight.

9.4.2 Gait Stability

Figure 9.34 illustrates the resultant nontrivial Floquet multiplier of the periodic running gait without or with elastic couplings. Obviously, coupling the rigid body segments using elastic materials does not negatively impact the gait stability. For certain instances, the additional elasticity might even improve the stability characteristic, as observed by a smaller Floquet multiplier at the speed $v = 2.1$ m/s due to the coupling between the upper body and thighs.

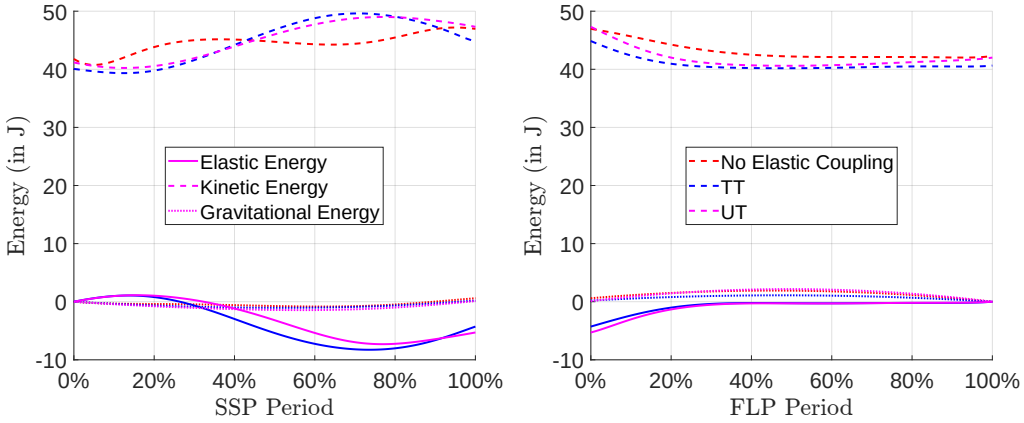

(a) Energy in normalized SSP.

(b) Energy in normalized FLP.

Figure 9.32: Energy profiles during SSP and FLP for running at $v = 2.3$ m/s without elastic coupling (in red), with elastic couplings between thighs (in blue) and between upper body and thighs (in magenta).

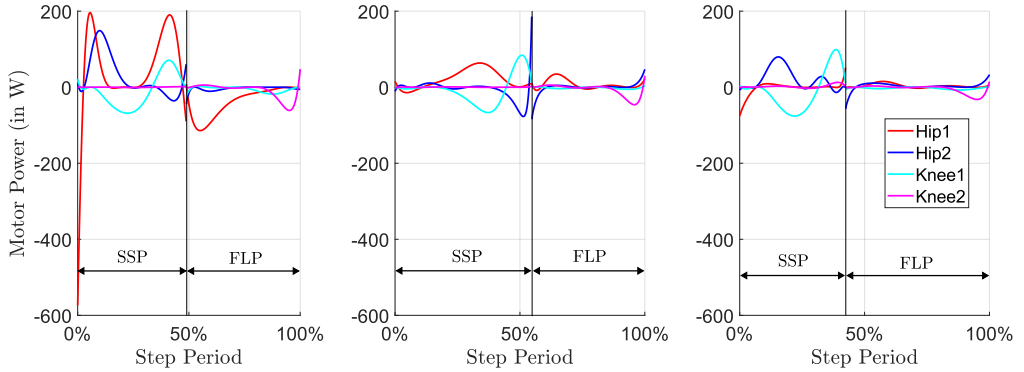

(a) No elastic coupling.

(b) Elastic coupling between thighs (TT).

(c) Elastic coupling between upper body and thighs (UT).

Figure 9.33: Mechanical power profiles in the actuators for an optimized running gait at $v = 2.3$ m/s with or without elastic couplings.

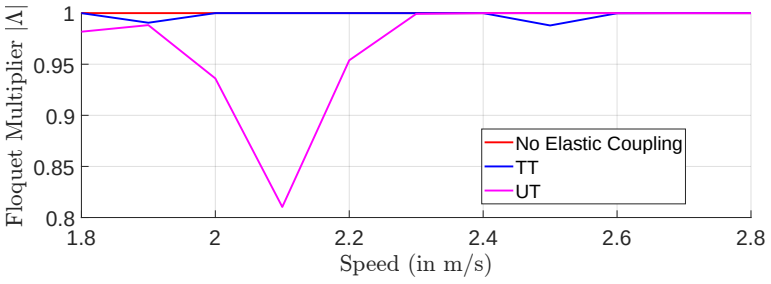

Figure 9.34: Magnitude of the nontrivial Floquet multiplier without or with elastic couplings.

9.5 Running on Compliant Ground

The configuration of elastic couplings utilized for running on rigid ground is similarly applied to compliant ground. Specifically, elastic couplings exhibiting nonlinear characteristics, optimized for varying speeds, are affixed between the thighs (TT) and between the upper body and thighs (UT). This section comprises an analysis of the improvements in energy efficiency facilitated by elastic couplings, as elucidated in Section 9.5.1, in conjunction with an assessment of gait stability, as explored in Section 9.5.2.

9.5.1 Improvement of Energy Efficiency

Figure 9.35 demonstrates enhanced energy efficiency through the application of elastic couplings. More precisely, the implementation of optimal elastic couplings between the thighs results in a reduction of 26.0 % in the average energy consumption across the range of speeds examined, while the coupling between the upper body and thighs leads to a decrease of 18.1 %.

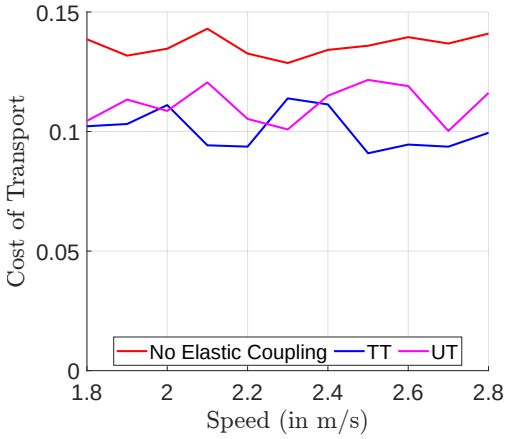

(a) Cost of transport of running.

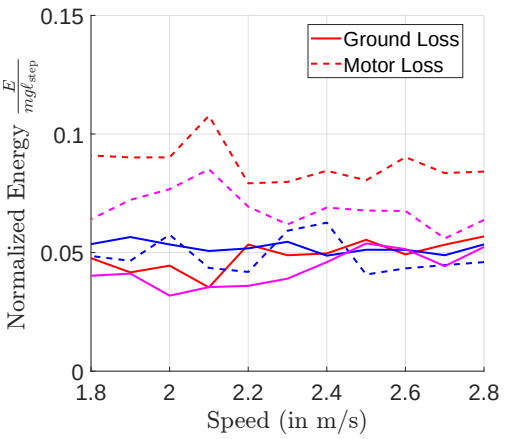

(b) Normalized energy losses, with ground losses shown in solid lines and motor losses shown in dashed lines.

Figure 9.35: Cost of transport and energy losses of running on compliant ground with or without elastic couplings.

The reduction is primarily attributed to a decrease in the deceleration loss using actuators, as illustrated in Figure 9.35b. More specifically, elasticity within the rigid body system is intended to aid the actuator in decelerating motion, thus momentarily storing kinetic energy as elastic potential energy, which is subsequently reutilized for the acceleration of

robot segments. Conversely, the damping dissipation in the compliant ground remains relatively constant regardless of the presence of elastic coupling.

Step Frequency

The analysis of the improved energy efficiency using elastic coupling is conducted by the optimal step frequency, as depicted in Figure 9.36a. Specifically, the elastic coupling between thighs reduces the optimal step frequency, which fundamentally differs from the effect related to the running gaits on rigid ground.

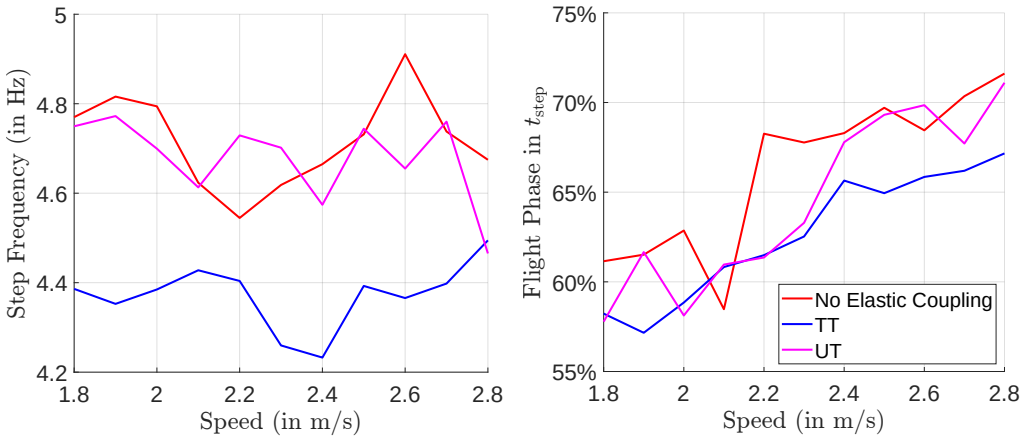

(a) Optimal step frequency of running.

(b) Relative flight duration in each step period.

Figure 9.36: Optimized step frequency and relative flight duration with respect to entire step period on compliant ground.

As illustrated in Figure 9.24a, the integration of elastic coupling, whether between the thighs or between the upper body and thighs, results in an increased step frequency when the ground is rigid. This frequency aligns with the natural free oscillation frequency, thereby enabling the robot to operate near resonance at a high frequency. On the other hand, the compliant nature of the ground significantly affects the free oscillation frequency of the gait, which is evident from the comparison of running gaits without elastic coupling on rigid and compliant surfaces, as shown in Figure 8.24b. Notably, the optimal step frequency is reduced on compliant ground, and the corresponding CoT is also lower compared to rigid ground. Consequently, the enhanced energy efficiency attributable to elastic coupling between the thighs is primarily a result of harnessing the ground's stiffness. Consistently, the relative duration of the FLP is diminished, as reported in Figure 9.36b.

In contrast, the elastic coupling between the upper body and thighs exerts minimal influence on the optimal step frequency, thus corresponding to a less significant decrease in the CoT.

Optimal Gait and Posture

The optimized running posture exhibiting elastic coupling between the thighs, as observed at velocities of $v = 1.8$, $v = 2.3$, and $v = 2.8$ m/s, is depicted in Figure 9.37, Figure 9.38, and Figure 9.39, respectively. As a consequence of the diminished flight duration, the maximal spatial separation between the body and the ground surface is reduced in comparison to the gait without elastic couplings, as described in Section 8.5.1.

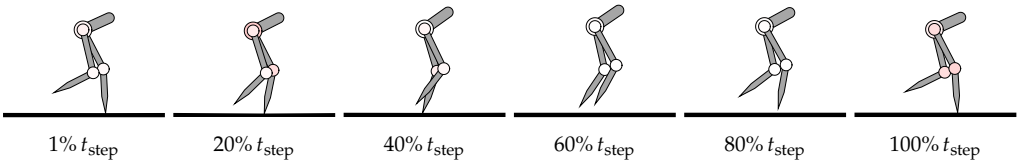

Figure 9.37: Optimized running with elastic coupling between thighs (TT) at speed $v = 1.8$ m/s.

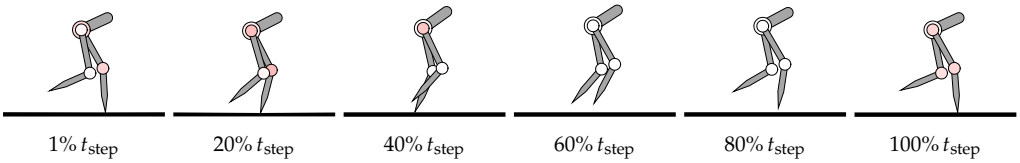

Figure 9.38: Optimized running with elastic coupling between thighs (TT) at speed $v = 2.3$ m/s.

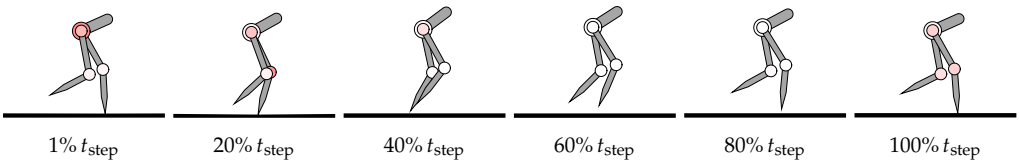

Figure 9.39: Optimized running with elastic coupling between thighs (TT) at speed $v = 2.8$ m/s.

The optimized running posture, with an elastic coupling between the upper body and thighs at speeds of $v = 1.8$, $v = 2.3$, and $v = 2.8$ m/s, is depicted in Figure 9.40, Figure 9.41, and Figure 9.42, respectively.

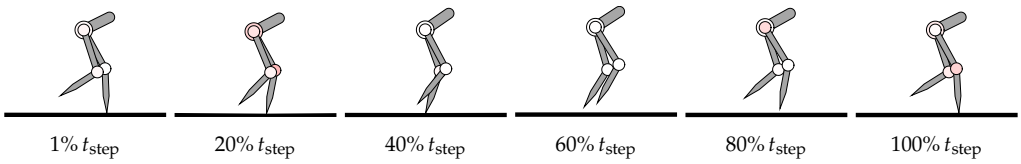

Figure 9.40: Optimized running with elastic coupling between upper body and thighs (UT) at speed $v = 1.8$ m/s.

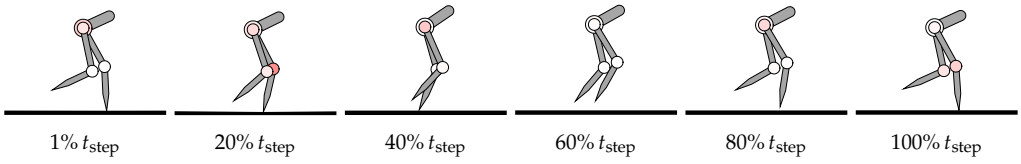

Figure 9.41: Optimized running with elastic coupling between upper body and thighs (UT) at speed $v = 2.3$ m/s.

Optimal Elastic Characteristices

Figure 9.43 illustrates the optimized nonlinear characteristics, which are presented exclusively within the active range of the spring, concerning the elastic coupling between thighs at varying speeds. Importantly, these optimal characteristics demonstrate a consistent multistable behavior across various speeds, with an increase in speed corresponding to larger stiffness. In the midphase of the SSP, the thighs experience minor angular displacements in proximity to the spring's equilibrium point, specifically when the angular displacement is equal to zero. At this stage, the presence of positive stiffness is crucial for assisting the actuator in facilitating the acceleration of the movement. As the SSP approaches its conclusion, just prior to take-off, the relative angle between the thighs approaches its maximum, at which point negative stiffness is employed to lock the optimal posture for the flight phase, thus increasing the optimal overall step frequency.
Figure 9.44 posits that the elastic coupling between the upper body and thighs predominantly exhibits linear behavior with positive stiffness under minor angular displacements, a feature characteristic of the intermediate phase of the SSP. As the active angular displacement attains its minimal value toward the conclusion of the SSP (immediately preceding take-off) and subsequently remains nearly constant throughout the flight phase, the inherent nonlinearity enables the adjustment of the body configuration, thus preserving an optimal posture without requiring actuator intervention.

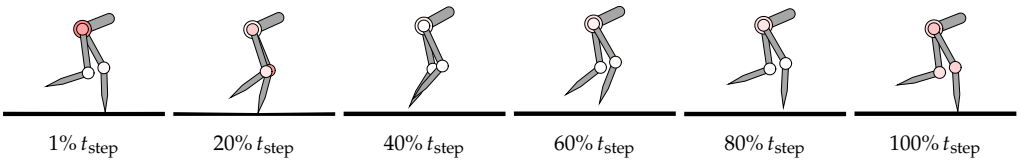

Figure 9.42: Optimized running with elastic coupling between upper body and thighs (UT) at speed $v = 2.8$ m/s.

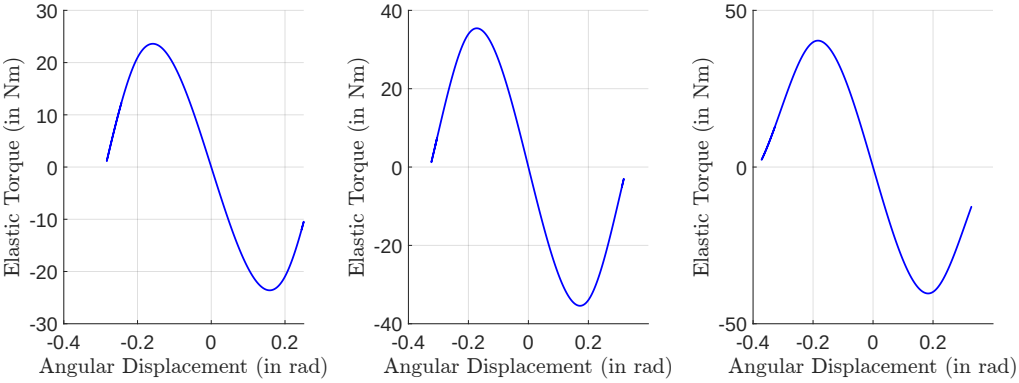

(a) Running speed $v = 1.8$ m/s. **(b)** Running speed $v = 2.3$ m/s. **(c)** Running speed $v = 2.8$ m/s.

Figure 9.43: Optimized nonlinear elastic characteristics (TT) across varying running speeds.

Energy in Periodic Gait

Figure 9.45 illustrates the energy during a step period of running at a velocity of $v = 2.3$ m/s. In contrast to running gaits at an equivalent speed on rigid surfaces, as shown in Figure 9.32, the gravitational potential energy in scenarios involving compliant ground assumes a more significant role, owing to the additional vertical degree of freedom present in the SSP. Furthermore, during the flight phase, the increased jump height suggests that a greater amount of kinetic energy is converted into gravitational energy at the onset of the FLP, which is subsequently released prior to landing.
Figure 9.45a posits that the deceleration immediately following the impact is predominantly absorbed by the compliant ground, as opposed to the actuator or elastic couplings, given the presumption of a higher stiffness parameter associated with the ground. During this brief interval, the elastic potential energy within the elastic couplings remains unaltered. This phenomenon partly accounts for the lesser enhancement in energy efficiency when elastic coupling is integrated into the robot, compared to conditions involving a rigid ground.
During the mid-stance phase, the elastic energy stored in the ground and elastic couplings is harnessed to accumulate kinetic energy essential for take-off. Consistent

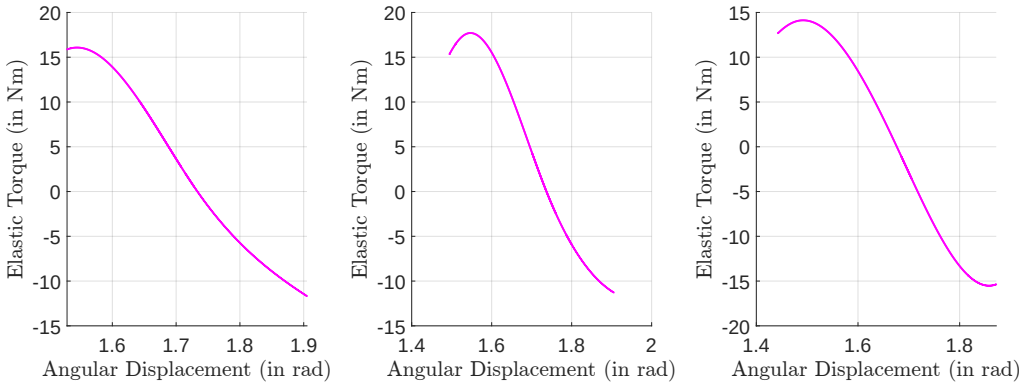

(a) Running speed $v = 1.8$ m/s. **(b)** Running speed $v = 2.3$ m/s. **(c)** Running speed $v = 2.8$ m/s.

Figure 9.44: Optimized nonlinear elastic characteristics (UT) across varying running speeds.

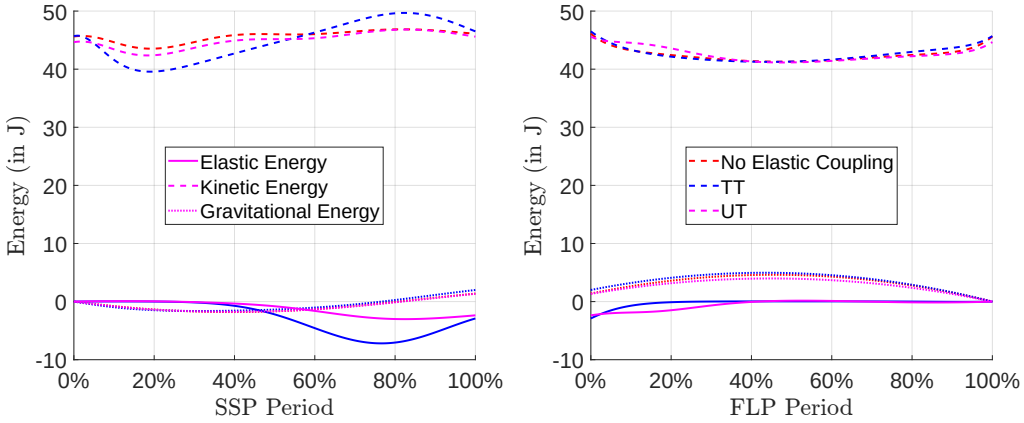

(a) Energy in normalized SSP. **(b)** Energy in normalized FLP.

Figure 9.45: Energy profiles during SSP and FLP for running at $v = 2.3$ m/s without elastic coupling (in red), with elastic couplings between thighs (in blue) and between upper body and thighs (in magenta). The solid lines in panel **(a)** depict the potential energy stored in the segment-to-segment elastic couplings; they do not include the elastic energy associated with the deformable ground.

with the findings regarding the gait on rigid ground reported in Figure 9.32, the robot initiates the accumulation of potential energy within the elastic couplings prior to take-off. This accumulation of elastic energy persists into the early stages of flight. Owing to the nonlinearity inherent in the optimal elastic characteristics, the posture remains approximately unchanged during the subsequent flight phase, resulting in a nearly constant level of elastic energy.

Mechanical Power in Actuator

Figure 9.46 presents the mechanical power exerted by the actuator across various configurations of elastic couplings at a running velocity of $v = 2.3$ m/s. In the absence of an elastic coupling, Figure 9.46a demonstrates notable positive mechanical power in both hip joints during the middle of the SSP, which is crucial for the accumulation of kinetic energy, as illustrated in Figure 9.45a. Analogous to locomotion on rigid ground, as shown in Figure 9.33a, the actuator in the knee joint of the stance leg generates considerable negative mechanical power to avert slippage of the stance foot on either rigid or compliant surfaces. At the onset of the FLP in Figure 9.46a, a pronounced deceleration of the hip joint is necessary for adjusting body posture during the flight.

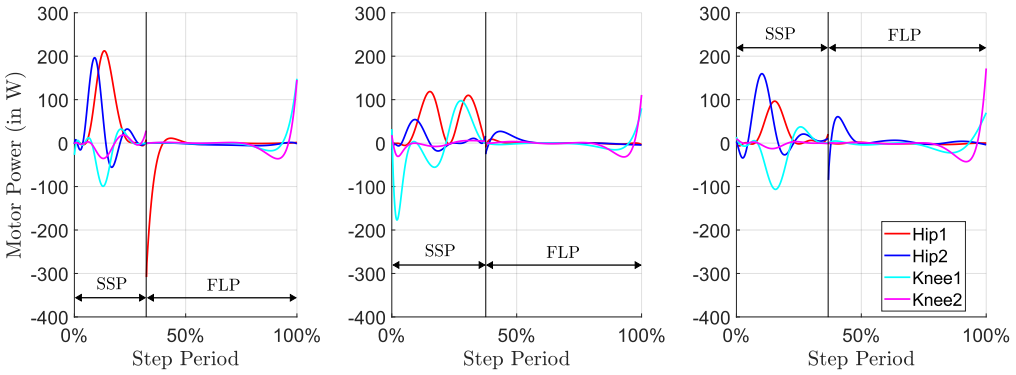

(a) No elastic coupling.

(b) Elastic coupling between thighs (TT).

(c) Elastic coupling between upper body and thighs (UT).

Figure 9.46: Mechanical power profiles in the actuators for an optimized running gait at $v = 2.3$ m/s without or with elastic couplings.

Figure 9.46b and Figure 9.46c demonstrate a considerable reduction in the positive mechanical power exerted by the actuators, attributed to the assistance provided by the elastic coupling during the acceleration phase in the middle of the SSP. Immediately after take-off, an optimal posture for flight is achieved due to the nonlinear elastic properties, thereby eliminating the necessity for negative mechanical power from the actuators and consequently reducing deceleration losses. In configurations both with and without elastic couplings, actuators are typically employed at the conclusion of the FLP to adjust the body posture, ensuring an optimal landing with minimal contact loss.

9.5.2 Gait Stability

The assessment of gait stability is based on the magnitude of the largest nontrivial Floquet multipliers, as illustrated in Figure 9.47. Notably, the incorporation of elastic

coupling does not adversely affect stability behavior. Indeed, at certain speeds, elastic coupling marginally enhances gait stability, maintaining consistent performance akin to running on rigid ground, as shown in Figure 9.34.

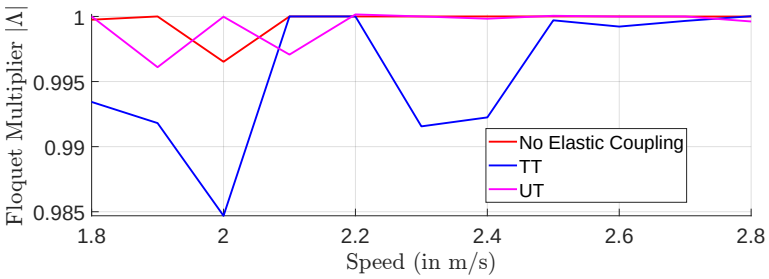

Figure 9.47: Magnitude of the nontrivial Floquet multiplier without or with elastic couplings.

9.6 Concluding Remarks

This chapter investigates the feasibility of integrating elastic couplings into a bipedal robotic model to enhance energy efficiency in locomotion such as walking and running. Numerical optimizations are conducted across various gait configurations, including instantaneous versus non-instantaneous double support phases (DSP) in walking, as well as running on rigid compared to compliant surfaces, each evaluated at diverse speeds. The results are encapsulated in the following summary:

- **Walking with Instantaneous DSP:** Adding elastic couplings significantly reduces both the overall cost of transport (CoT) and, in particular, the actuator deceleration losses. Coupling between the upper body and thighs (UT) or between the thighs (TT) both yield substantial energy savings (over 70 %), primarily by exploiting free oscillations of the mechanical system. However, introducing elastic couplings tends to increase the magnitude of the nontrivial Floquet multiplier of the underactuated walking gait, reducing the convergence rate to the stable limit cycle.

- **Walking with Non-Instantaneous DSP:** In the fully actuated non-instantaneous DSP formulation, adding elastic couplings does not degrade gait stability. Nonlinear elastic couplings placed between the upper body and thighs can reduce CoT by as much as 60 %, primarily through minimizing deceleration losses in the underactuated single support phase. Crucially, the system exploits a longer DSP in which elastic potential energy is accumulated, then released during the SSP to accelerate the robot's segments.

- **Running on Rigid Ground:** Elastic couplings substantially reduce energy consumption for running on rigid ground: TT and UT couplings reduce CoT by approximately 50 % and 60 %, respectively, across the examined speed range. Deceleration immediately following impact is largely absorbed by the elastic couplings, allowing stored energy to be released in mid-stance and reducing positive actuation requirements. Stability is not adversely affected, and may even improve at specific speeds.
- **Running on Compliant Ground:** While introducing compliance into the robot's body still yields notable CoT reductions (average savings of around $20 - 30$ %), the presence of an already-compliant substrate means that deceleration is partially absorbed by the ground, leaving less benefit available from additional elastic couplings. Nonlinear elastic characteristics tend to be multistable, helping lock the leg configuration at certain phases (e.g., just before flight), thereby minimizing extra actuator effort. Gait stability is not compromised and sometimes shows marginal improvements.

In summary, the findings affirm that incorporating optimally designed elastic couplings into a bipedal robot's rigid body structure can greatly enhance energetic efficiency in both walking and running, provided that the optimal placement of couplings (e.g., UT vs. TT) and the selection of spring characteristics (e.g., multistable vs. monostable) are aligned with the natural oscillations of each gait. Specifically, the storage of energy during deceleration and its release during acceleration significantly diminishes the cost of transport and reduces the net mechanical work exerted by the actuators.
Nevertheless, this chapter optimized each speed-specific elastic coupling independently to attain the optimal performance at that specified speed. A practical subsequent step involves the investigation of a single set of coupling parameters for multiple speeds, employing more sophisticated numerical methodologies capable of managing the resulting high-dimensional optimization processes. This multi-velocity approach will more accurately emulate real-world applications, where modifications to hardware across varying speeds are typically impractical or undesirable.

10 Conclusions and Future Works

10.1 Conclusions

This dissertation investigates the energy efficiency and stability of periodic walking and running gaits of a planar biped robot. Utilizing Hybrid Zero Dynamics (HZD) control, the research explores four primary scenarios: walking with either instantaneous or non-instantaneous double support phases (DSP) on rigid ground, and running on either rigid or compliant ground. The robot model is comprised of five rigid segments (incorporating an upper body, two thighs, and two shanks) equipped with four actuated revolute joints and point feet. Periodic gait trajectories, which sustain a constant average speed, are established using a multiple shooting methodology and are subsequently optimized through a Sequential Quadratic Programming (SQP) algorithm, with a focus on enhancing locomotion efficiency. Energy efficiency is evaluated through the application of the dimensionless cost of transport, while gait stability is assessed in accordance with Floquet theory. The investigation into energy efficiency spans a variety of locomotion speeds.
The research is ultimately directed towards two primary objectives: firstly, to examine the impact of gait variation and ground compliance on the efficiency and stability of locomotion; and secondly, to investigate the feasibility of implementing adjustable parallel elastic couplings between robot segments as a means to enhance the energy efficiency across the various explored locomotion scenarios.
The preliminary phase of this research is dedicated to examining bipedal locomotion through the use of a robotic model that is solely comprised of rigid body segments. The principal findings of the efficiency analysis are:

- **Walking with Instantaneous DSP:** Optimal periodic walking gaits are achieved through the exploitation of the natural oscillation of the swing leg in the midphase of a step cycle. The associated energy consumption demonstrates an approximately linear relationship with walking speed. A considerable fraction of the energy dissipation is attributed to the actuator's role in decelerating motion to either sustain body posture or reduce the approach velocity prior to ground contact. Although

asymptotic orbital stability is established (the nontrivial Floquet multiplier below unity), minor perturbations exhibit a slow convergence to the reference gait.

- **Walking with Non-Instantaneous DSP:** Integrating a non-instantaneous DSP within the walking sequence facilitates faster disturbance rejection and enhances gait initialization from rest due to a fully actuated model. However, maintaining a closed kinematic chain during the DSP restricts the robot's ability to employ extensive swing-leg motions, thereby reducing overall energy efficiency compared to the instantaneous DSP scenario. To realize a highly efficient DSP, it is crucial to incorporate extended foot models that permit rolling motion on the ground. Despite its lower efficiency, this approach remains advantageous in scenarios involving significant perturbations or challenging environments where rapid convergence is imperative.

- **Running on Rigid Ground:** The cost of transport during running exhibits an almost linear relationship with running speed. At speeds exceeding approximately 2.2 m/s, running efficiency surpasses that of walking. Despite inelastic impacts causing significant force and torque surges at touchdown, the stability analysis employing the Floquet multipliers verifies the presence of stable limit cycles. A trade-off is evident whereby gaits demonstrating enhanced stability (indicated by smaller nontrivial Floquet multipliers) may result in a marginal increase in the cost of transport (less efficiency).

- **Running on Compliant Ground:** At high velocities, elastic deformation of the compliant ground contributes to energy recovery, thereby diminishing the work demanded from actuators. Although damping losses are present, the overall cost of transport has the potential to fall below that encountered with rigid ground. The reaction force and torque profiles exhibit increased smoothness as a result of impact attenuation, which likely mitigates stress on mechanical components. The complexity of simulations increases significantly due to the stiff dynamics and the increased degrees of freedom introduced during the compliant contact, necessitating more advanced numerical integration and explicit constraint stabilization methodologies.

Subsequently, an efficiency study incorporating parallel elastic couplings between robotic segments is undertaken across the same speed range as the configuration without such elastic couplings. The primary results of the efficiency analysis are as follows:

- **Walking with Instantaneous DSP:** In underactuated gaits that involve instantaneous impact transition events, the incorporation of elastic couplings—whether between the thighs or between the upper body and thighs—can lead to a reduction

in the cost of transport by over 70 %. On the other hand, the added elasticity results in a modest increase in the nontrivial Floquet multiplier, which consequently decelerates the convergence rate to the reference limit cycle.

- **Walking with Non-Instantaneous DSP:** Fully actuated DSP enhances the robustness of the gait against disturbances. By integrating nonlinear elastic components between the upper body and thighs, the overall cost of transport is reduced by as much as 60 %. During the DSP, energy is stored as elastic potential, enabling the robot to utilize free oscillations in the underactuated single support phase. This supplementary elasticity, unlike in the underactuated scenario, does not negatively impact the gait stability.

- **Running on Rigid Ground:** Elastic couplings positioned either between the upper body and thighs or between the thighs contribute to enhanced energy efficiency. This enhancement is quantitatively demonstrated by a reduction in the cost of transport up to 60 % across the investigated speed range. In particular, the deceleration subsequent to impact is partly converted into elastic potential energy, which is then released to aid in propulsion.

- **Running on Compliant Ground:** Although ground compliance alone results in a decreased cost of transport compared to rigid ground, the incorporation of elastic couplings can provide additional savings of up to 26 % by enhancing ground elasticity during the mid-stance phase. Nonlinear, multistable spring configurations are capable of securing the leg in place at pivotal moments, effectively reducing the step frequency and the effort exerted by actuators. Gait stability remains largely unchanged or may experience slight enhancement.

The thesis presents a diverse range of bipedal walking and running gaits and examines their energy efficiency and gait stability. By simultaneously optimizing gait trajectory and elastic coupling characteristics, highly efficient gaits can be identified, wherein the natural dynamics of the system align with locomotion requiring reduced actuation for the given scenarios. Depending on the specific application, suitable gaits can be selected based on the insights generated from this research.

10.2 Future Works

Beyond the settings explored here, additional gait scenarios merit attention. For instance, [190] and [192] analyze biped walking with instantaneous DSP and the improved energy efficiency using nonlinear elastic couplings on inclined ground surfaces, which can be further investigated for running gaits. Walking on stairs with positive and negative inclinations is preliminarily investigated in [208], where the walking gait sequence is

designed with single-step or multiple-step periods. For enhancing stability on stairs, the walking gait with non-instantaneous DSP can be investigated. Also, energy efficiency improvement using elastic couplings can be considered in this future work.
The investigation into the generation of stable running motion on compliant ground reveals significant numerical challenges, primarily due to the presence of three unactuated degrees of freedom, which are therefore considered within the zero dynamics submanifold via ordinary differential equations. Importantly, the enforcement of zero dynamics necessitates the assumption that virtual constraints on the actuated joints are impeccably satisfied. Although these constraints are explicitly integrated into the robot's full-order dynamics, numerical errors accumulate, resulting in slight unphysical violations on the constraint surface. Given the substantial stiffness parameter of the compliant ground, such minor deviations result in considerable reaction forces that markedly affect robot dynamics. To address constraint violations, explicit stability methodologies, such as closed-loop simulation following Baumgarte Stabilization or Coordinate Projection, are advantageous. These approaches enhance the formulation of optimization frameworks that utilize collocation or multiple shooting methods to generate periodic gaits. While the dimensionality of the optimization problem may increase significantly, a reduction in the nonlinearity of the differential equations is anticipated, leading to an overall improvement in convergence behavior during optimization. Consequently, future research endeavors are committed to comparing these methodologies in terms of numerical accuracy and efficiency.
An enhanced optimization framework has the potential to be employed for generating optimal elastic couplings that are appropriate for a variety of walking and running scenarios at multiple velocities. While this dissertation focuses on optimizing elastic couplings for specific speeds, real-world robots often function across a spectrum of velocities. A singular coupling design, which is optimized across a spectrum of velocities for various gaits, obviates the requirement for the physical reconfiguration of the robot. However, the associated optimization challenge engenders heightened computational complexity owing to its increased dimensionality, thereby requiring highly efficient numerical methods and optimization formulations.
Moreover, an efficient optimization framework, particularly suited for real-time applications, facilitates the generation of transient gaits in response to significant perturbations and complex environmental conditions, contingent upon measured system states. Specifically, leveraging the insights developed within this thesis, the control principle devised for the fully actuated non-instantaneous double support phase can be employed to achieve enhanced stability during transient steps. As a further advancement, the controller may be applied, for instance, in scenarios involving running with an actuated flat foot, which is regarded as fully actuated during the single support phase, to augment gait stability.

The progression from simulation to hardware implementation holds significant importance. As illustrated in Figure 10.1, a robotic prototype has been designed for the purpose of experimentation. However, the considerable resistance present in the electric drivetrain prevents the robot from being utilized to validate highly efficient gaits, where the passive dynamics (free oscillation) of the segments are essential. Thus, designing a bipedal prototype equipped with adjustable or replaceable elastic couplings would facilitate the validation of the proposed control and optimization methodologies in real-world conditions, which encompass unmodeled dynamics, parameter inaccuracies, and actuator saturations. Enhanced parameter identification and the development of robust real-time controllers will be indispensable in bridging the disparity between theoretical forecasts and empirical performance.

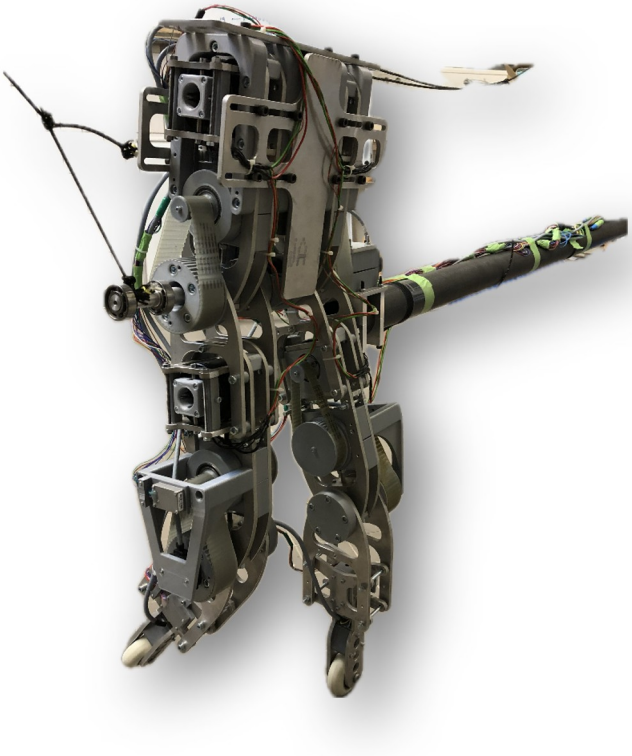

Figure 10.1: Bipedal robot prototype with five rigid body segments.

Acknowledgement: The Artificial Intelligence (AI) tools *ChatGPT-O1* and *Writefull* are employed to refine text formulation and correct grammatical inaccuracies in the entire dissertation.

Appendix

A Geometry in Double Support Phase

The explicit holonomic constraint $\mathbf{q}_{\mathrm{dd}} = \hat{\mathbf{\Omega}}(\hat{\mathbf{q}}_{\mathrm{d}})$ in Section 3.3.1 is derived according to the illustration Figure A.1.

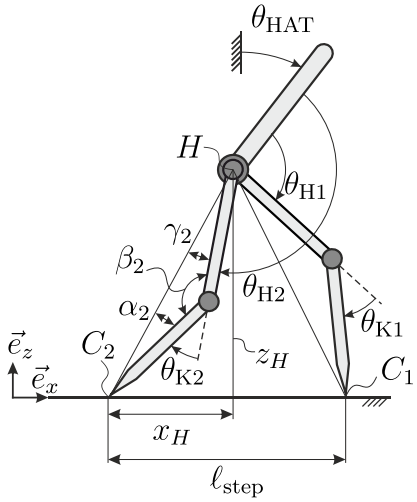

Figure A.1: Geometric parameters of the closed kinematic chain established by the two stance legs during the continuous double support phase.

The vector $\mathbf{r}_{HC_1}$ extending from the hip to foot 1 is articulated in terms of the thigh ℓ_{T} and shank ℓ_{S} as demonstrated by

$$\mathbf{r}_{HC_1} = r_{HC_1,x}\vec{e}_x + r_{HC_1,z}\vec{e}_z \ , \tag{A.1}$$

with accompanying assumptions as detailed in

$$\begin{aligned} r_{HC_1,x} &= \ell_{\mathrm{T}} \sin\left(\theta_{\mathrm{HAT}} + \theta_{\mathrm{H1}}\right) + \ell_{\mathrm{S}} \sin\left(\theta_{\mathrm{HAT}} + \theta_{\mathrm{H1}} + \theta_{\mathrm{K1}}\right) \ , \\ r_{HC_1,z} &= \ell_{\mathrm{T}} \cos\left(\theta_{\mathrm{HAT}} + \theta_{\mathrm{H1}}\right) + \ell_{\mathrm{S}} \cos\left(\theta_{\mathrm{HAT}} + \theta_{\mathrm{H1}} + \theta_{\mathrm{K1}}\right) \ . \end{aligned} \tag{A.2}$$

Considering the prescribed step length ℓ_{step}, the following relation holds

$$\begin{aligned} x_H &= r_{HC_1,x} - \ell_{\text{step}} \,, \\ z_H &= r_{HC_1,z} \,. \end{aligned} \tag{A.3}$$

Consequently, the magnitude of vector $\mathbf{r}_{HC_2}$ is given by

$$|\mathbf{r}_{HC_2}| = \sqrt{x_H^2 + z_H^2} \,. \tag{A.4}$$

The law of cosines is subsequently employed in the analysis of the triangle present in leg 2, resulting in

$$|\mathbf{r}_{HC_2}|^2 = \ell_{\text{T}}^2 + \ell_{\text{S}}^2 - 2\ell_{\text{T}}\ell_{\text{S}} \cos(\beta_2) \,. \tag{A.5}$$

Given the condition of identical segment lengths $\ell_{\text{T}} = \ell_{\text{S}}$, the subsequent expression can be derived

$$\begin{aligned} \beta_2 &= \arccos\left(1 - \frac{|\mathbf{r}_{HC_2}|^2}{2\ell_{\text{T}}^2}\right) \,, \\ \gamma_2 &= \alpha_2 = \frac{\pi - \beta_2}{2} \,. \end{aligned} \tag{A.6}$$

Therefore, the conclusion follows as

$$\hat{\mathbf{\Omega}}(\hat{\mathbf{q}}_{\text{d}}) = \begin{bmatrix} \theta_{\text{H2}} \\ \theta_{\text{K2}} \end{bmatrix} = \begin{bmatrix} \pi + \arctan\left(\frac{x_H}{z_H}\right) - \gamma_2 - \theta_{\text{HAT}} \\ 2\gamma_2 \end{bmatrix} \,. \tag{A.7}$$

B Matrix Algorithm

This chapter of the appendix elucidates the algorithm for constructing orthogonal basis vectors of a matrix relative to a specified eigenvector, as well as the iterative QR-algorithm employed for the determination of eigenvalues for matrices exceeding four dimensions. The fundamental procedural steps of both algorithms incorporate Givens rotations, as detailed in [56].

Algorithm 1: Constructing Orthogonal Basis Vectors Using Givens Rotations

Input : Eigenvector $\mathbf{v} \in \mathbb{R}^n$

Output: Orthonormal basis $\mathbf{Q} := [\mathbf{q}_1, \mathbf{Q}_\perp] \in \mathbb{R}^{n \times n}$ where $\mathbf{q}_1 = \mathbf{u}$ and $\mathbf{Q}_\perp := [\mathbf{q}_2, \ldots, \mathbf{q}_n]$ are orthogonal to $\mathbf{u}$

Normalize the eigenvector: $\mathbf{u} \leftarrow \mathbf{v}/\|\mathbf{v}\|$ `// Normalization`

Initialize orthogonal matrix: $\mathbf{Q} \leftarrow \mathbf{I}_n$ `// Initialize Q as identity`

for $k \leftarrow n$ **to** 2 **do**

  Compute $r \leftarrow \sqrt{u_{k-1}^2 + u_k^2}$

  if $r = 0$ **then**

    Set $c \leftarrow 1, s \leftarrow 0$ `// Avoid division by zero`

  else

    Compute $c \leftarrow u_{k-1}/r, \quad s \leftarrow u_k/r$ `// Givens rotation parameters`

  Form Givens rotation matrix $\mathbf{G}_k(c, s)$ acting on rows $k-1$ and k `// Zero out` u_k

  Update $\mathbf{u} \leftarrow \mathbf{G}_k(c, s)\mathbf{u}$

  Update $\mathbf{Q} \leftarrow \mathbf{Q}\mathbf{G}_k^\top(c, s)$ `// Accumulate rotations`

return $\mathbf{Q} = [\mathbf{u}, \mathbf{Q}_\perp]$, where $\mathbf{Q}_\perp$ consists of $n-1$ orthonormal vectors orthogonal to $\mathbf{u}$

Algorithm 2: QR Algorithm for Determining Eigenvalues

Input : Matrix $\mathbf{A} \in \mathbb{R}^{n \times n}$, maximum iterations N

Output : Approximate eigenvalues of the matrix $\mathbf{A}$

Compute Hessenberg form: $\mathbf{H}_0 \leftarrow \text{Hessenberg}(\mathbf{A})$ `// Using Algorithm 3`

for $k \leftarrow 1$ **to** N **do**

  Compute QR decomposition: $\mathbf{H}_{k-1} = \mathbf{Q}_k \mathbf{R}_k$ `// Using Algorithm 4`

  Update matrix: $\mathbf{H}_k \leftarrow \mathbf{R}_k \mathbf{Q}_k$ `// Form next iterate`

return Diagonal elements of $\mathbf{H}_N$ as approximations to the eigenvalues of $\mathbf{A}$

Algorithm 3: Transforming Matrix $\mathbf{A}$ to Upper Hessenberg Form

Input : An $n \times n$ matrix $\mathbf{A} \in \mathbb{R}^{n \times n}$

Output : An upper Hessenberg matrix $\mathbf{H} \in \mathbb{R}^{n \times n}$

Initialize $\mathbf{H} \leftarrow \mathbf{A}$ `// Initialize H`

for $k \leftarrow 1$ **to** $n - 2$ **do**

  for $i \leftarrow n$ **to** $k + 2$ **do**

    Compute $r \leftarrow \sqrt{H_{k+1,k}^2 + H_{i,k}^2}$

    if $r = 0$ **then**

      Set $c \leftarrow 1, s \leftarrow 0$ `// Avoid division by zero`

    else

      Compute $c \leftarrow H_{k+1,k}/r, \quad s \leftarrow H_{i,k}/r$ `// Givens rotation parameters`

    Form Givens rotation matrix $\mathbf{G}_{i,k}(c, s)$ acting on rows $k + 1$ and i `// Zero out` $H_{i,k}$

    Update $\mathbf{H} \leftarrow \mathbf{G}_{i,k}^\top \mathbf{H} \mathbf{G}_{i,k}$ `// Apply rotation from both sides`

return $\mathbf{H}$

Algorithm 4: QR Decomposition Using Givens Rotations

Input : Matrix $\mathbf{A} \in \mathbb{R}^{m \times n}$ with $m \geq n$

Output: An orthogonal matrix $\mathbf{Q} \in \mathbb{R}^{m \times m}$ and an upper triangular matrix $\mathbf{R} \in \mathbb{R}^{m \times n}$ such that $\mathbf{A} = \mathbf{QR}$

Initialize $\mathbf{R} \leftarrow \mathbf{A}$ `// Initialize R`

Initialize $\mathbf{Q} \leftarrow \mathbf{I}_m$ `// Initialize Q as identity`

for $j \leftarrow 1$ **to** n **do**

  for $i \leftarrow m$ **to** $j + 1$ **do**

    Compute $r \leftarrow \sqrt{R_{j,j}^2 + R_{i,j}^2}$

    if $r = 0$ **then**

      Set $c \leftarrow 1, s \leftarrow 0$ `// Avoid division by zero`

    else

      Compute $c \leftarrow R_{j,j}/r, \quad s \leftarrow R_{i,j}/r$ `// Givens rotation parameters`

    Form Givens rotation matrix $\mathbf{G}_{i,j}(c, s)$ acting on rows j and i `// Zero out` $R_{i,j}$

    Update $\mathbf{R} \leftarrow \mathbf{G}_{i,j}^\top \mathbf{R}$ `// Apply rotation to R`

    Update $\mathbf{Q} \leftarrow \mathbf{Q}\mathbf{G}_{i,j}$ `// Accumulate rotations into Q`

return $\mathbf{Q}$, $\mathbf{R}$

C Definition of Bézier Curve

The delineation of m independent Bézier curves $\mathbf{q}_\mathrm{r}(s, \boldsymbol{\alpha})$ is realized through the mapping $\mathbf{q}_\mathrm{r} : \mathbb{R} \times \mathbb{R}^{m\times(n+1)} \to \mathbb{R}^m$; $s, \boldsymbol{\alpha} \mapsto \mathbf{q}_\mathrm{r}(s, \boldsymbol{\alpha})$, with $s \in [0, 1]$ operating as the independent variable confined within a normalized interval. The characteristic features are determined by the parameters (control points) $\boldsymbol{\alpha} := [\boldsymbol{\alpha}_0, \dots, \boldsymbol{\alpha}_n] \in \mathbb{R}^{m\times(n+1)}$, and n specify the order of the Bézier curves $\mathbf{q}_\mathrm{r}(s, \boldsymbol{\alpha})$.
The Bézier curve, along with its first and second partial derivatives with respect to s, are articulated in alignment with the definitions established in [45, Sections 5.1 and 5.2] as [1]

$$\mathbf{q}_\mathrm{r}(s, \boldsymbol{\alpha}) := \sum_{i=0}^{n} \underbrace{\binom{n}{i}(1-s)^{n-i}s^i}_{b_i^n(s)} \boldsymbol{\alpha}_i \ , \tag{C.1a}$$

$$\frac{\partial \mathbf{q}_\mathrm{r}(s, \boldsymbol{\alpha})}{\partial s} := n \sum_{i=0}^{n-1} \underbrace{\binom{n-1}{i}(1-s)^{n-1-i}s^i}_{b_i^{n-1}(s)} (\boldsymbol{\alpha}_{i+1} - \boldsymbol{\alpha}_i) \ , \tag{C.1b}$$

$$\frac{\partial^2 \mathbf{q}_\mathrm{r}(s, \boldsymbol{\alpha})}{\partial s^2} := n(n-1) \sum_{i=0}^{n-2} \underbrace{\binom{n-2}{i}(1-s)^{n-2-i}s^i}_{b_i^{n-2}(s)} (\boldsymbol{\alpha}_{i+2} - 2\boldsymbol{\alpha}_{i+1} + \boldsymbol{\alpha}_i) \ , \tag{C.1c}$$

where $b_i^n(s)$ with $b_i^n : \mathbb{R} \to \mathbb{R}$ is identified as the Bernstein polynomial, and

$$\binom{n}{k} := \begin{cases} \frac{n!}{k!(n-k)!} & \text{for } 0 \le k \le n, \\ 0 & \text{otherwise,} \end{cases} \tag{C.2}$$

represents the binomial coefficient.

[1] For the purpose of clarification, the notation $\boldsymbol{\alpha}_i \in \mathbb{R}^{m\times 1}$ with $i \in [0, n]$ denotes a column vector within the parameter matrix $\boldsymbol{\alpha}$.

Example Bézier Curve

A quintic (fifth-order) Bézier curve $q_\mathrm{r}(s, \boldsymbol{\alpha})$, defined by the equidistant control points $\boldsymbol{\alpha} \in \mathbb{R}^{1\times 6}$, is depicted in Figure C.1. Its partial derivatives with respect to the independent variable $s \in [0, 1]$ are presented in Figure C.2. It is noteworthy that the commencement $q_\mathrm{r}(s = 0, \boldsymbol{\alpha}) = [1, \mathbf{0}]\boldsymbol{\alpha}^\top$ and conclusion points $q_\mathrm{r}(s = 1, \boldsymbol{\alpha}) = [\mathbf{0}, 1]\boldsymbol{\alpha}^\top$ of the Bézier curve $q_\mathrm{r}(s, \boldsymbol{\alpha})$ align with the initial and terminal parameters of $\boldsymbol{\alpha}$, respectively. This demonstrates the localized influence of control points on the properties of the Bézier curve.

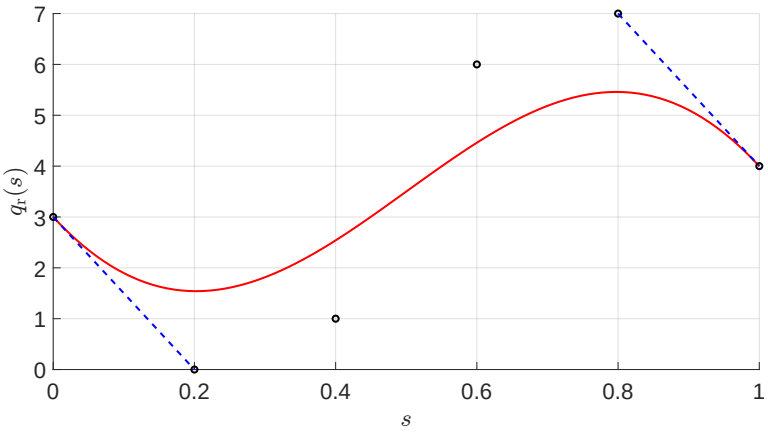

Figure C.1: A five-order Bézier curve $q_\mathrm{r}(s, \boldsymbol{\alpha})$ is formulated using six equidistant control points $\boldsymbol{\alpha} := [3, 0, 1, 6, 7, 4]$, represented by circled markers. The tangent line at points $s = 0$ and $s = 1$ is illustrated by the blue dashed line.

Moreover, the tangent to the Bézier curve $q_\mathrm{r}(s, \boldsymbol{\alpha})$ at both the initial point $s = 0$ and the terminal point $s = 1$ is solely determined by the first pair and the last pair of parameters in $\boldsymbol{\alpha}$, as illustrated in Figure C.1. Specifically, the tangent corresponds to the straight line joining the paired control points. To substantiate this, the slope of these tangents in Figure C.1 can be directly derived from the first derivative $\partial q_\mathrm{r}(s, \boldsymbol{\alpha})/\partial s$, as evidenced in Figure C.2a.

Attributable to the fifth order of the example curve $q_\mathrm{r}(s, \boldsymbol{\alpha})$, its second derivative, as depicted in Figure C.2b, exhibits a continuous polynomial behavior within the interval $s \in [0, 1]$. This characteristic inherently facilitates the design of actuator behavior that is devoid of sudden transitions.

Elevating the polynomial order facilitates the creation of complex gait trajectories, potentially leading to improved energy efficiency. However, augmenting the polynomial order also necessitates the optimization of a greater number of parameters. To achieve an optimal balance, polynomials of the sixth order are chosen for the thesis.

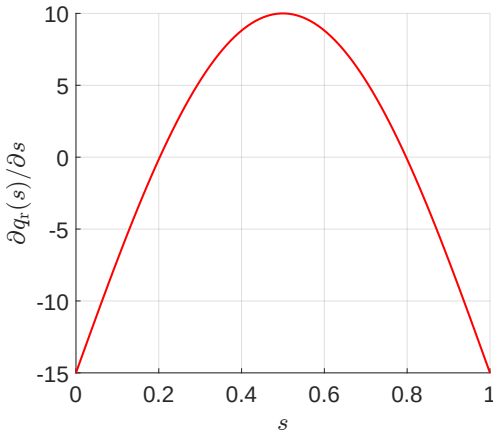

(a) The first partial derivative $\partial q_{\mathrm{r}}(s, \boldsymbol{\alpha})/\partial s$.

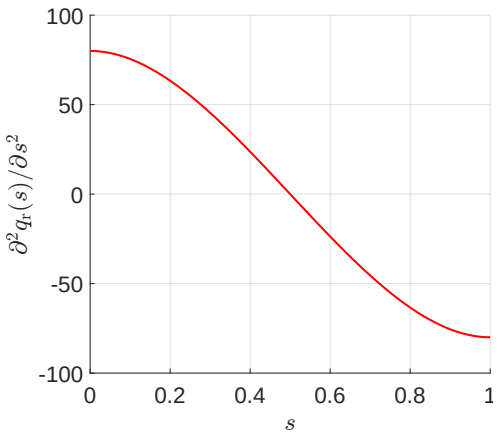

(b) The second partial derivative $\partial^2 q_{\mathrm{r}}(s, \boldsymbol{\alpha})/\partial s^2$.

Figure C.2: The associated partial derivatives of the Bézier curve $q_{\mathrm{r}}(s, \boldsymbol{\alpha})$ discussed in Figure C.1.

List of Figures

Bibliography

[1] Acary, V. (2012): Higher order event capturing time-stepping schemes for nonsmooth multibody systems with unilateral constraints and impacts. *Applied Numerical Mathematics*. Selected Papers from NUMDIFF-12 **62**(10), pp. 1259–1275.

[2] Adamy, J. (2024): *Nonlinear Systems and Controls*. 2nd ed. Heidelberg: Springer Berlin.

[3] Adolfsson, J., H. Dankowicz, and A. Nordmark (2001): 3D Passive Walkers: Finding Periodic Gaits in the Presence of Discontinuities. *Nonlinear Dynamics* **24**(2), pp. 205–229.

[4] Akbari Hamed, K. and A. D. Ames (2020): Nonholonomic Hybrid Zero Dynamics for the Stabilization of Periodic Orbits: Application to Underactuated Robotic Walking. *IEEE Transactions on Control Systems Technology* **28**(6), pp. 2689–2696.

[5] Al-Shuka, H. F. N., B. Corves, W.-H. Zhu, and B. Vanderborght (2016): Multi-level control of zero-moment point-based humanoid biped robots: a review. *Robotica* **34**(11), pp. 2440–2466.

[6] Alves, J., N. Peixinho, M. T. da Silva, P. Flores, and H. M. Lankarani (2015): A comparative study of the viscoelastic constitutive models for frictionless contact interfaces in solids. *Mechanism and Machine Theory* **85**, pp. 172–188.

[7] Ambrósio, J. A. C. and A. Kecskeméthy (2007): Multibody Dynamics of Biomechanical Models for Human Motion via Optimization. In: *Multibody Dynamics*. J. C. García Orden, J. M. Goicolea, and J. Cuadrado eds. Dordrecht: Springer Netherlands, pp. 245–272.

[8] Ames, A. D., K. Galloway, K. Sreenath, and J. W. Grizzle (2014): Rapidly Exponentially Stabilizing Control Lyapunov Functions and Hybrid Zero Dynamics. *IEEE Transactions on Automatic Control* **59**(4), pp. 876–891.

[9] Angeles, J. and A. Kecskeméthy (1995): Dynamics Modelling. In: *Kinematics and Dynamics of Multi-Body Systems. CISM International Centre for Mechanical Sciences, vol 360*. J. Angeles and A. Kecskeméthy eds. Vienna: Springer, pp. 57–73.

[10] Anitescu, M. (2006): Optimization-based simulation of nonsmooth rigid multibody dynamics. *Mathematical Programming* **105**(1), pp. 113–143.

[11] Åström, K. J. and R. M. Murray (2020): *Feedback Systems: An Introduction for Scientists and Engineers*. 2nd ed. Princeton, NJ: Princeton University Press.

[12] Badrikouhi, M. and M. Bamdad (2022): Smooth Trajectory Planning Based on Direct Collocation Method for Cable-Driven Parallel Robots with Central Spine. *Mechanics of Solids* **57**(3), pp. 652–670.

[13] Balaji, N. N., J. Gross, and M. Krack (2024): Harmonic Balance for quasi-periodic vibrations under nonlinear hysteresis. *Journal of Sound and Vibration* **590**, p. 118570.

[14] Banerjee, N., X. Long, R. Du, F. Polido, S. Feng, C. G. Atkeson, M. Gennert, and T. Padir (2015): Human-supervised control of the ATLAS humanoid robot for traversing doors. In: *2015 IEEE-RAS 15th International Conference on Humanoid Robots (Humanoids)*, pp. 722–729.

[15] Banerjee, S. and A. Roy (2014): *Linear Algebra and Matrix Analysis for Statistics*. 1st ed. New York: Chapman and Hall/CRC.

[16] Bauchau, O. A. and A. Laulusa (2007): Review of Contemporary Approaches for Constraint Enforcement in Multibody Systems. *Journal of Computational and Nonlinear Dynamics* **3**(011005).

[17] Bauer, F., U. Römer, A. Fidlin, and W. Seemann (2016): Optimal elastic coupling in form of one mechanical spring to improve energy efficiency of walking bipedal robots. *Multibody System Dynamics* **38**(3), pp. 227–262.

[18] Bauer, F., U. J. Römer, A. Fidlin, and W. Seemann (2016): Optimization of energy efficiency of walking bipedal robots by use of elastic couplings in the form of mechanical springs. *Nonlinear Dynamics* **83**(3), pp. 1275–1301.

[19] Beckerle, P., T. Verstraten, G. Mathijssen, R. Furnémont, B. Vanderborght, and D. Lefeber (2017): Series and Parallel Elastic Actuation: Influence of Operating Positions on Design and Control. *IEEE/ASME Transactions on Mechatronics* **22**(1), pp. 521–529.

[20] di Bernardo, M., C. Budd, A. R. Champneys, and P. Kowalczyk (2008): *Piecewise-Smooth Dynamical Systems: Theory and Applications*. 1st ed. Vol. 163. Applied Mathematical Sciences. London: Springer-Verlag.

[21] Betts, J. T. (1998): Survey of Numerical Methods for Trajectory Optimization. *Journal of Guidance, Control, and Dynamics* **21**(2), pp. 193–207.

[22] Betts, J. T. (2010): *Practical Methods for Optimal Control and Estimation Using Nonlinear Programming, Second Edition*. 2nd ed. Philadelphia, PA: Society for Industrial and Applied Mathematics.

[23] Bevanda, P., S. Sosnowski, and S. Hirche (2021): Koopman operator dynamical models: Learning, analysis and control. *Annual Reviews in Control* **52**, pp. 197–212.

[24] Bezanson, J., A. Edelman, S. Karpinski, and V. B. Shah (2017): Julia: A Fresh Approach to Numerical Computing. *SIAM Review* **59**(1), pp. 65–98.

[25] Bohannon, R. W. (1997): Comfortable and maximum walking speed of adults aged 20—79 years: reference values and determinants. *Age and Ageing* **26**(1), pp. 15–19.

[26] Bordalba, R., T. Schoels, L. Ros, J. M. Porta, and M. Diehl (2023): Direct Collocation Methods for Trajectory Optimization in Constrained Robotic Systems. *IEEE Transactions on Robotics* **39**(1), pp. 183–202.

[27] Bratta, A., M. Focchi, N. Rathod, and C. Semini (2023): Optimization-Based Reference Generator for Nonlinear Model Predictive Control of Legged Robots. *Robotics* **12**(1), p. 6.

[28] Brogliato, B. (2016): *Nonsmooth Mechanics: Models, Dynamics and Control*. 3rd ed. Communications and Control Engineering. Switzerland: Springer Cham.

[29] Bruder, D., X. Fu, R. B. Gillespie, C. D. Remy, and R. Vasudevan (2021): Data-Driven Control of Soft Robots Using Koopman Operator Theory. *IEEE Transactions on Robotics* **37**(3), pp. 948–961.

[30] Carvalho, A. S. and J. M. Martins (2019): Exact restitution and generalizations for the Hunt–Crossley contact model. *Mechanism and Machine Theory* **139**, pp. 174–194.

[31] Castillo, G. A., B. Weng, W. Zhang, and A. Hereid (2020): Hybrid Zero Dynamics Inspired Feedback Control Policy Design for 3D Bipedal Locomotion using Reinforcement Learning. In: *2020 IEEE International Conference on Robotics and Automation (ICRA)*, pp. 8746–8752.

[32] Chaturvedi, E., C. Sandu, and A. Sandu (2025): A nonsmooth dynamics framework for simulating frictionless spatial joints with clearances. *Multibody System Dynamics* **63**(1-2), pp. 3–37.

[33] Chen, C., P. Xiang, J. Zhang, R. Xiong, Y. Wang, and H. Lu (2024): Deep Reinforcement Learning Based Co- Optimization of Morphology and Gait for Small-Scale Legged Robot. *IEEE/ASME Transactions on Mechatronics* **29**(4), pp. 2697–2708.

[34] Chevallereau, C., G. Abba, Y. Aoustin, F. Plestan, E. Westervelt, C. Canudas-De-Wit, and J. Grizzle (2003): RABBIT: a testbed for advanced control theory. *IEEE Control Systems Magazine* **23**(5), pp. 57–79.

[35] Chevallereau, C., E. R. Westervelt, and J. W. Grizzle (2005): Asymptotically Stable Running for a Five-Link, Four-Actuator, Planar Bipedal Robot. *The International Journal of Robotics Research* **24**(6), pp. 431–464.

[36] Collins, S., A. Ruina, R. Tedrake, and M. Wisse (2005): Efficient Bipedal Robots Based on Passive-Dynamic Walkers. *Science* **307**(5712), pp. 1082–1085.

[37] Dai, H., A. Valenzuela, and R. Tedrake (2014): Whole-body motion planning with centroidal dynamics and full kinematics. In: *2014 IEEE-RAS International Conference on Humanoid Robots*, pp. 295–302.

[38] Darvish, K., L. Penco, J. Ramos, R. Cisneros, J. Pratt, E. Yoshida, S. Ivaldi, and D. Pucci (2023): Teleoperation of Humanoid Robots: A Survey. *IEEE Transactions on Robotics* **39**(3), pp. 1706–1727.

[39] DeDonato, M., V. Dimitrov, R. Du, R. Giovacchini, K. Knoedler, X. Long, F. Polido, M. A. Gennert, T. Padir, S. Feng, H. Moriguchi, E. Whitman, X. Xinjilefu, and C. G. Atkeson (2015): Human-in-the-loop Control of a Humanoid Robot for Disaster Response: A Report from the DARPA Robotics Challenge Trials. *Journal of Field Robotics* **32**(2), pp. 275–292.

[40] Dehghani, R., A. Fattah, and E. Abedi (2015): Cyclic gait planning and control of a five-link biped robot with four actuators during single support and double support phases. *Multibody System Dynamics* **33**(4), pp. 389–411.

[41] Deuflhard, P. (2011): *Newton Methods for Nonlinear Problems: Affine Invariance and Adaptive Algorithms*. 1st ed. Springer Series in Computational Mathematics. Heidelberg: Springer Berlin.

[42] Diehl, M., H. Bock, H. Diedam, and P.-B. Wieber (2006): Fast Direct Multiple Shooting Algorithms for Optimal Robot Control. In: M. Diehl and K. Mombaur eds. Lecture Notes in Control and Information Sciences. Berlin, Heidelberg: Springer, pp. 65–93.

[43] Ding, L., H. Gao, Z. Deng, J. Song, Y. Liu, G. Liu, and K. Iagnemma (2013): Foot–terrain interaction mechanics for legged robots: Modeling and experimental validation. *The International Journal of Robotics Research* **32**(13), pp. 1585–1606.

[44] Exley, T. and A. Jafari (2021): Maximizing energy efficiency of variable stiffness actuators through an interval-based optimization framework. *Sensors and Actuators A: Physical* **332**, p. 113123.

[45] Farin, G. (2002): *Curves and Surfaces for CAGD: A Practical Guide*. 5th ed. The Morgan Kaufmann Series in Computer Graphics. San Francisco, CA: Academic Press.

[46] Farris, D. J. and G. S. Sawicki (2011): The mechanics and energetics of human walking and running: a joint level perspective. *Journal of The Royal Society Interface* **9**(66), pp. 110–118.

[47] Featherstone, R. (2008): *Rigid Body Dynamics Algorithms*. 1st ed. New York, NY: Springer New York.

[48] Fliess, M., J. Levine, P. Martin, and P. Rouchon (1999): A Lie-Backlund approach to equivalence and flatness of nonlinear systems. *IEEE Transactions on Automatic Control* **44**(5), pp. 922–937.

[49] Flores, P. (2010): A parametric study on the dynamic response of planar multibody systems with multiple clearance joints. *Nonlinear Dynamics* **61**(4), pp. 633–653.

[50] Flores, P. and J. Ambrósio (2010): On the contact detection for contact-impact analysis in multibody systems. *Multibody System Dynamics* **24**(1), pp. 103–122.

[51] Flores, P., M. Machado, M. T. Silva, and J. M. Martins (2011): On the continuous contact force models for soft materials in multibody dynamics. *Multibody System Dynamics* **25**(3), pp. 357–375.

[52] Flores, P. (2022): Contact mechanics for dynamical systems: a comprehensive review. *Multibody System Dynamics* **54**(2), pp. 127–177.

[53] Flores, P., J. Ambrósio, and H. Lankarani (2023): Contact-impact events with friction in multibody dynamics: Back to basics. *Mechanism and Machine Theory* **184**, p. 105305.

[54] Galloway, K., K. Sreenath, A. D. Ames, and J. W. Grizzle (2015): Torque Saturation in Bipedal Robotic Walking Through Control Lyapunov Function-Based Quadratic Programs. *IEEE Access* **3**, pp. 323–332.

[55] Ghaednia, H., X. Wang, S. Saha, Y. Xu, A. Sharma, and R. L. Jackson (2017): A Review of Elastic–Plastic Contact Mechanics. *Applied Mechanics Reviews* **69**(060804).

[56] Golub, G. H. and C. F. Van Loan (2013): *Matrix Computations*. 4th ed. Baltimore, MD: Johns Hopkins University Press.

[57] Gong, Y. and J. W. Grizzle (2022): Zero Dynamics, Pendulum Models, and Angular Momentum in Feedback Control of Bipedal Locomotion. *Journal of Dynamic Systems, Measurement, and Control* **144**(121006).

[58] Gonzalez-Aguirre, J. A., R. Osorio-Oliveros, K. L. Rodríguez-Hernández, J. Lizárraga-Iturralde, R. Morales Menendez, R. A. Ramírez-Mendoza, M. A. Ramírez-Moreno, and J. d. J. Lozoya-Santos (2021): Service Robots: Trends and Technology. *Applied Sciences* **11**(22), p. 10702.

[59] Griffin, B. and J. Grizzle (2017): Nonholonomic virtual constraints and gait optimization for robust walking control. *The International Journal of Robotics Research* **36**(8), pp. 895–922.

[60] Grizzle, J., J. Hurst, B. Morris, H.-W. Park, and K. Sreenath (2009): MABEL, a new robotic bipedal walker and runner. In: *2009 American Control Conference*, pp. 2030–2036.

[61] Grizzle, J. W., C. Chevallereau, R. W. Sinnet, and A. D. Ames (2014): Models, feedback control, and open problems of 3D bipedal robotic walking. *Automatica* **50**(8), pp. 1955–1988.

[62] Gros, S., M. Zanon, R. Quirynen, A. Bemporad, and M. Diehl (2020): From linear to nonlinear MPC: bridging the gap via the real-time iteration. *International Journal of Control* **93**(1), pp. 62–80.

[63] Haeufle, D. F. B., M. D. Taylor, S. Schmitt, and H. Geyer (2012): A clutched parallel elastic actuator concept: Towards energy efficient powered legs in

prosthetics and robotics. In: *2012 4th IEEE RAS & EMBS International Conference on Biomedical Robotics and Biomechatronics (BioRob)*, pp. 1614–1619.

[64] Hagenmeyer, V. and E. Delaleau (2003): Exact feedforward linearization based on differential flatness. *International Journal of Control* **76**(6), pp. 537–556.

[65] Hairer, E. and G. Wanner (1999): Stiff differential equations solved by Radau methods. *Journal of Computational and Applied Mathematics* **111**(1), pp. 93–111.

[66] Hamed, K. A., N. Sadati, W. A. Gruver, and G. A. Dumont (2012): Stabilization of Periodic Orbits for Planar Walking With Noninstantaneous Double-Support Phase. *IEEE Transactions on Systems, Man, and Cybernetics - Part A: Systems and Humans* **42**(3), pp. 685–706.

[67] Haug, E. (2018): Simulation of friction and stiction in multibody dynamics model problems. *Mechanics Based Design of Structures and Machines* **46**(3), pp. 296–317.

[68] Hereid, A., C. M. Hubicki, E. A. Cousineau, J. W. Hurst, and A. D. Ames (2015): Hybrid zero dynamics based multiple shooting optimization with applications to robotic walking. In: *2015 IEEE International Conference on Robotics and Automation (ICRA)*, pp. 5734–5740.

[69] Hereid, A., C. M. Hubicki, E. A. Cousineau, and A. D. Ames (2018): Dynamic Humanoid Locomotion: A Scalable Formulation for HZD Gait Optimization. *IEEE Transactions on Robotics* **34**(2), pp. 370–387.

[70] Hertz, H. (1882): Ueber die Berührung fester elastischer Körper. *Journal für die reine und angewandte Mathematik* **92**, pp. 156–171.

[71] Hirukawa, H., S. Hattori, K. Harada, S. Kajita, K. Kaneko, F. Kanehiro, K. Fujiwara, and M. Morisawa (2006): A universal stability criterion of the foot contact of legged robots - adios ZMP. In: *Proceedings 2006 IEEE International Conference on Robotics and Automation, 2006. ICRA 2006.* Pp. 1976–1983.

[72] Hobbelen, D. and M. Wisse (2008): Controlling the Walking Speed in Limit Cycle Walking. *The International Journal of Robotics Research* **27**(9), pp. 989–1005.

[73] Hu, C., S. Xie, L. Gao, S. Lu, and J. Li (2023): An overview on bipedal gait control methods. *IET Collaborative Intelligent Manufacturing* **5**(3), e12080.

[74] Hubicki, C., J. Grimes, M. Jones, D. Renjewski, A. Spröwitz, A. Abate, and J. Hurst (2016): ATRIAS: Design and validation of a tether-free 3D-capable spring-mass bipedal robot. *The International Journal of Robotics Research* **35**(12), pp. 1497–1521.

[75] Hunt, K. H. and F. R. E. Crossley (1975): Coefficient of Restitution Interpreted as Damping in Vibroimpact. *Journal of Applied Mechanics* **42**(2), pp. 440–445.

[76] Hutter, M., C. D. Remy, M. A. Hoepflinger, and R. Siegwart (2013): Efficient and Versatile Locomotion With Highly Compliant Legs. *IEEE/ASME Transactions on Mechatronics* **18**(2), pp. 449–458.

[77] Hwang, K.-S., J.-L. Lin, and K.-H. Yeh (2015): Learning to Adjust and Refine Gait Patterns for a Biped Robot. *IEEE Transactions on Systems, Man, and Cybernetics: Systems* **45**(12), pp. 1481–1490.

[78] Hwangbo, J., J. Lee, A. Dosovitskiy, D. Bellicoso, V. Tsounis, V. Koltun, and M. Hutter (2019): Learning agile and dynamic motor skills for legged robots. *Science Robotics* **4**(26), eaau5872.

[79] Isidori, A. (1995): *Nonlinear Control Systems*. 3rd ed. London: Springer-Verlag.

[80] Jacobson, N. (2009): *Basic Algebra I*. 2nd ed. Mineola, New York: Dover Publications.

[81] Jain, A. (2011): *Robot and Multibody Dynamics: Analysis and Algorithms*. 1st ed. New York, NY: Springer New York.

[82] Johannink, T., S. Bahl, A. Nair, J. Luo, A. Kumar, M. Loskyll, J. A. Ojea, E. Solowjow, and S. Levine (2019): Residual Reinforcement Learning for Robot Control. In: *2019 International Conference on Robotics and Automation (ICRA)*, pp. 6023–6029.

[83] Johnson, K. L. (1987): *Contact Mechanics*. Cambridge, UK: Cambridge University Press.

[84] Kaneko, K., M. Morisawa, S. Kajita, S. Nakaoka, T. Sakaguchi, R. Cisneros, and F. Kanehiro (2015): Humanoid robot HRP-2Kai — Improvement of HRP-2 towards disaster response tasks. In: *2015 IEEE-RAS 15th International Conference on Humanoid Robots (Humanoids)*, pp. 132–139.

[85] Kaneko, K., H. Kaminaga, T. Sakaguchi, S. Kajita, M. Morisawa, I. Kumagai, and F. Kanehiro (2019): Humanoid Robot HRP-5P: An Electrically Actuated Humanoid Robot With High-Power and Wide-Range Joints. *IEEE Robotics and Automation Letters* **4**(2), pp. 1431–1438.

[86] Kashiri, N., J. Malzahn, and N. G. Tsagarakis (2017): On the Sensor Design of Torque Controlled Actuators: A Comparison Study of Strain Gauge and Encoder-Based Principles. *IEEE Robotics and Automation Letters* **2**(2), pp. 1186–1194.

[87] Kashiri, N., A. Abate, S. J. Abram, A. Albu-Schaffer, P. J. Clary, M. Daley, S. Faraji, R. Furnemont, M. Garabini, H. Geyer, A. M. Grabowski, J. Hurst, J. Malzahn, G. Mathijssen, D. Remy, W. Roozing, M. Shahbazi, S. N. Simha, J.-B. Song, N. Smit-Anseeuw, S. Stramigioli, B. Vanderborght, Y. Yesilevskiy, and N. Tsagarakis (2018): An Overview on Principles for Energy Efficient Robot Locomotion. *Frontiers in Robotics and AI* **5**(129).

[88] Kelly, M. (2017): An Introduction to Trajectory Optimization: How to Do Your Own Direct Collocation. *SIAM Review* **59**(4), pp. 849–904.

[89] Khan, M. S. and R. K. Mandava (2023): A review on gait generation of the biped robot on various terrains. *Robotica* **41**(6), pp. 1888–1930.

[90] Köbis, M. A. and M. Arnold (2014): Numerical solution of penalty formulations for constrained mechanical systems using heterogeneous multiscale methods. *Journal of Computational and Applied Mathematics* **262**, pp. 193–204.

[91] Kolathaya, S., A. Hereid, and A. D. Ames (2016): Time dependent control Lyapunov functions and hybrid zero dynamics for stable robotic locomotion. In: *2016 American Control Conference (ACC)*, pp. 3916–3921.

[92] Kong, N. J., J. Joe Payne, J. Zhu, and A. M. Johnson (2024): Saltation Matrices: The Essential Tool for Linearizing Hybrid Dynamical Systems. *Proceedings of the IEEE* **112**(6), pp. 585–608.

[93] Krack, M. and J. Gross (2019): *Harmonic Balance for Nonlinear Vibration Problems*. 1st ed. Mathematical Engineering. Switzerland: Springer, Cham.

[94] Kuindersma, S., R. Deits, M. Fallon, A. Valenzuela, H. Dai, F. Permenter, T. Koolen, P. Marion, and R. Tedrake (2016): Optimization-based locomotion planning, estimation, and control design for the atlas humanoid robot. *Autonomous Robots* **40**(3), pp. 429–455.

[95] Lacquaniti, F., Y. P. Ivanenko, and M. Zago (2012): Patterned control of human locomotion. *The Journal of Physiology* **590**(10), pp. 2189–2199.

[96] Lanczos, C. (1962): *The Variational Principles of Mechanics*. 2nd ed. Toronto: University of Toronto Press.

[97] Lee, C., S. Kwak, J. Kwak, and S. Oh (2017): Generalization of Series Elastic Actuator Configurations and Dynamic Behavior Comparison. *Actuators* **6**(3), p. 26.

[98] Li, T., Z. Yu, J. Chen, Y. Liu, M. Zheng, L. Meng, G. Ma, W. Zhang, W. Zhang, and Q. Huang (2014): Stability control for biped walking based on phase modification during double support period. In: *2014 IEEE International Conference on Robotics and Biomimetics (ROBIO 2014)*, pp. 1290–1295.

[99] Li, Y., B. Li, J. Ruan, and X. Rong (2011): Research of mammal bionic quadruped robots: A review. In: *2011 IEEE 5th International Conference on Robotics, Automation and Mechatronics (RAM)*, pp. 166–171.

[100] Li, Z., X. Cheng, X. B. Peng, P. Abbeel, S. Levine, G. Berseth, and K. Sreenath (2021): Reinforcement Learning for Robust Parameterized Locomotion Control of Bipedal Robots. In: *2021 IEEE International Conference on Robotics and Automation (ICRA)*, pp. 2811–2817.

[101] Lichtwark, G. A. and C. J. Barclay (2010): The influence of tendon compliance on muscle power output and efficiency during cyclic contractions. *Journal of Experimental Biology* **213**(5), pp. 707–714.

[102] Lim, H.-o. and A. Takanishi (2006): Biped walking robots created at Waseda University: WL and WABIAN family. *Philosophical Transactions of the Royal Society A: Mathematical, Physical and Engineering Sciences* **365**(1850), pp. 49–64.

[103] Liu, Q., J. Liang, and O. Ma (2020): A physics-based and data-driven hybrid modeling method for accurately simulating complex contact phenomenon. *Multibody System Dynamics* **50**(1), pp. 97–117.

[104] Liu, R., F. Nageotte, P. Zanne, M. de Mathelin, and B. Dresp-Langley (2021): Deep Reinforcement Learning for the Control of Robotic Manipulation: A Focussed Mini-Review. *Robotics* **10**(1), p. 22.

[105] Liu, X., Y. Sun, S. Wen, K. Cao, Q. Qi, X. Zhang, H. Shen, G. Chen, J. Xu, and A. Ji (2024): Development of Wheel-Legged Biped Robots: A Review. *Journal of Bionic Engineering* **21**(2), pp. 607–634.

[106] Liu, Y.-Y. and A.-L. Barabási (2016): Control principles of complex systems. *Reviews of Modern Physics* **88**(3), p. 035006.

[107] Lunze, J. (2020): *Regelungstechnik 1: Systemtheoretische Grundlagen, Analyse und Entwurf einschleifiger Regelungen*. 12th ed. Heidelberg: Springer Vieweg Berlin.

[108] Ma, J., G. Chen, L. Ji, L. Qian, and S. Dong (2020): A general methodology to establish the contact force model for complex contacting surfaces. *Mechanical Systems and Signal Processing* **140**, p. 106678.

[109] Ma, W.-L., S. Kolathaya, E. R. Ambrose, C. M. Hubicki, and A. D. Ames (2017): Bipedal Robotic Running with DURUS-2D: Bridging the Gap between Theory and Experiment. In: *Proceedings of the 20th International Conference on Hybrid Systems: Computation and Control*. HSCC '17. New York, NY, USA: Association for Computing Machinery, pp. 265–274.

[110] Machado, M., P. Moreira, P. Flores, and H. M. Lankarani (2012): Compliant contact force models in multibody dynamics: Evolution of the Hertz contact theory. *Mechanism and Machine Theory* **53**, pp. 99–121.

[111] Margolis, G. B., G. Yang, K. Paigwar, T. Chen, and P. Agrawal (2024): Rapid locomotion via reinforcement learning. *The International Journal of Robotics Research* **43**(4), pp. 572–587.

[112] Martin, A. E., D. C. Post, and J. P. Schmiedeler (2014): Design and experimental implementation of a hybrid zero dynamics-based controller for planar bipeds with curved feet. *The International Journal of Robotics Research* **33**(7), pp. 988–1005.

[113] Mazumdar, A., S. J. Spencer, C. Hobart, J. Salton, M. Quigley, T. Wu, S. Bertrand, J. Pratt, and S. P. Buerger (2017): Parallel Elastic Elements Improve Energy Efficiency on the STEPPR Bipedal Walking Robot. *IEEE/ASME Transactions on Mechatronics* **22**(2), pp. 898–908.

[114] McGeer, T. (1990): Passive Dynamic Walking. *The International Journal of Robotics Research* **9**(2), pp. 62–82.

[115] Meng, X., Z. Yu, X. Chen, Z. Huang, C. Dong, and F. Meng (2023): Online Running-Gait Generation for Bipedal Robots with Smooth State Switching and Accurate Speed Tracking. *Biomimetics* **8**(1), p. 114.

[116] Merkin, D. R. (1997): *Introduction to the Theory of Stability*. 1st ed. Texts in Applied Mathematics. New York, NY: Springer.

[117] Mitra, A. C., E. Fernandes, K. Nawpute, S. Sheth, V. Kadam, and S. J. Chikhale (2018): Development and Validation of a Simulation Model of Automotive Suspension System using MSC-ADAMS. *Materials Today: Proceedings*. 7th International Conference of Materials Processing and Characterization, March 17-19, 2017 **5**(2, Part 1), pp. 4327–4334.

[118] Morris, B. and J. Grizzle (2005): A Restricted Poincaré Map for Determining Exponentially Stable Periodic Orbits in Systems with Impulse Effects: Application to Bipedal Robots. In: *Proceedings of the 44th IEEE Conference on Decision and Control*, pp. 4199–4206.

[119] Mou, H., J. Xue, J. Liu, Z. Feng, Q. Li, and J. Zhang (2023): A Multi-Agent Reinforcement Learning Method for Omnidirectional Walking of Bipedal Robots. *Biomimetics* **8**(8), p. 616.

[120] Müller, P. C. (1995): Calculation of Lyapunov exponents for dynamic systems with discontinuities. *Chaos, Solitons & Fractals*. Some Nonlinear Oscillations Problems in Engineering Sciences **5**(9), pp. 1671–1681.

[121] Naimi, A., J. Deng, V. Vajpayee, V. Becerra, S. R. Shimjith, and A. J. Arul (2022): Nonlinear Model Predictive Control Using Feedback Linearization for a Pressurized Water Nuclear Power Plant. *IEEE Access* **10**, pp. 16544–16555.

[122] Nayfeh, A. H. and B. Balachandran (1995): *Applied Nonlinear Dynamics: Analytical, Computational, and Experimental Methods*. Hoboken, New Jersey: John Wiley & Sons.

[123] Neunert, M., F. Farshidian, A. W. Winkler, and J. Buchli (2017): Trajectory Optimization Through Contacts and Automatic Gait Discovery for Quadrupeds. *IEEE Robotics and Automation Letters* **2**(3), pp. 1502–1509.

[124] Neunert, M., M. Stäuble, M. Giftthaler, C. D. Bellicoso, J. Carius, C. Gehring, M. Hutter, and J. Buchli (2018): Whole-Body Nonlinear Model Predictive Control Through Contacts for Quadrupeds. *IEEE Robotics and Automation Letters* **3**(3), pp. 1458–1465.

[125] Nocedal, J. and S. J. Wright (2006): *Numerical Optimization*. 2nd ed. Springer Series in Operations Research and Financial Engineering. New York, NY: Springer.

[126] Noghredani, N. and N. Pariz (2021): Robust adaptive control for a class of nonlinear switched systems using state-dependent switching. *SN Applied Sciences* **3**(3), p. 290.

[127] Oh, S. and K. Kong (2017): High-Precision Robust Force Control of a Series Elastic Actuator. *IEEE/ASME Transactions on Mechatronics* **22**(1), pp. 71–80.

[128] Paine, N., S. Oh, and L. Sentis (2014): Design and Control Considerations for High-Performance Series Elastic Actuators. *IEEE/ASME Transactions on Mechatronics* **19**(3), pp. 1080–1091.

[129] Park, H.-W., A. Ramezani, and J. W. Grizzle (2013): A Finite-State Machine for Accommodating Unexpected Large Ground-Height Variations in Bipedal Robot Walking. *IEEE Transactions on Robotics* **29**(2), pp. 331–345.

[130] Park, H. Y., J. H. Kim, and K. Yamamoto (2022): A New Stability Framework for Trajectory Tracking Control of Biped Walking Robots. *IEEE Transactions on Industrial Informatics* **18**(10), pp. 6767–6777.

[131] Perko, L. (2013): *Differential Equations and Dynamical Systems*. 3rd ed. Vol. 7. Texts in Applied Mathematics. New York, NY: Springer.

[132] Peyré-Tartaruga, L. A., A. H. Dewolf, P. E. di Prampero, G. Fábrica, D. Malatesta, A. E. Minetti, A. Monte, G. Pavei, V. Silva-Pereyra, P. A. Willems, and P. Zamparo (2021): Mechanical work as a (key) determinant of energy cost in human locomotion: recent findings and future directions. *Experimental Physiology* **106**(9), pp. 1897–1908.

[133] Pfeiffer, F. and C. Glocker (1996): *Multibody Dynamics with Unilateral Contacts*. First published: 21 August 1996. Online ISBN: 978-3-527-61838-5. Hoboken, New Jersey: John Wiley & Sons.

[134] Pfeiffer, F. (2008): On non-smooth dynamics. *Meccanica* **43**(5), pp. 533–554.

[135] Pfeiffer, F. (2012): On non-smooth multibody dynamics. *Proceedings of the Institution of Mechanical Engineers, Part K: Journal of Multi-body Dynamics* **226**(2), pp. 147–177.

[136] Posa, M., C. Cantu, and R. Tedrake (2014): A direct method for trajectory optimization of rigid bodies through contact. *The International Journal of Robotics Research* **33**(1), pp. 69–81.

[137] Posa, M., S. Kuindersma, and R. Tedrake (2016): Optimization and stabilization of trajectories for constrained dynamical systems. In: *2016 IEEE International Conference on Robotics and Automation (ICRA)*, pp. 1366–1373.

[138] Pratt, G. A. and M. M. Williamson (1995): Series Elastic Actuators. In: *Proceedings of the 1995 IEEE/RSJ International Conference on Intelligent Robots and Systems (IROS '95): Human Robot Interaction and Cooperative Robots*. Vol. 1. Pittsburgh, PA, USA: IEEE, pp. 399–406.

[139] Pratt, J. E., A. Torres, P. Dilworth, and G. A. Pratt (1996): Virtual Actuator Control. In: *Proceedings of the 1996 IEEE/RSJ International Conference on Intelligent Robots and Systems (IROS '96)*. Vol. 3. Osaka, Japan: IEEE, pp. 1219–1226.

[140] Pratt, J., C.-M. Chew, A. Torres, P. Dilworth, and G. Pratt (2001): Virtual Model Control: An Intuitive Approach for Bipedal Locomotion. *The International Journal of Robotics Research* **20**(2), pp. 129–143.

[141] Pratt, J., T. Koolen, T. de Boer, J. Rebula, S. Cotton, J. Carff, M. Johnson, and P. Neuhaus (2012): Capturability-based analysis and control of legged locomotion, Part 2: Application to M2V2, a lower-body humanoid. *The International Journal of Robotics Research* **31**(10), pp. 1117–1133.

[142] Qian, X., H. Shen, Y. Yin, and D. Guo (2024): Nonlinear Model Predictive Control for a Dynamic Positioning Ship Based on the Laguerre Function. *Journal of Marine Science and Engineering* **12**(2), p. 294.

[143] Reher, J., E. A. Cousineau, A. Hereid, C. M. Hubicki, and A. D. Ames (2016): Realizing dynamic and efficient bipedal locomotion on the humanoid robot DURUS. In: *2016 IEEE International Conference on Robotics and Automation (ICRA)*, pp. 1794–1801.

[144] Reher, J., C. Kann, and A. D. Ames (2020): An Inverse Dynamics Approach to Control Lyapunov Functions. In: *2020 American Control Conference (ACC)*, pp. 2444–2451.

[145] Reher, J. and A. Ames (2021): Dynamic Walking: Toward Agile and Efficient Bipedal Robots. *Annual Review of Control, Robotics, and Autonomous Systems* **4**, pp. 535–572.

[146] Roaas, A. and G. B. J. Andersson (1982): Normal Range of Motion of the Hip, Knee and Ankle Joints in Male Subjects, 30–40 Years of Age. *Acta Orthopaedica*, pp. 205–208.

[147] Römer, U. J., C. Kuhs, M. J. Krause, and A. Fidlin (2016): Simultaneous optimization of gait and design parameters for bipedal robots. In: *2016 IEEE International Conference on Robotics and Automation (ICRA)*, pp. 1374–1381.

[148] Roozing, W., Z. Ren, and N. G. Tsagarakis (2018): Design of a Novel 3-DoF Leg with Series and Parallel Compliant Actuation for Energy Efficient Articulated Robots. In: *2018 IEEE International Conference on Robotics and Automation (ICRA)*, pp. 6068–6075.

[149] Sahoo, A. K. and S. Chakraverty (2022): Machine Intelligence in Dynamical Systems: A State-of-Art Review. *Wiley Interdisciplinary Reviews: Data Mining and Knowledge Discovery* **12**(4), e1461.

[150] Sastry, S. (1999): *Nonlinear Systems: Analysis, Stability, and Control*. 1st ed. Interdisciplinary Applied Mathematics. New York, NY: Springer.

[151] Scheint, M., M. Sobotka, and M. Buss (2009): Virtual holonomic constraint approach for planar bipedal walking robots extended to double support. In: *Proceedings of the 48h IEEE Conference on Decision and Control (CDC) held jointly with 2009 28th Chinese Control Conference*, pp. 8180–8185.

[152] Schupp, G., H. Netter, L. Mauer, and M. Gretzschel (1999): Multibody System Simulation of Railway Vehicles with SIMPACK. In: *The Manchester Benchmarks*

for Rail Vehicle Simulation. S. Iwnicki ed. 1st ed. London: Routledge / CRC Press. Chap. 11, pp. 101–118.

[153] Schwenzer, M., M. Ay, T. Bergs, and D. Abel (2021): Review on model predictive control: an engineering perspective. *The International Journal of Advanced Manufacturing Technology* **117**(5), pp. 1327–1349.

[154] Seifried, R., W. Schiehlen, and P. Eberhard (2010): The role of the coefficient of restitution on impact problems in multi-body dynamics. *Proceedings of the Institution of Mechanical Engineers, Part K: Journal of Multi-body Dynamics* **224**(3), pp. 279–306.

[155] Silva, M. F., J. A. T. Machado, and A. M. Lopes (2005): Modelling and simulation of artificial locomotion systems. *Robotica* **23**(5), pp. 595–606.

[156] Simeon, B. (2013): *Computational Flexible Multibody Dynamics: A Differential-Algebraic Approach*. 1st ed. Differential-Algebraic Equations Forum. Heidelberg: Springer Berlin.

[157] Simoes, A. A., E. Stratoglou, A. Bloch, and L. J. Colombo (2023): Virtual nonholonomic constraints: A geometric approach. *Automatica* **155**, p. 111166.

[158] Singh, B., A. Vijayvargiya, and R. Kumar (2022): Kinematic Modeling for Biped Robot Gait Trajectory Using Machine Learning Techniques. *Journal of Bionic Engineering* **19**(2), pp. 355–369.

[159] Singh, B., S. Patel, A. Vijayvargiya, and R. Kumar (2023): Data-driven gait model for bipedal locomotion over continuous changing speeds and inclines. *Autonomous Robots* **47**(6), pp. 753–769.

[160] Sontag, E. D. (1998): *Mathematical Control Theory: Deterministic Finite Dimensional Systems*. 2nd ed. Vol. 6. Texts in Applied Mathematics. New York, NY: Springer.

[161] Sreenath, K., H.-W. Park, I. Poulakakis, and J. Grizzle (2013): Embedding active force control within the compliant hybrid zero dynamics to achieve stable, fast running on MABEL. *The International Journal of Robotics Research* **32**(3), pp. 324–345.

[162] Stöckel, T., R. Jacksteit, M. Behrens, R. Skripitz, R. Bader, and A. Mau-Moeller (2015): The mental representation of the human gait in young and older adults. *Frontiers in Psychology* **6**, p. 943.

[163] Strogatz, S. H. (2019): *Nonlinear Dynamics and Chaos: With Applications to Physics, Biology, Chemistry, and Engineering*. 2nd ed. Boca Raton: CRC Press.

[164] Sugihara, T. and M. Morisawa (2020): A survey: dynamics of humanoid robots. *Advanced Robotics* **34**(21-22), pp. 1338–1352.

[165] Suleiman, W., F. Kanehiro, K. Miura, and E. Yoshida (2011): Enhancing Zero Moment Point-Based Control Model: System Identification Approach. *Advanced Robotics* **25**(3-4), pp. 427–446.

[166] Tang, X., X. Wang, X. Ji, Y. Zhou, J. Yang, Y. Wei, and W. Zhang (2022): A Wearable Lower Limb Exoskeleton: Reducing the Energy Cost of Human Movement. *Micromachines* **13**(6), p. 900.

[167] Tran Thien, H., C. Van Kien, and H. P. H. Anh (2020): Optimized stable gait planning of biped robot using multi-objective evolutionary JAYA algorithm. *International Journal of Advanced Robotic Systems* **17**(6), p. 1729881420976344.

[168] Tucker, M. and A. D. Ames (2023): An Input-to-State Stability Perspective on Robust Locomotion. *IEEE Control Systems Letters* **7**, pp. 2599–2604.

[169] Udwadia, F. E. (2000): Fundamental Principles of Lagrangian Dynamics: Mechanical Systems with Non-ideal, Holonomic, and Nonholonomic Constraints. *Journal of Mathematical Analysis and Applications* **251**(1), pp. 341–355.

[170] Udwadia, F. E. and R. E. Kalaba (2000): Nonideal Constraints and Lagrangian Dynamics. *Journal of Aerospace Engineering* **13**(1), pp. 17–22.

[171] Verstraten, T., P. Beckerle, R. Furnémont, G. Mathijssen, B. Vanderborght, and D. Lefeber (2016): Series and Parallel Elastic Actuation: Impact of natural dynamics on power and energy consumption. *Mechanism and Machine Theory* **102**, pp. 232–246.

[172] Vukobratović, M. and B. Borovac (2004): Zero-moment point — thirty five years of its life. *International Journal of Humanoid Robotics* **01**(01), pp. 157–173.

[173] Vyasarayani, C. P., T. Uchida, A. Carvalho, and J. McPhee (2011): Parameter identification in dynamic systems using the homotopy optimization approach. *Multibody System Dynamics* **26**(4), pp. 411–424.

[174] Warner, F. W. (1983): *Foundations of Differentiable Manifolds and Lie Groups*. 1st ed. Graduate Texts in Mathematics. New York, NY: Springer.

[175] Westervelt, E., J. Grizzle, and D. Koditschek (2003): Hybrid zero dynamics of planar biped walkers. *IEEE Transactions on Automatic Control* **48**(1), pp. 42–56.

[176] Westervelt, E. R., G. Buche, and J. W. Grizzle (2004): Experimental Validation of a Framework for the Design of Controllers that Induce Stable Walking in Planar Bipeds. *The International Journal of Robotics Research* **23**(6), pp. 559–582.

[177] Westervelt, E., J. Grizzle, C. Chevallereau, J.-H. Choi, and B. Morris (2018): *Feedback Control of Dynamic Bipedal Robot Locomotion*. Boca Raton, FL: CRC Press.

[178] Williams, D. S. and A. E. Martin (2019): Gait modification when decreasing double support percentage. *Journal of Biomechanics* **92**, pp. 76–83.

[179] Williams, D. S. and A. E. Martin (2020): Does a Finite-Time Double Support Period Increase Walking Stability for Planar Bipeds? *Journal of Mechanisms and Robotics* **13**(011019).

[180] Wittenburg, J. (2008): *Dynamics of Multibody Systems*. 2nd ed. Heidelberg: Springer Berlin.

[181] Woernle, C. (2022): *Mehrkörpersysteme: Eine Einführung in die Kinematik und Dynamik von Systemen starrer Körper*. 3rd ed. Heidelberg: Springer Vieweg Berlin.

[182] Xi, W., Y. Yesilevskiy, and C. D. Remy (2016): Selecting gaits for economical locomotion of legged robots. *The International Journal of Robotics Research* **35**(9), pp. 1140–1154.

[183] Xu, Z., J. Xie, and K. Hashimoto (2025): Human-Inspired Gait and Jumping Motion Generation for Bipedal Robots Using Model Predictive Control. *Biomimetics* **10**(1), p. 17.

[184] Yamamoto, K., T. Kamioka, and T. Sugihara (2020): Survey on model-based biped motion control for humanoid robots. *Advanced Robotics* **34**(21-22), pp. 1353–1369.

[185] Yang, G., L. Yang, and M. Cao (2019): Simulation analysis of timing belt movement characteristics based on RecurDyn. *Vibroengineering Procedia* **22**, pp. 13–18.

[186] Yang, T., E. R. Westervelt, J. P. Schmiedeler, and R. A. Bockbrader (2008): Design and control of a planar bipedal robot ERNIE with parallel knee compliance. *Autonomous Robots* **25**(4), pp. 317–330.

[187] Zentner, L. and S. Linß (2019): *Compliant systems, Mechanics of elastically deformable mechanisms, actuators and sensors*. Berlin, Boston: De Gruyter Oldenbourg.

[188] Zhao, H., S. Nadubettu Yadukumar, and A. D. Ames (2012): Bipedal robotic running with partial hybrid zero dynamics and human-inspired optimization. In: *2012 IEEE/RSJ International Conference on Intelligent Robots and Systems*, pp. 1821–1827.

[189] Zhu, H., M. Luo, T. Mei, J. Zhao, T. Li, and F. Guo (2016): Energy-efficient bio-inspired gait planning and control for biped robot based on human locomotion analysis. *Journal of Bionic Engineering* **13**(2), pp. 271–282.

Own Publications

[190] Luo, Y., U. J. Römer, and A. Fidlin (2021): The Influence of ground inclination on the energy efficiency of a bipedal walking robot. *Proc. Appl. Math. Mech.* **20**(1), e202000142.

[191] Luo, Y., U. J. Römer, S. Riegraf, A. Fidlin, M. Zirkel, and L. Zentner (2021): Anwendung einer Homotopie-Optimierungs-Methode zur Identifikation der Modellparameter eines Roboterprototyps. In: *3. VDI-Fachtagung Schwingungen 2021*. Würzburg: VDI Verlag, pp. 259–272.

[192] Luo, Y., M. Zirkel, U. J. Römer, L. Zentner, and A. Fidlin (2021): Improving energy efficiency of bipedal walking using nonlinear compliant mechanisms. *Proc. Appl. Math. Mech.* **21**(1), e202100197.

[193] Luo, Y., U. J. Römer, L. Zentner, and A. Fidlin (2022): Improving Energy Efficiency of a Bipedal Walker with Optimized Nonlinear Elastic Coupling. In: *Advances in Nonlinear Dynamics. NODYCON Conference Proceedings Series.* Cham: Springer International Publishing, pp. 253–262.

[194] Luo, Y., U. J. Römer, M. Zirkel, L. Zentner, and A. Fidlin (2024): Efficiency Study of the Non-instantaneous Double Support Phase in HZD Controlled Bipedal Robot. In: *Advances in Nonlinear Dynamics, Volume II*. W. Lacarbonara ed. Cham: Springer Nature Switzerland, pp. 73–82.

[195] Luo, Y., U. Römer, M. Zirkel, L. Zentner, and A. Fidlin (2024): Optimierte Energieeffizienz des zweibeinigen Gehens auf nachgiebigem Untergrund durch elastische Kopplung. *Zehnte IFToMM D-A-CH Konferenz 2024: 05./06. März 2024, Universität Rostock*.

[196] Zirkel, M., Y. Luo, U. J. Römer, A. Fidlin, and L. Zentner (2021): Parameter Study of Compliant Elements for a Bipedal Robot to Increase Its Walking Efficiency. In: *Microactuators, Microsensors and Micromechanisms*. L. Zentner and S. Strehle eds. Cham: Springer International Publishing, pp. 58–75.

[197] Zirkel, M., Y. Luo, U. J. Römer, A. Fidlin, and L. Zentner (2023): Development of a Database to Simulate and Adapt Compliant Mechanisms to a Given Characteristic for Improving Energy Efficiency of a Walking Robot. In: *Microactuators,*

Microsensors and Micromechanisms. A. K. Pandey, P. Pal, Nagahanumaiah, and L. Zentner eds. Cham: Springer International Publishing, pp. 46–60.

Supervised Theses

[198] Arbogast, P. L. (2023): *Energieeffizientes Rennen eines zweibeinigen Roboters auf nachgiebigem Untergrund*. Master Thesis. Karlsruhe: Karlsruhe Institute of Technology (KIT).

[199] Büttner, D. (2024): *Entwicklung eines Prüfstandsaufbaus zur Messung der mechanischen Verluste in Elektromotoren*. Bachelor Thesis. Karlsruhe: Karlsruhe Institute of Technology (KIT).

[200] Halschka, M. (2022): *Konzeption, Konstruktion und Messtechnik von mechatronischen Teilsystemen eines zweibeinigen Roboterprototyps*. Bachelor Thesis. Karlsruhe: Karlsruhe Institute of Technology (KIT).

[201] Hoenig, M. (2023): *Experimentelle Charakterisierung des elektrischen Antriebsstrangs eines Roboterprototyps*. Bachelor Thesis. Karlsruhe: Karlsruhe Institute of Technology (KIT).

[202] Horneff, N. (2024): *Development of a Kalman Filter for the Hybrid Dynamical System of a Bipedal Robot Prototype*. Master Thesis. Karlsruhe: Karlsruhe Institute of Technology (KIT).

[203] Kruthoff, C. J. (2022): *Konstruktion einer neuartigen elektrischen Antriebseinheit zum Ermöglichen von passiver Dynamik*. Bachelor Thesis. Karlsruhe: Karlsruhe Institute of Technology (KIT).

[204] Lamm, L. (2021): *Auslegung und Inbetriebnahme eines Prüfstandes zur Parameteridentifikation eines elektrischen Antriebsstrangs*. Bachelor Thesis. Karlsruhe: Karlsruhe Institute of Technology (KIT).

[205] Riegraf, S. (2021): *Die Anwendung der Homotopiemethode auf die Parameteridentifikation eines Roboterbeins*. Bachelor Thesis. Karlsruhe: Karlsruhe Institute of Technology (KIT).

[206] Singhal, D. (2022): *Inbetriebnahme eines Roboterprototyps*. Master Thesis. Karlsruhe: Karlsruhe Institute of Technology (KIT).

[207] Wildt, L. (2022): *Influence of Stairs on the Energy Efficiency of the Walking Gait of a Bi-Pedal Robot*. Bachelor Thesis. Karlsruhe: Karlsruhe Institute of Technology (KIT).

[208] Zhang, Z. (2022): *Energy Efficiency of Bipedal Robots on Stairs with Multiple Step Periods*. Bachelor Thesis. Karlsruhe: Karlsruhe Institute of Technology (KIT).

[209] Zubiaurre Andres, X. (2021): *Energy-efficient Distribution of Walking Speeds in the Environment with Variating Ground Inclination Angles*. Master Thesis. Karlsruhe: Karlsruhe Institute of Technology (KIT).